

DEVELOPMENT AND IMPROVEMENT OF AIRBORNE REMOTE SENSING RADAR
PLATFORMS

By

Copyright 2013

Emily J. Arnold

Submitted to the graduate degree program in Aerospace Engineering and the Graduate Faculty of
the University of Kansas in partial fulfillment of the requirements for the degree of Doctor of
Philosophy.

Chairperson: Dr. Richard Hale

Dr. Mark Ewing

Dr. Christopher Allen

Dr. Ronald Barrett-Gonzalez

Dr. Shahriar Keshmiri

Dr. Jie-Bang Yan

Date Defended: 26 June 2013

The Dissertation Committee for Emily J. Arnold
certifies that this is the approved version of the following dissertation:

DEVELOPMENT AND IMPROVEMENT OF AIRBORNE REMOTE SENSING RADAR
PLATFORMS

Chairperson: Dr. Richard Hale

Date approved: 26 June 2013

ABSTRACT

With the recent record ice melt in the Arctic as well as the dramatic changes occurring in the Antarctic, the need and urgency to characterize ice sheets in these regions has become a research thrust of both the NSF and NASA. Airborne remote sensing is the most effective way to collect the necessary data on a large scale with fine resolution. Current models for determining the relationship between the world's great ice sheets and global sea-level are limited by the availability of data on bed topography, glacier volume, internal layers, and basal conditions. This need could be satisfied by equipping long range aircraft with an appropriately sensitive suite of sensors. The goal of this work is to enable two new airborne radar installations for use in cryospheric surveying, and improve these systems as well as future systems by addressing aircraft integration effects on antenna-array performance.

An aerodynamic fairing is developed to enable a NASA DC-8 to support a 5-element array for CReSIS's Multi-channel, Coherent, Radar Depth Sounder (MCoRDS). This fairing is roughly 100" X 60" X 11" in size, weighs 420 lbs, and connects to the aircraft via a nadir viewport frame. The fairing is required to withstand five different and extreme combinations of aerodynamic, inertial, and thermally-induced loading. To ensure maximum electrical performance for the housed radar antennas, the material choice for all structural components below the ground plane is limited to dielectric materials. Ultimate load failure tests are foregone in favor of conservative design factors of safety. The structure is designed to have no failures at ultimate load. To maximize science mission range, the maximum allowable drag increase due to the fairing is required to be 5% or less. The presence of the fairing increases the total aircraft drag by only 1.3%. To date, the DC-8 flying laboratory has flown 75 science missions with the MCoRDS array, has logged almost 955 flight hours, and has collected more than 210 TB of unique science data.

Several structures are also developed to enable a NASA P-3 to support a 15-element MCoRDS array, as well as three other radar antenna-arrays used for cryospheric surveying. Three external fairings house the 15-element MCoRDS array. These fairing are primarily fabricated from S-2 glass/epoxy and are attached to the airframe via custom metallic pylons connected at existing wing hardpoints. Two of the fairings are located on opposite wings

outboard of the engines, and the third spans inboard wing hardpoints and extends across the belly of the fuselage. The outboard wing fairings are approximately 120" X 20" X 4" and weigh 160 lbs each, while the inboard fairing is approximately 210" X 20" X 4" and weighs 270 lbs. Custom outer mold-line S-2 glass/epoxy panels as well as metallic support structures are installed into the former bomb bay of the P-3 to support the three other antenna-arrays. Once again, ultimate load failure tests are foregone in favor of conservative design factors, and the structure is designed to withstand nine conservative load cases. The presence of the external fairings reduces roll control power by 2.54% and increases the total drag by 2.7%, but both of these performance reductions are acceptable for both pilot handling qualities and science mission range. To date, the P-3 has completed 122 arctic missions in 886 flight hours and has collected 129 TB of MCoRDS data. The entire sensor suite of the P-3 has collected roughly 240 TB of unique data.

Since the initial deployment of these systems, several studies are performed to reduce aircraft integration effects and improve antenna-array electrical performance. The first study investigates the effects of near-field coupling due to in-plane parasitic, or conductive, elements placed along the length of an antenna. It is found that when the length of these conductive elements are 0.125λ or less the change in S_{11} performance is less than 5%. In addition, the presence of the parasitic elements has little effect on the overall shape of the antenna radiation pattern.

A second study investigates the effects of extreme thermal gradients on transmission line phase stability. For the cables used on the P-3 array, the phase stability is measured to be 2.2×10^{-4} deg./ft/ $^{\circ}$ F, which agrees well with published data. The expected phase shifts on CReSIS's current airborne platforms are shown to not significantly affect beamforming.

Thirdly, a compensation method is developed to improve beamforming and clutter suppression on wing-mounted arrays by mitigating phase center errors due to wing-flexure. This compensation method is applied to the Minimum Variance Distortionless Response (MVDR) beamforming algorithm to improve clutter suppression by using element displacement information to apply appropriate phase shifts. Wing-flexure is shown to shift and fill radiation pattern nulls. The uncompensated array demonstrates an experimental Signal to Interference Noise Ratio (SINR) as low as 18 dB for 90% of interferer angles, while the compensated array showed an experimental SINR of at least 33 dB for 90% of interferer angles. The compensation

demonstrated an average SINR increase of 5-10 dB, depending on elevation angles being considered, and an average improvement of 15% in a figure of merit derived and documented herein. The limitation of this compensation method is that it does not account for changes in mutual coupling.

Finally, the effects of control surface deflection on wing-mounted arrays are also investigated. While control surface deflection is shown to have little effect on uniformly- and Chebyshev-weighted arrays, it is found that the deflection caused filling and shifting of nulls for MVDR-weighted arrays. While pattern deviations are less than 0.3 dB within the mainbeam, control surface deflection is shown to shift nulls by as much as 12° and decrease null depth by as much as 25 dB. At large elevation angles ($>\pm 55^\circ$) the FM was on average 0.2 less than the FM at small elevation angles.

The hardware contributions of this work have substantially contributed to the state-of-the-art for polar remote sensing, as evidenced by new data sets made available to the science community and widespread use and citation of the data. The investigations of aircraft integration effects on antenna-arrays will improve future data sets by characterizing the performance degradation. The wing-flexure compensation will greatly improve beam formation and clutter suppression. Increased clutter suppression in airborne radars is crucial to improving next generation ice sheet models and sea-level rise predictions.

ACKNOWLEDGEMENTS

I would first like to thank my committee for their guidance during my many years at KU. I appreciate their willingness to be on my committee and their generosity with their time. Whether in a formal classroom setting or during informal discussions, I have received invaluable instruction from each of them.

I would like to thank Zonta International for their support in selecting me as a two time Amelia Earhart Fellowship winner. As a female in aerospace engineering there are few honors greater than having your name associated with Amelia Earhart. I would also like to acknowledge the support of NASA and the NSF. This work was supported in part by NASA Headquarters under the NASA Earth and Space Science Fellowship Program Grant No. NNX12AN95H. It was also supported under NSF grant ANT-0424589 and NASA grants NNX10AT68G.

Next I would like to thank the faculty and staff at CReSIS. To Jennifer Laverentz and Jackie St. Aubyn thanks for taking care of business and always responding to my constant inquiries about my travel reimbursements. To Dr. Fernando Rodriguez-Morales and Dr. Jilu Li thank you for enduring my barrage of questions and your generosity with your time. To Carson Gee and Riley Epperson thank you for handling my complete ineptitude with computers with such patience and mercy. To John Hunter and your army of undergraduates thank you for your readiness to manufacture anything at a moment's notice.

I am especially grateful to CReSIS director, Dr. Prasad Gogineni. Under his direction of the Center I have travelled to both coasts of this county, visited many countries across the world, and lived at the bottom of the planet for a month, all while studying and contributing to a problem of global significance. I owe these experiences and many other opportunities to his hard work.

Seven years ago after completing my introductory circuits course, I vowed to never take another electrical engineering class for as long as I live. My endeavors in a multidisciplinary field of study were only made possible with the guidance of Dr. Stephen Yan. As my unofficial advisor on antennas and radar systems, just about everything I know about electromagnetics I learned from Stephen. I am very grateful for his generosity with both his time and knowledge. I thank the remaining members of my committee for their additional contributions to my education across disciplines.

I am most indebted to my advisor Dr. Richard Hale. Six years ago he recognized a potential in me and hired me to work in his composites lab. It was his encouragement that persuaded me to pursue my PhD, and I know I would not be where I am today without his help and guidance. I owe most of my academic and professional development to Dr. Hale. His unwavering support and investment in me did not go unnoticed. I will forever be grateful for the opportunities he has afforded me.

Lastly and most importantly I would like to thank my family. Though I know you do not really understand what it is that I do, you have always been supportive and interested in my work. You have always encouraged me to pursue my interests, celebrated even my smallest accomplishments, and loved me despite my failures.

And to my husband, my best friend, my partner in crime, without you the late nights, hard work, and struggles would be meaningless. You are my sanity in this world of chaos.

“Thy firmness makes my circle just, And makes me end where I begun.”

TABLE OF CONTENTS

	<u>Page #</u>
ABSTRACT	iii
ACKNOWLEDGEMENTS	vi
LIST OF FIGURES.....	xii
LIST OF TABLES	xviii
LIST OF SYMBOLS.....	xix
LIST OF ABBREVIATIONS	xxi
1 INTRODUCTION.....	24
1.1 Motivation	24
1.1.1 Enabling New Platforms for Cryospheric Surveying	24
1.1.2 Reducing Array Fairing Impact on Radiation Performance	26
1.1.3 Improving Beam formation on Airborne Remote Sensing Platforms	26
1.1 CReSIS Platforms and Radars.....	29
1.1.1 NASA DC-8.....	30
1.1.2 NASA P-3	31
1.1.1 Twin Otter	32
1.1.2 Meridian UAS	34
1.1.3 MCoRDS/I.....	34
1.1.4 Ku-band Radar	36
1.1.5 Snow Radar	36
1.1.6 Accumulation Radar	37
1.2 Following Chapter Summary	37
2 APPLICATIONS AND ADVANCEMENTS IN AIRBORNE REMOTE SENSING....	39
3 MULTIDISCIPLINARY DESIGN PROCESS FOR AIRBORNE REMOTE SENSING ANTENNA-ARRAYS	53
3.1 Initial Layout and Mold Line Generation.....	53
3.2 External Load Generation	54
3.3 Preliminary Considerations for Structural Impacts on Antenna Performance	55
3.3.1 Reflections and Transmissions from Fairing Structure	55
3.3.2 Dielectric Loading from Fairing Structure	59
3.4 Detailed Design and Electromagnetic Simulation.....	60
3.5 Challenges and Limitations of Designing Airborne Array Fairings	61
3.5.1 Material Selection	61
3.5.2 Ground Plane Requirements	62

	3.5.3	Maintaining Aircraft and Array Performance	62
4		DEVELOPMENT OF THE DC-8 ARRAY FAIRING	64
	4.1	Design Overview	64
	4.2	Load Case Generation	65
	4.3	Structural Analysis and Design	67
	4.3.1	Structural Analysis Overview	67
	4.3.1	Preliminary Design Iterations	68
	4.3.2	Detailed Design.....	70
	4.4	Modal Analysis.....	77
	4.5	DC-8 Missions and Results	78
5		DEVELOPMENT OF THE P-3 ARRAY	80
	5.1	Design Overview	81
	5.2	Load Case Generation	84
	5.3	Structural Analysis and Detailed Design.....	86
	5.3.1	Structural Analysis Overview	86
	5.3.2	Detailed Design of MCoRDS Array	88
	5.3.3	Detailed Design of Bomb Bay Panels.....	93
	5.4	Modal and Fatigue Analyses	95
	5.4.1	Modal Analysis	95
	5.4.2	Fatigue Analysis.....	96
	5.5	Stability and Control Analysis	97
	5.5.1	Controllability	97
	5.5.2	Stability	98
	5.6	Verification of Design	99
	5.7	Improvement of MCoRDS Array.....	102
	5.7.1	Improved Lower Skin Design.....	102
	5.7.2	Center Antenna Modifications.....	107
	5.7.3	Other Improvements	109
	5.8	P-3 Missions and Results	110
6		TRANSMISSION LINE THERMAL PHASE STABILITY	113
	6.1	Experimental Setup and Procedure	113
	6.2	Results	114
7		ANTENNA FAIRING NEAR-FIELD MUTUAL COUPLING.....	117
	7.1	Near-Field Coupling.....	117

7.2	Near-Field Coupling of Doubler Configurations	119
7.2.1	Relative Doubler Location.....	119
7.2.1	Relative Doubler Length.....	121
7.2.2	Summary of Effects of Near-Field Parasitic Elements	127
8	BEAMFORMERS FOR CLUTTER CANCELATION.....	128
8.1	Introduction	128
8.2	Array Fundamentals	128
8.2.1	Two-Element Uniformly Spaced Linear Array	128
8.2.2	N-Element Uniformly-Spaced Linear Array	129
8.3	Chebyshev Beamformer	131
8.4	MVDR Beamformer.....	132
9	EFFECTS OF WING FLEXURE FOR WING-MOUNTED PHASED ARRAY	135
9.1	Introduction	135
9.1.1	Description of the Twin Otter MCoRDS Array.....	135
9.1.2	Description of the Full-scale Simulation Model.....	137
9.1.3	Description of the Scaled Model Demonstrator.....	138
9.2	Simulation and Measurement Procedures	141
9.2.1	Simulation Procedures	141
9.2.2	Measurement Procedures	143
9.3	Simulation Results.....	143
9.4	Measurement Results	146
9.5	Summary of Results for the Effects of Wing Flexure	148
10	COMPENSATING FOR FLEXURE ERRORS DUE TO AIRCRAFT INTEGRATION.....	150
10.1	Array Deformation Compensation	150
10.2	Merit Figure.....	152
10.3	Simulation Results.....	154
10.4	Measurement Results	158
10.5	Limitations.....	161
10.5.1	Discussion of Limitations	161
10.5.2	Sensitivity Analysis of Compensation Method to Steering Vector Errors	168
10.5.3	Summary of Compensation Limitations	169
10.6	Expected Performance Increase	171
10.7	Application To The P-3 Array.....	175
11	EFFECTS OF CONTROL SURFACE DEFLECTION ON ARRAY PERFORMANCE.....	178

11.1	Introduction	178
11.2	Simulation Results.....	178
11.3	Experimental Measurement Results	181
11.4	Coupling Compensation	184
12	SUMMARY AND RECOMMENDATIONS	188
12.1	Summary	188
12.2	Conclusions	190
12.3	Recommendations	191
13	REFERENCES	194
	APPENDIX A: NEAR-FIELD COUPLING RESULTS	A-1
	APPENDIX B: EXPECTED PERFORMANCE INCREASE DUE TO COMPENSATION METHOD	B-1
	B.1 Collinear Array.....	B-1
	B.2 Parallel Array	B-2
	APPENDIX C: PARALLEL ARRAY SENSITIVITY ANALYSIS.....	C-1
	APPENDIX D: EFFECTS OF VIBRATION ON ARRAY PERFROMANCE	D-1
	D.1 Introduction	D-1
	D.2 Phase and Amplitude Variations Due to Vibration.....	D-3
	D.3 Phase and Amplitude Frequency Spectrum.....	D-7
	D.4 Summary of Effects of Vibration	D-8

LIST OF FIGURES

	<u>Page #</u>
Figure 1.1: Illustration of Surface Clutter [7]	27
Figure 1.2: Signal Phase Shift Caused from Relative Element Displacement	28
Figure 1.3: NASA DC-8 with Installed Instrument Package	30
Figure 1.4: DC-8 in Flight with MCoRDS Fairing Installed	31
Figure 1.5: NASA P-3 with Installed Instrument Package	32
Figure 1.6: P-3 In-flight with CReSIS Instruments Installed	32
Figure 1.7: Twin Otter with installed instrument package	33
Figure 1.8: Twin Otter with MCoRDS Array in Antarctica	33
Figure 1.9: Meridian UAS with Ground Penetrating Radar Antennas	34
Figure 1.10: Meridian Taking-off from Pegasus Airfield during 2011 Antarctic Flight Testing ..	34
Figure 2.1: CAO and AToMS [26]	39
Figure 2.2: NCALM Cessna Skymasters with ALSM System [27]	39
Figure 2.3: LST Skyvan Research Aircraft [32]	40
Figure 2.4: NASA G-III with UAVSAR [33]	41
Figure 2.5: HiCARS Antenna Mounted on Basler Wings [38]	42
Figure 2.6: AWI Depth Sounder and Accumulation Radar Antennas [41]	43
Figure 2.7: Boeing Joined Wing Concept for AFRL SensorCraft [55]	45
Figure 2.8: Navy E-2C Hawkeye with AEW Radar [67]	48
Figure 2.9: Modified G550 with CAEW [69]	48
Figure 2.10: S100B Argus AEW&C [70]	49
Figure 2.11: NASA's HALE UAV Helios [76]	50
Figure 2.12: Genetic Algorithm Applied to Radiation Pattern of Arrays with Different Numbers of Elements	51
Figure 3.1: Example 3-D CFD Output for High Speed Dive	54
Figure 3.2: Example of CFD Output for Mapping Pressures	55
Figure 3.3: Plane Wave Incident to an Interface between Two Dissimilar Media	57
Figure 3.4: Three-Medium Problem and Equivalent Problem with the Same Net Reflected and Transmitted Signal	58
Figure 3.5: Reflectivity as a Function of Laminate Thickness	59
Figure 4.1: Exploded View of the DC-8 Fairing	65
Figure 4.2: DC-8 Fairing FEA Modeled Pressure Regions	68
Figure 4.3: Nadir 7 Port Location and Dimensions	69
Figure 4.4: Configurations Identified for the MCoRDS Trade Study	69
Figure 4.5: Preliminary Design Concepts for Smaller Fairing	71
Figure 4.6: Planform View of Lower Fairing Region Plot	72
Figure 4.7: Spar Disposition and Single C-Channel Representative Cross Section	72
Figure 4.8: Spar Orientation	73

Figure 4.9: Spar Rib Insert.....	73
Figure 4.10: DC-8 Fairing Attachments	74
Figure 4.11: Upper Fairing Maximum Tensile Stress Plot and Critical Region.....	75
Figure 4.12: Upper Fairing .f06 Critical Tensile Stress Element	75
Figure 4.13: DC-8 MCoRDS Fairing.....	76
Figure 4.14: Antenna-array and Cabling Arrangement	76
Figure 4.15: DC-8 Fairing First Fundamental Mode at 60 Hz.	77
Figure 4.16: DC-8 Flight Lines during 2009 Antarctic Campaign [98]	78
Figure 4.17: DC-8 Echogram from 2009 Survey of Thwaites Glacier.....	79
Figure 5.1: Complete CREStS Sensor Suite Installed on the P-3	80
Figure 5.2: MCoRDS Installation Uses Existing WS42 and WS83 Inboard and WS465, WS499, and WS533 Outboard Hard Points.....	81
Figure 5.3: Inboard Assembly with Junction Rib	82
Figure 5.4: Exploded View of the MCoRDS Fairing	82
Figure 5.5: Exploded View of the Attachment Pylon.....	83
Figure 5.6: Exploded View of the Bomb Bay Assembly	84
Figure 5.7: P-3 Vertical Wing Deflection Limits	86
Figure 5.8: P-3 Surface Dynamic Pressure Contours in High Speed Dive and $\alpha = +5^\circ$	86
Figure 5.9: 2D Profile of the Antenna Fairing, with the Leading Edge Ice Shapes	87
Figure 5.10: P-3 Outboard Fairing FEA Pressure Regions	88
Figure 5.11: P-3 MCoRDS Fairing Cross Sections	89
Figure 5.12: P-3 MCoRDS Array Rib Insert	90
Figure 5.13: MCoRDS Lower Skin, Fairing Ribs, and Antennas	91
Figure 5.14: MCoRDS Fairing Leading and Trailing Edge Cross-section.....	91
Figure 5.15: MCoRDS Center Antenna with Junction Ribs.....	92
Figure 5.16: Aft Bomb Bay Replacement Panel.....	93
Figure 5.17: Forward Bomb Bay Panel and Support Structures with Thickness Regions Highlighted	94
Figure 5.18: Forward Bomb Bay Panel with Angle Brackets	95
Figure 5.19: First Fundamental Modes of the P-3 (a) Inboard Array at 53 Hz and (b) Outboard Array at 55 Hz.....	96
Figure 5.20: Second Fundamental Modes of the P-3 (a) Inboard Array at 89 Hz and (b) Outboard Array at 109 Hz.....	96
Figure 5.21: P-3 Roll Controllability with and without the MCoRDS Outboard Fairing	98
Figure 5.22: Ground Proof Load Test Setup for the Inboard Fairing	99
Figure 5.23: Block Diagram of Modal Test Setup.....	100
Figure 5.24: Modal Test Setup (Photo by Rick Hale)	101
Figure 5.25: Measured FRF of the Inboard Fairing	101
Figure 5.26: Measured FRF of Aft Bomb Bay Panel	102
Figure 5.27: Lower Skin with Notches to Break-up Embedded Doublers	104

Figure 5.28: Doubler Study Setup	104
Figure 5.29: Antenna S_{11} Varying Doubler Offset (left) and Gap Size (right).....	105
Figure 5.30: Carbon Fiber Doublers with Separation of 1.25" (left) and 5.25" (right)	106
Figure 5.31: P-3 Outboard MCoRDS Fairing Doubler Designs.....	107
Figure 5.32: P-3 Inboard MCoRDS Fairing Doubler Design.....	107
Figure 5.33: P-3 Nadir Port Above Center Antenna.....	108
Figure 5.34: P-3 Array Center Section with Mock Fuselage in Anechoic Chamber.....	108
Figure 5.35: P-3 Center Antenna Cross- and Along-Track Patterns Before and After Port Modifications	109
Figure 5.36: Ferrites Placed Along Feed Cables	110
Figure 5.37: P-3 and King Air OIB Flight Lines from the 2011 Campaign [100]	111
Figure 5.38: Echogram of 2011 P-3 MCoRDS Data	112
Figure 6.1: Thermal Stability Test Set-up.....	114
Figure 6.2: Phase Change per Meter as a Function of Temperature Change	115
Figure 6.3: Twin Otter Simulated Patterns with and without Thermal Effects	116
Figure 7.1: Yagi-Uda Antenna.....	117
Figure 7.2: HFSS [®] Simulation of P-3 Antenna with Ground Plane and Doublers.....	119
Figure 7.3: Stepped Doubler Geometry	120
Figure 7.4: Antenna S_{11} for Various Out of Plane Doubler Locations	121
Figure 7.5: Antenna Radiation Pattern for Various Doubler Locations	121
Figure 7.6: HFSS Model with Doublers Placed Along the Full Length of the Antenna	122
Figure 7.7: Geometry for Full Length Doubler Study	122
Figure 7.8: Antenna S_{11} as a Function of Doubler Length and Offset for Configurations with 1, 2, and 3 Antennas.....	123
Figure 7.9: Normalized Radiation Pattern for Various Doubler Offsets with Doubler Lengths of 0.26λ (a) and 0.095λ (b).....	124
Figure 7.10: Scaled Dipole with Doublers, Two Dummy Antennas, and a Ground Plane	124
Figure 7.11: 500 MHz Dipole S_{11} as a Function of Doubler Length and Offset	125
Figure 7.12: 1 GHz Dipole S_{11} as a Function of Doubler Length and Offset.....	125
Figure 7.13: Normalized Radiation Pattern of 500 MHz Dipole for Various Doubler Offsets with Doubler Lengths of 0.26λ (a) and 0.095λ (b)	126
Figure 7.14: Normalized Radiation Pattern of 1 GHz Dipole for Various Doubler Offsets with Doubler Lengths of 0.26λ (a) and 0.095λ (b)	127
Figure 8.1: Reflected Signal from Smooth Ice and Scattered Ice from Rough Ice	128
Figure 8.2: Two-Element Array Geometry.....	129
Figure 8.3: N-Element Array with Three Arriving Signals	130
Figure 9.1: 2008 and 2011 Twin Otter Array Orientation and Folded Dipole Geometry	136
Figure 9.2: Top View of Twin Otter with Array Labeling and Arrangement	137
Figure 9.3: Full-Scale Twin Otter Simulation of Nominal Wing (a) and Flexed Wing (b)	137
Figure 9.4: Simulated Twin Otter Folded Dipole	138

Figure 9.5: 1.2 GHz scaled Model Dipole Antenna with Integrated Balun (dimensions in inches)	139
Figure 9.6: Front and Back View of the Twin Otter scaled Model Demonstrator	139
Figure 9.7: Top View of the Displaced Array	140
Figure 9.8: Lateral Track, Tab, and Scale	140
Figure 9.9: Scaled Model Array Setup in Anechoic Chamber	141
Figure 9.10: Parallel (left) and Collinear (right) Array Simulated Patterns with Uniform Weights	144
Figure 9.11: Parallel (left) and Collinear (right) Array Simulated Patterns with Chebyshev Weights	144
Figure 9.12: Parallel (left) and Collinear (right) Array Simulated Patterns with MVDR Weights and Nulls at $\pm 40^\circ$	145
Figure 9.13: Parallel (left) and Collinear (right) Array Simulated Patterns with MVDR Weights and Nulls at $\pm 70^\circ$	145
Figure 9.14: Parallel (left) and Collinear (right) Array Simulated Patterns with MVDR Weights and Asymmetric Nulls at -54° and 50°	146
Figure 9.15: Parallel (left) and Collinear (right) Array Measured Patterns with Uniform Weights	146
Figure 9.16: Parallel (left) and Collinear (right) Array Measured Patterns with Chebyshev Weights	147
Figure 9.17: Parallel (left) and Collinear (right) Array Measured Patterns with MVDR Weights and Nulls at $\pm 40^\circ$	147
Figure 9.18: Parallel (left) and Collinear (right) Array Measured Patterns with MVDR Weights and Nulls at $\pm 70^\circ$	148
Figure 9.19: Parallel (left) and Collinear (right) Array Simulated Patterns with MVDR Weights and Asymmetric Nulls at -54° and 50°	148
Figure 10.1: Phase Shift Due to Deformation	151
Figure 10.2: Compensation Flow Chart	152
Figure 10.3: Comparison of Uncompensated and Compensated Simulated Array Patterns with MVDR Weights, $\alpha=1$, and Nulls at $\pm 40^\circ$	154
Figure 10.4: Comparison of Uncompensated and Compensated Simulated Array Patterns with MVDR Weights, $\alpha=2$, and Nulls at $\pm 40^\circ$	155
Figure 10.5: Comparison of Uncompensated and Compensated Simulated Array Patterns with MVDR Weights, $\alpha=1$, and Nulls at $\pm 70^\circ$	156
Figure 10.6: Comparison of Uncompensated and Compensated Simulated Array Patterns with MVDR Weights, $\alpha=2$, and Nulls at $\pm 70^\circ$	156
Figure 10.7: Comparison of Uncompensated and Compensated Simulated Array Patterns MVDR Weights, $\alpha=1$, and Asymmetric Nulls at -54° and 50°	157
Figure 10.8: Comparison of Uncompensated and Compensated Simulated Array Patterns MVDR Weights, $\alpha=2$, and Asymmetric Nulls at -54° and 50°	157
Figure 10.9: Comparison of Uncompensated and Compensated Measured Array Patterns with MVDR Weights, $\alpha=1$, and Nulls at $\pm 40^\circ$	158

Figure 10.10: Comparison of Uncompensated and Compensated Measured Array Patterns with MVDR Weights, $\alpha=2$, and Nulls at $\pm 40^\circ$	159
Figure 10.11: Comparison of Uncompensated and Compensated Measured Array Patterns with MVDR Weights, $\alpha=1$, and Nulls at $\pm 70^\circ$	159
Figure 10.12: Comparison of Uncompensated and Compensated Measured Array Patterns with MVDR Weights, $\alpha=2$, and Nulls at $\pm 70^\circ$	160
Figure 10.13: Comparison of Uncompensated and Compensated Measured Array Patterns MVDR Weights, $\alpha=1$, and Asymmetric Nulls at -54° and 50°	160
Figure 10.14: Comparison of Uncompensated and Compensated Measured Array Patterns MVDR Weights, $\alpha=2$, and Asymmetric Nulls at -54° and 50°	161
Figure 10.15: Scaled Model Phases of Each Element for Displacement Cases $\alpha = 0$, $\alpha = 1$, and $\alpha = 2$	162
Figure 10.16: Scaled Model Corrected Phases of Each Element for Displacement Cases $\alpha = 0$, $\alpha = 1$, and $\alpha = 2$	163
Figure 10.17: Phase and Magnitude Mismatch Between Ideal and Actual Steering Vector before (a) and after (b) Compensation for Negative Elevation Angles	164
Figure 10.18: Phase and Magnitude Mismatch Between Ideal and Actual Steering Vectors before (a) and after (b) Compensation for Positive Elevation Angles	165
Figure 10.19: Simulated Scaled Model Magnitude and Phase Mismatches for Negative Angles (a) and Positive Angles (b)	166
Figure 10.20: Steering Vector Magnitude and Phase Mismatches from Twin Otter Antenna Only Simulations	167
Figure 10.21: Compensation Method Ability without Mutual Coupling Effects	167
Figure 10.22: Collinear Array FM Sensitivity for Steering Vector Magnitude and Phase Mismatch (left) and Sensitivity Standard Deviation (right)	168
Figure 10.23: Collinear Array Experimental SINR Sensitivity for Steering Vector Magnitude and Phase Mismatch (left) and Sensitivity Standard Deviation (right)	169
Figure 10.24: Comparison of Collinear Array FM for One Null Placed Below 55° (a) and at All Angles (b).....	172
Figure 10.25: Comparison of Collinear Array SINR for One Null Placed Below 55° (a) and at All Angles (b).....	172
Figure 10.26: Comparison of Collinear Array Average FM for Three Nulls Placed Below 55° (a) and at All Angles (b).....	173
Figure 10.27: Comparison of Collinear Array Average SINR for Three Nulls Placed Below 55° (a) and at All Angles (b)	173
Figure 10.28: P-3 Outboard Array HFSS [®] Model	176
Figure 10.29: Comparison of Uncompensated and Compensated Simulated P-3 Outboard Array Patterns with MVDR Weights, and Nulls at $\pm 40^\circ$	176
Figure 10.30: Comparison of Uncompensated and Compensated Simulated P-3 Outboard Array Patterns with MVDR Weights, and Nulls at $\pm 70^\circ$	177

Figure 10.31: Comparison of Uncompensated and Compensated Simulated P-3 Outboard Array Patterns with MVDR Weights, and Asymmetric Nulls at -54° and 50°	177
Figure 11.1: Twin Otter Wing with and without Aileron Deflection and Dipole Antenna	178
Figure 11.2: Comparison of Simulated Twin Otter Radiation Patterns with Control Surface Deflections	179
Figure 11.3: Simulated Radiation Pattern with Control Deflections and MVDR Weights, Nulls at $\pm 40^\circ$	180
Figure 11.4: Simulated Radiation Pattern with Control Deflections and MVDR Weights, Nulls at $\pm 70^\circ$	180
Figure 11.5: Simulated Radiation Pattern with Control Deflections and MVDR Weights, Nulls at -54° and 50°	181
Figure 11.6: Measured Patterns with Control Surface Deflections and Uniform Weights	181
Figure 11.7: Measured Patterns with Control Surface Deflections with Chebyshev Weights and Sidelobes Set to 30 dB	182
Figure 11.8: Measured Patterns with Control Surface Deflections and Nulls at $\pm 40^\circ$	183
Figure 11.9: Measured Patterns with Control Surface Deflections and Nulls at $\pm 70^\circ$	183
Figure 11.10: Measured Patterns with Control Surface Deflections Nulls at -54° and 50°	183
Figure 11.11: Simulated (left) and Measured (right) Patterns with Mutual Coupling Compensation, Null at $\pm 40^\circ$	185
Figure 11.12: Simulated (left) and Measured (right) Patterns with Mutual Coupling Compensation, Null at $\pm 70^\circ$	186
Figure 11.13: Simulated (left) and Measured (right) Patterns with Mutual Coupling Compensation, Null at -54° and 50°	186

LIST OF TABLES

	<u>Page #</u>
Table 1.1: Summary of MCoRDS System Characteristics [16]	35
Table 1.2: Summary of Ku Radar System Characteristics [20].....	36
Table 1.3: Summary of Snow Radar System Characteristics [21].....	36
Table 1.4: Summary of Accumulation Radar Characteristics [22].....	37
Table 3.1: Dielectric Properties of Common Aerospace Fibers and Matrices of Composites (at X-Band Frequencies)	60
Table 4.1: Overall DC-8 MCoRDS Dimensions	65
Table 4.2: Summary of DC-8 Load Conditions.....	66
Table 5.1: P-3 MCoRDS Fairing Overview	82
Table 5.2: Attachment Pylon Details	83
Table 5.3 : Summary of P-3 Load Cases	85
Table 5.4: 2D CFD Drag Coefficients of the Fairing with and without Ice	87
Table 5.5: Selected Metallic Fatigue Strengths [102].....	97
Table 5.6: Airplane Stability with and without the Antenna Fairings and Pylons	99
Table 9.1: Overview of Array Configurations	142
Table 10.1: Values of A Based on Pattern Null Shift from Desired Location.....	152
Table 10.2: Values of B Based on Reduction of Null Depth with Respect to the Nominal Array.....	152
Table 10.3: Summary of Performance Statistics for Collinear Array and 1 Null.....	174
Table 10.4: Summary of Performance Statistics for Collinear Array and 3 Nulls	174

LIST OF SYMBOLS

LATIN

<u>Symbol</u>	<u>Description</u>	<u>Units</u>
\bar{a}_0	Steering vector	(V)
A	Parameter in figure of merit calculation	(~)
\bar{A}	Steering vector matrix	(V)
B	Parameter in figure of merit calculation	(~)
c	Speed of light	(ft/s)
C	Coupling Matrix	(~)
C_p	Pressure coefficient	(~)
D	Fastener diameter	(in)
D	Largest antenna dimension	(m)
d	Antenna element spacing	(in)
E	Electric field intensity	(V/in)
F	Frequency	(Hz)
FM	Figure of merit	(~)
i	Interferer	(~)
I	Current	(A)
k	Wave number	(in ⁻¹)
L	Length	(in)
\bar{n}	Noise vector	(~)
N	Load factor	(g)
P	Pressure	(psi)
q	Dynamic pressure	(psi)
R	Propagation distance of signal	(in)
\bar{R}	Correlation matrix	(~)
S	Scattering parameter	(dB)

T	Transmission coefficient	(~)
t	Thickness	(in)
$\tan(\phi)$	Loss tangent	(~)
V	Propagation velocity	(~)
V	Velocity	(kts)
V	Voltage	(V)
\bar{w}	Array weight vector	(~)
\bar{x}	Antenna response vector	(~)
y	Total array response	(~)
z	Vertical axis	(in)
Z	Impedance matrix	(Ω)
Z_{ld}	Driving Impedance	(Ω)

GREEK

<u>Symbol</u>	<u>Description</u>	<u>Units</u>
α	Angle of attack	(deg)
α	Coefficient of thermal expansion	(in/in ^o F)
α	Physical constant	(~)
β	Physical constant	(~)
Γ	Dihedral angle	(deg)
Γ	Reflection coefficient	(~)
γ	Propagation constant	(in ⁻¹)
Δ	Change or shift	(varies)
ϵ	Permittivity	(F/m)
ϵ_r	Relative dielectric constant	(~)
η	Intrinsic impedance	(Ω)
θ	Elevation angle	(deg)

λ	Wavelength.....	(in)
μ	Permeability.....	(H/m)
v	Volumetric ratio.....	(~)
σ	Conductivity.....	(S/in)
ϕ	Phase angle.....	(deg)
ω	Frequency.....	(rad/s)

SUBSCRIPTS AND SUPERSSCRIPTS

<u>Symbol</u>	<u>Description</u>
eff.....	Effective
F.....	Fiber
i.....	Incident
m.....	Mixture
R.....	Resin
r.....	Reflected
o.....	Free space

LIST OF ABBREVIATIONS

<u>Acronym</u>	<u>Description</u>
AAA.....	Advanced Aircraft Analysis
ADC.....	Analog-to-Digital Converter
AEW.....	Airborne Early Warning
AEW & C.....	Airborne Early Warning and Control
AFRL.....	Air Force Research Laboratory
AF.....	Array Factor
ALSM.....	Airborne Laser Swath Mapping

AToMS	Airborne Taxonomic Mapping System
AWI.....	Alfred Wegener Institute
CAD.....	Computer Aided Design
CAEW	Conformal Airborne Early Warning and Control
CAO.....	Carnegie Airborne Observatory
CFD.....	Computational Fluid Dynamics
CReSIS	Center for Remote Sensing of Ice Sheets
EM	Electromagnetic
FEA.....	Finite Element Analysis
FEM.....	Finite Element Model
FM-CW	Frequency Modulated Continuous-Wave
FRF	Frequency Response Function
FS.....	Fuselage Station
GPS	Global Positioning System
HALE	High Altitude Long Endurance
HF	High Frequency
HFSS.....	High Frequency Structure Simulator
HiCARS.....	High Capacity Radar Sounder
HUT.....	Helsinki University of Technology
IMU.....	Inertial Measurement Unit
IPCC	Intergovernmental Panel on Climate Change
LIDAR	Light Detection and Ranging
LST	Laboratory of Space Technology
MCoRDS/I.....	Multichannel Coherent Radar Depth Sounder/Imager
MUSIC.....	MUltiple Signal Classification
MVDR	Minimum Variance Distortionless Response
NASA	National Aeronautics and Space Administration
NATO	North American Trade Organization
NCALM.....	National Center for Airborne Laser Mapping

NIR	Near Infrared
NSF	National Science Foundation
OIB	Operation IceBridge
OML	Outer Mold Line
PPM	Parts Per Million
PRF	Pulse Repetition Frequency
PSG	Positive Symmetric Gust
SAR.....	Synthetic Aperture Radar
SBR.....	Space Based Radar
SINR	Signal to Interference Noise Ratio
SL.....	Sidelobe
STAP.....	Space-Time Adaptive Processing
STC	Science and Technology Center
UAS	Unmanned Aircraft System
UAV.....	Unmanned Aerial Vehicle
UAVSAR.....	Uninhabited Aerial Vehicle Synthetic Aperture Radar
UHF	Ultra-High Frequency
VHF	Very High Frequency
VNA.....	Vector Network Analyzer
WS	Wing Station

1 INTRODUCTION

Two airborne platform systems¹ equipped with ice-penetrating radars were developed for the purpose of imaging and sounding ice sheets in Greenland and Antarctica. These platforms were specifically developed as part of the National Aeronautics and Space Administration's (NASA) Operation IceBridge (OIB) project [1]. This work was completed in conjunction with the ongoing research of the Center for Remote Sensing of Ice Sheets (CReSIS) and represent an advancement in cryospheric surveying. Specifically, these instruments represent the first time the ice bed has been imaged from high altitude (30,000 ft) and transonic speeds ($M=0.85$) [2], and the largest ice and snow imaging radar suite ever to fly [3]. Collectively, these instruments have flown nearly 200 Arctic and Antarctic science missions, amassing 1841 flight hours, and collecting excess of 250 TB of unique science data. This data is readily available to anyone (www.cresis.ku.edu/data), and for scientists worldwide CReSIS has become a primary source of data on polar ice sheet thickness and other properties. Since the initial deployment of these complex systems several studies have focused on improving radar array performance.

1.1 Motivation

1.1.1 *Enabling New Platforms for Cryospheric Surveying*

Ice sheet mass balance and its relationship to sea-level rise are of great interest to the science community because the rising sea-level was proposed to be an indicator of global warming [2]. The Intergovernmental Panel on Climate Change (IPCC) reported that the rate of sea-level rise during 1993-2003 nearly doubled compared to the previous 30 years, and it projects another 7 to 23 inches of sea-level rise by the end of the century [5]. However, the same report cautions that

¹ Within the context of this document, the term “airborne platform systems” is meant to refer to the support structures that enable the aircraft and radar to be used for cryospheric surveying. Any claims regarding the development of either “airborne platform systems”, “airborne radar installations”, or “instrument suite installations” should not be interpreted as claims for developing either the aircraft or radar digital systems. Instead these terms should be understood to mean the integrating structures of the two systems.

none of the models used to generate projections include dynamic processes associated with rapid changes being observed in ice sheets in Greenland and Antarctica. Bed topography and basal characteristics are critical boundary conditions and keys to understanding the processes causing rapid changes and improving ice-sheet models for generating sea-level projections. The IPCC documents the need for such information to make best estimates of future sea-level changes [6]. Most of the rapid changes being observed occur around ice-sheet margins including outlet glaciers and fast-flowing ice streams. It is extremely difficult and dangerous to carry out surface-based measurements over these areas due to heavy crevassing. While satellite measurements have provided a wealth of information, the instruments on these space-based platforms are only capable of collecting data with relatively coarse resolution. Such instruments also lack the capability of imaging the bed topography, which is of highest importance for establishing the boundary conditions governing glacial motion [7]. The most effective way to obtain the desired information on bed topography and basal conditions with fine resolution on a large scale is through the use of airborne platforms equipped with advanced ice-penetrating radars [5].

CRISIS is a Science and Technology Center (STC) funded by National Science Foundation (NSF). This collaborative organization's mission is to collect mass balance data of Greenlandic and Antarctic ice sheets and provide it to glaciologists to develop computer models for predicting sea-level change [7]. CRISIS has developed a series of ice penetrating radars and advanced processing algorithms to generate data sets crucial to modeling ice sheet dynamics. These radars measure surface topography, near-surface and deep internal layers, snow accumulation over land and sea ice, ice thickness, basal conditions (whether the bed is wet or frozen), and the bed topography.

Basal conditions and bed topography are of particular interest to scientists as they are critical boundary conditions and keys to understanding the internal processes causing rapid changes in outlet glacier and ice sheet margins [7]. To meet the data needs of scientists the fleet of aircraft used for collecting ice sheet data has increased dramatically over the last decade. In particular, as part of NASA's OIB mission both a DC-8 and a P-3 were converted into flying laboratories. IceBridge began in 2009 with the purpose of filling the gap in measurements between the loss of ICESat and the targeted launch of ICESat-II in 2016 [9]. The superior range of the DC-8 allows for measurements in areas previously unreachable by other aircraft. Meanwhile, the P-3 is well suited for low-altitude, long-range, and heavy lift missions. The payload capabilities of the P-3

enable CReSIS to fly all four of their radars on a single platform for the first time. The development of both the DC-8 and P-3 airborne platform systems, and in particular the detailed design and implementation of the integrated structural and aerodynamic fairings and the related aircraft integration, are included within the scope of this work, and represent contributions to the field of airborne remote sensing by increasing the number of available platforms for cryospheric surveying.

1.1.2 *Reducing Array Fairing Impact on Radiation Performance*

The supporting structure of an antenna-array, called a fairing, can greatly affect the array's performance. Ideally materials used in the construction of the antenna fairings are electrically transparent to the radar signal. But as electromagnetic waves pass between dissimilar media (i.e. from the fairing into free space), part of the signal will be reflected even when using ideal materials. Higher frequencies are particularly susceptible to this phenomenon as the structure appears electrically thicker. In addition, these same transparent materials will load the antenna when they are in close proximity. This loading can cause a resonance shift of the antenna, as well as affect the gain, return loss magnitude and bandwidth, and radiation pattern of the element.

The aforementioned effects all results when ideal, electrically transparent materials are used in close proximity to the radiating elements, but to meet structural requirements for the fairings metallic components are generally required, particularly at structural joints. Conductive materials in the near-field of an element can change the antenna's impedance as well as its radiation pattern. Included in this work was a study to determine some design rules to help mitigate the effects of the fairing on the array performance. In particular, the near-field coupling of in-plane parasitic elements was investigated and is addressed in Chapter 7.

1.1.3 *Improving Beam formation on Airborne Remote Sensing Platforms*

Airborne sounding and imaging of fast-flowing glaciers and ice sheet margins with heavily crevassed surfaces and warm ice is very challenging. The backscattered signals from crevassed surfaces often mask weak ice-bed echoes resulting from warm ice in fast-flowing glaciers. Thus, high-sensitivity radars are required to overcome large ice attenuation. These radars must also have advanced signal processing capabilities and radiating structures with very low spatial sidelobes and precise null placement to suppress the surface-clutter. One-way spatial sidelobes of -35 dB or lower are required to reduce cross-track surface-clutter. While Synthetic Aperture

Radar (SAR) processing can be used to synthesize a narrow beam in the along-track direction, it is ineffective in the cross-track direction.

Advanced beamforming algorithms, such as Minimum Variance Distortionless Response (MVDR), are required for cross-track beam formation and clutter suppression. Figure 1.1 [7] shows how surface clutter affects the radar echogram and how the MVDR beamformer can be applied to reduce surface-clutter and reveal the weak bed echo. The top photograph in this figure shows the smooth ice surface of the region in which data was gathered to produce the echogram in the middle column. In this echogram the bed return is clearly visible and is represented by the red curve in the middle of the plot. The bed return is easily identifiable because the nadir bed return is the strongest returned signal. The aircraft radiation pattern shown in the top left of Figure 1.1 demonstrates that smooth ice surfaces will reflect off-nadir signals away from the receiver. The middle row of images show the nature of the radar echoes when the ice surface is heavily crevassed. In this instance, the rough surface back-scatters the off-nadir signals towards the receiver. The signals from the ice surface mask the bed echo return such that the ice-bed interface cannot be determined. The final row of images in Figure 1.1 demonstrate how MVDR is used to produce a specific set of antenna element weights that will result in an array radiation pattern that spatially filters the off-nadir clutter. By placing pattern nulls in the direction of the clutter, received energy from these directions is diminished, and the bed echo is identified.

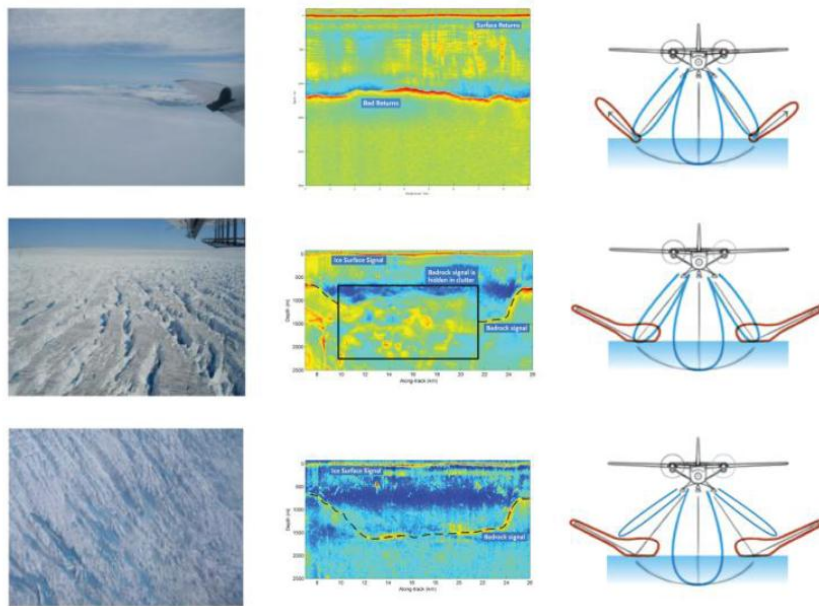


Figure 1.1: Illustration of Surface Clutter [7]

Large cross-track antenna-arrays with high gains are required to image the bedrock deep below the ice sheets. Large arrays, when combined with the advanced signal processing algorithms, are highly sensitive to the aircraft's motion and deformation. To obtain spatial sidelobes of -35 dB (one-way) or lower and accurate beamforming, the relative amplitudes fed to individual elements in the array must be matched to within 0.5 dB, while the relative phases must be matched to within 1 degree or less [10]. Advanced signal processing algorithms such as MVDR and MULTiple Signal Classification (MUSIC) used for cross-track antenna-array beam formation and direction of arrival estimates to generate 3-D topography also impose even tighter tolerances on amplitude and phase mismatches between array elements [11].

To facilitate the largest array possible, the antenna elements are often mounted externally to the wings of the aircraft. By attaching the antenna-array to the wings, the electrical performance is influenced by the motion of the airframe as in-flight aerodynamic and inertial loads cause the wing to flex from its nominal position. The wing deformation will translate to the array and will cause relative phase errors between elements as shown in Figure 1.2, where λ is the wavelength of the incoming signal. Because the total pattern of the phased array is controlled by the relative phases between the elements, these phase errors are of great interest.

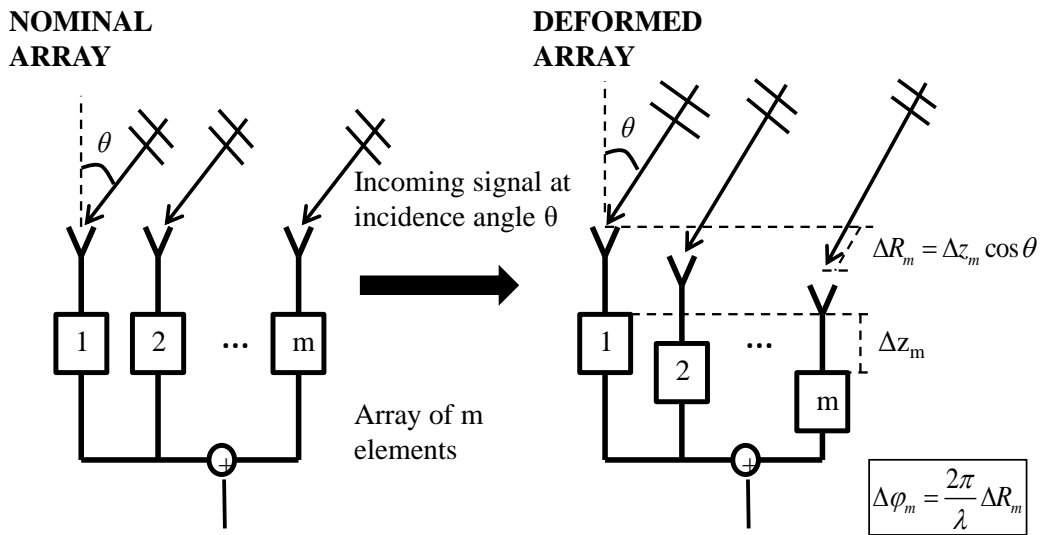


Figure 1.2: Signal Phase Shift Caused from Relative Element Displacement

Understanding the array deformation effects on airborne arrays could potentially improve data sets already obtained over previous field seasons, as well as improve future data sets through the use of adaptive beamforming. Post-processing can be applied to the received signals to synthesize receive-antenna patterns with low-sidelobes and perform null-placement at angles

of ice surface-clutter. Nevertheless, this beamforming algorithm is very susceptible to amplitude and phase mismatches. To correct for these mismatches, both the effects and the mechanics of the deformation must be known and directly measured or estimated by looking at both flight data (i.e. speeds and altitudes from in-flight Global Positioning System (GPS)) and structural analysis models.

Conversely, for the transmit beam, only real-time compensation methods can be used. For previous missions, a single set of element weights were determined and used throughout the course of the flight. If real-time deformations of the wing were known, either through the use of flight data or the addition of accelerometers, then the transmit array pattern could be compensated.

As part of this work, a compensation method was developed for array deformation due to wing flexure to improve beam formation and clutter suppression. This method was demonstrated to be effective with both full scale simulations and scaled model measurements of a wing mounted array. In addition, the effects of extreme temperature gradients and control surface deflection were also investigated and are documented herein.

1.1 CReSIS Platforms and Radars

CReSIS is a global leader in collecting data on ice bed topography, glacier volume, internal layers, and basal conditions and providing this information to glaciologists. Over the last four years there have been three primary airborne platforms used by CReSIS for surveying missions in Greenland and Antarctica. Two of these systems, the NASA DC-8 and P-3, were developed as direct result of this work. The third system, a DHC-6 Twin Otter, was recently retired in 2011. Two other airborne systems are still under development for CReSIS. The Meridian Unmanned Aircraft System (UAS) was designed and built by the University of Kansas for the purposes of cryospheric surveying, but is still in the flight test stage. A Basler (modified DC-3) is currently in the detailed design stages, and its purpose is to replace the retired Twin Otter. Currently the DC-8 and P-3 are the only active airborne systems for CReSIS.

The CReSIS sensor package consists of four different radars, though all four of these systems are not simultaneously flown on all the platforms. Each radar antenna-array installation is unique to the platform. When operated simultaneously over different frequency bands ranging

from 180 MHz to 18 GHz, the sensor package provides a full profile of the ice column to reveal important sub-glacial features.

The following sections provide an overview of realized CReSIS platforms and sensors.

1.1.1 *NASA DC-8*

The NASA DC-8 is a four-engine jet aircraft operated by the Dryden Flight Research Center in Edwards, CA that was converted into a flying research laboratory in 1987 [12]. The DC-8 has a range in excess of 5,000 nm and an operation ceiling of 41,000 ft, though it has performed surveying missions at altitudes as low as 1650 ft [13]. Typical mission cruise speeds range from 220 to 330 kts [14].

The DC-8 has been equipped by CReSIS with a five-element Multichannel Coherent Radar Depth Sounder/Imager (MCoRDS/I) array that is housed in a custom fairing under the fuselage, two Ku radar horns, and two snow radar horns. The Ku and Snow radar horns are installed inside the wing root fairing. It is noted that over the most recent field season the Ku-band and Snow radars were operated as an integrated system. Figure 1.3 is a Computer-Aided Design (CAD) image of the DC-8 with MCoRDS, Ku, and Snow radar antennas installed, and Figure 1.4 is a photograph of the aircraft in-flight during a surveying mission. Chapter 4 will provide a detailed description of the MCoRDS fairing development.

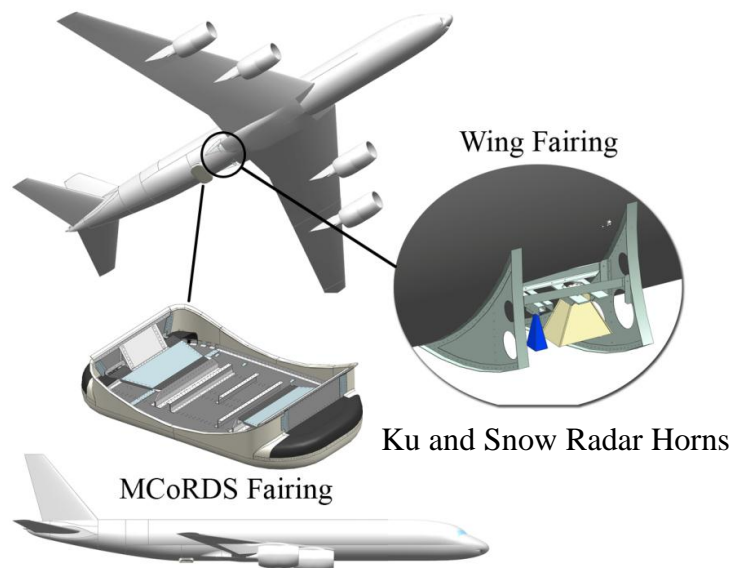


Figure 1.3: NASA DC-8 with Installed Instrument Package



Figure 1.4: DC-8 in Flight with MCoRDS Fairing Installed
(Photo courtesy of Kyle Krabill)

1.1.2 NASA P-3

The NASA P-3B is a four-engine turboprop aircraft. Originally developed by Lockheed Martin as a sub hunter for the Navy, the P-3 was converted into a flying laboratory by the Wallops Flight Facility in 1991 [15]. The range of the P-3 is in excess of 3,000 nm, and it has an operation ceiling of 28,000 ft [14]. It has also been used for low-altitude, long-duration missions. Nominal mission cruise speeds range from 240-400 kts [16].

The P-3 flying laboratory carries a 15-element MCoRDS array on the wings, as well as an 8-element accumulation array, two Snow radar horns, and two Ku radar horns in the bomb bay fairing. It is noted that over the most recent field season the Ku-band and Snow radars were operated as an integrated system. Figure 1.5 is a CAD image of the P-3 with all four radar instruments, and Figure 1.6 is a photograph of the aircraft during one of the initial test flights. Chapter 5 will provide a detailed description of the development of the P-3 MCoRDS array.

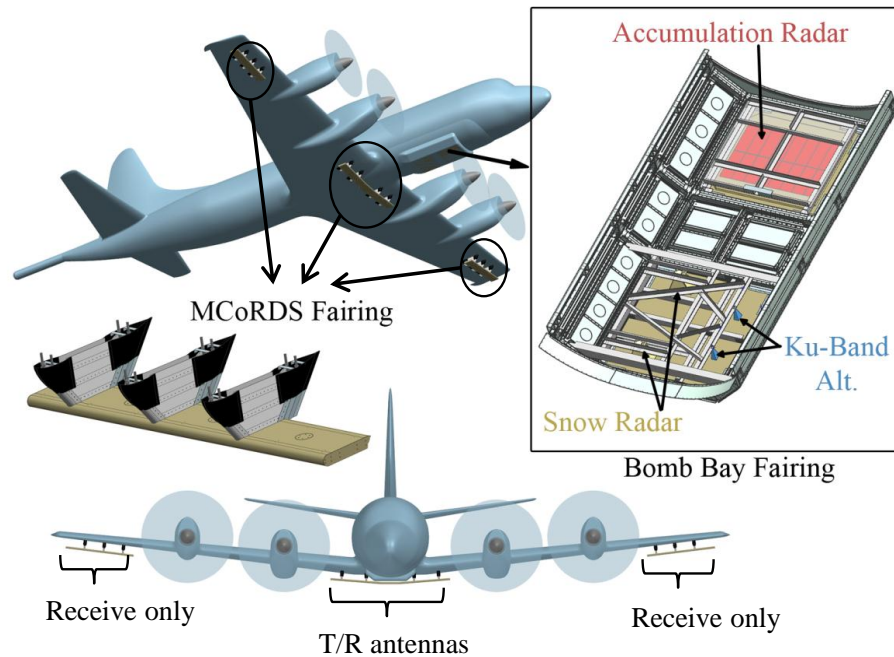


Figure 1.5: NASA P-3 with Installed Instrument Package



Figure 1.6: P-3 In-flight with CRISIS Instruments Installed

(Photo by Rick Hale)

1.1.1 Twin Otter

The de Havilland Twin Otter is a twin turboprop aircraft with cruise speed of 120 kts and range of about 780 nm [14]. The aircraft can be configured with either standard landing gear or skis, and is well suited for low-altitude surveying of ice sheets. The aircraft has been equipped with the MCoRDS/I, Ku-band altimeter, and accumulation radar as well as a GPS and an Inertial Measurement Unit (IMU) to record aircraft position and attitude [16]. The MCoRDS/I array consists of 12 folded dipoles that are mounted to the wings with custom hard points. The Ku and accumulation radar antennas are installed inside the aircraft in a nadir-looking camera view port. Figure 1.7 shows a CAD image of the Twin Otter and an overview of systems installed on it.

Figure 1.8 is a photograph of the aircraft parked at Pegasus Field near McMurdo Base in Antarctica.

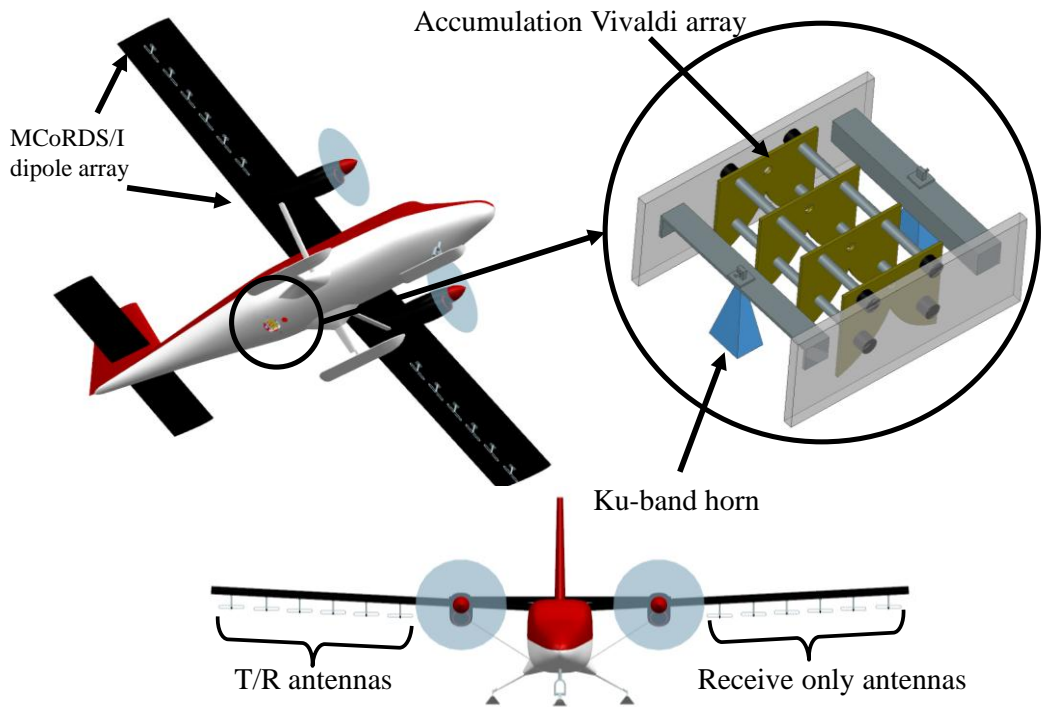


Figure 1.7: Twin Otter with installed instrument package



**Figure 1.8: Twin Otter with MCoRDS Array in Antarctica
(Photo by Fernando Rodriguez-Morales)**

1.1.2 *Meridian UAS*

The Meridian UAS was designed and developed by the University of Kansas Aerospace Engineering Department, and the project was funded by the NSF to support the on-going research at CReSIS. The Meridian was designed with a cruise speed of 130 kts. The range performance of the aircraft was one of the driving design factors, and with full payload the range is roughly 950 nm [17]. The main payload of the Meridian is an 8-element array of ice-penetrating radar Vivaldi antennas that are attached to the wing. The UAS was also designed to carry an optical/infrared camera and an aerosol detector. Figure 1.9 is a CAD image of the Meridian with its array of ice-penetrating radar antennas. Figure 1.10 was taken during the 2011 flight tests near McMurdo Base in Antarctica.

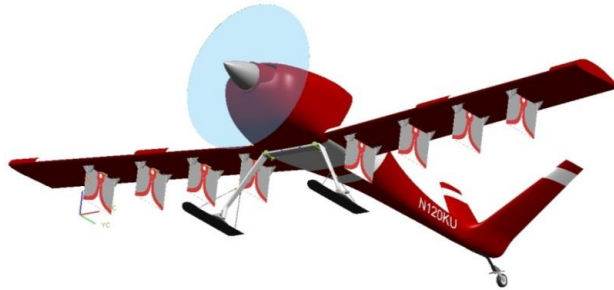


Figure 1.9: Meridian UAS with Ground Penetrating Radar Antennas
(Image by Bill Donovan)



Figure 1.10: Meridian Taking-off from Pegasus Airfield during 2011 Antarctic Flight Testing
(Photo by Shah Keshmiri)

1.1.3 *MCoRDS/I*

The MCoRDS/I, or often referred to as simply MCoRDS, is a Very High Frequency (VHF) band radar glacier depth sounder used to image the ice-bedrock interface as well as deep internal

layers. This radio echo sounder is the primary radar that CReSIS operates. The depth sounder was first developed in 1990 by CReSIS [18] and has been subsequently improved over last two decades. The radar can support up to 15 channels (7 antenna elements in transmit and all 15 in receive). Table 1.1 gives an overview of the MCoRDS system, but a complete description of the system can be found in [19] and [16].

Table 1.1: Summary of MCoRDS System Characteristics [16]

Parameter	Value	Unit
Frequency band	180-210	MHz
Pulse duration (selectable)	1,3,10	μ s
PRF	10	kHz
Sample rate	111	MHz
Transmitted power (peak)	500	W
Receiver noise figure	~ 5	dB
Loop sensitivity	~ 210	dB
Minimum detectable signal	~ -161	dBm
Range resolution in ice	18.4 (5.6)	ft (m)

The MCoRDS/I employs an antenna-array in the cross-track direction. The array configuration is specific to each platform, and various types of dipoles are used in each application. Variations of the MCoRDS/I have been flown on a Twin Otter, as well as NASA's DC-8 and P-3. The Twin Otter MCoRDS array consists of 12 folded dipoles, with six dipoles installed on each wing. Between the 2008 field season and the 2011 field seasons, the center frequency of the antenna-array was shifted from 150 MHz to 195 MHz. In addition, during the 2008 field season the dipole antennas were flown parallel to the direction of flight and the left sub-array was used for receive while the right sub-array was used for transmit. During the following field seasons the 195 MHz dipoles were flown perpendicular to the direction of flight, and the right six elements were once again used for transmission, but all 12 elements were used for reception.

The DC-8 array consists of a five-element staggered collinear array of planar-bowtie antennas. The array is housed in a custom fairing attached to the belly of the DC-8. The P-3 array consists of 15 bowtie antennas. The array is divided into three sub-arrays that are housed in custom fairings. A 7-element sub-array is slung under the aircraft's fuselage and is shared for transmit and receive. Two 4-element sub-arrays are attached to hardpoints on the outboard wings

and are used for reception only. Detailed descriptions of the DC-8 and P-3 arrays will be provided in Chapter 4 and Chapter 5, respectively.

1.1.4 *Ku-band Radar*

The Ku-band radar is an ultra-wideband Frequency Modulated Continuous-Wave (FM-CW) radar that operates over the 12-18 GHz frequency band and measures surface topography and near surface layering. Like the MCoRDS/I, the Ku-band radar has been flown on the Twin Otter, DC-8, and P-3. In each of these installations, the radar has employed a 2-element array housed inside the aircraft that transmits through an electromagnetic (EM) transparent radome. The 2-element array consists of a transmit and receive horn antenna. Table 1.2 provides a summary of the Ku-band radar parameters, and a full description can be found in [20]. Chapter 5 details the integration of the radar into the P-3 bomb bay.

Table 1.2: Summary of Ku Radar System Characteristics [20]

Parameter	Value	Unit
Frequency band	12-18	GHz
Max operation altitude	<4	km
Chirp length	<250	μ s
PRF	2	kHz
Transmitted power (peak)	0.2	W
Vertical resolution in snow	1.6 (4)	in (cm)

1.1.5 *Snow Radar*

The ultra-wideband snow radar operates over 2-6.5 GHz and measures snow thickness over sea ice, surface topography, and near surface layering. Table 1.3 gives an overview of the snow radar parameters, and a complete description can be found in [21]. Chapter 5 details the integration of the radar into the P-3 bomb bay.

Table 1.3: Summary of Snow Radar System Characteristics [21]

Parameter	Value	Unit
Frequency band	2-8	GHz
Chirp length	<250	μ s
PRF	2	kHz
Sample rate	58-63	MHz
Transmitted power (peak)	100	mW
Vertical Resolution in snow	1.6 (4)	in (cm)

The snow radar has flown on the DC-8 and P-3 platforms since the 2009 field season. The radar employs a 2-element antenna-array made up of TEM horn antennas. One of the horns operates as the transmit antenna while the other operates as the receive antenna.

1.1.6 *Accumulation Radar*

The accumulation radar provides fine resolution imagery of near surface layers up to 100 meters deep. The Ultra-High Frequency (UHF) radar operates over the 600-900 MHz band. Table 1.4 gives a brief summary of the system parameters. A full description can be found in [22], and Chapter 5 details the integration of the radar into the P-3 bomb bay.

Table 1.4: Summary of Accumulation Radar Characteristics [22]

Parameter	Value	Unit
Frequency band	600-900	MHz
Chirp length	2	μ s
PRF	50	kHz
ADC sample rate	125	MHz
Transmitted power (peak)	5	W
Minimum detectable signal	-150	dBm
Range resolution in ice	19.7	in

The accumulation radar has flown on the Twin Otter and the P-3. The Twin Otter accumulation antenna-array consisted of a 4-element Vivaldi antenna-array. The P-3 array consisted of eight PC board elliptical dipoles that are arranged in a 2 X 4 planar array configuration.

1.2 Following Chapter Summary

Chapter 2 provides a survey of airborne platforms and their associated payload that have been used for remote sensing, as well as a review of related work. Chapter 3 provides an overview of the multidisciplinary design process used to develop new fairings for airborne arrays. Chapters 4 and 5 present the design and development of the DC-8 and P-3 fairings, respectively. Chapter 6 addresses a study that was performed to investigate the effects of extreme thermal gradients on transmission line phase stability and how that affects beam formation. Chapter 7 documents an extensive study that investigates the effects of near-field parasitic elements from which a design rule was produced. Chapter 8 provides array and beamforming theory. The effects of wing-flexure and array deformation are presented in Chapter 9, and

Chapter 10 demonstrates the method of compensating for these deformations to improve beam formation. Chapter 11 identifies the effects of control surface deflection on array beam formation. Finally, Chapter 12 contains the summary and conclusions of the work completed in this dissertation as well as recommendations for further study.

2 APPLICATIONS AND ADVANCEMENTS IN AIRBORNE REMOTE SENSING

The history of airborne remote sensing began in 1858 when Gaspard-Felix Tournachon attached a camera to a hot air balloon and took photos over Paris [23]. Early attempts by others also included the use of kites, pigeons, and rockets [24]. World War I greatly increased the use of airborne remote sensing as systematic aerial photography was needed for reconnaissance. Today the applications of airborne remote sensing are numerous and diverse, but the most widely used technique remains visible and near infrared (NIR) imagery [25].

The Carnegie Airborne Observatory (CAO), shown in Figure 2.1, and the National Center for Airborne Laser Mapping's (NCALM) Cessna Skymaster with the Airborne Laser Swath Mapping (ALSM) system, shown in Figure 2.2 demonstrate common examples of science applications of airborne remote sensing overseen by universities.



Figure 2.1: CAO and AToMS [26]



Figure 2.2: NCALM Cessna Skymasters with ALSM System [27]

The CAO is a Dornier 228 aircraft that carries an Airborne Taxonomic Mapping System (AToMS) which includes both a visible light and NIR spectrometers and a Light Detection And Ranging (LIDAR) scanner [28]. The AToMS operates in the 1.5×10^{-5} to 9.9×10^{-5} inch (380-2510 nm) wavelength range with 2×10^{-7} inch (5 nm) spectral resolution and provides measurements related to ecosystem composition, structure, and function [28]. This system, operated by Stanford, has been used in the African savanna to map treefall caused by herbivores [29] as well as over the Amazon Rainforest to identify tree species [30].

The NSF supported and University of Houston operated NCALM ALSM system is installed on a Cessna Skymaster and is used to accurately map large areas of land. ALSM includes several LIDARs, an aerial camera, a hyperspectral spectrometer, and a GPS. In April of 2009 NCALM used the Skymaster to map the ancient Mayan city of Caracol [31]. In four days the entire city was mapped using the canopy-penetrating LIDAR, surpassing results of 25 years of ground mapping.

Both the CAO and NCALM's ALSM system utilize LIDAR and spectrometers, which are some of the most common sensors used for science applications of airborne remote sensing. Similar to the CReSIS systems, both the AToMS and ALSM are nadir looking systems, but neither of these sensors is capable of penetrating deep into ice sheets as required by depth sounding radar. Both LIDARs and spectral cameras operate in the wavelength range of 10^{-5} to 10^{-7} inches, whereas sensors for ice sounding operate with a minimum wavelength of 6.6" (16.7 cm). The lower frequencies (longer wavelengths) of the CReSIS sensors are required to overcome large ice attenuation.

Additional examples of science applications of airborne remote sensing are two L-band SAR radars. The HUT-2D is shown in Figure 2.3, and NASA's Gulfstream III with its Uninhabited Aerial Vehicle Synthetic Aperture Radar (UAVSAR) is shown in Figure 2.4.



Figure 2.3: LST Skyvan Research Aircraft [32]



Figure 2.4: NASA G-III with UAVSAR [33]

In 1994 the Laboratory of Space Technology (LST) at the Helsinki University of Technology (HUT) acquired a Short SC7 Skyvan for the purpose of carrying remote sensing instruments. The HUT-2D is an L-band interferometric radiometer that was developed by the university specifically to be flown on the Skyvan. The antenna-array for this radiometer consists of 36 elements in a U-shape arrangement that operates with a 1.4135 GHz central frequency [34]. This unique array geometry shape was selected for ease of integration onto the aircraft, as it allows for installation around the rear cargo bay door of the Skyvan [34]. The intended purpose of this instrument is to provide data to the European Space Agency's soil moisture and ocean salinity projects through radiometric measurements of natural targets [34]. As such the array only operates in receive mode.

The Skyvan with HUT-2D is a good representative example of the types of airborne antenna-arrays used for science application in remote sensing. This radar-platform system consists of one sensor that attaches near the mold-line of the fuselage. This system is comparable to the microwave and UHF radars used by CReSIS in that it does not require a large cross-track array or advanced beamforming [35]. A survey of other radar-platform systems reveals that CReSIS is rather unique in mounting the large antenna-arrays to the flexible wings of the aircraft. The HUT-2D is sensitive to platform attitude, but not airframe deformation. Vibrations due to mounting the array to the cargo door were measured, and resulting displacement levels were found to be acceptable for array performance [35].

A Gulfstream III has been structurally modified to carry the Uninhabited Aerial Vehicle Synthetic Aperture Radar (UAVSAR) developed by NASA [36]. UAVSAR is a reconfigurable, polarimetric L-band synthetic aperture radar that was originally designed for the NASA Global Hawk. The antenna-array consists of 48 radiating element with a center frequency of 1.26 GHz

and a bandwidth of 80 MHz [36]. In 2012, this system was used to map the *Deepwater Horizon* oil spill in the Gulf of Mexico [37].

In 2009 the Gulfstream UAVSAR was used to map glacier motion in an area just north of the Jakobshavn Glacier [36]. Over a one day period the system recorded a maximum glacier displacement of 15.7". Though this platform has demonstrated the capability for cryospheric surveying, it is not capable of supplying scientists with information on the critical boundary conditions such as bed topography. This system only operates over a small frequency range, whereas current observations require multispectral measurements to capture the full ice profile.

Two of the few existing platform-radar systems capable of sounding the ice bed include a VHF ice-penetrating radar operated by the Institute for Geophysics at the University Texas and the Alfred Wegener Institute's (AWI) radio echo sounder. Both of these depth sounding radars are flown on Baslers. The High Capability Radar Sounder (HiCARS) antenna-array, shown in Figure 2.5, consists of two flat dipoles that are mounted underneath either wing of the Basler. This system has an operational frequency of 60 Hz, a bandwidth of 15 MHz, and is flown over the ice sheets of Antarctica [38].



Figure 2.5: HiCARS Antenna Mounted on Basler Wings [38]

AWI's echo sounder, shown in Figure 2.6 on Polar 6, looks very similar to the HiCARS system. This system was originally flown on a Donier 228 (like the CAO system), and operates at 150 MHz [40]. The AWI Polar 6 also flies an accumulation radar antenna array, seen outboard of the radio echo sounder antennas that is capable of penetrating the ice 500-660 feet [41].



Figure 2.6: AWI Depth Sounder and Accumulation Radar Antennas [41]

(Photo by Martin Gehrman, AWI)

Unlike the CReSIS MCoRDS radar, HiCARS and AWI radio echo sounders do not operate as phased arrays. Instead single antenna elements on each wing operate as transmit and receive antennas individually. Though these systems operate at appropriate frequencies to overcome large ice attenuation, they lack the ability for cross-track beam formation. The inability for cross-track beamforming means these systems cannot suppress off-nadir clutter in these directions.

From the previous examples, it is clear that CReSIS is unique in attaching large cross-track arrays to the flexible airframe. The sensors require custom support structures that do not greatly degrade the performance of the antenna-array or the aircraft. Both the HiCARS and AWI echo sounder required externally mounted support structures for their systems. Like CReSIS's MCoRDS radar, these radars are used for sounding the ice-bed interface of ice sheets, but these systems do not possess the same ability to suppress off-nadir clutter signals needed to sound some of the most difficult regions. In addition, the P-3 and DC-8 have three to five times the range of the Basler, which enables the coverage of more area and the ability to survey areas that are unreachable by the Basler [14].

However mounting the large antenna arrays to the flexible airframe comes with a price, and further technical advancements are required to meet the necessary radar requirements for next-generation depth sounders to sound ice sheet margins and outlet glaciers. Radars used for sounding and imaging ice sheets often operate in the High Frequency (HF) and VHF spectrums. At these frequencies array element size and spacing are driving factors for the size of the array (number of elements) that can fit on the airborne platform. To facilitate the largest array possible, the antenna elements are often mounted externally to the wings of the aircraft, but the electrical

performance is influenced by the motion of the airframe. The wing deformation will translate to the array and will cause relative phase errors between elements that can distort the radiation pattern.

Wing deflections cause large magnitude displacements at low frequencies. During science mission flights, data is generally recorded during straight and level, steady-state flight conditions. While this condition will keep the wing deflection rather constant, wind gusts and other disturbances will cause perturbations about the steady state deformation. In addition as the aircraft burns fuel over the course of a flight, the wing loading will decrease due to the weight reduction. This means over the course of a mission the relative displacements (and thus phase errors) will change.

There have been many investigations into the effects of array element phase errors on radiation patterns. It has been shown that the displacement of array elements causes pointing errors, broadening of the main beam, reduced gain, and increased sidelobe levels [42]-[44]. These studies have demonstrated the necessity to monitor element phase errors and their effects on the antennas performance. This work aims to expand on these observations and correct for distortions, particularly in off-nadir beamformation.

In [45], structural, electromagnetic, and thermal modeling was coupled such that a phased array response could be monitored for various states of static thermally-induced loading. The coupled modeling did not include mutual coupling between elements or the temperature distribution of the structure, but was used to determine the changes in the gain pattern and sidelobe levels of a phased array for various temperature soaks. Without including mutual coupling effects the physics of the problem is not accurately captured. The study in [45] simply aimed to identify how the gain and sidelobe levels of the array changed with the temperature gradient. No effort was made to either prevent array deformation or correct for it. Though the study showed that thermally-induced loading caused a gain reduction of less than 0.15 dB, it is a good example of how real loads and displacements of an array can be applied to EM simulations to capture the real performance of the array. This work is similar in that wing deformation are modeled and applied to the array to capture the effects, though as will be shown in Chapter 9 these deformations are much larger and greatly distort the array patterns. The study in [45] does not offer compensation to the effects of deformation whereas this work does.

Mitigation of performance degradation in a phased array due to element errors has been handled in various ways. Some have simply defined acceptable levels of deformation based on certain array performance characteristics such as Signal to Interference Noise Ratio (SINR), gain loss, and sidelobe level increase [46]-[47]. These types of studies often lead to stricter design requirements of the support structure. In at least one case of a large, deployable space based radar, the stiffness requirements for the structure were derived directly from the allowable displacements of the antenna phase center [48]. Similarly, the NATO Research Task Group SET-131 has been developing smart structures to actively control vibrations in a UAV fuselage skin in which a conformal antenna-array has been embedded [49]-[50]. The Task Group uses a combination of accelerometers and piezo-ceramic patches installed near the antennas to sense deformations and induce annihilating vibrations to mitigate the antenna performance loss. CReSIS has previously installed accelerometers in the P-3 MCoRDS array, but found that these sensors were a source of interference in the highly sensitive receivers and thus had to be removed.

Structural deformations have also been identified as an area of concern in the case of the SensorCraft antenna-arrays [51]. The Air Force Research Laboratory (AFRL) developed the idea of the SensorCraft, shown in Figure 2.7, as a high endurance Unmanned Aerial Vehicle (UAV) for military intelligence, surveillance and tracking missions. In the early 2000's Boeing developed a joined-wing configuration that has since been investigated by the AFRL [52]. Many of these investigations have focused on solving problems relating to the aeroelasticity of the airframe as well as the controllability of the aircraft [53]-[55].

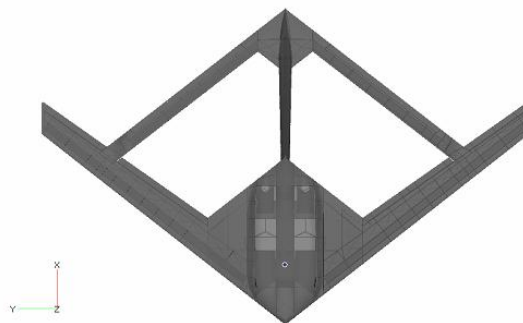


Figure 2.7: Boeing Joined Wing Concept for AFRL SensorCraft [55]

The current concept for the SensorCraft has large antenna-arrays placed along the wing structure. At least one effort has been made to minimize antenna phase center errors by

determining allowable control surface deflections that will trim the aircraft while also minimizing wing deflections [56]. This aircraft contains several control surfaces, and control algorithms are still under development. The P-3 and DC-8 platforms only have one set of ailerons and flaps and control algorithms are well established. As such a similar approach is not practical for reducing deflections in the current CReSIS arrays.

An alternative to preventing phase center displacements is to allow the array to deform, but apply appropriate phase corrections to each element. This is by far the more common approach to handling phase center errors. The most commonly documented purpose for correcting phase center errors is to prevent mainbeam pointing errors, particularly in Space Based Radar (SBR) applications [57]-[59]. It is well known that pointing errors can be corrected by applying a phase shift to each element that is equivalent to $(2\pi/\lambda)z$, where λ is the wavelength and z is the out-of-plane displacement of the element. Correcting for mainbeam pointing errors is essential in SBR because these radars generally utilize antenna-arrays with hundreds to thousands of elements. Beamwidth of an array is inversely proportional to aperture size. As such, small pointing errors can easily prevent SBR from detecting desirable targets as beamwidth can be on the order of a couple degrees. The CReSIS radars have a much wider beamwidth and are less sensitive to mainbeam pointing errors. Though correcting for mainbeam pointing errors in the CReSIS radars has some benefit, correcting off-nadir beam formation, specifically in the placement of nulls, is much more critical in improving the radars ability to sound the most difficult regions in ice sheets. As will be shown in Chapter 10, the compensation method developed for this work will expand on current methods for correcting for array distortion to correct for off-nadir null formation.

Improving direction of arrival estimates is another motivation for phase center error correction. The study performed in [60] found that rapid fluctuation in the phase center position greatly degraded the array's direction finding ability. The ability to accurately detect the direction of arrival of incoming signals was restored by using a series of averages to estimate the array's correlation matrix over one cycle of fluctuation. Probably the most well know group to study direction finding abilities in the presence of array vibration was the NATO Research Task Group 50 [61]-[63]. The group found that first order vibration modes and steady bending of a conformal array in a UAV wing cause greater distortion of the array's radiation pattern than higher order vibration modes. The group also built a scale model demonstrator to show that

direction of arrival estimates of a vibrating array could be improved by taking enough data samples [42]. The antennas used in this test operate at 1.8 GHz, and the array is much more sensitive to small displacements as compared to CReSIS's VHF array (see Appendix D). In the case of steady deflection, phase center errors were corrected using the same relationship to correct for mainbeam pointing errors. A reference antenna was included on the demonstrator along with the antenna-array of interest. As the array was deflected relative phase differences in each of the elements were measured with respect to the reference element. Direction finding in the case of steady deflections was shown to improve by applying the relative phase offsets.

The compensation method in the work presented herein uses measured antenna element displacements to apply corrections instead of a reference antenna and complex signals. Direct element displacement measurements were favored instead of a reference antenna as the use of such an antenna would be difficult to implement on the airborne platform. First a reference antenna cannot be isolated from airframe deformations (though mounting on the fuselage would minimize these effects), as was done in [62]. Also, addition of a reference antenna would also likely require additional external structures to house the antenna as available nadir ports/windows are limited on the DC-8 and P-3.

A final motivation for compensating for phase center errors is improving clutter cancellation. Clutter often conceals desirable signals, but it can be suppressed by beam patterns with very low sidelobe levels or by placing nulls in the pattern. In [64], random phase center errors in a 90 X 90 element array were shown to increase sidelobe levels by roughly 10 and 20 dB depending on the level of displacement. Through an iterative method that required repeated radiation pattern measurements the phase center errors were corrected and sidelobes returned to their nominal levels. In [65] repeated measurements of an array's correlation matrix were required to compensate for array deformation and improve null formation when using the MVDR beamformer. This study focused on sonar applications, and as such the compensation is not susceptible to mutual coupling phenomena. Similarly, the study in [66] showed that null formation could be improved in the presence of array deformation by cycling each antenna element's phase until the total array pattern power was first maximized and then minimized (sum and difference patterns) in the desired directions. This method also required repeated array measurements, and as such is not practical to apply to the CReSIS sensors. Surveying missions are performed from aircraft that fly over some of the most remote regions in the world. To apply

the compensation methods in [64]-[66] to the MCoRDS array, a receive antenna would need to simultaneously follow the ground path of the aircraft so continuous measurements could be made, or the array would need to continuously scan across the field of view.

One of the most common applications of clutter suppression is the Airborne Early Warning (AEW) systems used by the military. The E-2C, shown in Figure 2.8, first went into service for the Navy in 1973 [14]. This aircraft is designed for carrier operations, and its mission is to locate, warn of, and identify possible incoming threats with its AEW system. The antenna-array of the AEW radar is enclosed in a 24 feet diameter radome that is mounted on top of the fuselage. The antenna-array is rotated at five to six revolutions per minute [14].



Figure 2.8: Navy E-2C Hawkeye with AEW Radar [67]

The Conformal Airborne Early Warning and Control (CAEW), shown in Figure 2.9, was developed from a modified Gulfstream 550. To date the CAEW aircraft has been delivered to both the Israeli Air Force and the Singapore Air Force to replace the aging E-2C. The radar antenna-arrays operate in the L- and S-bands, are housed inside the modified fuselage, and provide 360° coverage of the airspace [68].



Figure 2.9: Modified G550 with CAEW [69]

The S100B Argus Airborne Early Warning and Control (AEW&C) system in Figure 2.10 is a modified Saab 340B. The Erieye radar antenna-array is housed in a 29.5 foot long, rectangular

radome that is attached along the top of the fuselage. The antenna-array operates between 2 to 4 GHz [68].



Figure 2.10: S100B Argus AEW&C [70]

Ground clutter is a continual problem in AEW systems when trying to detect moving targets. In the initial deployment of these systems, the large antenna-arrays were used to constrain all sidelobes to -35 dB or better [71]. It was later determined that in some cases even deeper cancellation over a narrower extent would be required. This led to investigating the use of Space-Time Adaptive Processing (STAP) in airborne radar.

First developed in the 1970's, it was not until a decade later that the implementation of STAP on airborne radar became an active research topic. STAP refers to the simultaneous processing of spatial and temporal samples from the antenna-array and echoes, respectively, to determine a bank of adaptive weight vectors [72]. For an N -element array with M -pulse waveforms, the combined processing of both angular and Doppler data increases the degrees of freedom in the system from $N+M$ to $N*M$. As one can imagine, this greatly increases the complexity and affordability of a system and has been one of the greatest obstacles to overcome in realizing such a system on airborne platforms [73]. As such, most research regarding STAP application on airborne radar focuses on reducing the computation complexity and data requirements [74].

CRISIS does not use the advanced processing of STAP in its radar systems (it is noted that STAP struggles to identify stationary targets [75]), and is instead limited to cross-track beam formation to suppress clutter. STAP was not investigated here, as the goal of this work was to improve CRISIS systems by modifying current beamforming and processing methods and not to develop a completely new radar system. In addition, the problem of phase center position errors

caused by mounting the antenna-arrays to opposing flexible wings is somewhat unique. All of the AEW systems shown in this chapter are enclosed in structures that prevent large deformations caused by aerodynamic loads. In fact, of the examples given in Chapter 2, only three have antenna-arrays mounted to the wing. Of the three examples, the SensorCraft has yet to be built and demonstrated, and the HiCARS and AWI systems have a single element on each wing that do not operate as part of a phased array.

NASA's Helios High Altitude Long Endurance (HALE) UAV, shown in Figure 2.11, is a flying wing with an array of antennas along the wing. The flying wing configuration of this UAV is incredibly flexible, and distorts the array radiation pattern. However, in [76] it is explicitly stated that only mainbeam pointing errors of the Helios array are desired to be corrected and the distortion of the pattern off-nadir is not a concern.



Figure 2.11: NASA's HALE UAV Helios [76]

The small number of elements in the CReSIS arrays is a limiting factor when it comes to advanced beam formation. The number of elements in an array can be thought of as degrees of freedom in beamforming. Small arrays do not have the same capability of suppressing sidelobes as larger arrays due to the lack of degrees of freedom. Figure 2.12 illustrates this point. The blue lines in the figures represent the radiation patterns generated through use of a genetic algorithm when applied to a 6-element array (left) and a 30-element array (right). The red lines represent the pattern goals for the mainbeam and the sidelobes. From the figure it is obvious that the 6 element array does not contain sufficient degrees of freedom to satisfy the pattern goals.

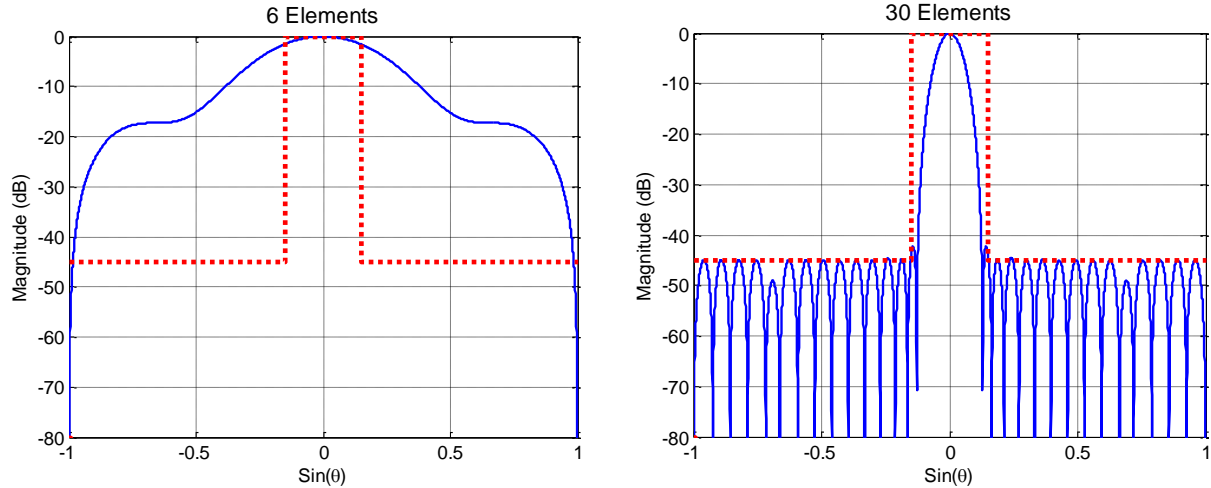


Figure 2.12: Genetic Algorithm Applied to Radiation Pattern of Arrays with Different Numbers of Elements

CRISIS radars are flown over some of the most dangerous and remote locations in the world. Due to the nature of these airborne platforms, CRISIS does not have the luxury of continually monitoring the element radiation patterns and applying corrections based on those measurements as was the case in [64], [65], and [66]. Included in the scope of this work is a method for mitigating phase center errors due to wing flexure and improving advanced beamforming required for suppressing ice sheet surface-clutter. This method requires only a single measurement of the element radiation patterns.

The wing deflection will not only change the response of the array due to the physical displacement of the phase centers, but also because the change in the array and ground plane shape will affect the mutual coupling between elements. To maintain straight and level flight during the science missions, the pilot must engage the ailerons to control the rolling of the aircraft caused by disturbances. The differential displacement of the ailerons will instantaneously change the array coupling. In addition, initial calibration flights for CRISIS radars are performed in sustained bank conditions and during continuous rolls for which differential aileron deflection (one up, one down) are commanded. The continuously changing shape of the wing will modify the array response because of the changes in coupling. In at least one study the changes in scattering from time-varying wing structures onto a fuselage mounted antenna-array was examined and a first order compensation was derived [77]. Included in the scope of this work is a study on how changes in control surface scattering affects the ability to form deep nulls when using the MVDR beamformer.

The airborne radar platform systems developed for this work represent a state-of-the-art contribution to the field of airborne remote sensing. The DC-8 and P-3 are the most advanced systems currently available for polar remote sensing and have greatly contributed to meeting the urgent need for ice sheet data. The multispectral sensor suites integrated onto these platforms provide a full profile view of the ice sheets that other polar sensing suites are currently unable to produce. In addition, the superior range and endurance of the DC-8 and P-3 allow for more coverage of areas of interest and are able to reach previously unreachable areas [14].

However, these extensive systems are more sensitive to airborne integration and thus require further advancements to overcome these effects. Most studies regarding array deformation compensation techniques are concerned with correcting for mainbeam pointing errors, whereas significant improvements to the CReSIS radar systems necessitates improved off-nadir beam formation. As compared to correcting for mainbeam distortion, correcting for pattern distortion at larger elevation angles is much more difficult. While there are a few studies in open literature that have demonstrated at least partial ability to restore the pattern, these studies generally require continual monitoring or scanning of the array, and as such are not beneficial for CReSIS applications. The compensation method developed as a result of this work to improve radiation pattern null formation is a low cost compensation that can be readily integrated into current and future CReSIS systems.

3 MULTIDISCIPLINARY DESIGN PROCESS FOR AIRBORNE REMOTE SENSING ANTENNA-ARRAYS

The current method used for integrating remote sensing radar systems for ice sheet sounding onto an aircraft is designing, analyzing, and fabricating airframes and radar systems separately. Other than the Meridian UAS, the aircraft used as platforms for the radars were not initially designed for cryospheric surveying. As such, the design of externally-mounted antenna-arrays and their associated mounting structure is driven by available hard points already existing in the airframe. While available mounting locations are specific to each aircraft, leading to unique array and fairing designs specific to the platform, a general design method was followed in the process of developing both the DC-8 and the P-3 antenna fairings. This design process considers aerodynamic, structural, and EM requirements and attempts to couple physics-based simulations for each, but does not include performing simulations simultaneously.

3.1 Initial Layout and Mold Line Generation

The first step in the design process is acquiring information on available hard points and viewports that can be used for mounting and installing the array. A preliminary design for the radar antenna-array should also be acquired as early in the design process as possible. Often the exact array design has not been established in the early design stages, but details such as antenna type and center frequency are often enough for the initial layout. If element spacing and ground plane requirements are not specified for the array during the preliminary design stage, it is suggested that an element spacing of 0.5λ in the cross-track direction and a ground plane offset of 0.25λ be used. At this spacing and offset, antenna element patterns add constructively, pattern minor lobes are minimized, and favorable radiation patterns are produced [78].

For the initial layout of the array it is important to maximize array aperture size while minimizing aircraft performance degradation and potential structural fatigue. It is desirable to maximize the cross-track aperture size as aperture size is directly proportional to directivity and indirectly proportional to mainbeam width [78]. The initial layout of the array should maximize the cross-track aperture size while also conforming to available hardpoints on the airframe. In addition the array must be adequately spaced from propellers and wing tips to avoid subjecting the structure to the adverse effects of prop wash and tip vortices. The flow behind propellers and

off the wing tips is not smooth and will increase the drag of the fairing as well as the structural fatigue. If the array is upstream of the aircraft control surfaces, potential dynamic effects of array induced turbulence on control surface effectiveness and aircraft handling must be considered.

With the initial size and layout of the array established, the outer mold line (OML) of the fairing can be defined. The cross-section of the fairing should be an appropriate aerodynamic shape, which is a function of the aircraft operating envelope. The overall size of the fairing should only be large enough to accommodate the array, but it is also important to keep in mind additional spacing needed for cabling, inspection access, and potentially a ground plane inside the fairing.

3.2 External Load Generation

Three different types of loads are considered during the analysis of the antenna fairings— aerodynamic, inertial, and thermally-induced—combined in several extreme sizing conditions. These loads should be derived from various conditions of the flight envelope and should include conditions for: 1) maximum dynamic pressure, 2) both minimum and maximum operational temperature limits, 3) maximum inertial load, and 4) maximum side slip. In addition to these extreme flight conditions, icing must also be considered (unless an anti-icing system is to be included in the design (although these would generally be potential interference sources in high performance antennas).

With the OML and load conditions defined, three- and two-dimensional computational fluid dynamic (CFD) analyses can be performed to determine the aerodynamic loads acting on the fairings. Figure 3.1 shows an example of the 3D CFD output for the outboard assembly on the P-3 in the high speed dive condition. In the figure, the color contour plot represents the dynamic pressure distribution.

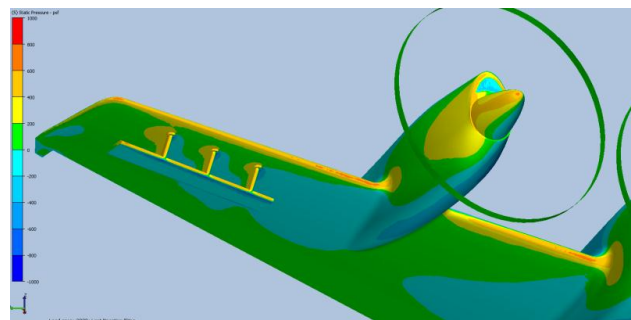
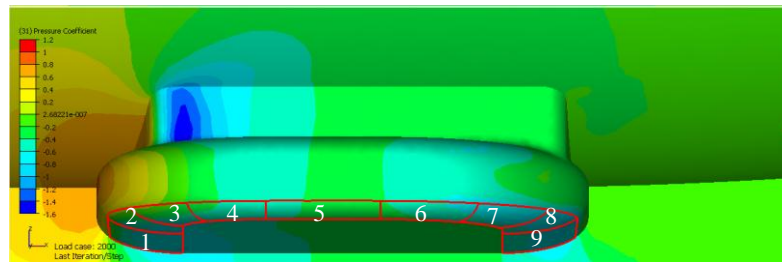


Figure 3.1: Example 3-D CFD Output for High Speed Dive

Pressures determined from CFD analyses must be mapped to structural finite element models. The surfaces of the installation can be divided into sections, and conservative, average pressure coefficients, C_p , determined for each section. Figure 3.2 shows an example of how the bottom surfaces of the DC-8 fairing were divided and how the pressures and coefficients of pressure were reported. The red outlined surfaces in Figure 3.2 are numbered from left to right. The pressure coefficients were used to determine the dynamic pressure loads modeled in the finite element analysis (FEA) model. Some software packages have the ability to directly map CFD pressures to an FEM. This tool should be used when available.



Surface #	1	2	3	4	5
P_{gage} (psf)	-168.66	-132.43	-115.13	-137.53	-102.59
$C_{P_{\text{gage}}}$ (~)	-0.60	-0.47	-0.41	-0.49	-0.36
Surface #	6	7	8	9	
P_{gage} (psf)	-128.99	-174.63	-185.79	-178.28	
$C_{P_{\text{gage}}}$ (~)	-0.46	-0.62	-0.66	-0.63	

Figure 3.2: Example of CFD Output for Mapping Pressures

To analyze the icing conditions, two separate two-dimensional CFD analyses were performed. The profile fairing was analyzed first without the presence of ice and then with ice build-up on the leading edge. The shape of the ice build-up was determined from [79], and the most conservative (highest drag) icing shape was used for the analysis to size the structures to withstand the highest pressure load case. In the case of the P-3 array it was found that in the presence of extreme leading edge glaze ice, the drag loads acting on the antenna fairing increased by a factor of 4.81 [80]. For the finite element model (FEM) analysis, pressure coefficients were increased by this factor to analyze the fairing in the icing condition.

3.3 Preliminary Considerations for Structural Impacts on Antenna Performance

3.3.1 *Reflections and Transmissions from Fairing Structure*

The dielectric properties of materials can affect antenna electrical performance through signal reflection and dielectric loading. The primary electrical properties of materials are

conductivity, relative permeability, relative permittivity or dielectric constant, and loss tangent. These properties determine the conduction and polarization loss experienced by the electric field as it travels through a medium. Metals are good conductors, and the attenuation of a signal in a metal is primarily from conduction losses. In fact, the conductivity of metals is so high that electric fields generally cannot penetrate through metals and are instead reflected. For this reason, only materials with small or negligible conductivity should be used in the primary radiating direction of an antenna.

Materials with small conductivity and whose primary losses are due to polarization effects are referred to as dielectrics. Polarization losses are determined by the permittivity of a material. Permittivity is given by Equation (3.1).

$$\varepsilon = \varepsilon' - j\varepsilon'' \quad (3.1)$$

where ε' is the real part of the permittivity and ε'' is the imaginary part. The relative permittivity is given by Equation (3.2) as the ratio of the real permittivity to the permittivity of free space ($\varepsilon_0 = 8.854 \times 10^{-12}$ F/m).

$$\varepsilon_r = \frac{\varepsilon'}{\varepsilon_0} \quad (3.2)$$

The loss tangent of a material is given by Equation (3.3) where σ is the conductivity and ω is the frequency. For good dielectrics where conductivity is small, the loss tangent is simply the ratio of the imaginary and real parts of the permittivity.

$$\tan(\phi) = \frac{\varepsilon''}{\varepsilon'} + \frac{\sigma}{\omega\varepsilon'} \quad (3.3)$$

The dielectric properties of a material not only cause losses, but as a signal travels across the interface of materials with different dielectric constants, part of the signal is reflected. Figure 3.3 shows a plane wave normally incident upon an interface between two dissimilar media and the resulting transmitted and reflected signals.

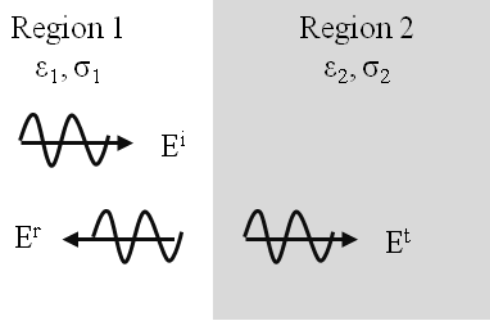


Figure 3.3: Plane Wave Incident to an Interface between Two Dissimilar Media

The reflection coefficient, denoted as Γ , is the ratio of the incident signal, E^i , to the reflected signal, E^r , and is a function of the material properties given by

$$\Gamma \equiv \frac{E^r}{E^i} = \frac{\eta_2 - \eta_1}{\eta_2 + \eta_1} \quad (3.4)$$

In Equation (3.4), η is the intrinsic impedance of each media given by Equation (3.5) where μ is the permeability of the materials.

$$\eta = \sqrt{\frac{j\omega\mu}{\sigma + j\omega\epsilon}} \quad (3.5)$$

For non-magnetic materials, the permeability is just that of free space ($\mu_0 = 4\pi \times 10^{-7}$ H/m). For dielectric materials where conductivity is negligible, Equation (3.5) is reduced to Equation (3.6).

$$\eta = \sqrt{\frac{\mu}{\epsilon}} \quad (3.6)$$

The transmission coefficient is the ratio of the transmitted signal to the incident signal and is given by

$$T \equiv \frac{E^t}{E^i} = \frac{2\eta_2}{\eta_2 + \eta_1} = 1 + \Gamma \quad (3.7)$$

This phenomenon is of interest in airborne arrays because the antenna signals will be partially reflected as they propagate through the fairing. As multiple materials are added to a fairing, such as with sandwich composites, multiple reflections will occur which can result in potentially significant losses in the transmitted signal. To solve for the total reflected and transmitted waves, the problem can be simplified by introducing an effective wave impedance, η_{eff} [81]. Figure 3.4 shows a three-medium problem and how it can be simplified to a two-

medium problem with the same transmitted and reflected fields. This transformation is possible by using a value of η_{eff} that produces the same ratio of EM fields just to the right of $z=-t$.

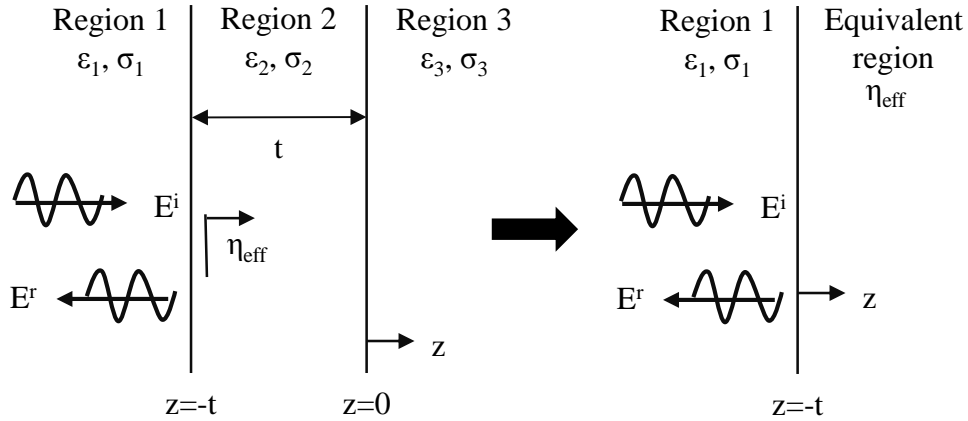


Figure 3.4: Three-Medium Problem and Equivalent Problem with the Same Net Reflected and Transmitted Signal

The effective intrinsic impedance can be found using Equation (3.8).

$$\eta_{\text{eff}} = \eta_2 \frac{\eta_3 + \eta_2 \tanh(\gamma_2 t)}{\eta_2 + \eta_3 \tanh(\gamma_2 t)} \quad (3.8)$$

where t is the thickness of Region 2, and γ is the propagation constant in the media given by

$$\gamma = \sqrt{j\omega\mu(\sigma + j\omega\epsilon)} \quad (3.9)$$

To find the reflected and transmitted field across the boundary at $z=-t$ equations (3.4) and (3.7) are used by replacing η_2 with η_{eff} . To find the transmitted field in Region 3, Equation (3.7) can be used with η_2 and η_3 , but generally the reflection coefficient at the first interface provides enough information on the effects of the fairing.

It is evident from equations (3.4) through (3.9) that reflection is minimized and transmission is maximized by using materials with similar dielectric properties. However, antennas generally radiate through the fairing into free space, and it is difficult to find materials with low relative dielectric constants that can also satisfy structural requirements. As such, typically the only other variable that may be manipulated in an effort to reduce reflection is the thickness of the laminate. Figure 3.5 shows the reflectivity as a function of laminate thickness. The laminate was assumed to be a glass/epoxy composite with properties representative of S-2 glass and 50% fiber volume. In addition, the signal was assumed to propagate from free space, through the laminate, and then

back into free space. From Figure 3.5 it can be seen that certain laminate thicknesses can result in no energy reflected back at the antenna.

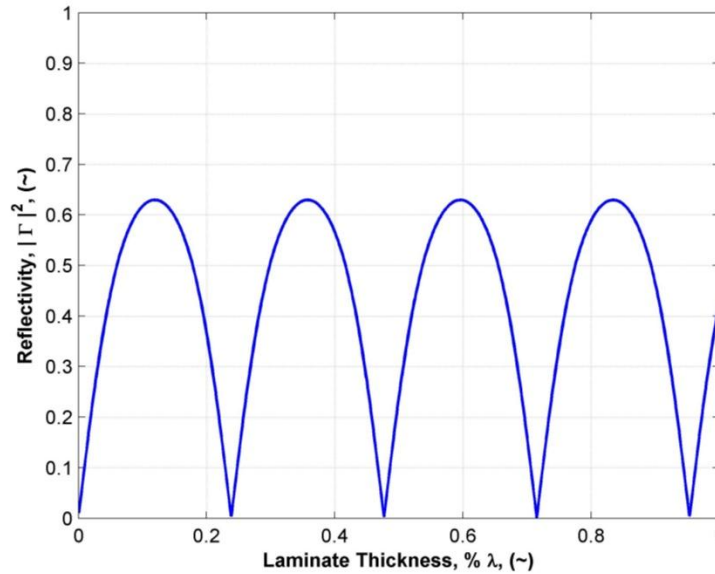


Figure 3.5: Reflectivity as a Function of Laminate Thickness

3.3.2 *Dielectric Loading from Fairing Structure*

Dielectric materials also cause dielectric loading of an antenna. The phase velocity of an electromagnetic wave decreases as the dielectric constant of the media increases by the factor $c/(\epsilon_r)^{1/2}$; therefore the wave is slower in a dielectric media as compared to free space [82]. This results in an apparent downward shift of the resonant frequency of the antenna, and the antenna must be designed for a higher center frequency. Varying thickness and relative permittivity of a dielectric adjoined to an antenna can affect the gain, return loss, and radiation pattern of the element [83]. Though the permittivity of a substrate is inversely related to an antenna's bandwidth and gain [84], potential benefits of dielectric loading include reducing antenna aperture size.

For reference, Table 3.1 [85] gives the dielectric constants and loss tangents for common fiber reinforcements and resins used in aerospace applications. The dielectric properties of materials are frequency dependent, and the data in Table 3.1 are for the X-band spectrum (8-12.5 GHz).

Table 3.1: Dielectric Properties of Common Aerospace Fibers and Matrices of Composites (at X-Band Frequencies)

Material Type	Relative Permittivity	Loss Tangent
<i>Reinforcements</i>		
E-glass	6.06	0.004
S-glass	5.2	0.007
D-glass	4	0.005
Kevlar	4.1	0.02
Quartz	3.8	0.0001
<i>Resins</i>		
Polyester	2.95	0.007
Epoxy	3.6	0.04
Polyimide	3.1	0.0055

According to [85], the dielectric constants of a fiber and matrix can be combined using Equation (3.10) to find the constant of a composite material.

$$\epsilon_m = \frac{U_R \epsilon_R + U_F \epsilon_F}{U_R + U_F} \quad (3.10)$$

where

- ϵ_m = relative permittivity of the mixture;
- ϵ_R = relative permittivity of the resin;
- ϵ_F = relative permittivity of the reinforcement fibers;
- v_R = volumetric ratio of the resin;
- v_F = volumetric ratio of the reinforcement fibers

3.4 Detailed Design and Electromagnetic Simulation

Once the preliminary design and loads have been defined, EM simulations and detailed design can begin. Initial EM simulations should begin as soon as the preliminary array configuration and fairing OML have been determined, and should use common geometry with the highest fidelity allowed by the current hardware convergence. If these simulations do not produce favorable results, then CFD simulations should be postponed until a new preliminary design has been established.

The detailed design of the fairing is driven by the results of the EM and structural analysis models and is very much an iterative process. It is important that these simulations run concurrently as structural and EM requirements will often conflict. It is recommended that a master CAD file be used to export geometry files directly into EM and structural analysis software to maintain congruency. It is noted that both simulations require less geometric detail than the CAD model used for fabrication, and the simplification of the geometry in the simulations should be closely monitored. It is generally accepted that features that are smaller than $\lambda/10$ will not significantly alter EM performance. When FEA produces results with positive margins of safety for all elements and EM simulations produce favorable results, the design stage is complete.

3.5 Challenges and Limitations of Designing Airborne Array Fairings

3.5.1 *Material Selection*

Common aerospace materials such as metal and carbon are both conductive and electrically lossy, and the proximity of these materials to antenna elements can greatly reduce their electrical performance. It is often difficult to avoid using these materials as strength and stiffness requirements cannot always be met with electrically transparent materials such as S-2 glass or quartz. When conductive elements are placed near an antenna, without extensive trade studies, it is best to keep their size to a minimum and the spacing between the antenna and conductor to a maximum. In the case of the P-3 array, the close proximity of metallic doublers eliminated the 10 dB return loss bandwidth of the antennas. A further discussion of the effects of the doublers will be left for Section 5.7.

While close proximity of materials can reduce electrical performance, the use of dielectric materials must also be done with care. The presence of dielectric materials can load the antenna, resulting in a shift in operating frequency. In addition, anytime a signal crosses the interface of two different materials, part of the signal is reflected and part of it is transmitted. The response of a signal across the interface of two different media has been thoroughly defined, so with some effort the reflected signal due to the presence of the fairing can be readily predicted and minimized.

3.5.2 Ground Plane Requirements

Another challenge of integrating an array onto an airborne platform is the ground plane requirements. Ground planes are commonly spaced $\lambda/4$ from antenna elements because at this distance transmitted and reflected waves add constructively. This offset increases the size and loads of the structure and care must also be given to the aerodynamics of the fairing. In the case of the DC-8 array, the aerodynamic loads for a $\lambda/4$ offset (15 inches) were too great, and aircraft performance requirements could not be met. As a result array performance had to be compromised and the offset was reduced. The ground plane offset was reduced to 0.07λ (4.25 inches), which reduced the bandwidth to 5% [81]. Other versions of this same radar have achieved bandwidths of 40% [87].

The offset between the fairing and the airframe also has potential to act as a convergent nozzle and choke the flow. Choking the flow causes it to transform from subsonic to supersonic. This transformation will cause a shock wave to form on the fairing and greatly increase the drag. Two-dimensional CFD studies can confirm whether the presence of the fairing chokes the flow.

3.5.3 Maintaining Aircraft and Array Performance

A final challenge in designing fairings for airborne arrays is maintaining both aircraft and array performance. The presence of the fairing external to the aircraft will increase the total drag of the platform and reduce range and endurance. For DC-8 Antarctic missions that are stationed out of Punta Arenas, Chile, the total mission duration ranges from 10-12 hours, but over half the mission is spent in ingress and egress. With such long distances to surveying sites, maintaining aircraft performance is particularly critical because reduction in aircraft endurance directly affects science flight hours.

In the case of the P-3 array, where the array fairings were attached to the wing in the region of the control surfaces, the controllability and stability of the aircraft had to be re-examined. CFD analyses were required to prove that aircraft x-, y-, and z-axis controllability and stability were maintained in the presence of the fairing [80]. In addition, CFD analyses were also used to show that vortex shedding off the fairing did not impinge on the control surfaces and empennage and reduce their effectiveness. These analyses will be expanded on in Section 5.5.

While the presence of an antenna fairing can reduce the performance of the aircraft, aircraft integration can also negatively affect the performance of the array. The primary integration effects that are investigated in this document are array deformation and control surface

deflection, but extreme thermal gradients, vibration, and the aircraft's velocity can also affect the radar's performance. The aircraft's vertical velocity causes a Doppler shift in the radar signal, while changes in the horizontal velocity cause unevenly spaced samples. These errors could be corrected in real-time using GPS data. By tracking the aircraft's horizontal ground speed, the pulse repetition frequency (PRF) of the radar could be synchronized to produce equally spaced samples, and knowledge of the aircraft's vertical velocity can be used to compensate for the resulting Doppler shift. These are areas for future investigations.

The extreme temperature gradients seen by the array while flying at altitude in polar regions cause signal phase shifts due to the thermal contraction of the antenna feed cables. Since the transmission lines are routed through parts of the aircraft that are not environmentally controlled, they are exposed to differential temperature of almost 170^{oF} during flight. Though the total length of coaxial cables used to excite the antennas are equal, the thermally exposed portions of the cables often vary as excess cable lengths are generally housed inside the cabin. As such relative phase shifts will occur due to thermal expansion or contraction.

This design method has been used successfully for several airborne radar platform systems, including the DC-8 and P-3. It serves as a multidisciplinary guide for both aerospace and electrical engineers. Design of airborne radar fairings requires compromise between electromagnetic, structural, and aircraft performance, and as such simulations of the systems should be closely coupled.

4 DEVELOPMENT OF THE DC-8 ARRAY FAIRING

The DC-8 MCoRDS fairing was developed in support of NASA's (Operation Ice Bridge) OIB. The superior endurance and cruise speed of the DC-8 has permitted longer and more extensive surveys than previous missions flown with other aircraft based out of Punta-Arenas, Chile. The DC-8 MCoRDS array is able to perform both high-altitude (3280 ft) surveying as well as low-altitude (32,800 ft) surveying required for sounding ice sheet margins with large surface-clutter. About 20% to 30% of the DC-8 missions require low altitude surveying.

With recent and unexpected speed up and retreat of glaciers in Greenland [88]-[90], the Larsen B ice shelf collapse, and the change in Antarctic ice sheet velocities [91]-[92] there was an increased sense of urgency to collect data from these regions. In addition, the loss of ICESat in 2009 caused a gap in polar observations. These reasons led to a very aggressive schedule for the design and development of the DC-8 MCoRDS array and fairing. An initial meeting between the CReSIS and NASA teams occurred in mid-January 2009, and initial design trade studies were performed shortly thereafter. Detailed engineering work began in mid-May, and the final installation of the fairing on the aircraft was completed by mid-August. The complete development and fabrication process was completed in seven months. This aggressive schedule was a major design driver for the fairing as structural components were often limited to standard stock sizes.

4.1 Design Overview

The fairing and its associated structure consists of a lower fairing, four C-channel spars, a ground plane, L-extrusion stiffeners for the ground plane, a series of attachment panels, L-extrusion stiffeners for the attachment panels, and an upper fairing. The metallic ground plane serves as a structural buck to which all other components attach. Figure 4.1 shows an exploded view of the DC-8 fairing generated with CAD software, and Table 4.1 summarizes the overall dimensions of the fairing. Detailed description of the final design and the design decisions that led to this design is in Section 4.3.

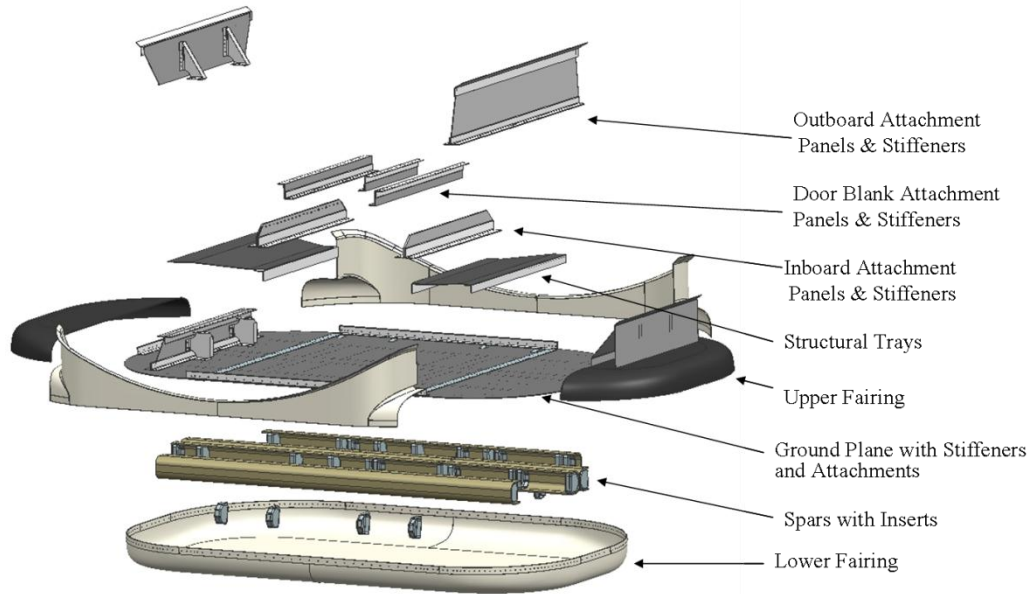


Figure 4.1: Exploded View of the DC-8 Fairing

Table 4.1: Overall DC-8 MCoRDS Dimensions

Span	98.5	inches
Chord	57.1	inches
Weight	413	lbs

4.2 Load Case Generation

Three different types of loads were considered during the analysis of the fairing— aerodynamic, inertial, and thermally-induced—combined in five extreme sizing conditions. The maximum dynamic pressure occurs during a 406 kt dive at sea level, which corresponds to a dynamic pressure of 572 psf (3.97 psi). The average dynamic pressure for cruise is 235 psf (1.63 psi). The minimum operational temperature limits are -65°F at sea-level and vary linearly to -105°F at 32,727 ft and above. The maximum operational temperature limit is 122°F. From the critical flight conditions, five load cases were identified as possible sizing conditions for the fairing. These conditions are summarized in Table 4.2.

Table 4.2: Summary of DC-8 Load Conditions

Case	Description
1	<i>Airplane High Speed Dive Flight Condition</i> q=572 psf, $N_x=2.5$, $N_y=4$, $\alpha= -5^\circ$, -4g vertical and 1.5g longitudinal inertial loads
2	<i>Airplane High Speed Dive with Worst Temperature Differential Flight Condition</i> q=572 psf, Temp=-65 °F, $N_x=2.5$, $N_y=4$, $\alpha= -5^\circ$, -4g vertical and 1.5g longitudinal inertial loads
3	<i>Airplane Cruise with Lowest Temperature Flight Condition</i> q=235 psf, Temp=-105 °F, $N_x=2.5$, $N_y=4$, -4g vertical and 1.5g longitudinal inertial loads
4	<i>Airplane Highest Temperature at Highest Appropriate Dynamic Pressure Flight Condition</i> q=400 psf, Temp=122 °F, $N_x=2.5$, $N_y=4$, -4g vertical and 1.5g longitudinal inertial loads
5	<i>Airplane at Maximum Aerodynamic Loads, Side Slip and Lateral Inertial Load Flight Condition</i> q=470 psf, Temp= 65 °F, $N_x=2.5$, $N_y=4$, $\beta = 5^\circ$, -4g vertical and 1.5g longitudinal and lateral inertial loads

Cases 1 and 2 were derived from the maximum possible dynamic pressure, as applied to an extremely conservative -5° angle of attack condition during a dive. For Case 2, the maximum dynamic pressure occurs at sea level. According to [12], the minimum temperature expected at sea level is -65°F . Subsequent input from Martin Trout, Lead Flight Test Engineer for the DC-8, suggested that the worst case dynamic pressure condition could have been limited to 3.5° angle of attack, 15,000' altitude, and 350 kts. This would have resulted in a dynamic pressure of 261 psf and a temperature of -83°F . Since load cases 2 and 3 conservatively bounded this condition, revised analyses were not performed.

For Condition 3, the absolute minimum temperature seen during flight occurs at 32,727 ft and above [12]; it would be inappropriate to apply the q_{\max} condition at this altitude, so a cruise dynamic pressure of 235 psf was used instead. Subsequent input from the Lead Flight Test Engineer for the DC-8 suggested the high Mach analysis could have been limited to 3.5° angle of attack, 35,000' altitude, and 0.82 M, or a maximum dynamic pressure of 235 psf, which supports this load case.

Load Case 4 denotes the maximum operating temperature with the highest dynamic pressure possible at NASA Dryden operating altitude. The maximum temperature is expected to occur on the runway at NASA Dryden; therefore the q_{\max} at 5,000 ft from [12] was used (400 psf).

Case 5 was derived from a worst case sideslip condition. The maximum sideslip was assumed to occur during the maximum maneuvering speed condition. According to [12], the maximum dynamic pressure is 470 psf at 20,000 ft. When considering the q_{\max} (dive) condition, it was also appropriate to add an aft inertial load of 1.5g to simulate the acceleration of the aircraft transitioning into a dive.

In addition to the limiting conditions listed above, the aerodynamic pressures were multiplied by a gust maneuvering load factor. Requirements state that a gust maneuvering load factor of 2.5 [94] must be applied to loads acting along the aircraft's x-axis (drag direction), and a gust maneuvering load factor of 4.0 [12] must be applied to loads acting along the aircraft's z-axis (lift direction). Inertial loads conservatively see a lateral (wing-axis) acceleration of 1.5, a fuselage-axis acceleration of 1.5, and a vertical z-axis acceleration of 4.0.

4.3 Structural Analysis and Design

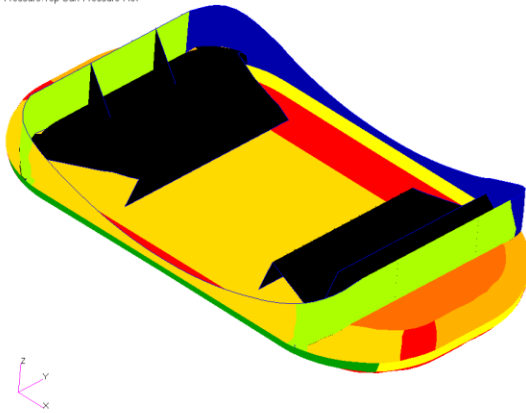
4.3.1 *Structural Analysis Overview*

Three-dimensional CFD analyses were performed by DARCorporation of Lawrence, KS to determine the aerodynamic loads acting on the fairing for load conditions 1-5. One-half of the fairing surface was divided into 45 separate surfaces and analyzed assuming a cruise condition with 30 kft altitude and Mach=0.8 ($q=235$ psf) at three different angles of attack (-5° , 0° , 5°). Of the three angle of attack conditions tested, the highest angle of attack, $\alpha = 5^\circ$, condition was determined to be the critical case as it resulted in the highest pressures. A full aerodynamic analysis can be found in [93].

Ultimate load failure tests were foregone in favor of conservative design factors of safety. As per NASA regulations, a factor of safety of 2.25 was used for metallic components, and a factor of safety of 3.0 was used for composite components [12]. No compressive, tensile, or buckling failures were allowed at ultimate load. Since it was conservative to assume no buckling to ultimate load and because stiffness variation in composite materials is better controlled than strength variation, a factor of safety of 2.25 against buckling was used for all structures.

Every structural component for the MCoRDS fairing was evaluated across all five load conditions using FEA software MSC Patran/NASTRAN Version 2008 r1 [95]. The pressures generated from the CFD analysis were mapped to the FEM as shown in Figure 4.2. Every component was analyzed for all possible failure modes (tension, compression, shear, and buckling where applicable), and maximum stress criteria was used to evaluate the structure against failure. For most components, load cases 2 and 3 were the critical load condition.

Patran 2008r1 17-Aug-09 12:08:13
Scalar Pressure:Top Surf Pressure Plot



Location	Color	Pressure
Front surface	Yellow	6.2 psi
Sides	Light Green	-4.9 psi
Back surface	Blue	-2.4 psi
Front Corners	Yellow	-8.6 psi
Back corners	Dark Yellow	-6.8 psi
Shoulder surfaces	Orange	-7.3 psi
Bottom flat surface	Yellow	-6.67 psi
Bottom curved perimeter	Red	-8.3 psi
Front surface	Green	7.5 psi
Sides	Yellow	-5.0 psi

Figure 4.2: DC-8 Fairing FEA Modeled Pressure Regions

4.3.1 *Preliminary Design Iterations*

An initial design trade study was performed between February and May 2009. At the time, fuselage modifications for mounting the array were still under consideration, but the Nadir 7 viewport located at Fuselage Station (FS) 1200 was the most likely location for the fairing to be installed. Figure 4.3 shows the Nadir 7 port location and dimensions.

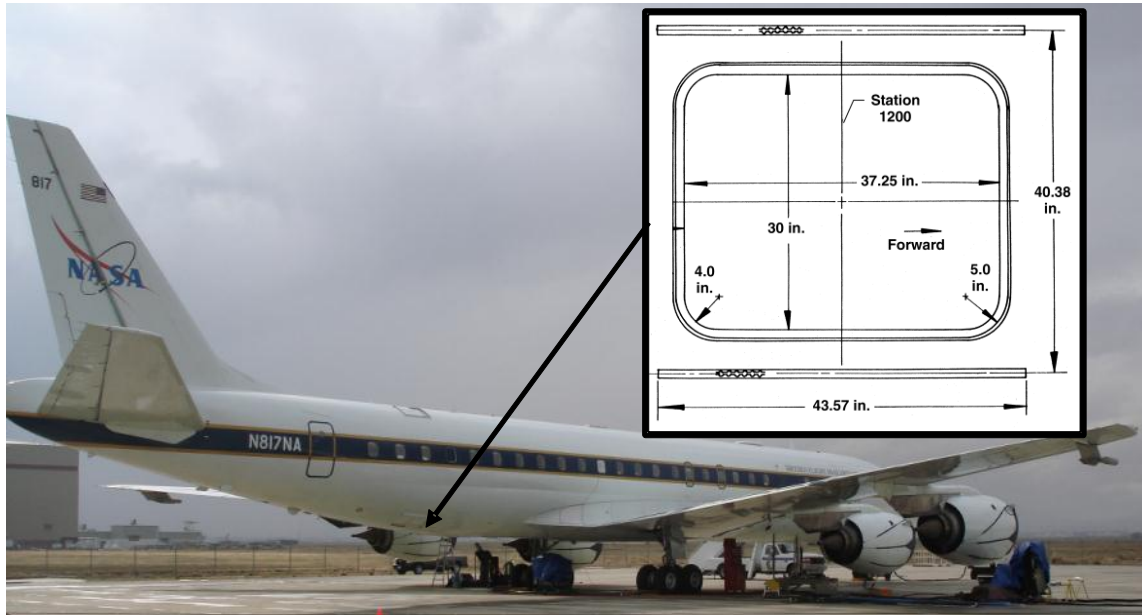


Figure 4.3: Nadir 7 Port Location and Dimensions

The trade study identified three possible configurations, shown in Figure 4.4, two of which utilized the nadir port and one that required extensive fuselage modifications. In the preliminary design stages, it was desired that the MCoRDS antenna-array consist of six dipole antennas.

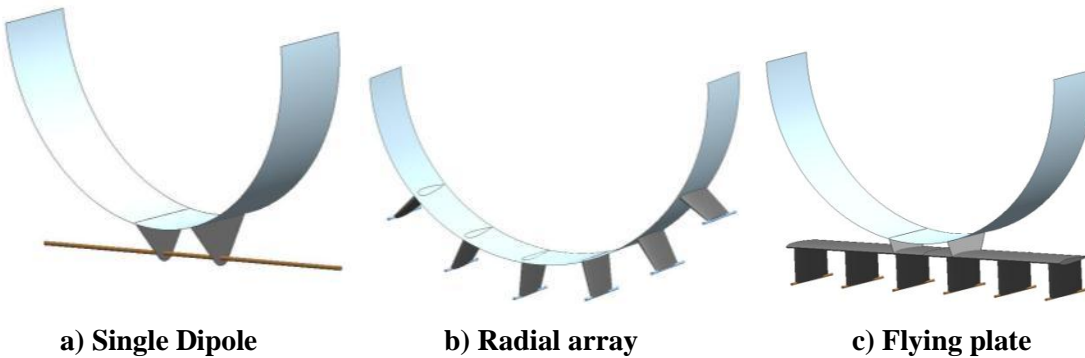


Figure 4.4: Configurations Identified for the MCoRDS Trade Study

The single dipole configurations had an equivalent aperture size to a six-element array, and it was the least expensive and easiest to manufacture of the three configurations. The radial array required extensive airframe modification to accommodate the array elements, and it was the most expensive of the three configurations due to the modifications. The flying plate configuration consisted of a ground plane that attached directly to the nadir port with dipoles offset from the ground plane by $\lambda/4$ (~15").

Due to large aerodynamic loads, considerations for electrical performance, and schedule, a design similar to the flying plate configuration was pursued. With the configuration selected, an initial array arrangement was generated and consisted of six to eight antenna elements, a ground plane with dimensions 158" X 158", and an antenna-ground plane separation of 15". It quickly became apparent that the antenna elements would need to be housed in a custom fairing, and the current array design was too large.

The overall size of the fairing was driven by the desire to minimize drag of the fairing and the limited number of hard points available for attachment. The six-element array offset 15" from the ground plane resulted in a large wetted area that produced loads that exceeded material and airframe limits and caused concern for tail strike during take-off rotation. To minimize the fairing wetted area, drag resulting from downwash from DC-8's wings, and transonic drag, it was desired that the span of the fairing not extend past the outer butt line of the DC-8 fuselage and that the thickness-to-chord ratio be kept below 18%. For these reasons, the 6-element linear dipole array was changed to a 5-element staggered array, and the ground plane offset was reduced from 15" (0.25λ) to 4.25" (0.07λ). This design compromise reduced the radar bandwidth to 9.5 MHz (5%) [81].

4.3.2 *Detailed Design*

After it became clear that the size of the initial array design would need to be greatly reduced, the design of the final fairing began to take shape. Figure 4.5 shows some of the preliminary design concepts for the smaller fairing. Concepts 1 and 2 (dimensions in the images are in inches) have a significantly larger chord than the final fairing design (57"). Though these designs produced more favorable aerodynamic results (due to smaller thickness-to-chord ratio), there were not enough hard points on the airframe to support the large chord.

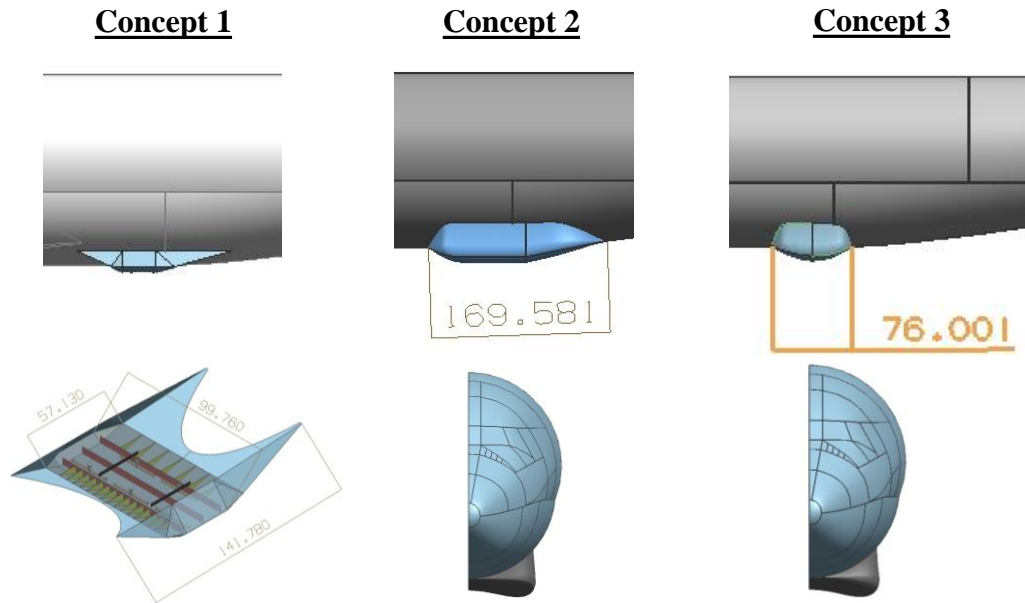


Figure 4.5: Preliminary Design Concepts for Smaller Fairing

With the outer moldline of the fairing defined, the internal structures were defined next. To ensure maximum electrical performance for the housed radar, the material choice for all structural components below the ground plane was limited to low-loss dielectric materials. It is for this reason that the four C-channel spars and the lower fairing are constructed of S2-glass fiber composites in an epoxy matrix.

The lower fairing has two regions. The regions located between the spars are composed of a total of twenty four layers of 9.0 oz 8HS weave S2-glass cloth with 0.5” thick Rohacell 71 IF foam core sandwiched in the middle. Figure 4.6 shows the thickness region plot for the lower fairing. The white regions are 0.23” thick, the light green are 0.47” and the red are 0.73” thick. The dark green regions represent the foam edge taper and the blue region represents the splice taper. The splice was required due to the width of the S2-glass cloth material used for fabrication and the wet layup techniques used in fabrication.

The design of the lower fairing was not only driven by the external loads but array performance as well. Chordwise full-length ribs were forgone in favor of the sandwich composite lower skin due to the placement of the antenna elements. It was desired to maintain constant antenna spacing, which left little available space for rib placement.

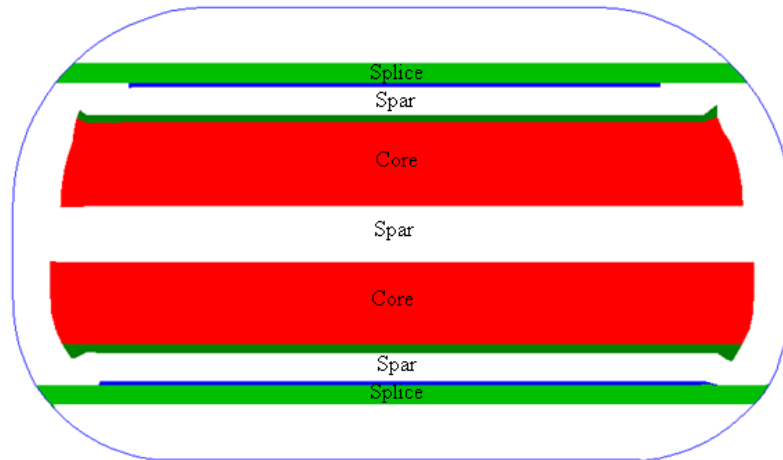


Figure 4.6: Planform View of Lower Fairing Region Plot

The initial design of the fairing consisted of three spars, but due to the high loads, conservative factors of safety, material restrictions, and lack of internal support structure a fourth spar was added. Figure 4.7 shows the positioning of the spars and their cross-section, and Figure 4.8 shows the orientations of the spars. Spar sizing resulted in a thickness of 0.26", which is equivalent to 40 layers of S-glass. All of the spars are of identical cross-section to reduce manufacturing time and cost, most notably in the use of common tooling.

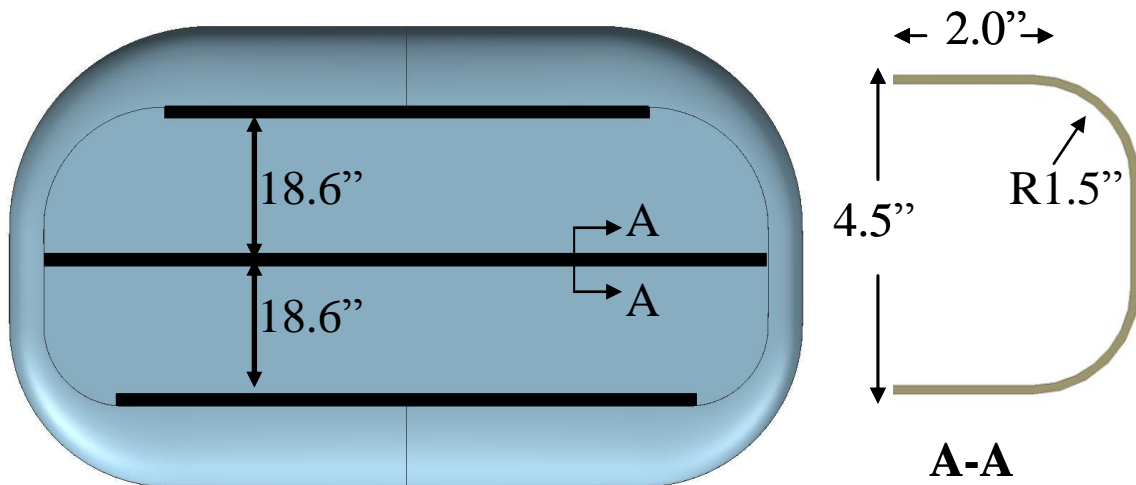


Figure 4.7: Spar Disposition and Single C-Channel Representative Cross Section

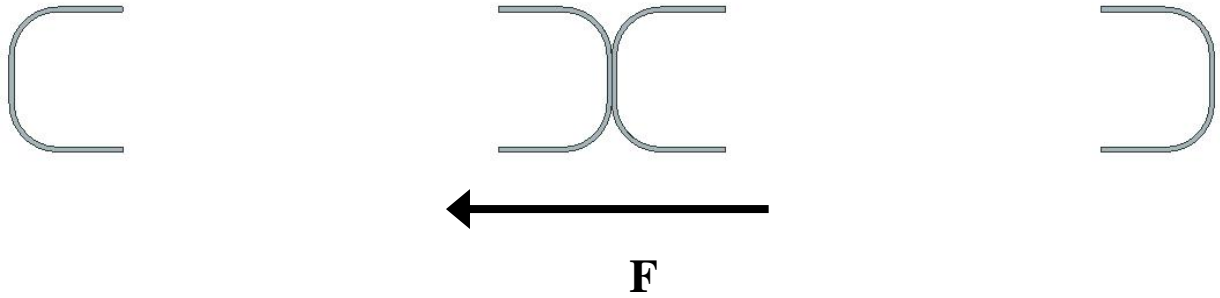


Figure 4.8: Spar Orientation

The only metallic components below the ground plane are the spar rib inserts, one of which is shown in Figure 4.9. There are a total of 50 of these rib inserts located along the spars and leading and trailing edges. These ribs were needed to transfer the loads from the lower fairing to the upper attachment structures. EM simulations demonstrated that metallic rib inserts did not significantly degrade antenna performance, so aluminum was selected to ease manufacturing.

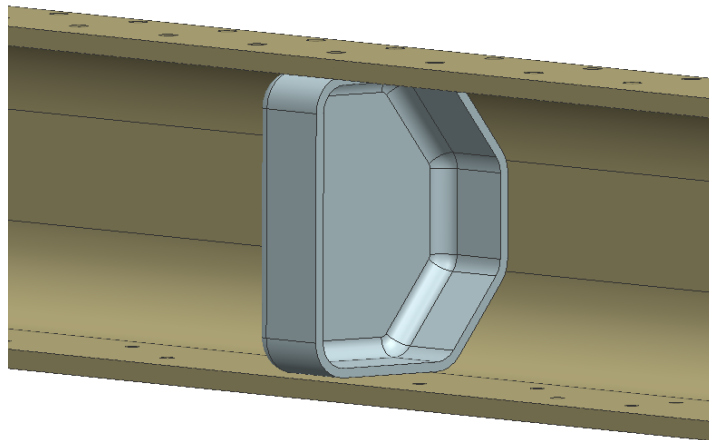


Figure 4.9: Spar Rib Insert

The ground plane is fabricated from 2024-T3 aluminum sheet. Due to stock material size limitations, the ground plane consists of three panels that are connected together with doublers and AN bolts. The ground plane serves as an electrically reflective plane for the antennas, as well as a structural buck to which the other structures attach. Sizing resulted in a ground plane thickness of 0.125", with two splices located 24" from centerline. The lower fairing is attached to the ground plane via standard-stock L-extrusions around the perimeter of the ground plane.

Since metallic components above the ground plane do not significantly degrade the array performance, all internal structure above the ground plane, including the, ground plane stiffeners,

attachment panels, and attachment panel stiffeners are fabricated from 2024-T3 or 2024-T351 aluminum. In a few instances, material substitutions of 6061-T6 or 7075-T651 were used based on material availability. Components were restricted to standard stock sizes to minimize cost and lead time for fabrication. All fasteners are either AN bolts, NAS bolts or MS24694 countersunk bolts.

The design of the internal structure above the ground plane was driven by available attachment points on the aircraft. The entire fairing assembly is attached to the airframe via the Nadir 7 port frame, the nadir door blank, and the surrounding fuselage frame longerons. Figure 4.10 shows the fairing attachments. It was necessary to connect the fairing to the fuselage longerons in addition to the viewport to reduce the unsupported length of the fairing. Structural limits could not be met without these attachments. The longeron attachments are asymmetric about the aircraft centerline due to the available information on hardpoints. This necessitated the false wall shown on the right side of Figure 4.10 so the loading on the fairing would be symmetric.

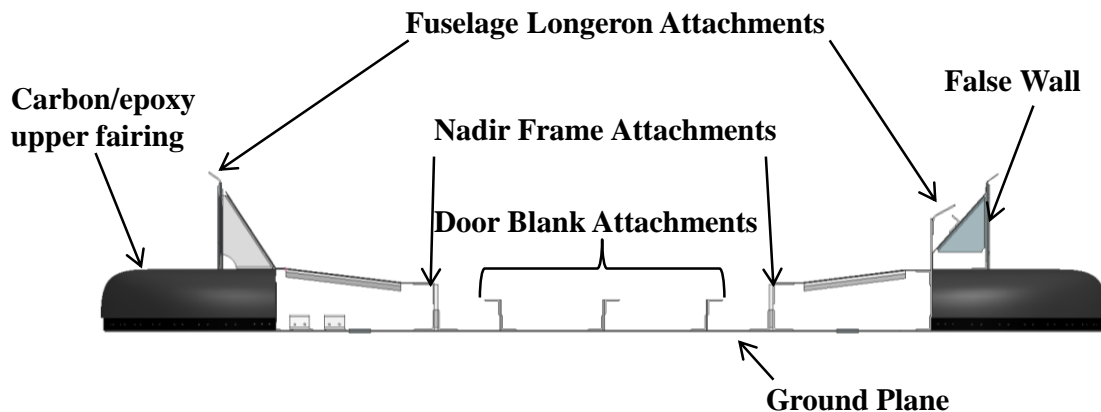


Figure 4.10: DC-8 Fairing Attachments

The upper fairing is fabricated from carbon/epoxy composite cloth. Carbon/epoxy was selected over glass/epoxy for its superior strength and stiffness. Although the carbon upper fairing helped reduce the tip displacements, and thus the loads in the structure, carbon has a significantly lower coefficient of thermal expansion than both the glass/epoxy and aluminum components. This resulted in the upper fairing being one of the most critical components in the structure. The maximum tensile stresses within the upper fairing laminate are shown in Figure 4.11 and Figure 4.12, respectively. As the figures show, the stresses in the transverse ply direction were most critical in tension.

Patran 2008r1 25-Aug-09 01:45:40

Fringe: load_case_2, A1:Static Subcase, Stress Tensor, , Y Component, Maximum,78 of 82 layers

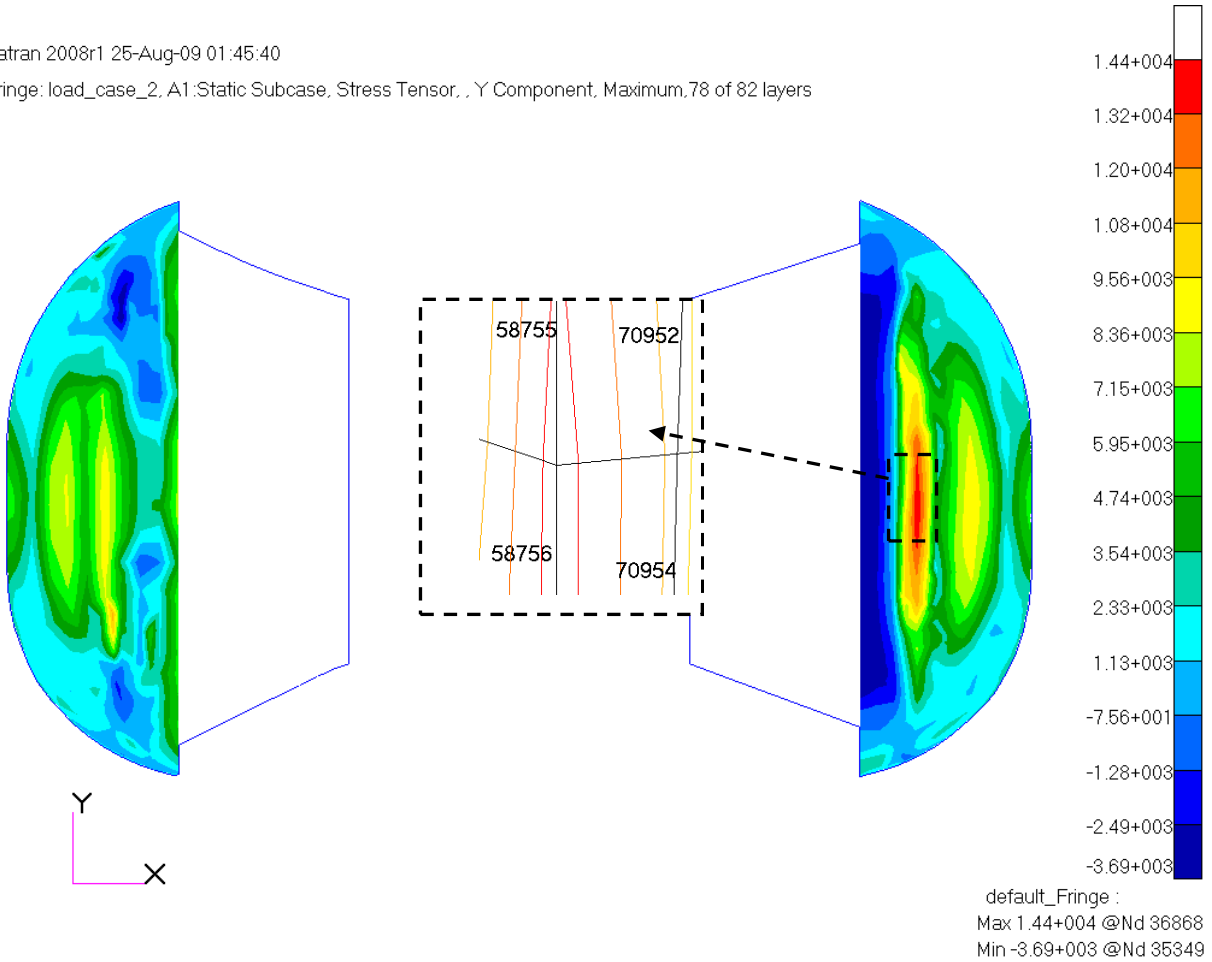


Figure 4.11: Upper Fairing Maximum Tensile Stress Plot and Critical Region

ELEMENT ID	PLY ID	STRESSES IN LAYERED COMPOSITE ELEMENTS (QUAD4)			COMPOSITE ELEMENTS (QUAD4)			PRINCIPAL STRESSES (ZERO SHEAR)			MAX SHEAR
		NORMAL-1	NORMAL-2	SHEAR-12	SHEAR XZ-MAT	SHEAR YZ-MAT	ANGLE	MAJOR	MINOR		
70954	1	-7.39635E+03	-9.48325E+03	2.54437E+01	2.57724E+00	-5.81151E+01	0.70	-7.39604E+03	-9.48356E+03	1.04376E+03	
70954	2	-7.34811E+03	-8.21890E+03	1.67454E+01	4.88320E+00	-1.10113E+02	1.10	-7.34779E+03	-8.21922E+03	4.35719E+02	
70954	3	-7.28624E+03	-6.96733E+03	-6.06417E+00	6.04435E+00	-1.37961E+02	-88.91	-6.96722E+03	-7.28636E+03	1.59569E+02	
70954	4	-6.64057E+03	-6.26359E+03	-8.82860E+01	7.05068E+00	-1.62096E+02	-77.45	-6.24394E+03	-6.66022E+03	2.08142E+02	
70954	5	-7.20338E+03	-4.42585E+03	-9.34954E+00	8.54277E+00	-1.95741E+02	-89.81	-4.42582E+03	-7.20341E+03	1.38880E+03	
70954	6	-7.15514E+03	-3.16150E+03	-1.80478E+01	9.76357E+00	-2.23270E+02	-89.74	-3.16142E+03	-7.15522E+03	1.99690E+03	
70954	7	-4.37183E+03	-4.46364E+03	-3.71336E+02	1.03054E+01	-2.36265E+02	-41.48	-4.04357E+03	-4.79189E+03	3.74163E+02	
70954	8	-4.10263E+03	-3.40662E+03	4.65686E+02	1.06925E+01	-2.45548E+02	63.39	-3.17327E+03	-4.33598E+03	5.81353E+02	
70954	9	-7.01042E+03	6.31556E+02	-4.41428E+01	1.10994E+01	-2.54724E+02	-89.67	6.31811E+02	-7.01067E+03	3.82124E+03	
70954	10	-6.96217E+03	1.89591E+03	-5.28411E+01	1.12351E+01	-2.57783E+02	-89.66	1.89622E+03	-6.96249E+03	4.42936E+03	
70954	11	-6.91393E+03	3.16026E+03	-6.15394E+01	1.10994E+01	-2.54724E+02	-89.65	3.16063E+03	-6.91431E+03	5.03747E+03	
70954	12	-6.86569E+03	4.42461E+03	-7.02377E+01	1.06925E+01	-2.45548E+02	-89.64	4.42505E+03	-6.86613E+03	5.64559E+03	
70954	13	-9.19018E+02	1.54092E+02	9.37437E+02	1.03054E+01	-2.36265E+02	59.89	6.97666E+02	-1.46259E+03	1.08013E+03	
70954	14	9.21907E+02	-2.63745E+02	-1.03179E+03	9.76357E+00	-2.23270E+02	-30.06	1.51905E+03	-8.60888E+02	1.18937E+03	
70954	15	-6.72097E+03	8.21766E+03	-9.63326E+01	8.54277E+00	-1.95741E+02	-89.63	8.21829E+03	-6.72159E+03	7.46994E+03	
70954	16	-6.67273E+03	9.48202E+03	-1.05031E+02	7.05068E+00	-1.62096E+02	-89.63	9.48270E+03	-6.67341E+03	8.07805E+03	
70954	17	3.19065E+03	1.53621E+03	-1.31484E+03	6.04435E+00	-1.37961E+02	-28.91	3.93684E+03	8.10016E+02	1.55341E+03	
70954	18	2.26459E+03	3.71481E+03	1.40919E+03	4.88320E+00	-1.10113E+02	58.61	4.57450E+03	1.40490E+03	1.58480E+03	
70954	19	-6.52800E+03	1.32751E+04	-1.31126E+02	2.57724E+00	-5.81151E+01	-89.62	1.32759E+04	-6.52887E+03	9.90240E+03	
70954	20	-6.47976E+03	1.45394E+04	-1.39824E+02	4.38925E-16	2.10536E-14	-89.62	1.45404E+04	-6.48069E+03	1.05105E+04	

Figure 4.12: Upper Fairing .f06 Critical Tensile Stress Element

As the .f06 screen capture shows, the maximum tensile stress in the upper fairing is 14.5 ksi in layer 20 and the maximum allowable for this particular material is 45 ksi. The corresponding margin of safety for tensile stress of the lower fairing is shown in Equation (4.1).

$$MS = \frac{\sigma_{allowable}}{FS * \sigma_{actual}} - 1 = \frac{45 \text{ ksi}}{3 * 14.5 \text{ ksi}} - 1 = 0.03 \quad (4.1)$$

Figure 4.13 shows a photograph of the fairing installed on the DC-8 as well as a CAD image of the final design. A full description of each component, including laminate stacking sequences, and component sizing can be found in [93].

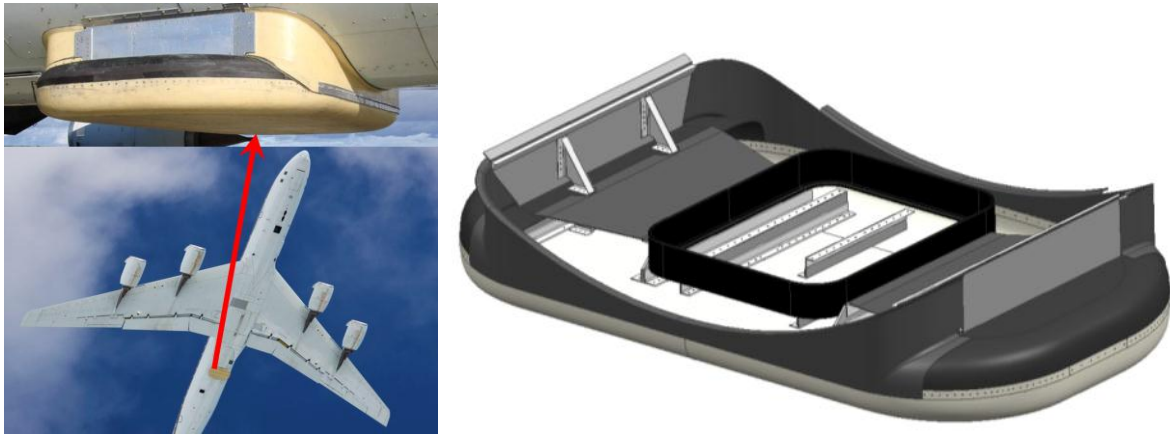


Figure 4.13: DC-8 MCoRDS Fairing

Figure 4.14 shows how the antennas are arranged inside the fairing as well as how the transmission lines are routed. Baluns, which are components used to balance currents from the coaxial cable, are connected between the transmission lines and the antennas. These baluns were required to be perpendicular to the antennas. Transmission lines are routed up through the ground plane and then through a bulkhead connector installed in a Nadir 7 door blank.

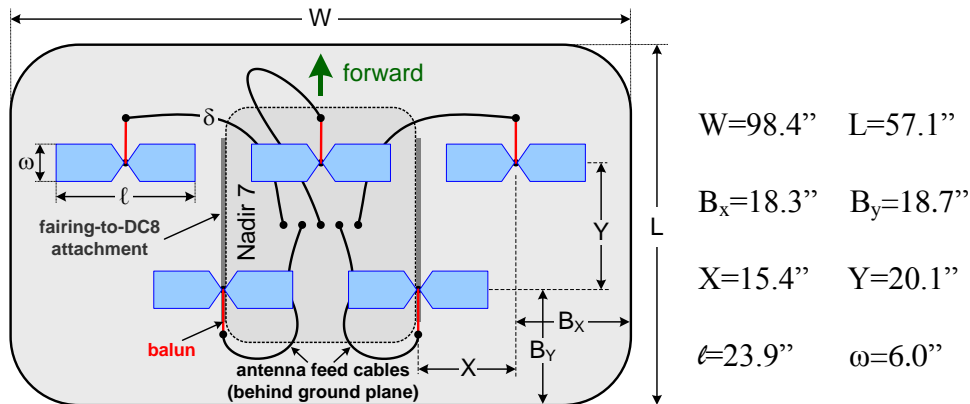


Figure 4.14: Antenna-array and Cabling Arrangement

4.4 Modal Analysis

The first and second fundamental structural modes of the fairing assembly occur between 60-62 Hz, and are represented by the first two modes of vibration of the unsupported upper fairing trays (Figure 4.15). The only aircraft operation that causes any concern for exciting structural modes in the fairing is vortex shedding caused by extension and retraction of the landing gear. NASA engineers determined that vortex shedding caused by the landing gear would occur between 15 and 25 Hz. With the first mode greater than 55 Hz, turbulence induced structural modes were not a concern.

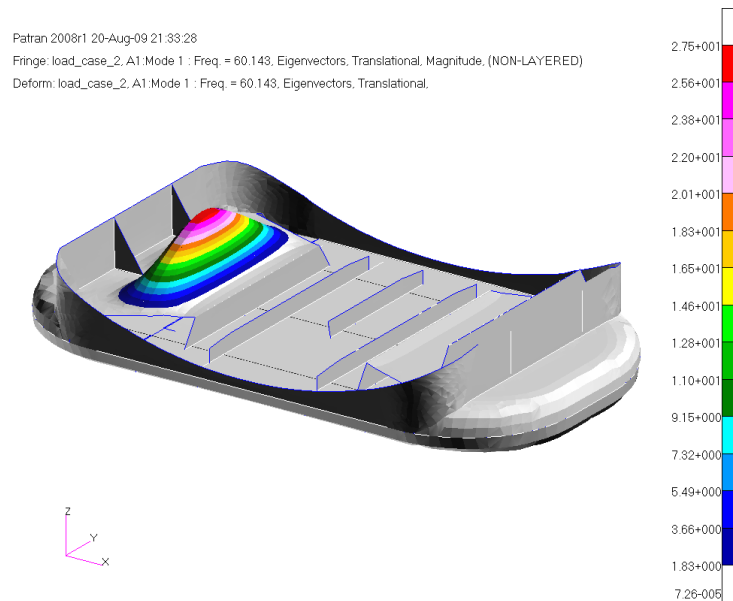


Figure 4.15: DC-8 Fairing First Fundamental Mode at 60 Hz.

The DC-8 MCoRDS fairing meets or exceeds safety requirements set forth in the DC-8 Airborne Laboratory Experimenter Handbook [12]. In all cases, conservative assumptions were made for material properties, loads, and factors of safety. Although no explicit fatigue analyses were performed, all stresses predicted in the fairing structure were well below normal endurance strengths of materials. Structural and aerodynamic performance was verified through ground and flight tests, which enabled the subsequent science missions described in the following section. According to Frank Cutler, NASA DC-8 mission manager, a low magnitude vibration in the fuselage aft of the Nadir 7 port was noticed during the higher dynamic pressure conditions of the flight envelope. However the vibrations were quantitatively assessed as being of lower magnitude than other recent instruments installed at Nadir 7, so no aircraft speed restrictions were required. In addition Cutler reported that a fuel flow check was made at an altitude of

35,000 ft and 0.74 M and no discernible difference was noted when compared to the aircraft's nominal configuration.

4.5 DC-8 Missions and Results

Since DC-8 Antarctic missions are stationed out of Punta Arenas, Chile, it was desired to keep the range reduction below 5%. From CFD and Advanced Aircraft Analysis software Version 3.2 (AAA) [97], it was determined that the presence of the fairing only increased the total aircraft drag by 1.3% [93]. Aerodynamic and aircraft performance analyses were performed by DARCorporation of Lawrence, KS.

The DC-8 was initially deployed for Antarctic surveys in Fall 2009 in which the Pine Island and Thwaites regions were the focus. Figure 4.16 shows the 2009 OIB Antarctic campaign flight lines flown by the DC-8. During this field season the DC-8 completed 21 science missions collecting more than 24 TB of MCoRDS data [13].

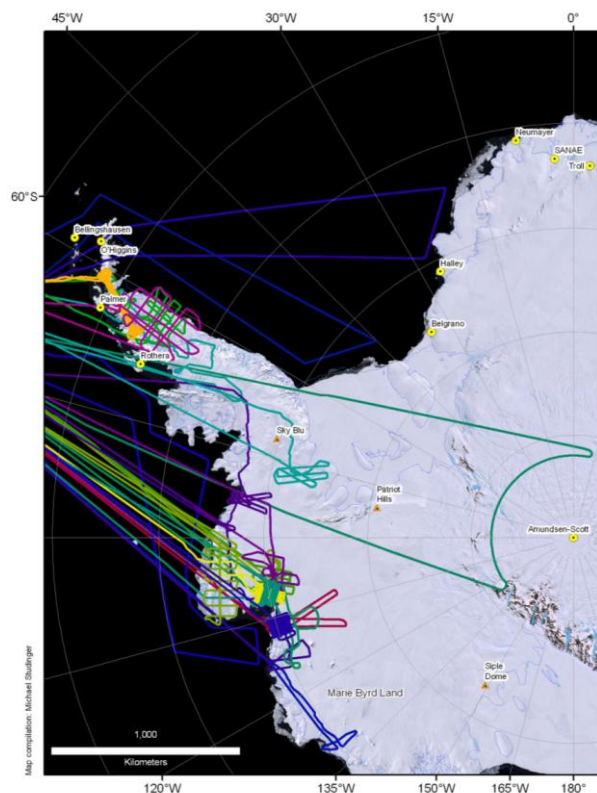


Figure 4.16: DC-8 Flight Lines during 2009 Antarctic Campaign [98]

The 2009 DC-8 dataset was validated and verified in [98] by comparing crossover data from the OIB dataset as well as comparing the data to previous area surveys such as the Airborne

Geophysical Survey of the Amundsen Embayment and BEDMAP. The study in [98] concluded that the 2009 OIB ice sheet thickness measurements are in agreement with historical measurements, and that the measurements hinted at thinning of the Pine Island and Thwaites glaciers.

Figure 4.17 shows an echogram created from the 2009 flights over the Thwaites Glacier outlet channel. The 10- μ s waveform pulse provides images of the bed echo, while the 1- μ s waveform pulse provided images of the surface. The difference in time-of-arrival for the images in Figure 4.17 is 15- μ s which yields an ice thickness of about 4,165 ft (1.3 km). Since the initial 2009 field campaign, the DC-8 has been re-deployed in Spring 2010 for Arctic surveys and Fall 2010, 2011, and 2012 for Antarctic surveys. To date, the DC-8 flying laboratory has flown 75 science missions with the MCoRDS array and has logged almost 955 flight hours, resulting in 154.2 TB of unique science data [100].

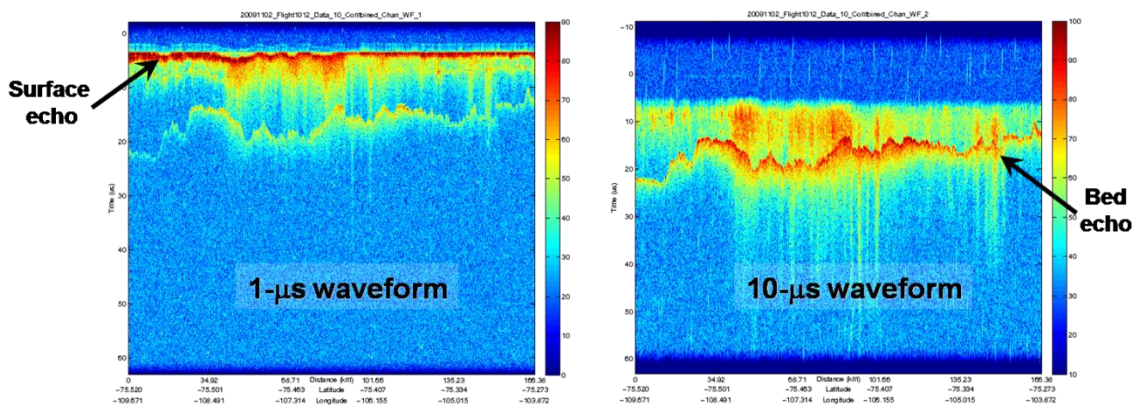


Figure 4.17: DC-8 Echogram from 2009 Survey of Thwaites Glacier

5 DEVELOPMENT OF THE P-3 ARRAY

The P-3 array was also developed in support of NASA's OIB. Originally designed as a submarine hunter for the Navy, the NASA P-3 has multiple locations for installing CReSIS instruments, including the former bomb bay and 10 hard points along the wings. Because of the extensive mounting locations, for the first time ever all four CReSIS sensors (MCoRDS, Snow, Ku, and accumulation radars) were able to be simultaneously installed (Figure 5.1). This instrument suite is capable of providing a complete vertical profile of the ice column at very fine resolutions (2") near the surface, moderate resolution (19.7") at a several hundred feet in depth, and yard-scale resolution at the ice-bed interface. While the DC-8 also supports Arctic surveying missions, the P-3 is the primary Arctic platform for NASA.

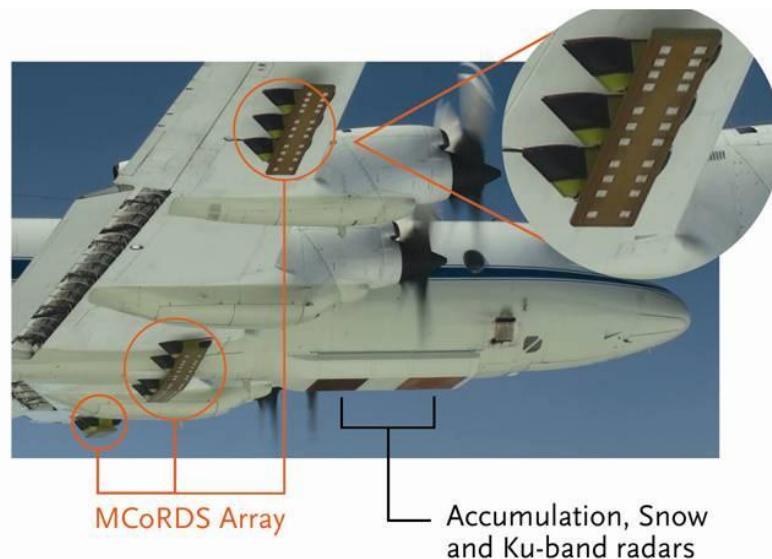


Figure 5.1: Complete CReSIS Sensor Suite Installed on the P-3

Once again, the need and urgency for data collection in Arctic regions led to an aggressive project schedule. As with the DC-8 project, this aggressive schedule was a major design driver. Initial project meetings occurred in September of 2009 followed by detailed design work completed in March 2010. Fabrication of the both the MCoRDS and bomb bay structure was completed in less than two months. The entire development, fabrication, and installation of the fairing took seven months.

5.1 Design Overview

Fewer design iterations were required in the development of the P-3 MCoRDS fairing than with the DC-8 fairing. This was due in large part to the experience gained during the DC-8 project. Availability of hard points, slower flight speeds, and a more forgiving drag-induced endurance limit also reduced design iterations. A total of ten hard points were available for mounting the array. Figure 5.2 shows the Wing Station (WS) locations of the hard points. It is noted that DARCorporation of Lawrence, KS completed the detailed design work of the attachment pylons and the internal attachment structure in the bomb bay, whereas the original contribution of this work is the detailed design of the MCoRDS antenna arrays and the bomb bay closure fairings/radomes.

- Available wing mounts located at:
 - Inboard: WS 42 and 83
 - Outboard: WS 465, 499, 533

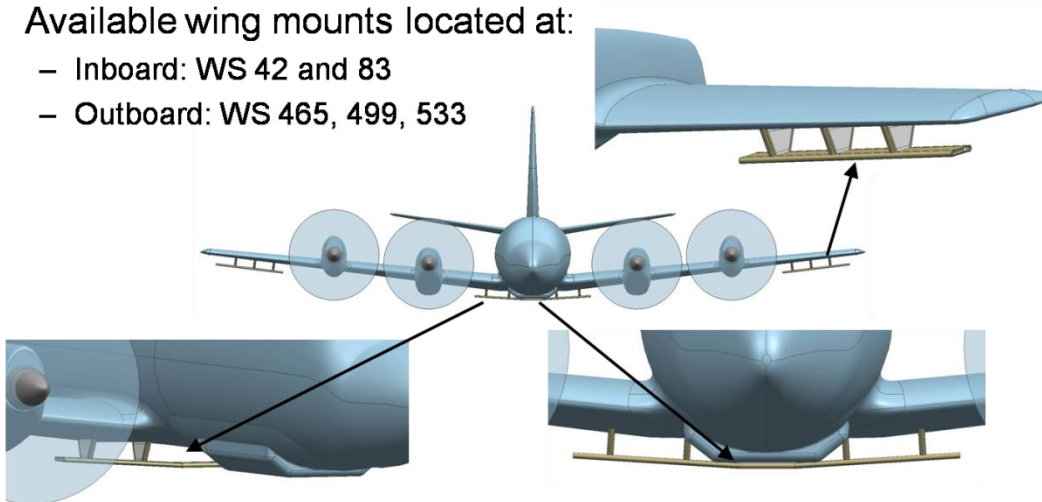


Figure 5.2: MCoRDS Installation Uses Existing WS42 and WS83 Inboard and WS465, WS499, and WS533 Outboard Hard Points

The MCoRDS fairing includes an outboard and inboard assembly. Each assembly consists of a lower skin, upper skin, a series of ribs and rib inserts, a forward and aft spar, and a leading and trailing edge. In addition to these components the inboard fairing also has a junction rib to help connect the three portions of the inboard fairing. Table 5.1 shows the dimensional overview of the outboard and inboard fairing designs. Figure 5.3 shows the inboard assembly and the junction rib, and Figure 5.4 shows an exploded view of the MCoRDS assembly with the names for each component.

Table 5.1: P-3 MCoRDS Fairing Overview

Parameter	Outboard Fairing	Inboard Fairing
Span	10.00 ft	17.32 ft
Chord	1.67 ft	1.67 ft
Weight	109 lbs	204 lbs

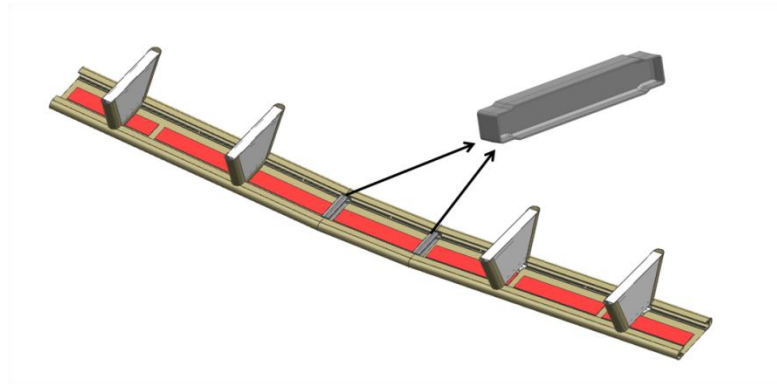


Figure 5.3: Inboard Assembly with Junction Rib

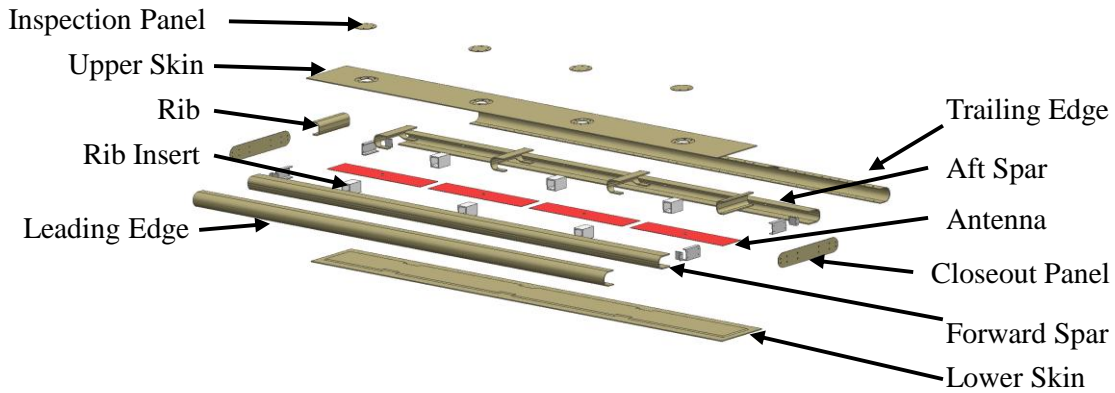


Figure 5.4: Exploded View of the MCoRDS Fairing

The attachment pylons are located at wing hardpoints on the P-3 and are used to attach the MCoRDS fairing to the aircraft. Each pylon is made of metallic parts and consists of skins, three ribs, a forward and aft spar, and a leading and trailing edge. A group of gussets are used to connect the spar, skin, and lower closeout rib. Custom machined clevis bolts are used to attach the pylons to the wings. These clevis bolts have a single through bolt in double shear to connect to the attachment gussets. Table 5.2 shows the dimensional overview of the attachment pylon. Figure 5.5 shows an exploded view of the pylon with the names of each component.

Table 5.2: Attachment Pylon Details

Parameter	Units
Height	1.08 ft
Max Chord	2.79 ft
Weight	16 lbs

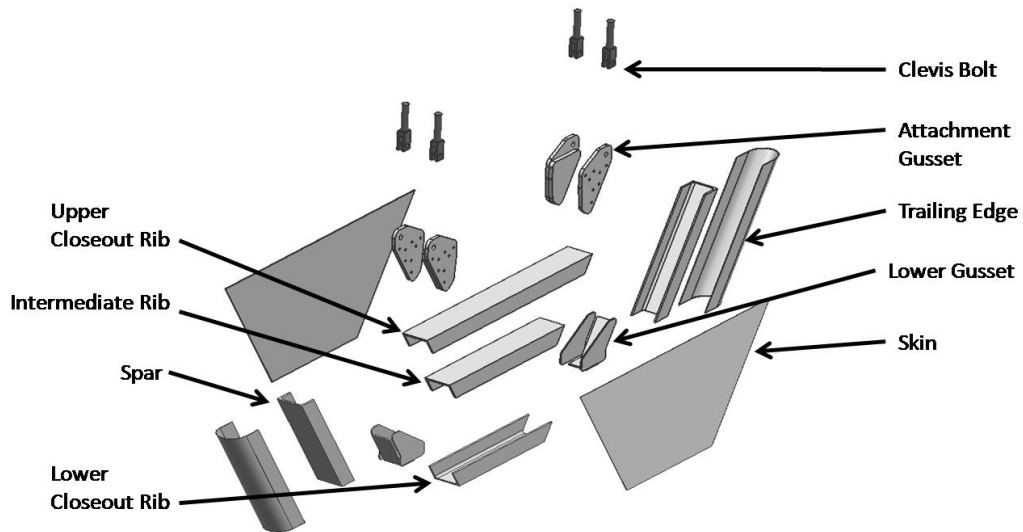


Figure 5.5: Exploded View of the Attachment Pylon

Custom outer moldline fiberglass panels were designed for the main forward and aft bays of the bomb bay. The Snow and KU radar antennas are installed in the forward bay, and the accumulation radar antennas are installed in the aft bay. A series of stock aluminum stiffeners were used to support both the forward and aft bay antennas. Figure 5.6 shows an exploded view of the bomb bay assembly. It is noted that the Snow radar antennas shown in this figure are the initial design that was intended to fly on the P-3. However the Vivaldi antenna-array was not completed by the project deadline, so the TEM horns have been flown instead. As a risk management strategy, the design of the internal bomb bay structure was such that the horn antennas could be readily integrated in case the Vivaldi array was not completed in time.

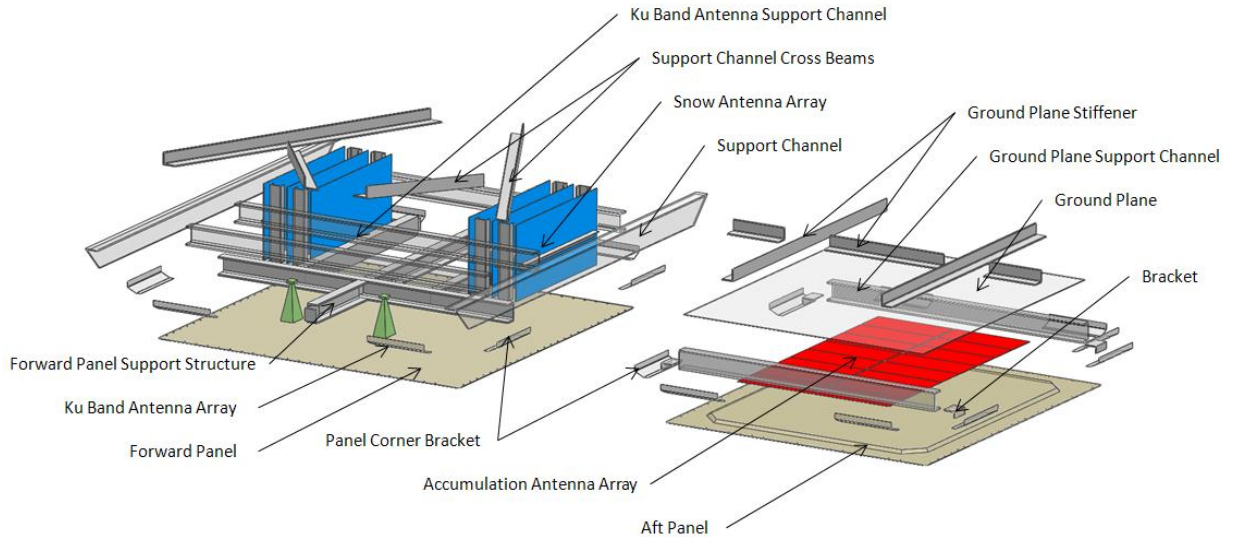


Figure 5.6: Exploded View of the Bomb Bay Assembly

5.2 Load Case Generation

A total of thirteen primary aerodynamic cases were analyzed by DARCorporation for the P-3, with a total of twenty-one trade study variants. The thirteen aerodynamic cases were mapped into the nine structural sizing cases summarized in Table 5.3. All nine potential sizing cases were analyzed in the FEM to size the structure. Determination of P-3 load conditions followed a similar process used for DC-8 load conditions described in Section 4.2. The load cases are conservative and aim to encompass all possible extreme flight conditions. Unlike the DC-8 load cases, NASA P-3 engineers recommended that gust load factors be applied as inertial loads and not aerodynamic load factors. In addition to aerodynamic, thermally-induced, and inertial loads, effects of icing, vibration, and wing flexure were also investigated for the P-3 array. In the icing load case, the ratio of drag in the icing condition to clean drag was computed. This drag load ratio was applied to the leading edges of the fairings and the pylons as an artificially elevated pressure. The mass of ice build-up on the leading edge of the fairings and the pylons was also included.

Table 5.3 : Summary of P-3 Load Cases

Case	Description
1	<i>Airplane in High Speed Dive Flight Condition</i> q = 555 psf, Alt = 8,000 ft, Temp = -75°F, V= 420 ktas, $\alpha = -5^\circ$, $\beta = 0^\circ$, -1g vertical inertial load
2	<i>Airplane Sideslip Flight Condition</i> q= 459 psf, Alt= 0 ft, Temp= -75 °F, V=331 ktas, $\alpha = 0^\circ$, $\beta = +31^\circ$, -1g vertical inertial load
3	<i>Airplane High Temperature Flight Condition</i> q= 212 psf, Alt = 0 ft, Temp = 122 °F, V=250 ktas, $\alpha = 0^\circ$, $\beta = 0^\circ$, -1g vertical inertial load
4	<i>Airplane Gust Flight Condition</i> q=440 psf, Alt=0 ft, Temp= -75 °F, V=324 ktas, $\alpha = +5^\circ$, $\beta = 0^\circ$, $N_x=1.5g$, $N_y=0.7g$, $N_z=-4.2g$
5	<i>Airplane Icing Condition</i> q=345 psf, Alt = 8,000 ft, Temp = - 75 °F, V= 331 ktas, $\alpha = 0^\circ$, $\beta = 0^\circ$, -1g vertical inertial load
6	<i>Airplane Cruise Condition (for load test and fatigue analysis)</i> q=304 psf, Alt = 8,000 ft, Temp=30.6 °F, V=338 ktas, $\alpha=0^\circ$, $\beta=0^\circ$, -1g vertical inertial load
7	<i>Wing dynamic landing</i> $N_x = \pm 4.2g$, $N_y = \pm 1.01g$, $N_z = -7.6g$
8	<i>Wing take-off roll vibration</i> Temp=-65.2 F, $N_z = -12g$
9	<i>Wing flex load case</i> Enforced wing deflection: PSG conditions at inboard and outboard installations Stall CFD pressure : q= 225 psf , Alt = 8 kft, Temp = 30.6 °F, V = 291 ktas, $\alpha = +16^\circ$, $\beta = 0^\circ$

In the wing flex load case, the most severe wing deflection curves in Figure 5.7 [101] were used—4 Positive Symmetric Gust (PSG) for the outboard installation and 7 PSG for the inboard installation. Although these flexure conditions are not specifically linked to the identified flight conditions in Table 5.3, they represent the worst-case wing flexure (note that the inboard installation deflects more at 7 PSG condition than at the 4 PSG condition, according to the chart) and were thus used to impose displacement boundary conditions for the MCoRDS structures.

The outer mold line bomb bay panels were sized to a uniformly-distributed pressure of 1 psi, and the internal structure was sized to a 4.1g downward inertial load.

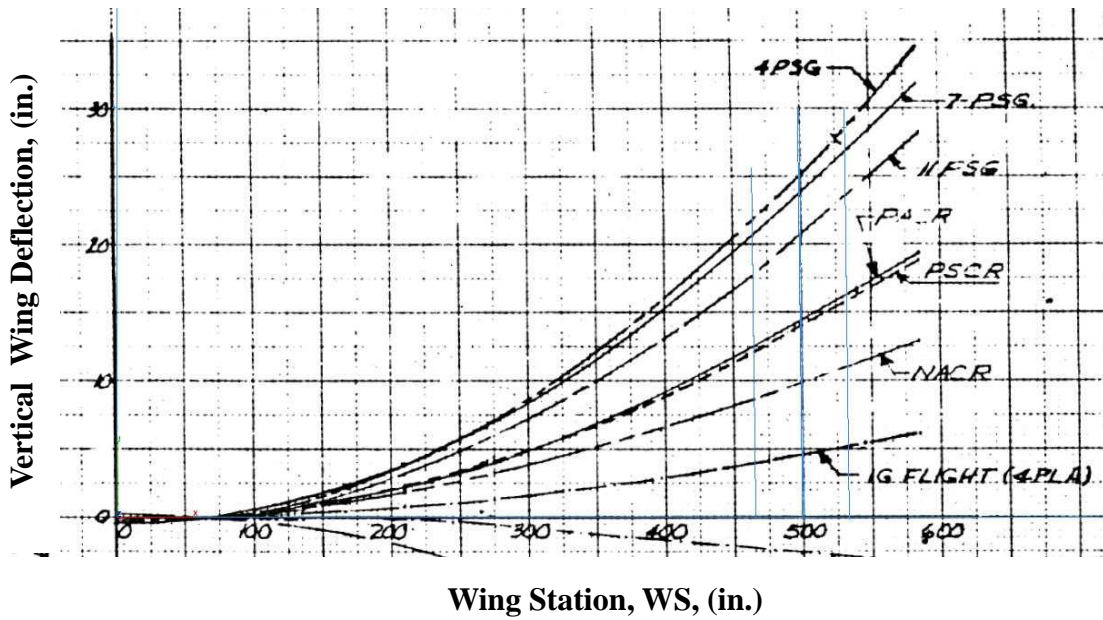


Figure 5.7: P-3 Vertical Wing Deflection Limits

5.3 Structural Analysis and Detailed Design

5.3.1 *Structural Analysis Overview*

Three- and two-dimensional CFD analyses were performed by DARCorporation to determine the aerodynamic loads acting on the fairings for all load conditions. A full aircraft and fairing model was analyzed in the CFD software. Figure 5.8 shows an example of the 3D CFD output for the aircraft and fairings in the high speed dive condition. The contour plot represents the dynamic pressure distribution.

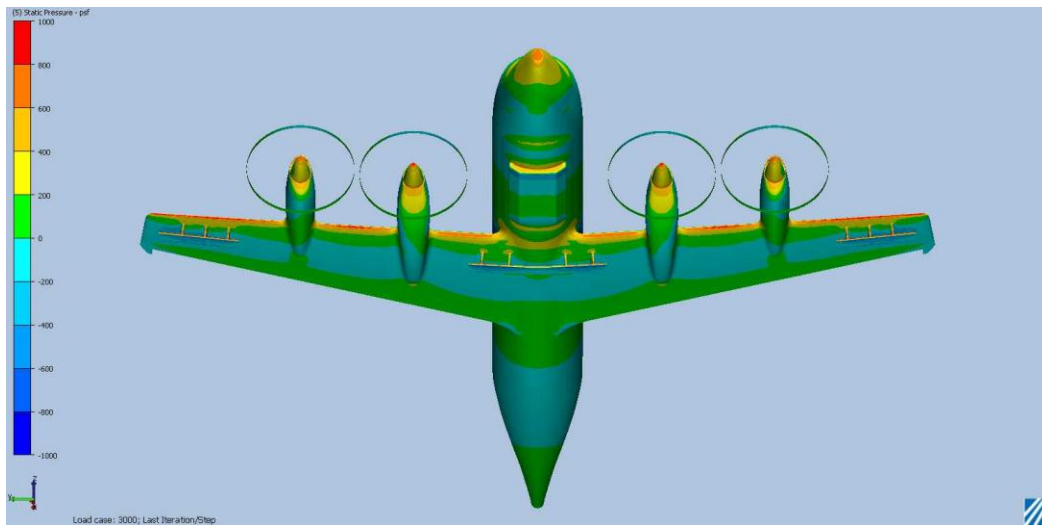


Figure 5.8: P-3 Surface Dynamic Pressure Contours in High Speed Dive and $\alpha = +5^\circ$

Since no de-icing system was included on the fairing, it was necessary to determine the aerodynamic effects of ice build-up. To examine the effects of icing on the aerodynamic loads acting on the antenna fairings and pylons, two separate 2D CFD analyses were conducted—one with the presence of the glaze shaped ice (refer to Figure 5.9 [80]), the other without. The shape of the leading edge ice is determined from the study in [71]. In the icing flight condition, with temperatures as low as -75°F , a much lower drag rime shaped ice would be expected to form on the leading edge rather than the higher drag glaze shaped ice. However, the glaze shaped ice was conservatively selected for structural sizing.

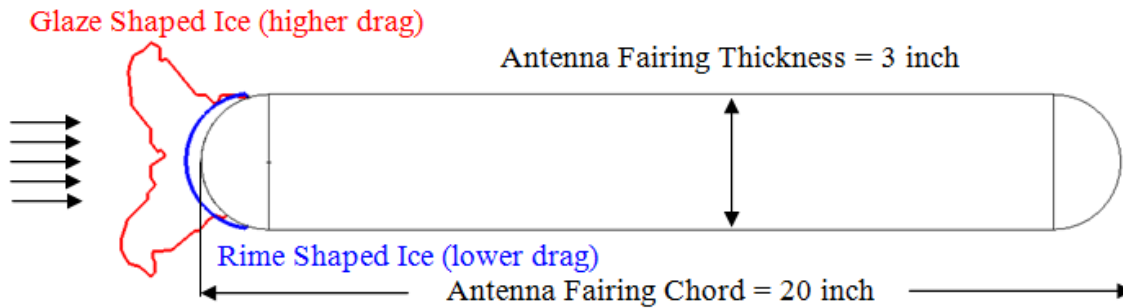


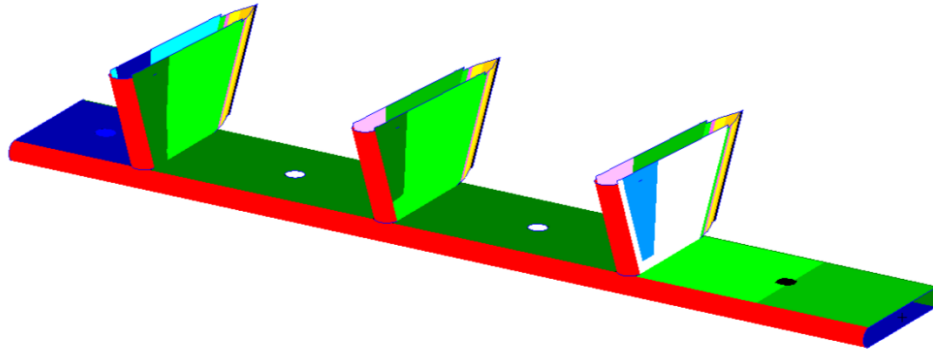
Figure 5.9: 2D Profile of the Antenna Fairing, with the Leading Edge Ice Shapes

Table 5.4 summarizes the 2D, transient CFD analysis drag results. It was found that with the presence of the extreme leading edge glaze ice, the drag loads acting on the antenna fairing increased by a factor of 4.81. To model the icing condition in the FEM, drag loads were increased by this ratio.

Table 5.4: 2D CFD Drag Coefficients of the Fairing with and without Ice

Case	Drag Coefficient (~)	Drag Loads (lbf/ft)
Without Leading Edge Ice	0.0732	42.0
With Leading Edge Ice	0.3518	202.3

Similar to the DC-8 design process, the surfaces of the installation were divided into sections, and conservative, average pressure coefficients, C_p , were determined for each section. The pressures generated from the CFD analysis were then mapped to the FEM as shown in Figure 5.10. Every component was analyzed for all possible failure modes (tension, compression, shear, and buckling where applicable), and a maximum stress criteria was used to evaluate the structure against failure.



Location	Color	Pressure	Location	Color	Pressure
Fairing Bottom Skin	White	-5.22 psi	Pylon Skin	Light Blue	-5.08 psi
Fairing & Pylon LE	Red	1.96 psi	Pylon Skin	Blue	-3.63 psi
Fairing & Pylon Skin	Dark Green	-1.60 psi	Pylon Skin	Light Pink	-1.09 psi
Fairing and Pylon Skin	Lime Green	-3.12 psi	Pylon TE	Pink	-0.58 psi
Outboard Upper Skin	Green	-2.25 psi	Pylon TE	Yellow	-0.02 psi
Fairing & Pylon Skin	Dark Blue	-3.41 psi	Pylon TE	Gold	-0.47 psi

Figure 5.10: P-3 Outboard Fairing FEA Pressure Regions

Ultimate load failure tests were foregone in favor of conservative design factors of safety. The same design criteria used for the DC-8 was also used for the P-3. For most structural components the high speed dive or wing flex load conditions were the critical conditions.

5.3.2 *Detailed Design of MCoRDS Array*

The overall dimensions of the MCoRDS array fairings were dictated by available hard points and the desire to minimize the wetted area of the structure. To minimize the adverse effects of propeller wash and wing tip vortices, it was required that the structure be at least one foot from the propeller and wing tips, as projected along the wing axis. The span of the fairings was determined by the maximum number of antenna elements that could fit in these space restrictions. The edges of the wing mounted antenna fairings are at least 16.5” (radially) away from the tip of the propeller blades and 21.8” (laterally) away from the wing tip. Since the length of the MCoRDS antennas is 27.2”, additional elements could not be added to the array without impinging on the non-laminar flow from the propellers and wing tips.

The height of the fairing was designed to be as small as possible and allow space for antenna feed cables. The connectors for the DC-8 antennas were roughly 2” tall. Since the antennas for the P-3 array were intended to be similar, it was determined that a fairing height of 3” could

accommodate the feed cables and was tall enough to allow for installation. The width of the array was designed to accommodate a single row of collinear antennas, as there was little interest from the radar team for either a planar array of collinear antennas or the ability to rotate the antennas for a parallel array.

To ensure maximum electrical performance for the housed antenna-array, the material choice for most structural components below and in parallel proximity to antenna elements was limited to low-loss dielectric materials. It is for this reason that spars, ribs, skins, and leading edges were constructed of S2-glass fiber composites in an epoxy matrix. Figure 5.11 shows the cross section of the MCoRDS fairing [80].

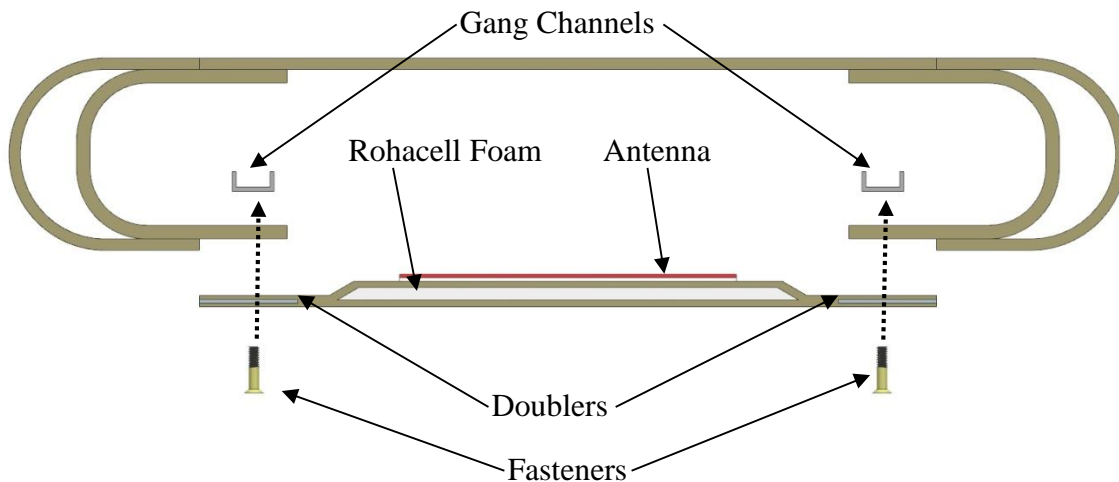


Figure 5.11: P-3 MCoRDS Fairing Cross Sections

The upper skin of the fairing is bonded to the spars. To allow for the initial installation and future maintenance of the array, it was determined that either the upper or lower skin of the fairing must be removable. A removable lower skin was favored because it would be easier to remove and install while the array was on the aircraft, and would not require the removal of the attachment pylons from the array for maintenance.

Similar to the DC-8 array, the presence of the antennas prevents fairing ribs from being attached the full length of the chord. As such the lower skins of the fairings required a sandwich composite construction and are composed of 0.25” thick Rohacell 71 IF foam core between layers of S2-glass.

In addition due to the high bearing loads present in the lower skin, embedded 0.05” thick metallic doublers were required along fastener lines. The analysis in [80] would show that

without the metallic doublers the S-2 glass/epoxy skin would need to be almost 0.15” thicker (almost twice the current thickness). This additional thickness would greatly increase the weight and drag of the fairing as the lower skin would protrude past the outer moldline of the fairing. The thicker radome would adversely affect radar performance due to the higher transmission losses and the shift in center frequency due to dielectric loading. Another ramification of opting for a removable lower skin was the need for blind fasteners and gang channels along the length of the array. The inclusion of doublers and gang channels in close proximity significantly impacted the performance of the antenna-array. Detailed discussion of the effects and design changes of these elements will be presented in Section 5.7.1.

Other than the doublers and the gang channels, the only other metallic components inside the fairing are the rib inserts. The rib inserts are made from standard 6061-T651 square tubing, and are located at pylon locations to transfer the loads from the fairing to the pylons. Similar to the rib inserts in the DC-8, EM simulations demonstrated that metallic rib inserts did not significantly degrade antenna performance. Aluminum extrusions machined on one end of the rib inner moldline profile were selected for ease of manufacturing. As Figure 5.12 shows, the aft half of the rib insert was required to fit inside the spar which produced a shape that would be difficult to fabricate using a composite hand-layup process.

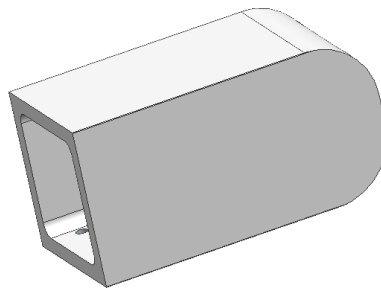


Figure 5.12: P-3 MCoRDS Array Rib Insert

The forward and aft spars of the assemblies are identical C-channels composed of 24 plies of ACG 6781 S2-glass. A C-channel design for the spars was favored because this cross-section is relatively simple to fabricate with composite materials, for both the part and the initial tooling. Experience with fabricating the box beam spars of the Meridian supported this decision.

The ribs are also C-channels with identical cross-sections to the spars. The purpose for making the ribs with the same external geometry as the spars was to reduce tooling costs and associated time to manufacture. As shown in Figure 5.13 the ribs located at pylon wing stations

have been modified such that they can accommodate the antennas. The foam core in the lower skin was notched to accommodate a bolted attachment between the skin and rib and rib inserts.

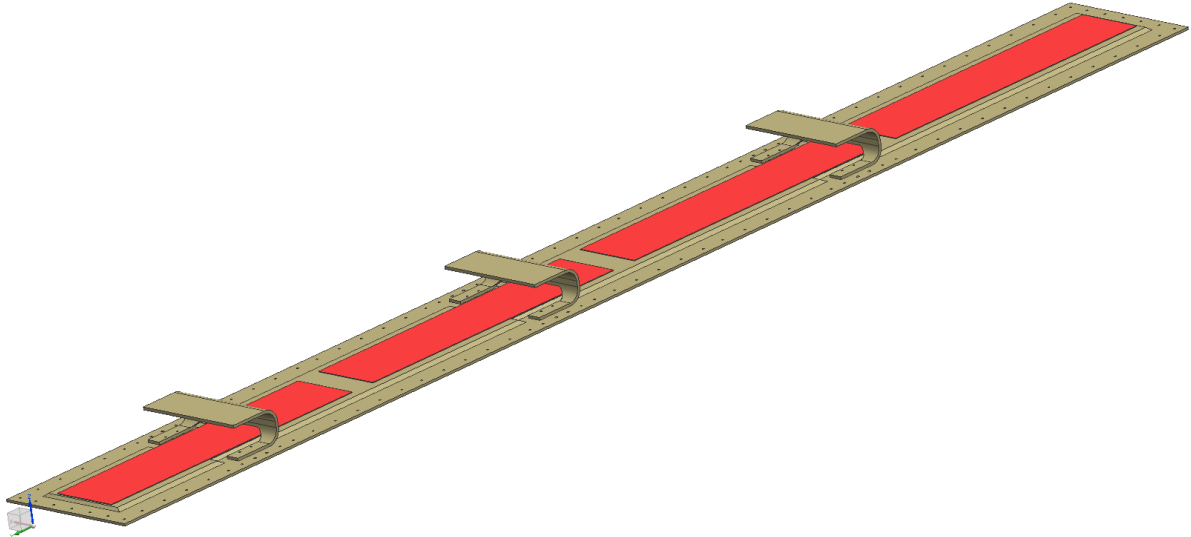


Figure 5.13: MCoRDS Lower Skin, Fairing Ribs, and Antennas

The leading and trailing edges were made identical to save on tooling costs and have the same lengths as the spars and skins. The leading and trailing edges are made of 20 layers of S2-glass, and their cross-section is shown in Figure 5.14. The leading edge is bonded to the assembly, while the trailing edge is bolted so the structure is removable and wiring can be readily accessed. In addition, future aerodynamic performance improvements can be facilitated by replacing this trailing edge shape with a sharper cross-section; however the low impact of the fairings on aircraft performance suggests this is not necessary (see sections 5.5 and 5.8).

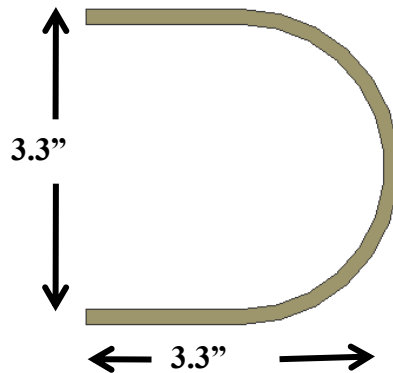


Figure 5.14: MCoRDS Fairing Leading and Trailing Edge Cross-section

The only structural component present in the inboard fairing that is not present in the outboard fairing is the junction rib. There are two junction ribs located at the intersections of the

side sections and the center section of the inboard assembly. These ribs are custom machined 7075-T6 parts. The rib is approximately 0.125” thick at the cap and 0.25” thick at the web. As shown in Figure 5.15, these large metallic structures are very close to the ends of the center antenna. Though the presence of the ribs degraded the performance of the antenna, [87] shows that the impact of these components is not as severe as elements placed parallel to the antenna. As the analysis in [80] would show, it would be difficult to design a manufacturable junction rib from composite materials using the available fabrication processes.

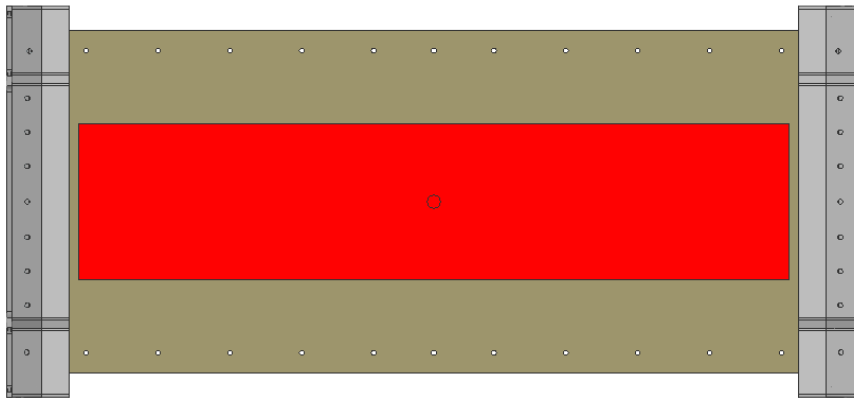


Figure 5.15: MCoRDS Center Antenna with Junction Ribs

The junction between the center and side sections of the inboard MCoRDS fairing is one of the most highly loaded sections in the fairing structure. As a tradeoff to include this center section of the fairing, the antenna performance was compromised. But as will be discussed in Section 5.7.2, modifications have been made to the center antenna such that it operates comparable to the other antennas.

All fastener patterns in the fairings, attachment pylons and bomb bay were designed to adhere to appropriate minimum edge and fastener-to-fastener spacing rules. For all materials, fastener-to-fastener spacing was required to be a minimum of $4D+0.05$ ” in metals and $5D+0.05$ ” in composites, where D is the diameter of the fastener hole. Generally $4D$ (or $5D$ in composites) is considered minimum fastener-to-fastener spacing, but manufacturing required a tolerance of at least ± 0.05 inches, so minimum spacing was adjusted to account for this tolerance. In composite materials, minimum edge spacing was required to be $3D+0.05$ ”, while minimum edge spacing in metallic components was only $2D+0.05$ ”. Again, the additional 0.05 ” was added for manufacturing tolerance.

5.3.3 *Detailed Design of Bomb Bay Panels*

The aft panel of the bomb bay, shown in Figure 5.16, was sized to be electrically transparent for the accumulation radar and measures 45.9” by 52.1”. It maintains a constant cross-section across the interior of the panel, with Rohacell foam core in the central region and monolithic S2 glass around the perimeter to facilitate fastening. The aft panel is composed of 20 plies of ACG 6781 S2-glass sandwiched around 0.5” thick Rohacell 71 IF foam core.

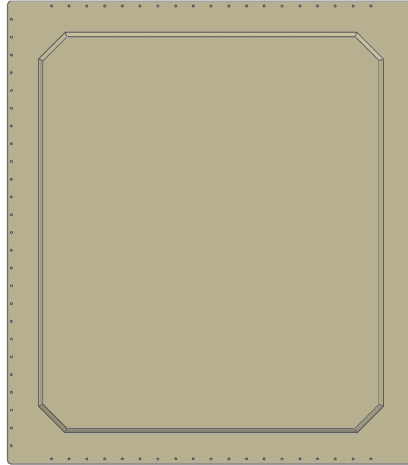


Figure 5.16: Aft Bomb Bay Replacement Panel

In order to facilitate the largest accumulation radar antenna array, internal support longerons were forgone in favor of the sandwich composite design. Similar to the MCoRDS array fairing, additional support structures, like longerons, attached to the panel would be prohibitive for a uniformly spaced array. Since the sandwich composite panel was shown to satisfy structural requirements, this design was favored to not compromise array performance. Analysis showed favorable transmissivity and reflectivity of the accumulation antennas for the panel laminate that resulted from structural sizing [102].

The forward bomb bay panel is 52.9” by 52.1”. It was sized to be electrically transparent for the Snow and Ku-band radar antennas and has numerous thinned regions in the proximity of these antennas. Since the Snow and Ku antenna-arrays do not require the full area of the forward bomb bay port, additional longerons were added to the panel to reduce its nominal thickness. Figure 5.17 shows the bomb bay FEA model with the antennas, antenna support structure, and panel in the forward bay. As this figure depicts, the panel region below the Snow radar antennas has been sized to accommodate Vivaldi arrays. The forward panel is nominally composed of 32 plies of ACG 6781 S2-glass (blue region). In the region of the Ku horn antenna footprint

(yellow), the panel is 10 plies thick (0.101”), and in the region of the Snow horn antenna footprint (red) the panel is 20 plies thick (0.202”). Analysis showed that it was difficult to achieve efficient radiation characteristics for these higher frequency antennas over their respective frequency bands when a sandwich composite design was used for the panel due to the destructive interference from the multiple reflections caused by the electrically dissimilar materials in the sandwich [102]. As such the monolithic panel design was favored.

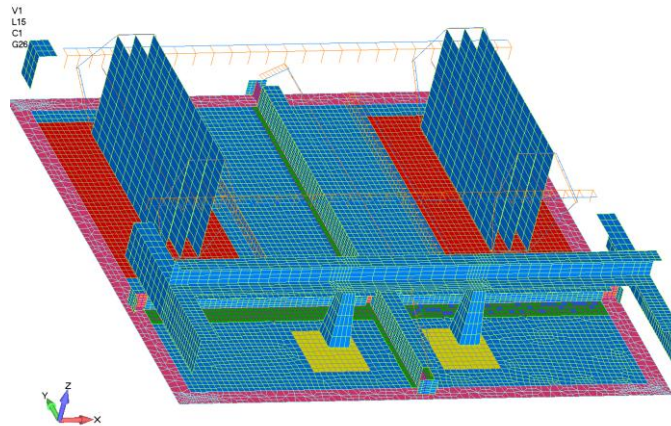


Figure 5.17: Forward Bomb Bay Panel and Support Structures with Thickness Regions Highlighted

Due to the conservative safety factors required by NASA, aluminum doublers were embedded around the perimeter of both panels to satisfy bearing load requirements. Since the surrounding structure of the bomb bay is metallic and the relative offset between the antennas and doublers is much larger than in the MCoRDS fairing, addition of these elements was not a concern for antenna performance. In addition to the bearing strips, metallic angled brackets were also required in the corners of the panels, as shown in Figure 5.18, to satisfy bearing requirements.

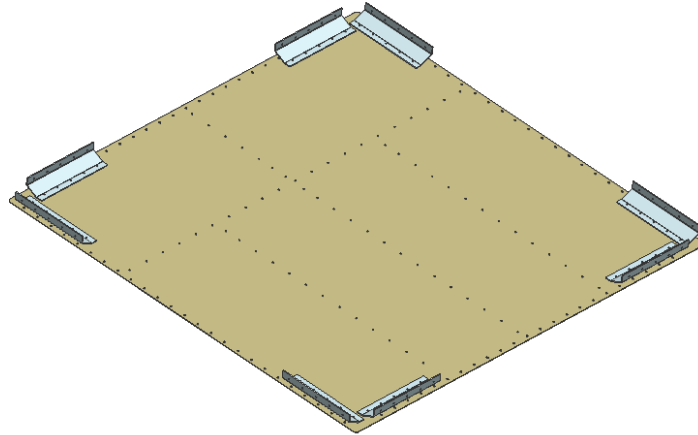


Figure 5.18: Forward Bomb Bay Panel with Angle Brackets

5.4 Modal and Fatigue Analyses

5.4.1 *Modal Analysis*

For the wing installations, the first 11 modes were extracted, and a full model was used to capture the possible asymmetric modes in the inboard wing installation. The first mode of the inboard wing installation is the center fairing flexing at 53 Hz, and the first mode of the outboard wing installation is the flexing of the outboard cantilevered fairing section at 55 Hz as shown in Figure 5.19. The second mode of the inboard fairing is the flexing of the cantilevered ends coupled with the span-wise translation of the entire fairing at 89 Hz, and the second mode of the outboard installation is the flexing of the inboard section of the fairing coupled with the span-wise translation of the entire outboard installation at 109 Hz. Figure 5.20 shows the second fundamental modes of the inboard and outboard fairings.

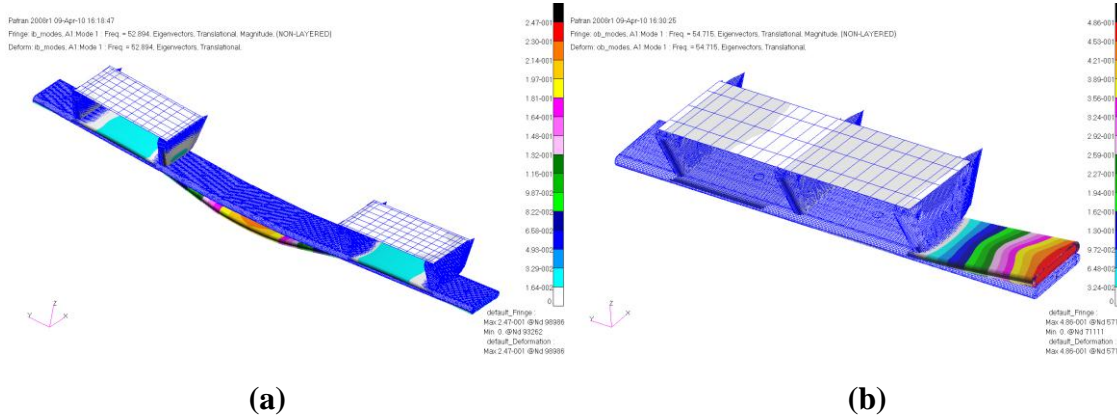


Figure 5.19: First Fundamental Modes of the P-3 (a) Inboard Array at 53 Hz and (b) Outboard Array at 55 Hz

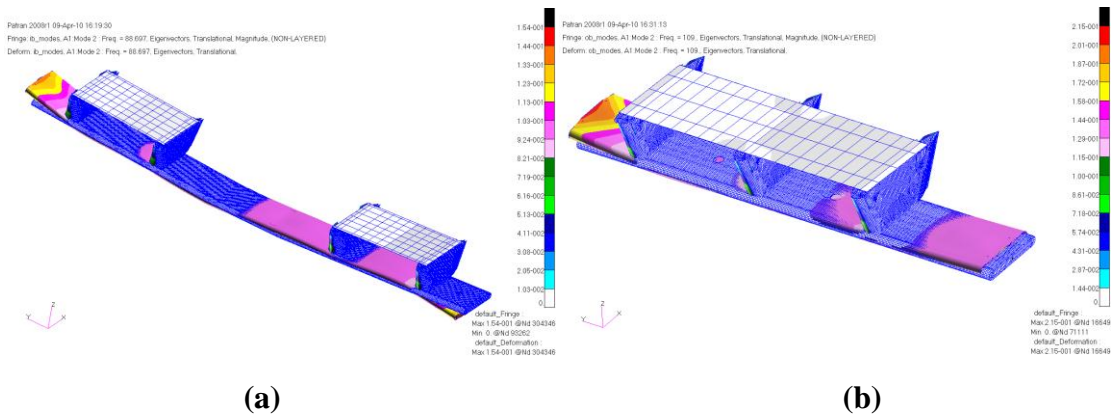


Figure 5.20: Second Fundamental Modes of the P-3 (a) Inboard Array at 89 Hz and (b) Outboard Array at 109 Hz

For the bomb bay, the first 16 modes were computed. The two critical modes of the structure occur at 59 Hz and 82 Hz. Neither of these modes are panel modes, and occur in the attachment longerons of the Snow horns. The most critical panel mode occurs at 53 Hz in the aft bomb bay panel [80].

5.4.2 *Fatigue Analysis*

Composite materials generally have much longer fatigue life than metals due to their higher inherent damping; however, damage growth in metals is a relevant concern. Table 5.5 shows the low- and high-cycle fatigue strength for metallic materials used in the P-3 fairings. To be conservative, the allowables were modified by dividing by a factor of safety of 2 and then multiplying by a stress concentration factor of 3 for circular open holes.

Table 5.5: Selected Metallic Fatigue Strengths [102]

Material	Minimum stress in each cycle (ksi)	Low Cycle		High Cycle	
		Cycles	Modified Fatigue Strength (ksi)	Cycles	Modified Fatigue Strength (ksi)
2024-T4	0	10,000	9.0	1,000,000	7.3
6061-T6	0	10,000	7.3	1,000,000	5.2
7075-T6	0	10,000	12.5	1,000,000	7.5

Low-cycle service life calculations assumed the wing antenna installations fly ten normal takeoff-landing cycles per day, seven days per week, and eight weeks per year for ten years. This yielded a total low cycle history of 5,600 cycles. High-cycle service life calculations assumed the wing installations fly ten hours per day, seven days per week, and eight weeks per year for ten years, which is a total of 20,160,000 seconds. It was assumed that every 20 seconds the aircraft makes a dive at a dynamic pressure of 440 psf or gets hit by a gust that is severe enough to increase the dynamic pressure to 440 psf. This yielded a total high cycle history of approximately 1,000,000 cycles. In both cases the minimum stress is zero and the maximum stress was determined by the cruise flight condition results. In [80], the pylon skins, spars, gussets, and fairing box beams were shown to not be fatigue critical.

5.5 Stability and Control Analysis

Due to the close proximity of the array to the aircraft control surfaces, CFD analysis results were used to determine the stability and control of the aircraft in the presence of the fairing. The stability and control analyses were performed by DARCorporation of Lawrence, KS, and shake down flights performed by NASA were used to verify the analysis.

5.5.1 *Controllability*

For the three axes of the aircraft, controllability in the x-axis was of most interest as there was concern that the presence of the fairing might cause flow separation over the ailerons. To determine the effects on airplane roll control power, the P-3 was simulated with three different aileron deflection angles, -10° , 0° , and 10° , with and without the outboard fairing. Figure 5.21 plots the airplane rolling moment coefficients that were generated from the CFD results. From

the figure, it can be seen that the reduction in roll control power due the presence of the fairing is 2.54%, which is negligible [80].

Changes in aircraft pitch (y-axis) and yaw (z-axis) controllability were also examined. The longitudinal separation between the horizontal and vertical tails of the P-3 is roughly 26 (antenna fairing) chord lengths, and the vertical separation is roughly five chord lengths. These separations were determined to be sufficient to have no impact on the pitch and yaw controllability of the P-3 [80].

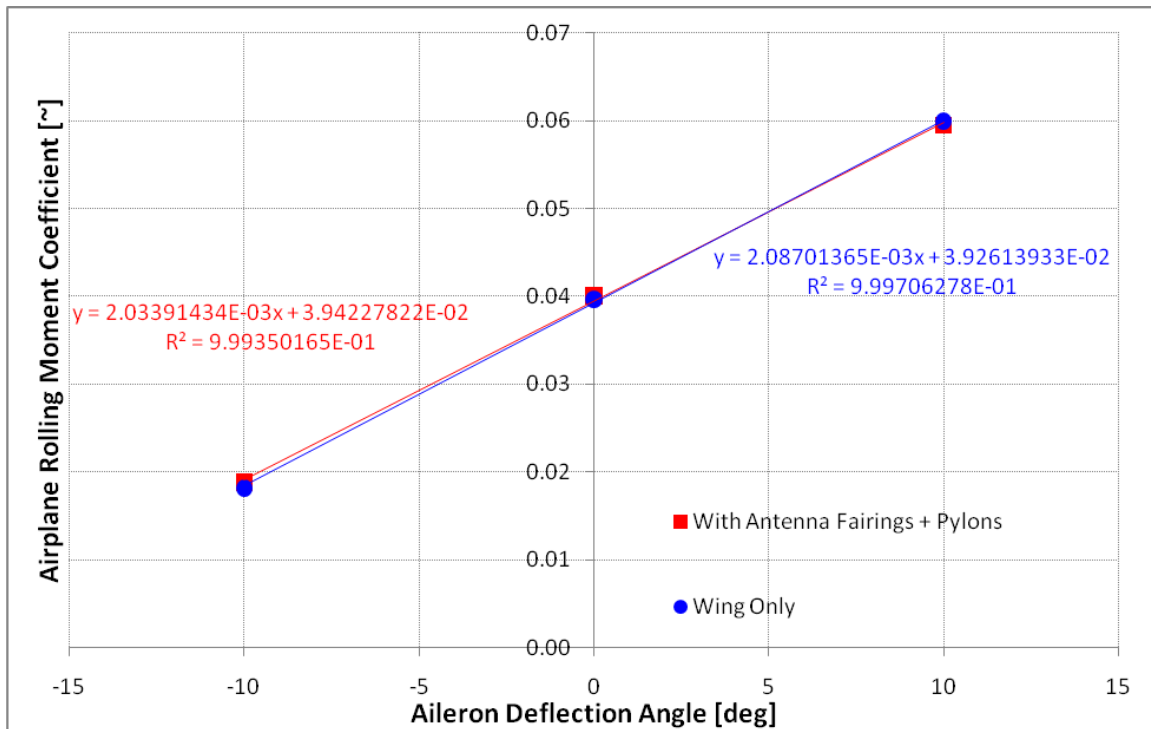


Figure 5.21: P-3 Roll Controllability with and without the MCoRDS Outboard Fairing

5.5.2 *Stability*

To determine the stability, the aircraft was modeled with and without the fairing in AAA Version 3.2 [97]. The stability about the three axes is defined as followed [102]:

- Roll Stability (x-axis): Must be negative
- Pitch Stability (y-axis): Must be negative
- Yaw Stability (z-axis): Must be greater than 0.0010 deg^{-1}

The effects of the wing-mounted antenna fairings and pylons on the airplane stability in all three axes are summarized in Table 5.6. From the analysis it was concluded that the airplane remains stable in the presence of the fairing.

Table 5.6: Airplane Stability with and without the Antenna Fairings and Pylons

	Roll Axis (deg⁻¹)	Pitch Axis (deg⁻¹)	Yaw Axis (deg⁻¹)
With Antenna Fairing and Pylons (Fwd CG)	-0.0017	-0.0403	0.0017
Without Antenna Fairing and Pylons (Fwd CG)	-0.0017	-0.0400	0.0017
<i>Change [%]</i>	<i>0.00</i>	<i>0.75</i>	<i>0.00</i>
With Antenna Fairing and Pylons (Aft CG)	-0.0016	-0.0211	0.0014
Without Antenna Fairing and Pylons (Aft CG)	-0.0016	-0.0215	0.0015
<i>Change [%]</i>	<i>0.00</i>	<i>1.86</i>	<i>6.67</i>

5.6 Verification of Design

Although conservative design factors were used in the analysis of the P-3 fairings, ground load and modal tests were required prior to first flight. The inboard fairing was selected as the test article since it is critically loaded and more accessible as compared to the outboard fairings. Figure 5.22 shows the load test assembly. Slings were placed over the fairing to distribute the applied load during the test. The slings were then connected to a whiffle tree, so the assembly could be loaded with the resultant force of the lift and drag. Pulleys were mounted to the floor to create the correct angle for the resultant force.



Figure 5.22: Ground Proof Load Test Setup for the Inboard Fairing
(photo by Rick Hale)

The loads applied to the fairing were derived from the cruise load condition. The cruise condition was selected because the loads at the more critical high speed dive condition could

have potentially damaged the P-3 airframe. The FEM model was used to predict strains at 25%, 50%, and 100% of the cruise condition. Fifteen strain gauges were installed on the clevis bolts that attached the fairing to the wing, and measured strains were compared to predicted strains. Although overall loads applied agree with those planned, the experimental strain response was difficult to map since all predicted limit strains for cruise conditions were below $124 \mu\epsilon$. This is due to the fact that the sizing dive condition has much higher dynamic pressures and the nature of the conservative safety factors required by NASA.

The finite element models of the fairings and bomb bay panels were also used to predict the natural frequencies and mode shapes. Once again the inboard fairing was selected as the test article as well as the aft bomb bay. The input force was measured by a Piezotronics model 708A50 force transducer and the response was measured by a Piezotronics model 336C04 accelerometer. Figure 5.23 and Figure 5.24 show the modal test setup.

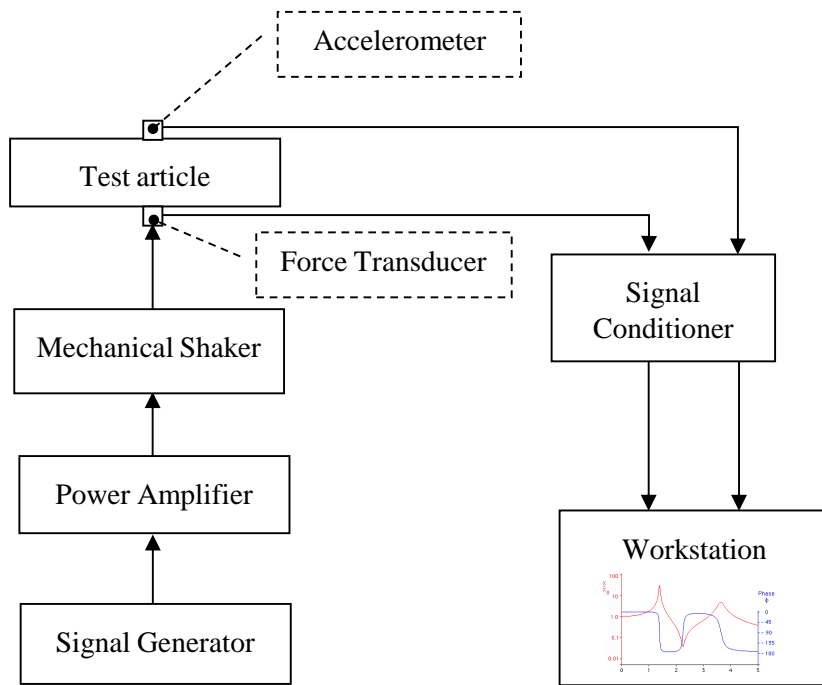


Figure 5.23: Block Diagram of Modal Test Setup

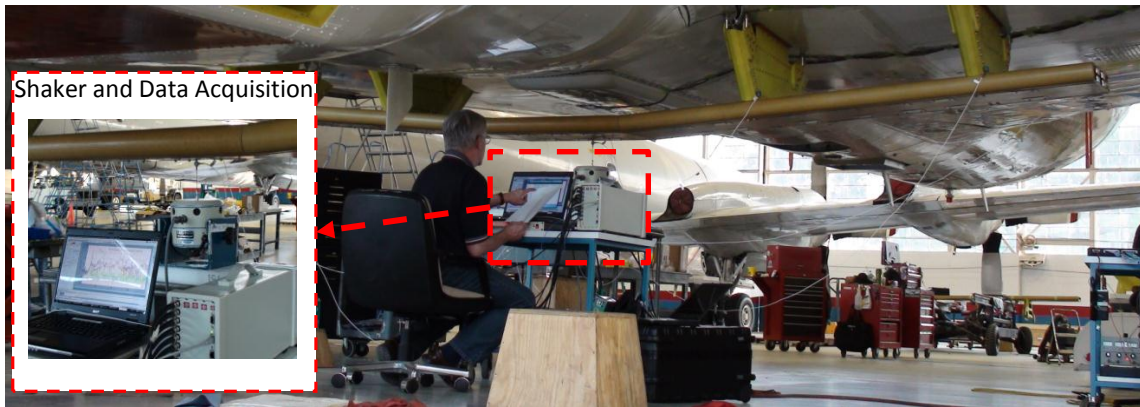


Figure 5.24: Modal Test Setup (Photo by Rick Hale)

Figure 5.25 shows the frequency response functions (FRF) for the inboard fairing. The first natural frequency was predicted by the FEM to occur at 55 Hz, and it measured as 45 Hz. The second natural frequency of the fairing was predicted to be 92 Hz and measured as 91 Hz. No resonant frequencies were found within the blade passage frequency range of 68 ± 5 Hz because the structure was designed to have anti-resonance in this range. The first natural frequency was likely overestimated by the FEM due to overestimation of the stiffness of the mechanical joints as well as manufacturing variations. Experiment and theory for the modal response are within 18%, and thus experimental characterization provided sufficient validity of the fairing FEM.

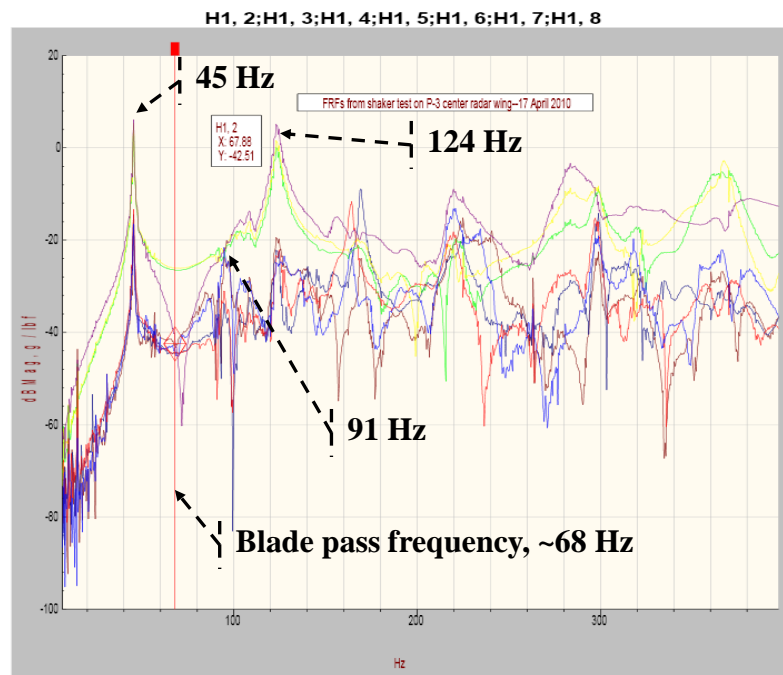


Figure 5.25: Measured FRF of the Inboard Fairing

The measured (FRF) of the aft bomb bay is shown Figure 5.26. A “twin mode” of center portion bending was observed at 46 Hz and 51 Hz. Twin modes for plates are generally caused by skewed dimensions of the plate (slightly unequal length of diagonal). Again the measured resonances were slightly lower than simulated values which is a possible result of cured ply thickness variation, material stiffness variation, or softening of mechanical joints in comparison with the FEM. Predictions and experimental characterization were as expected, and thus the modal test provided sufficient validity of the bomb bay finite element models.

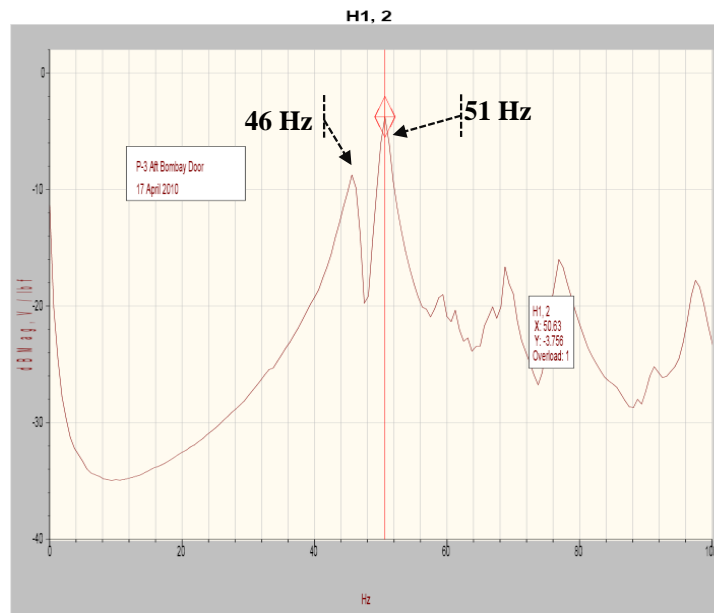


Figure 5.26: Measured FRF of Aft Bomb Bay Panel

5.7 Improvement of MCoRDS Array

Over the course of several field campaigns, a number of modifications were made to the P-3 antenna fairings to promote increased radar performance. The most significant modification was a redesign of the fairing lower skin.

5.7.1 *Improved Lower Skin Design*

In the lower skins of the antenna fairings, 0.05” thick 2024-T3 aluminum doublers are embedded in the laminate along fastener lines (parallel to the antennas) such that bearing load requirements are met. In addition, gang channels are installed along these same locations to allow for blind fasteners to attach the lower skins. Please refer to Figure 5.11 for relative placement of the doublers and gang channels with respect to the antenna.

In the original skins, the doublers were oversized and continuous along the length of the skin to reduce manufacturing complexities. The presence of these metallic components in the near-field of the antenna induce mutual coupling and effectively change the input impedance of the antenna which resulted in degraded antenna S_{11} performance (ratio of reflected power to incident power at the port). Simulations and measurements of the P-3 array in the presence of these conductive components were performed to determine the severity of performance degradation. It was found that the long, continuous doublers severely degraded performance, and the -10 dB S_{11} bandwidth was almost non-existent. The doublers also caused the resonant frequency of the antennas to shift from 195 MHz to 240 MHz as well [87].

With the doublers embedded in the laminate, there were few options to improve the first iteration of lower skins before the installation deadline. Attempts to use carbon fiber composites as doublers were made, but, surprisingly, electrical performance was worse with carbon doublers as compared to aluminum doublers. Also attempts to machine the top half of the skin and doublers resulted in severely damaging the entire skin. With the project delivery date quickly approaching and material supplies dwindling, it was determined the best way to improve the existing lower skins was to cut notches to break up the continuous metallic doublers. Figure 5.27 shows a photo of one of the notched lower skins with the antennas. The width of the notches cut in the skin ranged from 0.65" to 0.95" and were roughly 2.5" long. The notched regions were secondarily reinforced with bonded glass panels on the bottom of the skin.

Slotting the skins restored the bandwidth to about 60 MHz, improved S_{11} by -20 dB on average, and reduced the resonant frequencies of the antennas to 175 MHz [87]. While slotting the doublers increased electrical performance overall, the center antenna of the array continued to perform poorly. The resonance frequency for the center antenna was about 15 MHz lower than the rest of the antennas, and its S_{11} was only slightly below -10 dB [87]. This particular antenna has both doublers along its length as well as at its ends at the junction rib locations. The end doublers are spaced ~0.3" from the edge of the antenna whereas the parallel doublers are spaced 1.25". The presence of doublers on either end of the antenna causes what is known as top-hat loading and lowers the resonance frequency [105].

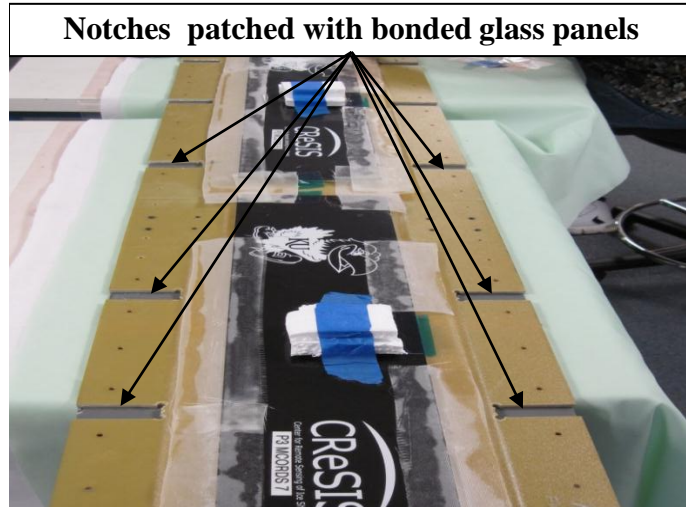


Figure 5.27: Lower Skin with Notches to Break-up Embedded Doublers

Between the first and second field season of the P-3, a study was performed to determine the antennas' sensitivity to the distance from the doubler, the gap size between doublers, and the material of the doubler. The study was performed by placing a single MCoRDS antenna on a 42.5" X 39.5" X 0.25" plate of polycarbonate that was offset from a 48" X 48" metallic ground plane by 16.75". Three 9.25" X 2.30" doublers were then placed parallel to the antenna on either side. Tests were performed outdoors, and Figure 5.28 shows the experimental setup.

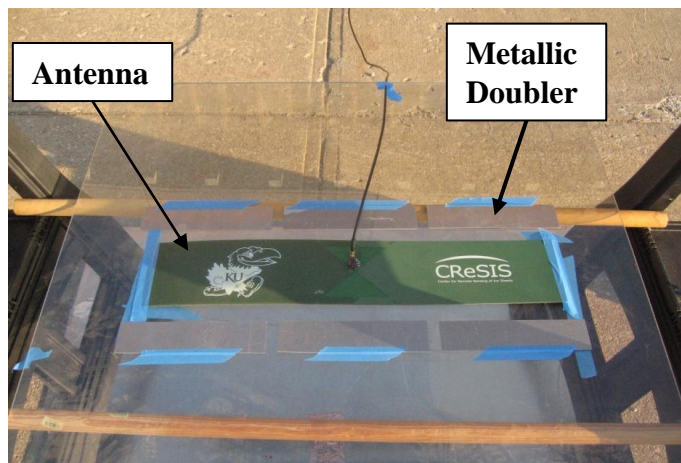


Figure 5.28: Doubler Study Setup

(Photo by Kyle Byers)

The antenna's sensitivity to the relative distance from the metallic doublers was tested, as well as its sensitivity to the gap size between doublers. The edge to edge spacing between the antenna and the doublers was varied at 1.25", 3.25", and 5.25" and the S_{11} of the antenna was

measured. The minimum distance was determined by the separation of the antenna and doublers in the P-3 fairing. In all cases the gap between doublers was maintained at 0.75". To test the sensitivity to gap size the six metallic doublers were maintained 1.25" from the edge of antenna, while the gaps were adjusted to 0.75", 1.25", and 2.25". The lower bound of the gaps was determined by average doubler gap size in the P-3 fairing. Figure 5.29 shows the test results for varying doubler-antenna separation and gap size. The doublers reduced the antenna S_{11} from -40 dB to -17 dB and shifted the resonance frequency from 195 MHz to 185 MHz [106]. The doublers had little effect on the lower end of the bandwidth, but the upper end of the bandwidth improved as the separation increased [106]. Unlike doubler separation, increasing doubler gap size had no effect on the bandwidth, but it did increase the magnitude of the S_{11} [106].

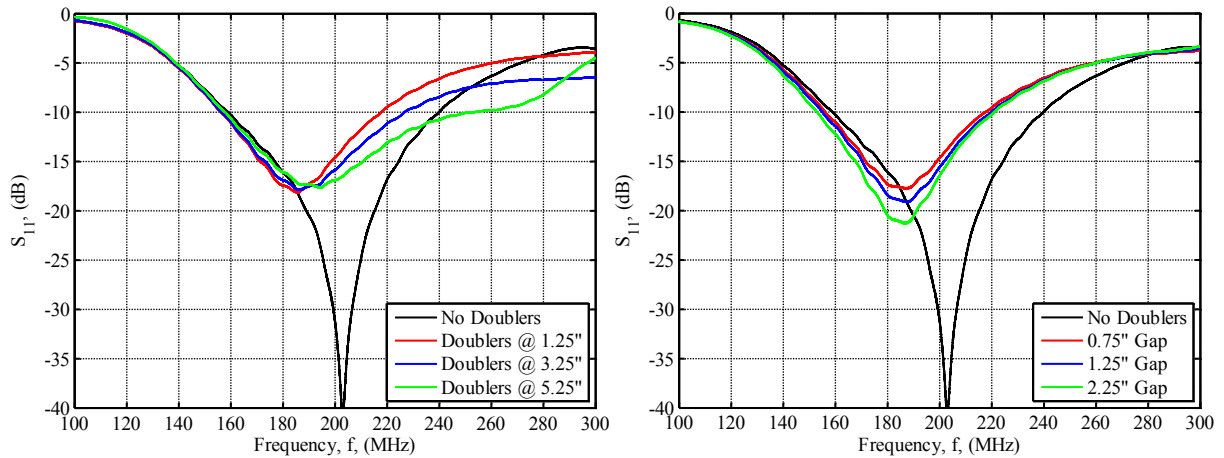


Figure 5.29: Antenna S_{11} Varying Doubler Offset (left) and Gap Size (right)

Carbon composite doublers were also fabricated with the same dimensions as the metallic doublers. To determine if and how fiber orientation affected the antenna's response, coupons with four different families were identified. These families comprised two extreme and two practical families and included: [100/0/0], [0/0/100], [33/33/33], and [25/50/25]. The extreme laminates were included in the study as bounding cases. Two different doubler sets of family [25/50/25] were fabricated—one with 0° surface plies and one with 45° surface plies—for a total of five different sets of doublers. This was done to determine whether surface ply orientation had any significant effect. Doubler-antenna separation was varied at 1.25", 3.25", and 5.25", while gap length was maintained at 0.75". Figure 5.30, shows the antenna's response for antenna-doubler separations of 1.25" and 5.25" respectively.

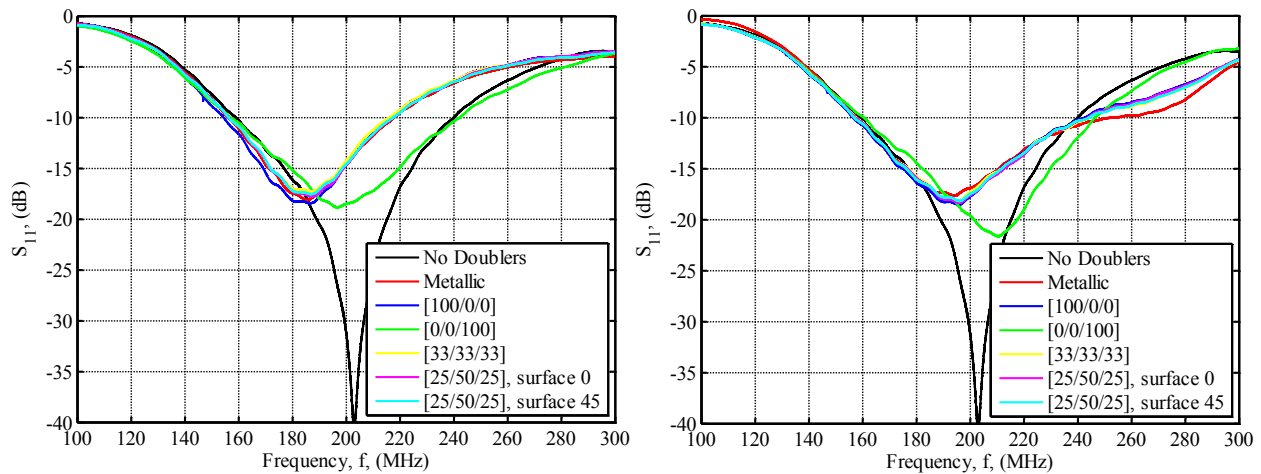


Figure 5.30: Carbon Fiber Doublers with Separation of 1.25" (left) and 5.25" (right)

Interestingly, the carbon fiber doublers caused almost identical response as the metallic doublers, as the center frequency shifted from 195 MHz to 185 MHz and S_{11} was decrease to -17 dB. The one exception to this was the extreme laminate with family [0/0/100]. The presence of these doublers elicited a very different response from the antenna as the resonant frequency shift was different and also seems to be dependent on the antenna-doubler separation. It appears for every two inches the separation increased, the resonant frequency increased by 5 MHz. The magnitude of S_{11} improved as the separation increased. The scope of this study was very limited, but with such a radically different response for the [0/0/100] doublers it is suggested that fiber orientation be further explored to see if the highly anisotropic conductivity inherent in carbon fibers can be exploited for any tangible RF benefit. Chapter 7 will explore the effects of the doublers for broader applications.

While the doubler sensitivity study was useful in gaining insight on how the doublers affect antenna performance, the modifications that could be made to a new lower skin were very limited. Because the gang channels were bonded into the fairing, the new doubler design was forced to conform to the gang channel layout. In the second iteration the doublers were reduced in size, such that they were only large enough to meet edge distance requirements. The widths of the doublers were reduced by 1.5", which translated into an increased antenna-doubler separation. In some cases the doublers were removed from the layup entirely where structural requirements could be met without them. Figure 5.31 and Figure 5.32 show the first and second iterations of the doublers for the outboard and inboard fairings, respectively. In Figure 5.32 only half of the inboard fairing is shown, but the doubler design is symmetric about the center fairing.

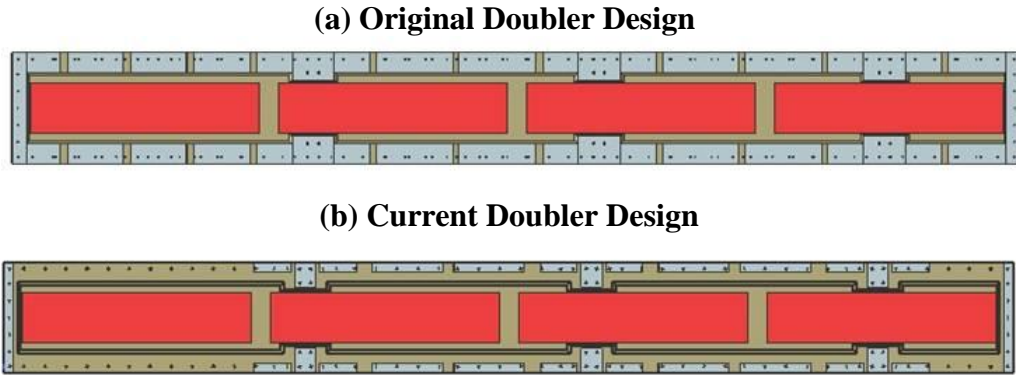


Figure 5.31: P-3 Outboard MCoRDS Fairing Doubler Designs

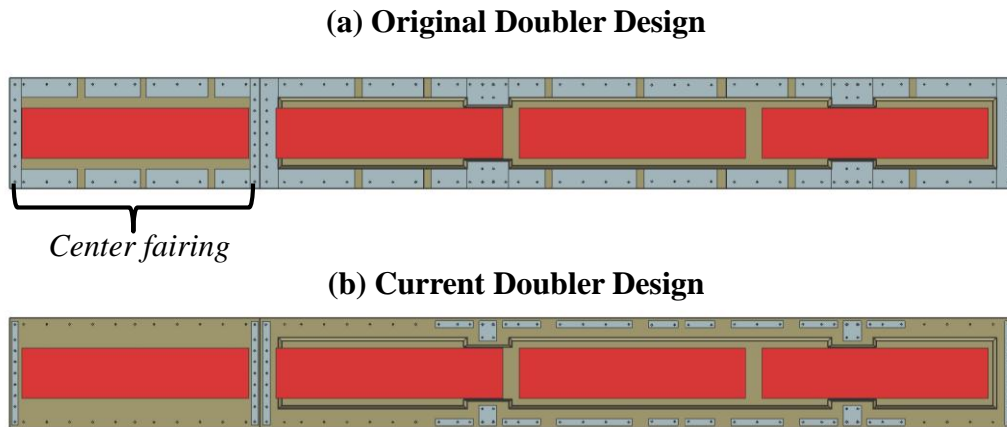


Figure 5.32: P-3 Inboard MCoRDS Fairing Doubler Design

In general, the new doubler design shifted the center frequencies of the antennas up by 25 MHz and increased the bandwidth by 5 MHz [87], but the greatest improvement was experienced by the center antenna which went from a 10 dB return loss to a 20 dB return loss in the bandwidth [87].

5.7.2 *Center Antenna Modifications*

After the first several field seasons, it became apparent that the center antenna was radiating only about half the power as the other elements. It has always been known that there is a nadir port on the P-3 directly above this antenna, but the effects of this port had never been investigated. Figure 5.33 shows that this port contains a series of metallic longerons as well as two navigation beacons.



Figure 5.33: P-3 Nadir Port Above Center Antenna

Simulations of this center antenna with the nadir port revealed that across the chirped frequency range of the radar, the nadir gain of this antenna decreased. Before the 2013 field season a full scale model of the P-3 fuselage in the region of the center antenna was fabricated. Using this fuselage section as well as a full mock-up of the center fairing section, various modifications to the antenna and the surrounding aircraft and fairing structures were tested in KU's anechoic chamber. Figure 5.34 shows the test setup for the along-track pattern measurement. The center fairing was held in place with low-loss dielectric foam, and adjacent pylon skins were simulated with sheet metal taped at appropriate locations.

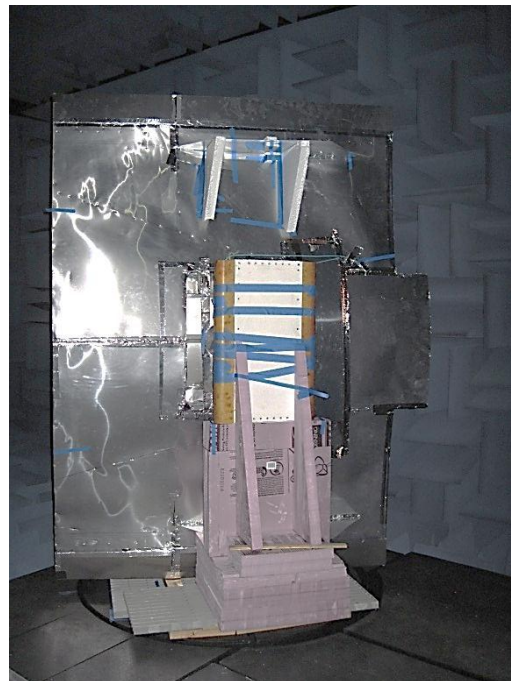


Figure 5.34: P-3 Array Center Section with Mock Fuselage in Anechoic Chamber

Adding a partial cover to the aft half of the port restored antenna nadir gain. This aft cover surprisingly showed better results than a full port cover or a partial cover of the forward half of the port (directly above the antenna). Figure 5.35 compares the center antenna cross- and along-track radiation patterns before and after the port modification. The chamber measurements and simulations of the center antenna suggested a 3 dB improvement in nadir gain. This improvement will propagate across the whole array as channel equalization is referenced to the antenna with lowest radiated power and all other channels are attenuated appropriately. A new balun was also installed on the center antenna that allows twice as much power to be fed to the antenna.

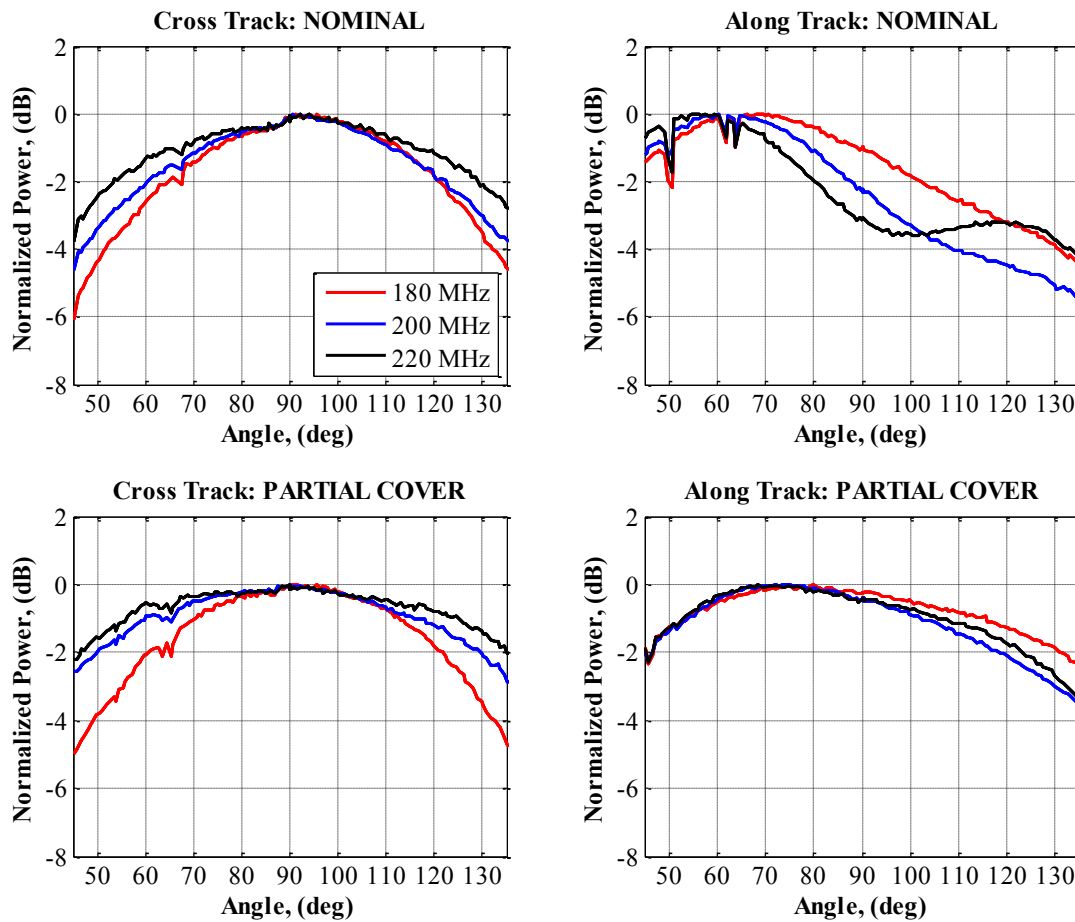


Figure 5.35: P-3 Center Antenna Cross- and Along-Track Patterns Before and After Port Modifications

5.7.3 *Other Improvements*

In addition to a lower skin redesign and center antenna modifications, several other improvements have been made to the fairing and antennas. Improvements made to the antenna

included: shortening the antennas to accommodate the dielectric loading, notching the ends of the antenna to reduce edge currents and thus mutual coupling between elements, and designing a new balun to reduce insertion loss [107]. Consistency in balun performance was a major issue and potentially a larger influence on the poor performance for the first fairing iteration.

In the second iteration of the fairing, accelerometer cables were removed from inside the fairing and ferrites were placed along antenna transmission lines. Although accelerometer measurements were never taken during science flights, the presence of the cable near the antennas was shown to negatively affect the antenna performance [87]. Ferrites placed along the feed cables, shown in Figure 5.36, reduce currents that are induced on the outer conductor of the cable. These currents can change the input impedance of the antenna and thus increase return loss.

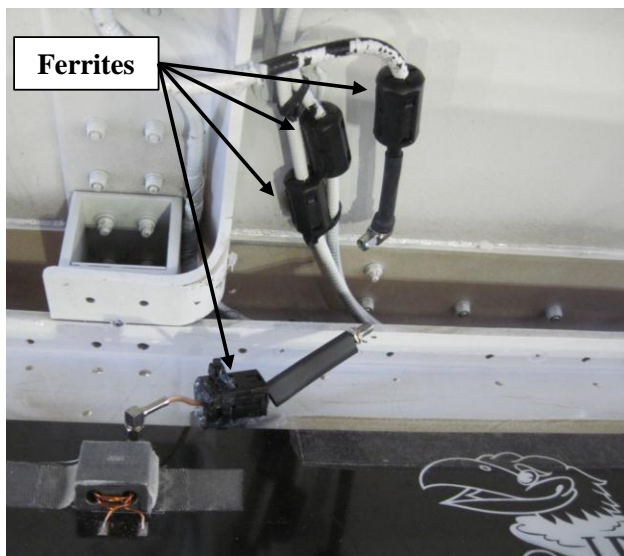


Figure 5.36: Ferrites Placed Along Feed Cables

Smaller, more flexible intermediate cables were also added between the transmission line and the antenna connector. These cables were necessary due to the stiff transmission lines stressing the connectors and potentially fatiguing them.

5.8 P-3 Missions and Results

The presence of the P-3 MCoRDS fairing was found to increase the total drag of the aircraft by 2.7%. Range reduction due to the fairings is acceptable since P-3 missions are crew limited (endurance). Initial flight tests of the P-3 also verified the stability and control analysis results that the fairing does not significantly degrade the handling capabilities of the aircraft.

The first flight season of the P-3 with the large 15-element MCoRDS array was from April 28th to May 28th of 2010. During this time the aircraft was stationed out of Kangerlussuaq, Greenland, and flights were concentrated over land-based ice on outlet glaciers. In the first campaign, a total of 13 science flights were flown for a total of 88 flight hours and almost 19 TB of MCoRDS data was collected [108]. The P-3 has since been redeployed in Spring 2011, 2012, and 2013. Figure 5.37 shows the 2011 flight lines. The brown lines were flown by a King Air, another OIB platform, and the yellow lines were flown by the P-3. To date, the P-3 has completed 122 arctic missions in 886 hours and collected 129 TB of MCoRDS data [108]. The entire sensor suite of the P-3 has collected roughly 240 TB of unique data.

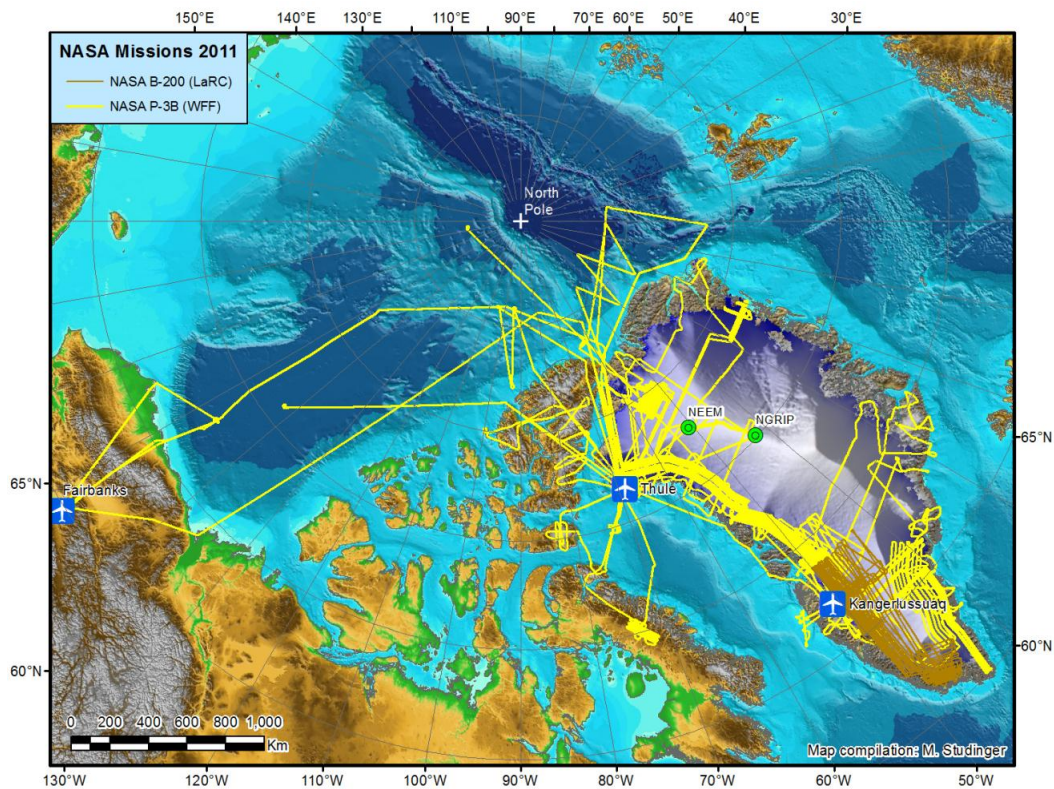


Figure 5.37: P-3 and King Air OIB Flight Lines from the 2011 Campaign [100]

Figure 5.38 shows a radar echogram that was produced from 2011 MCoRDS data collected near the NEEM ice core site. The ice thickness in this location is around 1.5 miles deep, and the bed rock is clearly visible in the figure. Deep internal ice layers are visible up to 1.33 mi below the surface. This echogram also includes an interesting feature that is highlighted in yellow. The internal layers are clearly visible, then a bed rock discontinuity feature is evident just upstream of the yellow highlighted region, and after this feature the internal layers become distorted. It

appears as if the feature near the ice-bed interface creates a turbulent flow in the ice sheet, though at these speeds the term is inappropriate. It is believed this disturbance is causing mixing of the layers however, likely due to partial melting, and results in the loss of the deep layers in the radar echogram. The data is unique, and is now causing the science community to define plans for deep ice radar surveys prior to any planned ice core drilling operations.

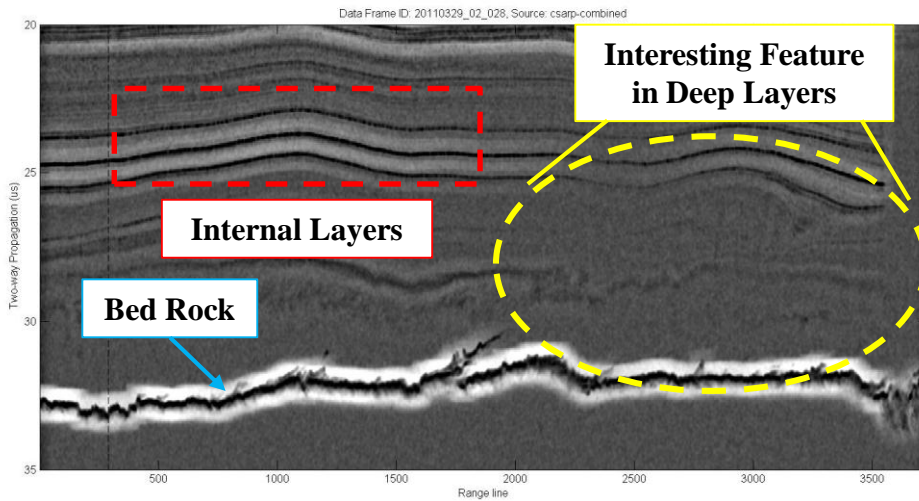


Figure 5.38: Echogram of 2011 P-3 MCoRDS Data

6 TRANSMISSION LINE THERMAL PHASE STABILITY

Due to the extreme temperature gradient caused by flying at altitude while in polar regions, the severity of signal phase shifts caused by the thermal contraction of the antenna feed cables was studied. In general the strain experienced by an object due to changes in temperature is governed by Equation (6.1), where α is the thermal coefficient of expansion and ΔT is the change in temperature from some reference temperature.

$$\frac{\Delta L}{L} = \alpha \Delta T \quad (6.1)$$

As a signal propagates down a transmission line, the phase of the signal that exits the line is a function of the length of the cable; therefore increasing (or decreasing) the length of the line will change the phase of the exiting signal. Equation (6.2) relates thermal strains to a signal phase shift. In the equation V represents the cable's relative (to the speed of light) velocity, which is a number less than one. Typical transmission lines have values of V that range from 0.65-0.85 [109].

$$\Delta \phi = \frac{2\pi}{\lambda} V \Delta L = \frac{2\pi}{\lambda} V (\alpha \Delta T L) \quad (6.2)$$

Changes in cable mechanical dimensions affect the propagation length of the cable, and can also effect the dielectric constant of the cable (and thus V in Equation (6.2)) [110]. Due to the Poisson Effect, as the cable length changes, the diameter of the outer conductor of the transmission line will expand or contract. This will not only change the impedance of the cable but it will also result in a mechanical force on the inner dielectric and change the density of the material. This density change will alter the material's dielectric constant.

The dielectric constant of the cable can also change due to molecular changes in the material. TeflonTM is a commonly used insulator in transmission lines due to the low loss nature of the material. However, TeflonTM undergoes a molecular phase transition around 64°F which results in a drastic change in the dielectric constant [111].

6.1 Experimental Setup and Procedure

To test the sensitivity of the CReSIS systems to extreme thermal gradients, a 309" cable of Andrew Heliax FSJ1-50A [112] (the same type used on the CReSIS radars) was placed inside a

climate controlled chamber where the temperature was varied between -13°F and 77°F (-25°C and 25°C). Figure 6.1 shows the experimental set-up. The cables (DUT) were raised $\sim\lambda$ off the floor using stands constructed from dielectric foam to ensure there were no undesirable interactions between the cable and the surrounding environment.

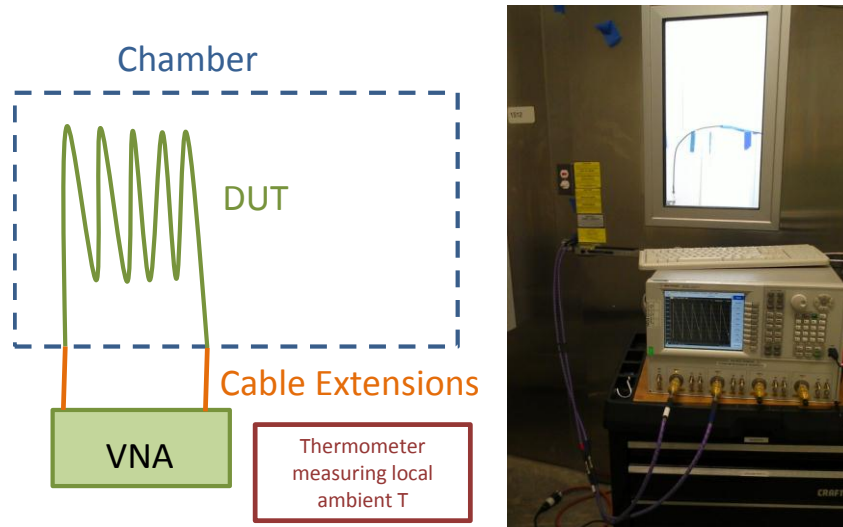


Figure 6.1: Thermal Stability Test Set-up

The cable extensions in Figure 6.1 were calibrated out using an eCal kit. These cables were 72" long and extended just inside the door frame. Insulation foam was used around the door to allow the cables to pass through and prevent thermal leakage. Agilent Technologies[®] N5230C PNA-L Vector Network Analyzer (VNA) was used to record the changes in S_{12} phase as the temperature was varied. Figure 6.1 shows the VNA outside of the climate chamber, and the cables being tested can be seen in the background through the window. Starting at the ambient temperature, measurements were recorded every 7°F (5°C). Once the chamber air temperature reached the desired temperature, the cable was allowed to soak at that temperature for at least 10 minutes. The climate chamber's integrated thermometer and an independent thermometer placed inside the chamber were used to measure and record the current temperature. Measurements were made for both increasing and decreasing temperatures to capture the hysteresis of the system.

6.2 Results

Figure 6.2 shows the results as the normalized phase change in degrees per ft. As the plot shows, the phase stability of the cable is 2.2×10^{-4} deg./ft/ $^{\circ}\text{F}$ which means cable length (phase) is

rather insensitive to the temperature change. After the initial experiments Reference [113] was found. This document contained experimental data for the coaxial cable used in the experiment. It also contained a relationship for the phase change in degrees as a function of temperature, which is shown in Equation (6.3).

$$\Delta\phi = \frac{3.66 \cdot 10^{-7} \cdot (PPM) \cdot L \cdot F}{V} \quad (6.3)$$

In the above equation, *PPM* is the total electrical length change in parts per million over the temperature range of interest, *L* is the cable length in feet, *F* is the frequency in MHz, and *V* is the cables relative velocity. At -13°F [113] reports the PPM to be -200. In the experiment, the cable length was 25.75', the frequency was 195 MHz, and the cable velocity is expected to be about 0.81 [113]. Using Equation (6.3), the expected phase shift is -0.454°. Using the experimental results in Figure 6.2, at -13°F, the phase shift per foot is -0.0198. For a cable length of 25.75' (7.85 m), the expected phase shift is -0.510°, which agrees very well with the data from [113].

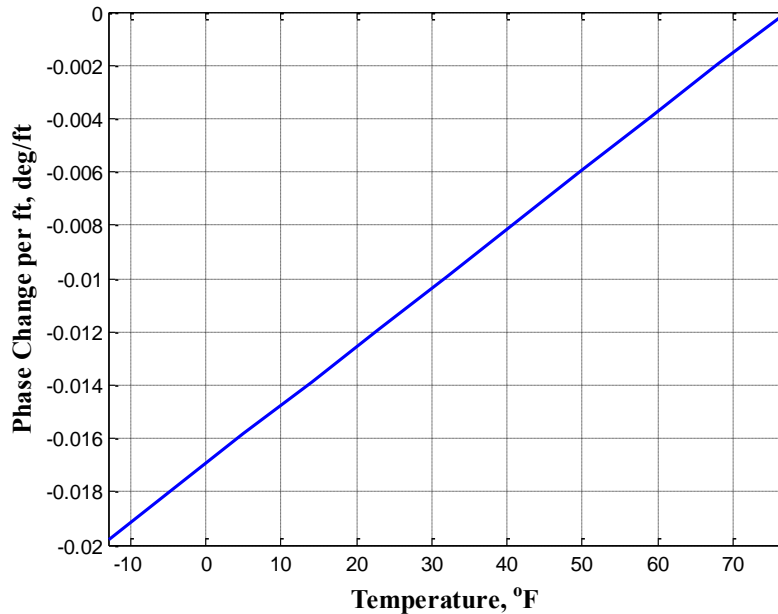


Figure 6.2: Phase Change per Meter as a Function of Temperature Change

To ensure these small phase changes do not significantly change the radiation pattern, the worst case shift was applied to Twin Otter antenna-array simulations. Given that the antennas are spaced approximately 40" apart, a successive phase shift of -0.065° was applied. Regardless of the type of weighting applied to the array, the phase shift due to the extreme thermal gradient had

negligible effect on the pattern. Figure 6.3 shows a simulated Twin Otter MVDR plot with and without thermal effects. For the P-3 and DC-8 arrays, the phase shifts would be even less as external differential cable lengths are even smaller. Therefore, it was concluded that phase shifts due to extreme thermal gradients do not need to be compensated.

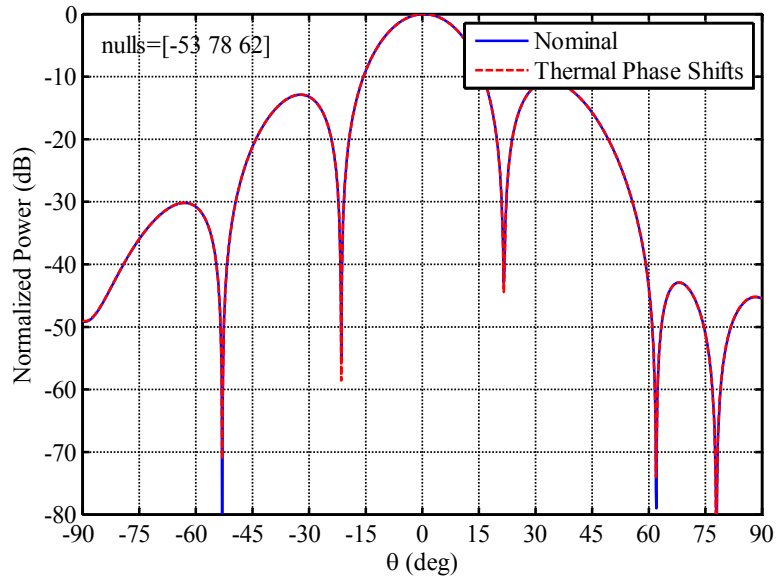


Figure 6.3: Twin Otter Simulated Patterns with and without Thermal Effects

7 ANTENNA FAIRING NEAR-FIELD MUTUAL COUPLING

7.1 Near-Field Coupling

Common aerospace materials such as metal and carbon reinforced composites are both conductive and electrically lossy. Conductive materials in the near-field of an antenna (distances less than $2D^2/\lambda$, where D is the largest dimension of the antenna [78]) alter the current distribution and effectively change the radiation resistance of the antenna [115]. Radiation resistance is the primary contributor to real input impedance, and changes in the input impedance will affect the antenna return loss. Antenna return loss is a measure of the efficiency of the antenna as it is the ratio of the incident power at the port to the reflected power.

Conductive elements with no current excitation of their own are known as parasitic elements. In the case of the Yagi-Uda antenna, parasitic elements were used to improve antenna performance by substantially increasing the directivity and gain of a dipole antenna [115]. This was achieved by placing parasitic elements in front of and behind the driven element. Shown in Figure 7.1, the elements forward of the active element act as directors, while the elements behind the active element act as reflectors. While it is possible to apply Yagi-Uda antenna theory to parasitic elements of a fairing to improve antenna performance, it is not very practical. In general, the parasitic elements required in the structural fairing do not lie in a plane that would direct the radiation in the desired direction. In addition, typical array sizes for Yagi-Uda antennas are on the order of 6λ [116], which is likely much too large for application on an airborne platform, and certainly so at the VHF frequencies of interest for imaging the ice bed.

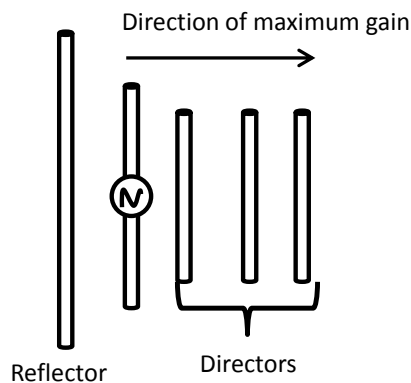


Figure 7.1: Yagi-Uda Antenna

When in the presence of a parasitic element, the input impedance of the antenna is dependent on the self-impedance (input impedance of antenna when isolated) and the mutual impedance between the antenna element and the parasitic element. For a two element system, this relationship is given by Equation (7.1).

$$Z_{1d} = \frac{V_1}{I_1} = Z_{11} + Z_{12} \left(\frac{I_2}{I_1} \right) \quad (7.1)$$

In Equation (7.1), Z_{1d} is referred to as the driving-point impedance, Z_{11} is the self-impedance, Z_{12} is the impedance of the antenna due to the current on parasitic element, and I_2/I_1 is the current ratio on the two elements. In general the calculation of the driving point impedance is quite tedious and only very simple systems have closed form solutions. To determine the coupling in complex systems full 3D-wave solvers are required.

In [117] the effects of a parasitic element parallel to a single dipole were studied. The width and spacing of the dipole and element were varied. The results of the study indicated that input impedance of the antenna oscillated about the self-impedance as a function of the spacing. The amplitudes of the oscillations were directly related to the width of the antenna. In addition, the study also found that the parasitic elements caused ripples in the radiation pattern of the antenna element, and the amplitude of these ripples were inversely related to the spacing of the parasitic element.

Both of the platforms that were developed as a part of this work included parasitic elements in the near-field of the antenna-array. These elements are required to satisfy structural requirements for the antenna fairings. Unlike the study in [117], multiple elements are placed along the length of the antenna and not just a single element. It is difficult to characterize the exact effects of multiple parasitic elements on the antenna without full 3D wave analysis as closed form solutions only exist for very simple systems (like that in [117]). During the initial design phase of the P-3 array, there was insufficient time to accurately characterize the effects of the parasitic elements on the antenna-array to determine acceptable design limitations. Though some experiments were performed (Section 5.7) to determine the effects of the near-field coupling, these tests were very limited, and no design rules were able to be extracted. This section aims to characterize the effects of the near-field coupling due to multiple parasitic elements for broader applications. To do so an antenna-doubler configuration, similar to that of the P-3, was used.

7.2 Near-Field Coupling of Doubler Configurations

7.2.1 *Relative Doubler Location*

Initially a series of simulations were performed to determine whether there is any dependence between antenna performance and relative placement of the doubler. These simulations included a single P-3 antenna with a ground plane and one doubler on either side of the antenna. Figure 7.2 shows the HFSS[®] model used for the simulations.



Figure 7.2: HFSS[®] Simulation of P-3 Antenna with Ground Plane and Doublers

Two lengths of doublers were simulated. The length of the smaller doubler was 4.4" (0.07λ), and the length of the longer doubler was 8.4" (0.14λ). These lengths were selected because they were common lengths of the P-3 doublers. Both doublers had a width of 1.23" (0.02λ), which is the same as the width of P-3 doublers. The location of the doublers were stepped in x , y , and z . Figure 7.3 shows the stepped geometry of the doublers. Along the x -axis the doublers were stepped along the length of the antenna in increments that were equivalent to 10% of the antenna length. In Figure 7.3 the x -location of the doublers is given by a , where a is measured from the edge of the antenna to the center of the doubler. The location of the doublers was stepped from the edge of the antenna, $b = 0$, in 0.5" increments. The maximum value of b was limited to 2.5" as this was the maximum allowable offset in the P-3 array. The doublers were also stepped along the z -axis from -0.5" to +0.5" in 0.5" increments. These steps lead to 198 permutations of doubler positions for each length of doubler.

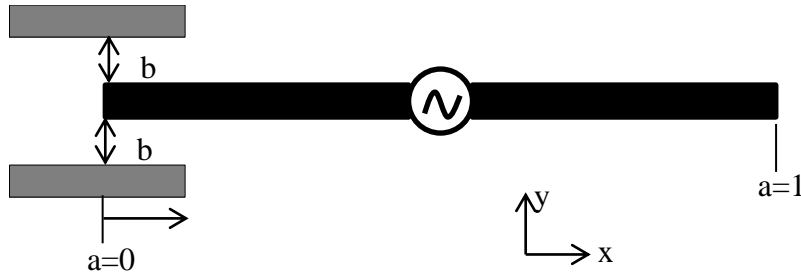


Figure 7.3: Stepped Doubler Geometry

The S_{11} (ratio of the reflected power at the port to the incident power) and normalized radiation pattern were found for each doubler location using HFSS[®] Version 14. In general, good S_{11} performance is considered -10 dB or lower. Figure 7.4 shows the S_{11} of the antenna as a function of x- and y-location of the larger doubler when $z = -0.5$ ". As the figure shows, the antenna performance becomes fairly invariant once the doubler is offset in y by at least 0.017λ . The same was found to be true for the smaller doubler and when the doubler was placed in the same z-plane as the antenna. Those plots can be found in Appendix A. For the plots in Figure 7.4, -10 dB is represented by a light blue color and warmer colors represent larger S_{11} magnitudes. While there is an area of large S_{11} magnitude around 200 MHz in the 0.033λ case, the bandwidth of the antennas remains fairly constant. Though the anomaly in the 0.033λ case represents better performance, it is only less than a 0.5% decrease in reflected power at the port as compared to the 0.025λ and 0.041λ cases.

Figure 7.5 shows the radiation patterns for all doubler locations (with the obvious exception when the doubler is centered along the length of the antenna and in the same plane, as this case shorts the antenna, and is not productive to investigate for this application). The pattern cross-section in Figure 7.5 is the xz-plane pattern. An elevation angle of 0° is along the z-axis (perpendicular to the planar antenna). As the figure shows there is very little variation in the pattern shape, regardless of doubler position.

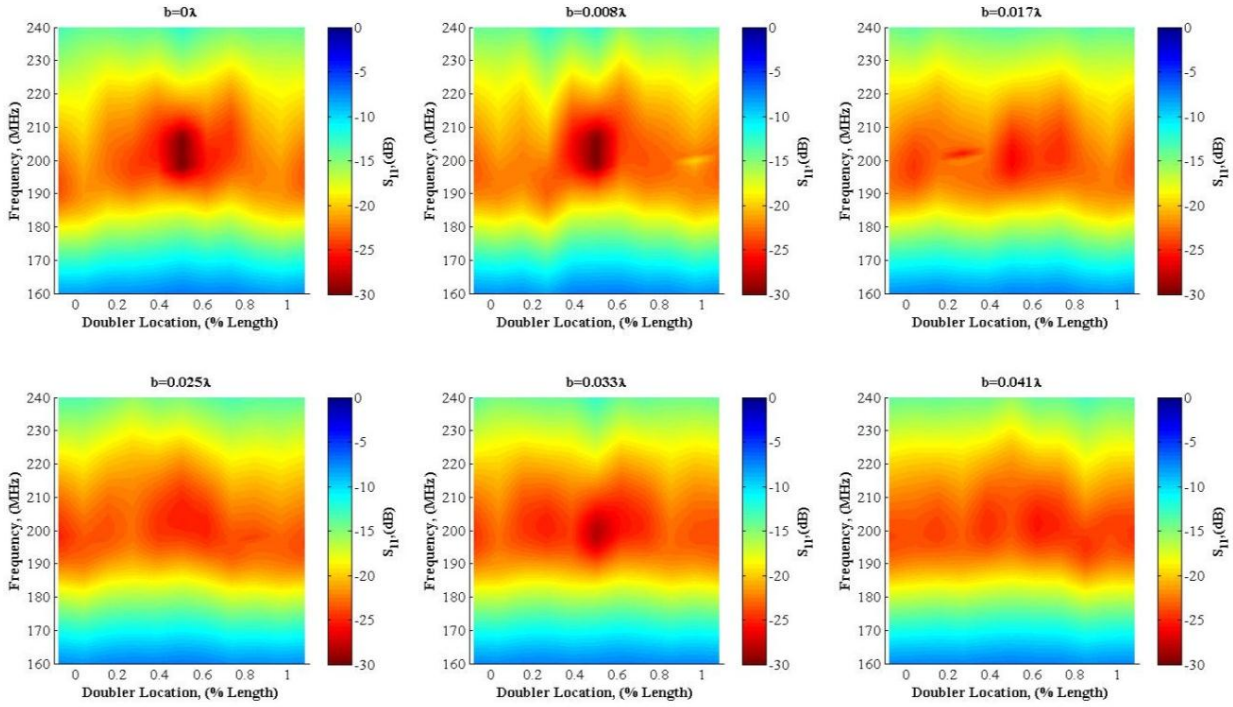


Figure 7.4: Antenna S_{11} for Various Out of Plane Doubler Locations

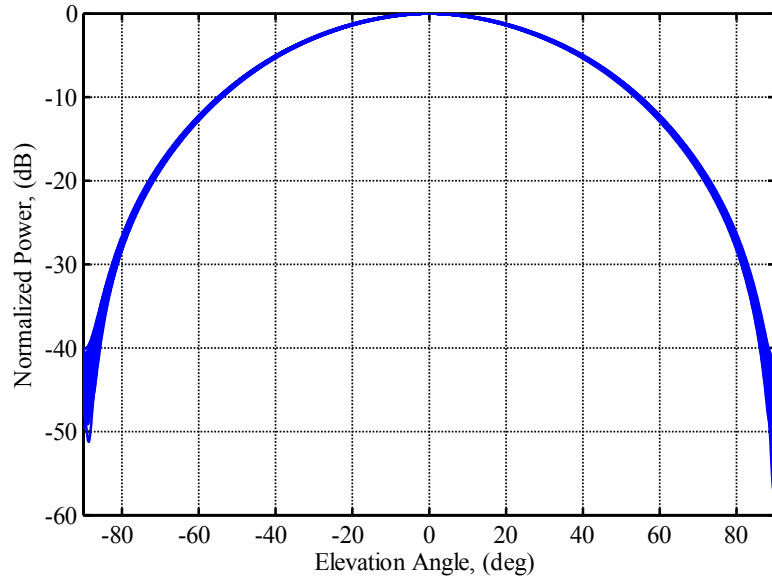


Figure 7.5: Antenna Radiation Pattern for Various Doubler Locations

7.2.1 *Relative Doubler Length*

While the doubler study of Section 7.2.1 was insightful, it does not represent a practical design in a real fairing. Seldom will a single doubler be required on either side of the antenna. A more likely design would include doublers along the full length of the antenna, as was the case

for the P-3. To better characterize the effects of a real doubler design, doublers were placed along the full length of the antenna, as shown in Figure 7.6.

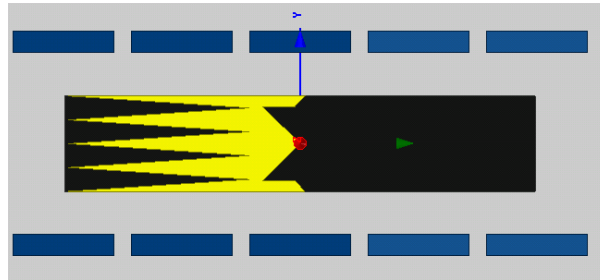


Figure 7.6: HFSS Model with Doublers Placed Along the Full Length of the Antenna

The doublers were modeled to extend past the length of the antenna by 0.05λ on either side. The length of the doublers, L , was then varied as was the y-axis offset, b . Figure 7.7 shows the geometry of the for the full length doubler study. The width of the doublers was held constant at 1.23”.

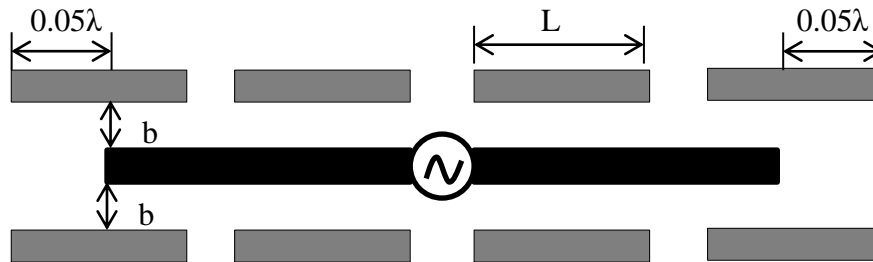


Figure 7.7: Geometry for Full Length Doubler Study

To simplify the modeling, the doublers were all given identical lengths. The lengths of the doublers simulated were based on the real parameters of the P-3 doublers. These were dictated by the size of the bolts, the number of bolts through a single doubler, the bolt spacing, and bearing edge distance requirements. The same antenna-doubler offsets, b , were used in this study as were used in the study of Section 7.2.1. In addition the antenna was simulated with one and two terminated elements to capture the mutual coupling effects when the antenna is placed in an array.

Figure 7.8 shows the antenna S_{11} as a function of doubler length, L , and offset, b . The figure contains the plots for the isolated antenna as well as when one and two additional elements are added. Also shown in the plots are lines corresponding to the antenna design center frequency (solid black) as well as lines corresponding to the bandwidth of the chirped signal of the radar. Ideally the antenna will have an S_{11} of -10 dB or lower in this region.

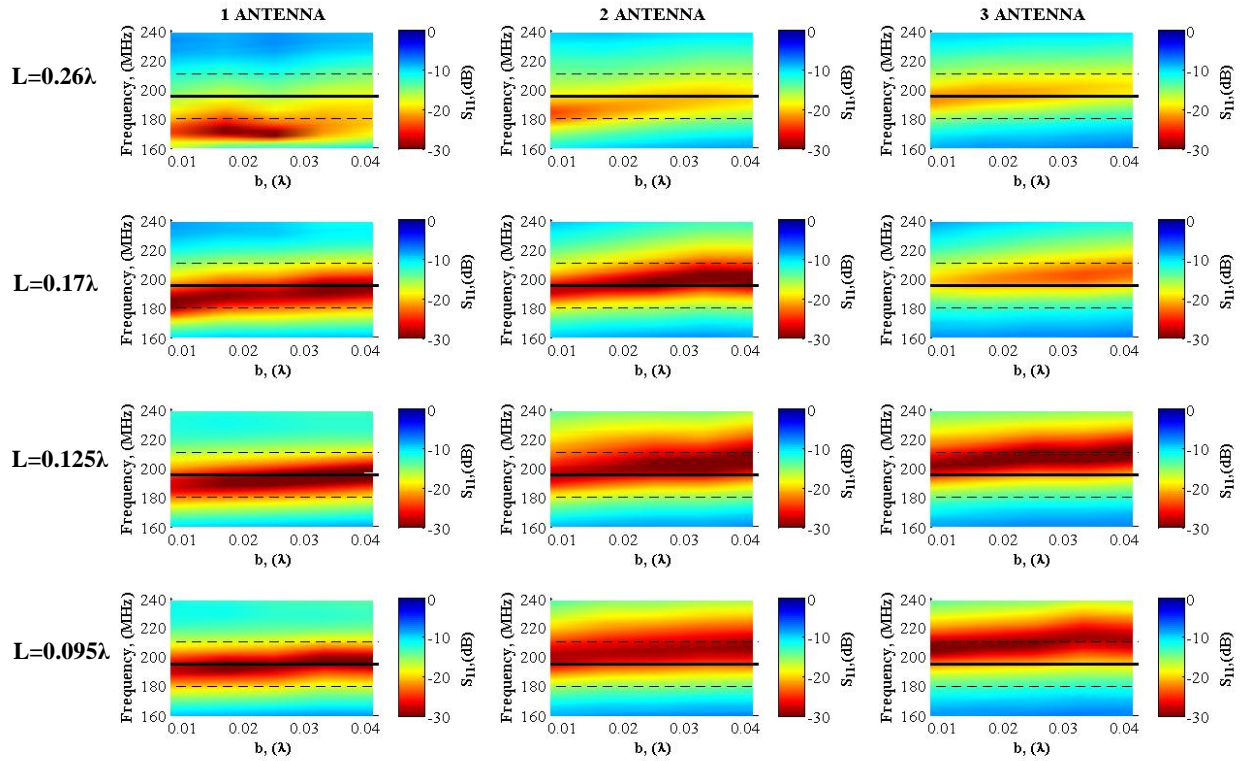


Figure 7.8: Antenna S_{11} as a Function of Doubler Length and Offset for Configurations with 1, 2, and 3 Antennas

It is apparent that the presence of the dummy elements increase the center frequency of the antenna, but identifying array effects is not the goal of the study. Examination down the length of each column in Figure 7.8 reveals that once the doubler length becomes 0.125λ or smaller the performance of the antenna become rather invariant, regardless of doubler offset. In Appendix A results for even smaller doublers can be found.

Figure 7.9 shows the normalized radiation pattern of the antenna for various doubler offsets and doubler lengths of 0.26λ and 0.095λ . From the figure it is apparent that the size and location of the doubler has no significant impact on the radiation pattern. It is noted that the dip in the pattern at nadir is actually caused by the presence of the other two antennas.

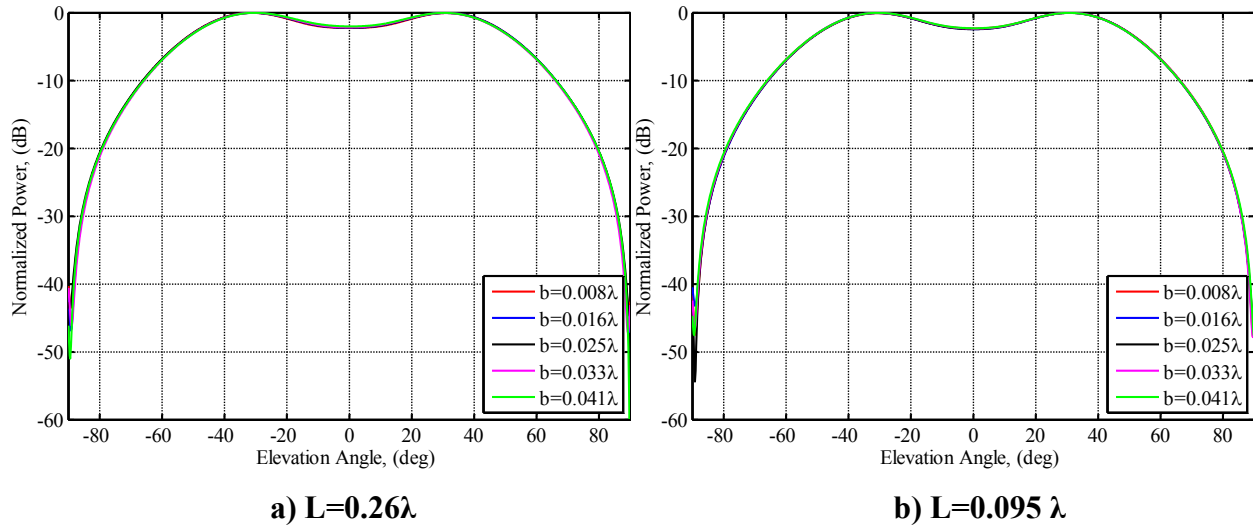


Figure 7.9: Normalized Radiation Pattern for Various Doubler Offsets with Doubler Lengths of 0.26λ (a) and 0.095λ (b)

To determine whether the observations made from Figure 7.8 and Figure 7.9 scale, simulations with 500 MHz dipoles and 1 GHz dipoles were performed. As Figure 7.10 shows, simple planar dipoles (orange) were used in the simulation instead of the P-3 antennas. This was done to save time, but since both antennas are dipoles they are expected to have similar responses.

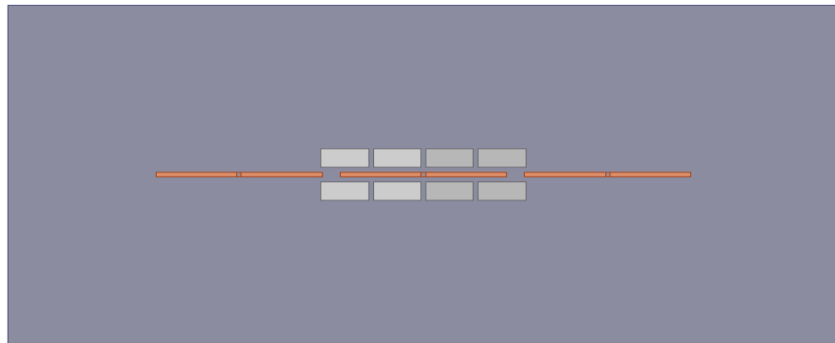


Figure 7.10: Scaled Dipole with Doublers, Two Dummy Antennas, and a Ground Plane

For the scaled simulations, the lengths and offsets of the doublers in terms of wavelengths were maintained. The width of the doublers was kept at $1.23''$ to isolate the effect due to doubler length and offset. Two dummy elements and a ground plane were also included in the simulations. Figure 7.11 and Figure 7.12 show the S_{11} for the 500 MHz and 1 GHz dipoles, respectively.

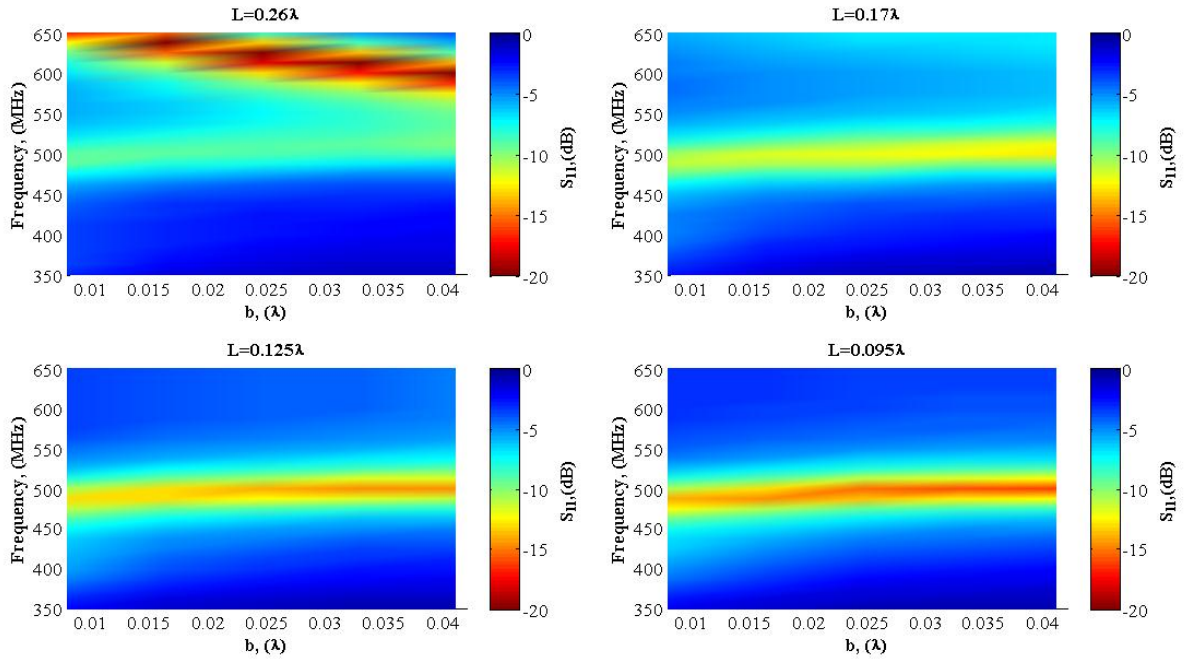


Figure 7.11: 500 MHz Dipole S_{11} as a Function of Doubler Length and Offset

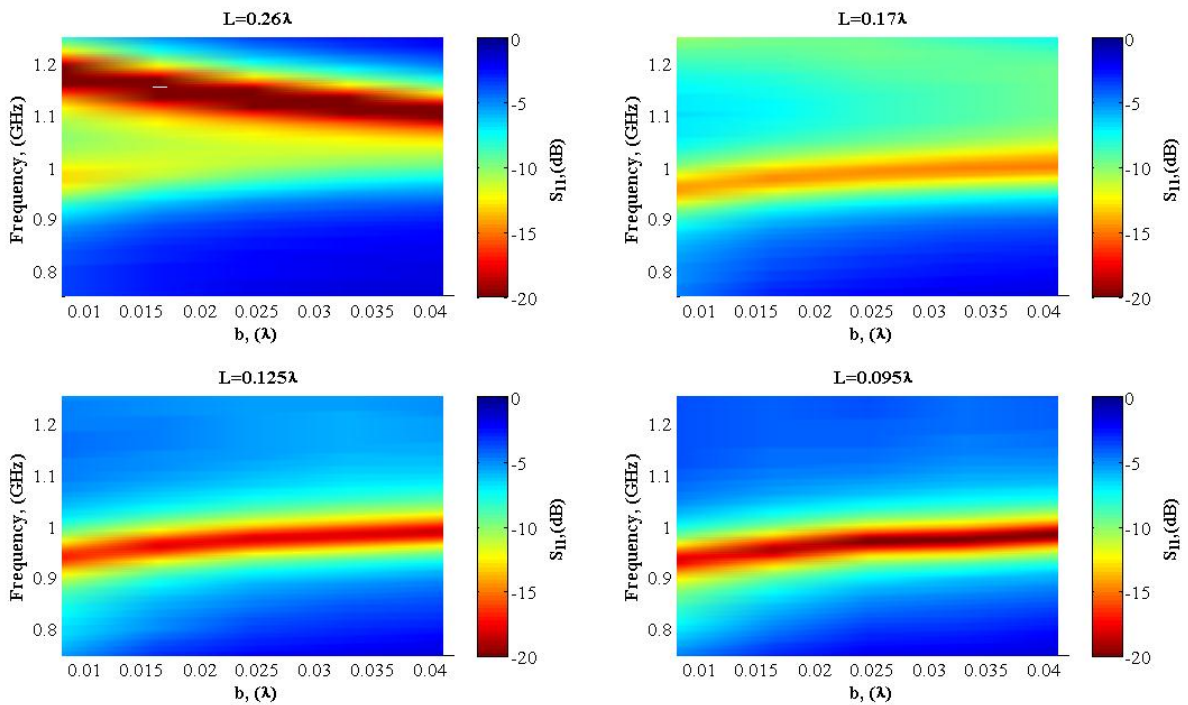


Figure 7.12: 1 GHz Dipole S_{11} as a Function of Doubler Length and Offset

Similar to what was observed with the 195 MHz P-3 antenna, once the doubler length became 0.125λ or smaller the performance of the antenna became relatively invariant with

respect to the doubler offset. For all three different antennas there is a slight upward shift of center frequency as doubler offset increased. This center frequency shift was on the order of 5% for all cases.

Figure 7.13 and Figure 7.14 show the normalized radiation patterns for the 500 MHz and 1 GHz antenna, respectively, with two different doubler lengths. While there are no significant changes in the overall radiation patterns, there is some widening present in the patterns. It appears that the patterns are stretched more when the doublers are closer to the antenna. There also seems to be small dependency of the stretch on the length of the doubler. Upon closer examination of the P-3 antenna radiation pattern, a similar trend was found, but it is less significant than for the 500 MHz and 1 GHz antennas.

Because the widening of the patterns seems to be more drastic for the higher frequencies, this may imply that there is some dependency on the doubler width. Across all three frequencies the doubler lengths and offsets were consistent in terms of frequency wavelength. The only variable that was not maintained in terms of wavelength was the width of the doubler, which was always 1.23" (0.02λ at 195 MHz, 0.05λ at 500 MHz, and 0.1λ at 1 GHz). Because there was variation in the design of the antenna (P-3 versus planar dipole), this statement cannot be assured without further investigations.

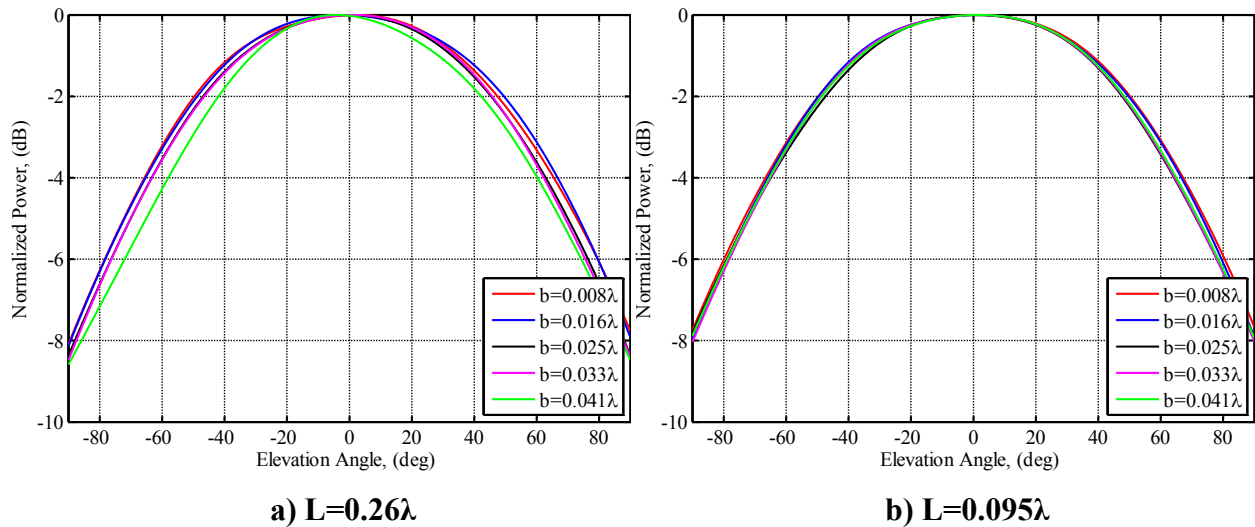


Figure 7.13: Normalized Radiation Pattern of 500 MHz Dipole for Various Doubler Offsets with Doubler Lengths of 0.26λ (a) and 0.095λ (b)

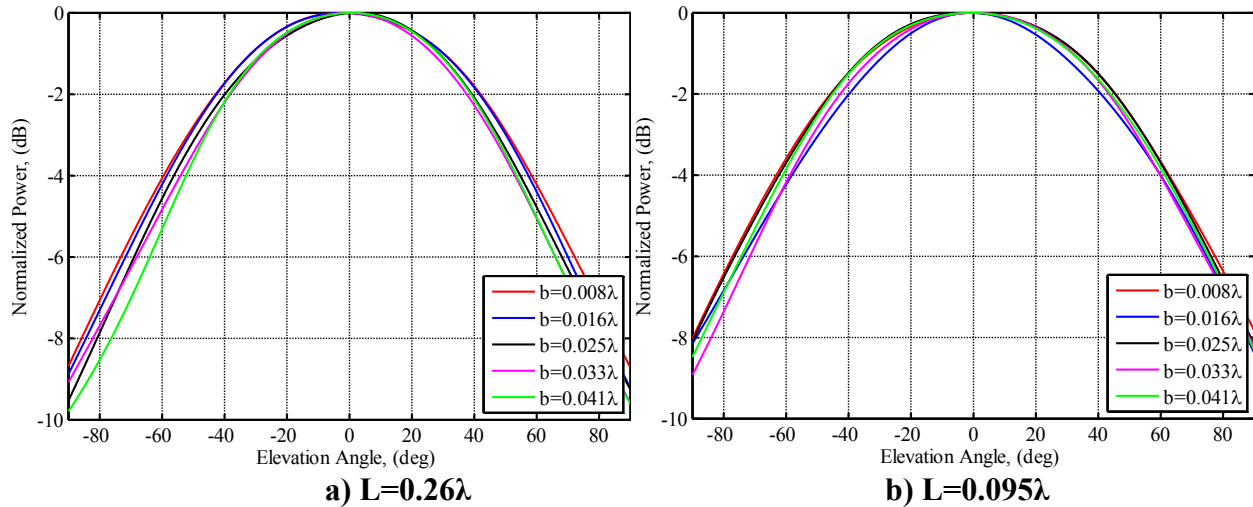


Figure 7.14: Normalized Radiation Pattern of 1 GHz Dipole for Various Doubler Offsets with Doubler Lengths of 0.26λ (a) and 0.095λ (b)

7.2.2 Summary of Effects of Near-Field Parasitic Elements

From the study in Section 7.2.1 it is apparent that once the antenna-doubler offset is at least 0.017λ there is very little change in antenna S_{11} regardless of the relative location of the doubler along the length of the antenna. Figure 7.9 showed that the relative location of a single set of doublers essentially has no effect on the element's normalized radiation pattern.

When considering doublers along the length of the antenna, for doubler lengths of 0.125λ or less the expected change to the antenna S_{11} was 5% or less regardless of the doubler offset. This was demonstrated for three different frequencies. The element radiation patterns appear to have a small dependency on the relative size and location of the full length doublers. Though there were no significant changes in the overall shape of the pattern, there was a widening of the pattern that was dependent on the relative location of the doublers. The phenomenon seemed to be more severe at higher frequencies. It was postulated that there is a dependency of the widening on the width of the doubler, but this statement cannot be verified without further investigation as two different dipoles were used.

8 BEAMFORMERS FOR CLUTTER CANCELATION

8.1 Introduction

Clutter in radar is defined as unwanted echoes from the environment. In the case of ice-sounding, rough ice surfaces are a source of clutter that can mask the desired bed echo signal. As shown in Figure 8.1 when the ice surface is smooth, off nadir signals will be reflected away, but in the case of the rough surface some of the energy is scattered towards the transmitter. This energy is called “back-scattered energy”.

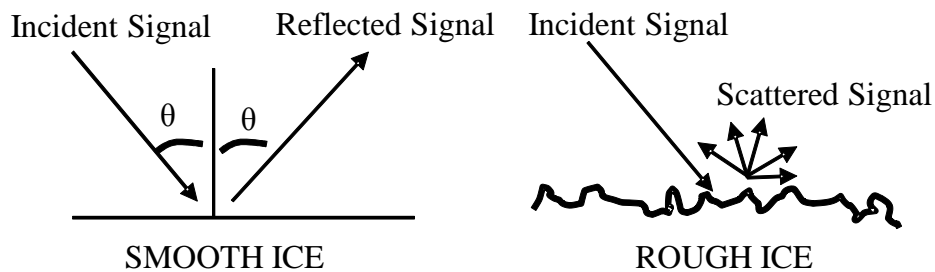


Figure 8.1: Reflected Signal from Smooth Ice and Scattered Ice from Rough Ice

Clutter-suppression can be achieved through manipulating the antenna radiation pattern where the antenna acts as a spatial filter to eliminate the clutter signal. The two main beamformers used by CReSIS to suppress clutter are Dolph-Chebyshev (or simply Chebyshev) and Minimum Variance Distortionless Response (MVDR). The following sections provide a brief overview of array theory and the two beamformers.

8.2 Array Fundamentals

8.2.1 *Two-Element Uniformly Spaced Linear Array*

One of the easiest arrays to analyze is the two-element, uniformly spaced linear array consisting of infinitesimal dipoles. The electric field of an infinitesimal dipole is given by Equation (8.1)

$$E_{\theta} = \frac{jkI_0L\sin(\theta)}{4\pi r} e^{-jkr} \quad (8.1)$$

In the equation k is the wavenumber, I_0 is the antenna current, L is the length of the dipole and r is the distance between the observation point and the array. If it is assumed that the dipoles are operating in the far-field region the following assumptions can be made:

$$\begin{aligned} r &= r && \text{for amplitudes} \\ r &= r \pm x \sin(\theta) && \text{for phases} \end{aligned}$$

For a two-element array with elements spaced a distance d apart, shown in Figure 8.2, the total electric field can be calculated as the sum of the electric field radiated by each element as follows.

$$E_\theta = \frac{jkI_0L \sin(\theta)}{4\pi r_1} e^{-jkr_1} + \frac{jkI_0L \sin(\theta)}{4\pi r_2} e^{-jkr_2} \quad (8.2)$$

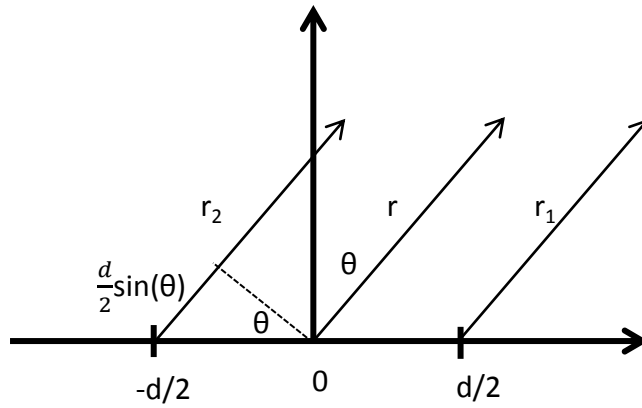


Figure 8.2: Two-Element Array Geometry

Using the far-field assumptions and the geometric relationships shown in Figure 8.2, the total pattern reduces to

$$E_\theta = \frac{jkI_0L \sin(\theta)}{4\pi r} e^{-jkr} \left[e^{-j\frac{kd \sin(\theta)}{2}} + e^{j\frac{kd \sin(\theta)}{2}} \right] \quad (8.3)$$

Upon comparing Equation (8.1) and (8.3), it becomes evident that the total radiation pattern of the array is a function of the element factor and an array factor (term in the brackets).

8.2.2 N-Element Uniformly-Spaced Linear Array

In general, the total radiation pattern of an array is the element pattern multiplied by the array factor (AF) which is a function of array geometry. So for an N-element array with each element spaced d , the array factor becomes:

$$AF = 1 + e^{j(kd \sin(\theta))} + e^{j(2kd \sin(\theta))} + \dots + e^{j(Nkd \sin(\theta))} \quad (8.4)$$

or:

$$AF = \sum_{n=1}^N e^{j(n-1)(kd \sin(\theta))} \quad (8.5)$$

When the AF is written in vector form as shown in Equation (8.6), it is called the array manifold or array steering vector.

$$\bar{a}(\theta) = \begin{bmatrix} 1 \\ e^{j(kd \sin(\theta))} \\ \vdots \\ e^{j((N-1)kd \sin(\theta))} \end{bmatrix} \quad (8.6)$$

To manipulate the radiation pattern, complex weights can be applied to the AF. These weights dictate the relative phase and amplitude of each element.

$$AF = \bar{w}^T * \bar{a}(\theta) \quad (8.7)$$

Now assume the N element array shown in Figure 8.3. Also assume one desired signal, s , which has incidence angle θ_0 , and two interferers with their respective incidence angles. The total received signal at each antenna is x , and the total array output is y .

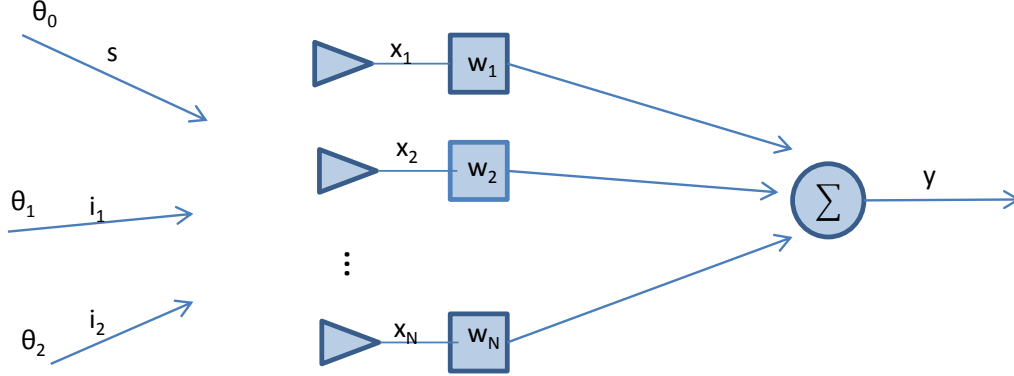


Figure 8.3: N-Element Array with Three Arriving Signals

The total array output for a discrete time, k , can be written as:

$$y(k) = \bar{w}^H * \bar{x}(k) \quad (8.8)$$

where:

$$\bar{x}(k) = \bar{a}_0 s(k) + \begin{bmatrix} \bar{a}_1 & \bar{a}_2 \end{bmatrix} \begin{bmatrix} i_1(k) \\ i_2(k) \end{bmatrix} + \bar{n}(k) = \bar{x}_s + \bar{x}_i + \bar{n} \quad (8.9)$$

\bar{x}_s = desired signal vector

\bar{x}_i = interfering signal vector

\bar{n} = noise vector

\bar{a}_i = N-element steering vector for the θ_i direction of arrival

H = Hermitian of the vector

Next the two beamformers used to generate the weight vector, \bar{w} , will be discussed.

8.3 Chebyshev Beamformer

Chebyshev weights are based on the Chebyshev polynomials, and give the narrowest mainbeam for a given sidelobe level for uniformly spaced arrays. This method was first developed by Dolph [109] in the 1940's. The polynomials are related by the following recursion relationship, where $z = \cos(u)$ and $u = kdsin(\theta)$.

$$\begin{aligned} T_0(z) &= 1 \\ T_1(z) &= z \\ T_m(z) &= 2zT_{m-1}(z) - T_{m-2}(z), \quad m = 2, 3, \dots \end{aligned} \quad (8.10)$$

It has been shown that the array factor for an even and odd element array can be reduced to equations (8.11) and (8.12), respectively [78].

$$AF = \sum_{n=1}^N w_n \cos[(2n-1)u] \quad (\text{even}) \quad (8.11)$$

$$AF = \sum_{n=1}^N w_n \cos[(2n)u] \quad (\text{odd}) \quad (8.12)$$

Recalling the trigonometric relationships for cosine functions:

$$\begin{aligned} \cos(2u) &= 2\cos^2 u - 1 \\ \cos(3u) &= 4\cos^3 u - 3\cos u \\ \cos(4u) &= 8\cos^4 u - 8\cos^2 u + 1 \end{aligned} \quad (8.13)$$

These expressions can be substituted into the equations for the array factors. By doing so, a polynomial will emerge that matches the form of the Chebyshev polynomial. The unknown weights of the array factor can be determined by equating the series representing the cosine terms to the appropriate Chebyshev polynomial.

8.4 MVDR Beamformer

The Minimum Variance Distortionless Response (MVDR) beamformer aims to minimize the array output noise variance while maintaining an undistorted desired signal. The optimal weights can be found by maximizing the beamformer Signal to Interference Noise Ratio (SINR):

$$SINR = \frac{E\left[|\bar{w}^H \bar{x}_s|^2\right]}{E\left[|\bar{w}^H (\bar{x}_i + \bar{n})|^2\right]} = \frac{\sigma_s^2 |\bar{w}^H \bar{a}_0|^2}{\bar{w}^H \bar{R}_{i+n} \bar{w}} \quad (8.14)$$

In the equation E is the mathematical expectation, the desired signal power is $\sigma_s^2 = E[|s(k)|^2]$, and R_{i+n} is the interference + noise correlation matrix. To maximize the SINR the denominator must be minimized (minimize variance/power of i+n) while keeping the numerator fixed (distortionless response). This results in the optimization problem:

$$\min \bar{w}^H \bar{R}_{i+n} \bar{w} \quad \text{such that} \quad \bar{w}^H \bar{a}_0 = 1 \quad (8.15)$$

Using the Lagrange method results in the following cost function:

$$J(\bar{w}) = \frac{\sigma_{MV}^2}{2} + \lambda(1 - \bar{w}^H \bar{a}_0) = \frac{\bar{w}^H \bar{R}_{i+n} \bar{w}}{2} + \lambda(1 - \bar{w}^H \bar{a}_0) \quad (8.16)$$

By taking the gradient of (8.16), setting it equal to zero, and using the constraint in (8.15) the optimum weights are found to be:

$$\bar{w}_{MVDR} = \frac{\bar{R}_{i+n}^{-1} \bar{a}_0}{\bar{a}_0^H \bar{R}_{i+n}^{-1} \bar{a}_0} \quad (8.17)$$

MVDR is generally used as a data-dependent beamformer in which the correlation matrix is determined by a received data sample. One of the difficulties in using the MVDR beamformer is extracting a data vector that does not include the desired signal to form the interferer plus noise correlation matrix. To estimate \bar{R}_{i+n} , CReSIS correlates the data vector for each pixel and uses data that comes after the bedrock return in the fast time axis to estimate the noise power. This process results in a correlation matrix that contains the desired signal. The desired signal can be removed from the correlation matrix, but only if it is precisely known. The precision required for \bar{a}_0 is another obstacle to overcome in the MVDR beamformer. Lacking exact knowledge of the desired signal steering vector can lead to a phenomenon called “self-nulling”. In this instance the beamformer misinterprets the desired signal as an interferer and suppresses it. CReSIS processing always assumes the desired ice-bed echo is from nadir, and the steering vector is derived from simple array theory or through electromagnetic simulations. The assumed nadir

direction of arrival will not be valid in areas with steep ice beds. As such, CRISIS has had variable success in processing the radar data using MVDR.

Another drawback with using the data-dependent method is the lack of control over the radiation pattern. The MVDR beamformer simply tries to maximize the power in the direction of the desired signal and minimize the power from all other directions. The direction of arrival of interferers is inherent in the \bar{R}_{i+n} correlation matrix, but if there are more interferers than degrees of freedom in the array, the radiation pattern degrades. Finally, it has been shown that phase center errors will lead to incorrect direction of arrival estimates [61]-[63]. This will lead to the self-nulling phenomenon as well as misplaced nulls.

An alternative to generating the correlation matrix using real-data is using a data independent method in which a number of signal are assumed and the received signal is determined from the complex array steering vectors. The interference-plus-noise correlation matrix is then generated with the complex antenna element patterns. First the steering vectors of the array for each interferer angle must be determined.

$$\bar{a}_i(\theta_1) = \begin{bmatrix} X_{11} + jY_{11} \\ X_{12} + jY_{12} \\ \vdots \\ X_{1N} + jY_{1N} \end{bmatrix} \begin{array}{l} \leftarrow \text{Complex pattern data of} \\ \text{element \#1 in the direction of } \theta_1 \\ \\ \leftarrow \text{Complex pattern data of} \\ \text{element \#N in the direction of } \theta_1 \end{array}$$

$$\bar{a}_i(\theta_2) = \begin{bmatrix} X_{21} + jY_{21} \\ X_{22} + jY_{22} \\ \vdots \\ X_{2N} + jY_{2N} \end{bmatrix} \begin{array}{l} \leftarrow \text{Complex pattern data of} \\ \text{element \#1 in the direction of } \theta_2 \\ \\ \leftarrow \text{Complex pattern data of} \\ \text{element \#N in the direction of } \theta_2 \end{array}$$

The number of angles that can be controlled is equivalent to the number of elements in the array. Generally, one degree of freedom is used to steer the beam, which leaves N-1 degrees of freedom to suppress clutter. Next the interferer steering vectors are assembled into a single N X N-1 matrix.

$$\bar{A} = \begin{bmatrix} X_{11} + jY_{11} & X_{21} + jY_{21} & \cdots & X_{M1} + jY_{M1} \\ X_{12} + jY_{12} & X_{22} + jY_{22} & \cdots & X_{M2} + jY_{M2} \\ \vdots & \vdots & \cdots & \vdots \\ X_{1N} + jY_{1N} & X_{2N} + jY_{2N} & \cdots & X_{MN} + jY_{MN} \end{bmatrix} \quad M = N - 1 \quad (8.18)$$

The N X N correlation matrix for the interferers is calculated as follows:

$$\bar{R}_i = \bar{A} * \bar{A}^T \quad (8.19)$$

The noise correlation matrix is related to the noise variance, σ_n , by the following relationship.

$$\bar{R}_n = \sigma_n * I_{N \times N} \quad (8.20)$$

Therefore the interference-plus-noise correlation matrix is as follows:

$$\bar{R}_{i+n} = \bar{R}_i + \bar{R}_n \quad (8.21)$$

The data-independent method just described was used in the studies presented next. The advantage with using the data-independent MVDR is more control over the radiation pattern, including user specified rules for null formation. A disadvantage of this method is that it requires the measurement of the real antenna radiation patterns, though it may be argued that such measurements are also required for the data-dependent method to accurately determine the steering vector.

9 EFFECTS OF WING FLEXURE FOR WING-MOUNTED PHASED ARRAY

9.1 Introduction

To study the effects of wing flexure on beam formation, simulations and measurements were performed based on CReSIS's MCoRDS radar antenna-array that is flown the DHC-6 Twin Otter aircraft. While the development of the Twin Otter array is not a part of the work presented in this document, it was selected for this study because its geometry is much simpler than that of other arrays making it easier to manipulate and simulate or measure.

The Twin Otter and its wing-mounted folded dipole array, was simulated using Ansys High Frequency Structure Simulator (HFSS)[®] Version 14 [115] as part of an initial study to understand the effects of aircraft integration effects on antenna-array performance. After the initial study was completed a scaled model of the Twin Otter array was fabricated and experimentally characterized in KU's anechoic chamber to verify the observation made through simulation. The following sections describe the real system, the full-scale simulation model, and the scaled model that was built. These sections are followed up by the results for both cases.

9.1.1 *Description of the Twin Otter MCoRDS Array*

The Twin Otter MCoRDS array consists of 12 folded dipoles with six dipoles installed on each wing. These antennas were custom fabricated by Polar Electronic Industries [119] for the Twin Otter missions. The folded dipole was fabricated from a 0.75" diameter aluminum rod and was attached to the aircraft via a 2" diameter aluminum support post [120]. Between the 2008 and 2011 field seasons, the center frequency of the antenna-array was shifted from 150 MHz to 195 MHz. In addition, the dipole antennas were flown parallel to the direction of flight during the 2008 field season and collinearly during the 2011 field season. This change was made to reduce coupling in the array. Figure 9.1 shows the comparison between the 2008 and 2011 Twin Otter MCoRDS array configurations.

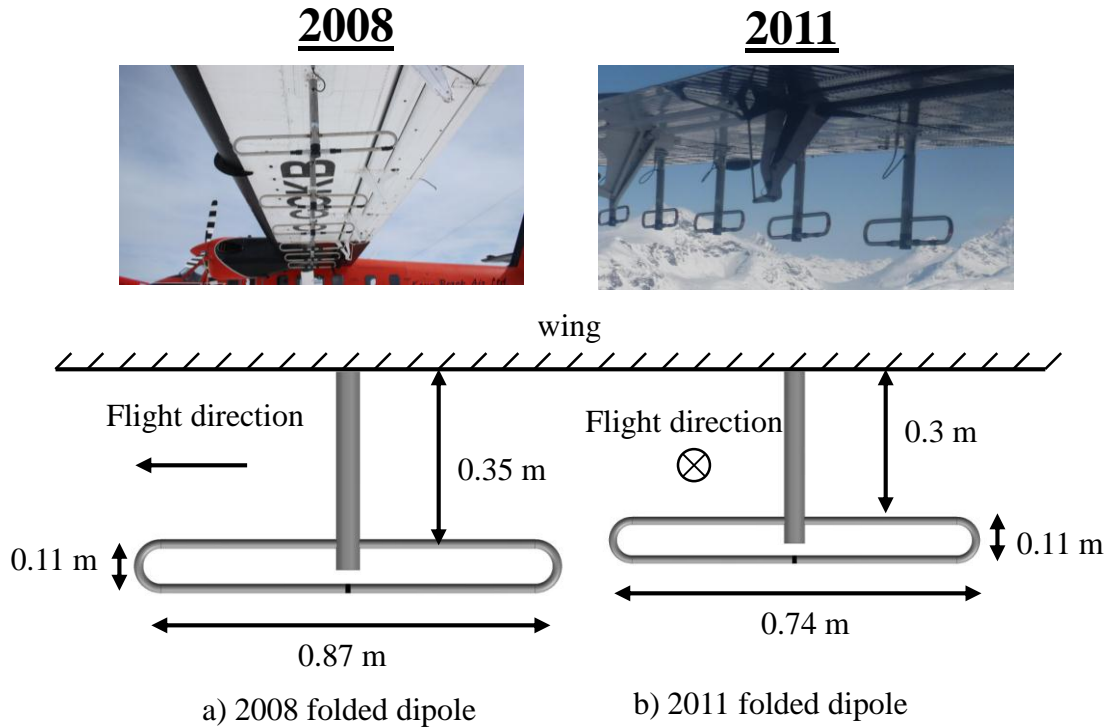


Figure 9.1: 2008 and 2011 Twin Otter Array Orientation and Folded Dipole Geometry

Although the antenna size, orientation, and frequency changed between the 2008 and 2011 field seasons, the array element spacing remained constant. Figure 9.2 shows the arrangement of the antenna elements as well as the labeling system that was used in this study. The spacing between adjacent elements starting with the inboard most elements (R1 or L1) is 38.2", 37.0", 37.4", 34.0", and 39.0", respectively. This non-uniform element spacing is a result of integrating the antennas into the existing wing structure. The distance between elements L1 and R1 is approximately 30 ft, and the two elements are spaced 4.6 ft from the engine and 11.8 ft from the fuselage side wall. The wing of the Twin Otter has a span of 65 ft and a dihedral angle (elevation angle of the wing) of 3°.

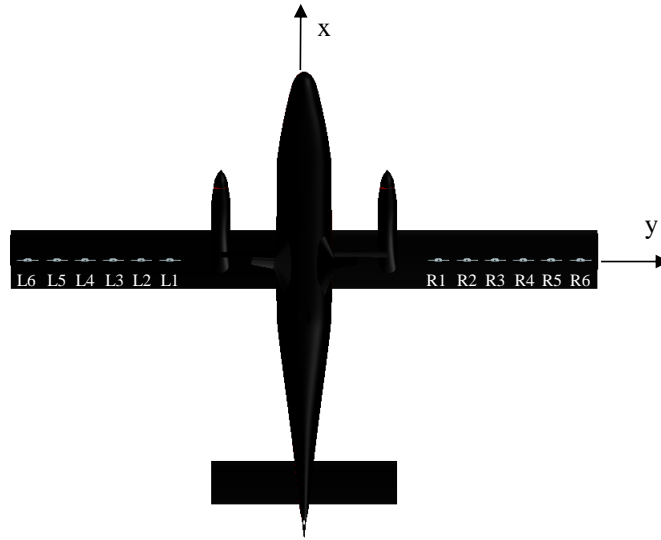


Figure 9.2: Top View of Twin Otter with Array Labeling and Arrangement

9.1.2 *Description of the Full-scale Simulation Model*

The full-scale simulation model included the wing outboard of the engine nacelle and the antenna elements. To simulate the wing flexure, the wing skin was discretized into seven segments and the end points of a segment are located at antenna wing stations. Figure 9.3 shows the nominal wing and the discretized, flexed wing. Using the parametric modeling feature of HFSS[®] Version 14, the z-location of the segment end points could be prescribed to simulate various levels of displacement.

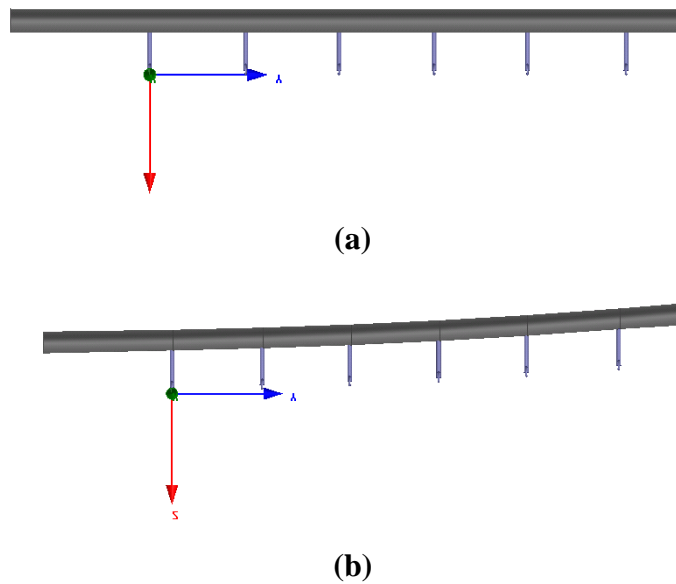


Figure 9.3: Full-Scale Twin Otter Simulation of Nominal Wing (a) and Flexed Wing (b)

The wing skin was modeled as a sheet body and was assigned as a perfect electric conducting boundary. The folded dipole shown in Figure 9.4 was modeled as a solid perfect conductor. A 50Ω lumped port (represented by the red square in Figure 9.4) is located in the center of the folded dipole.

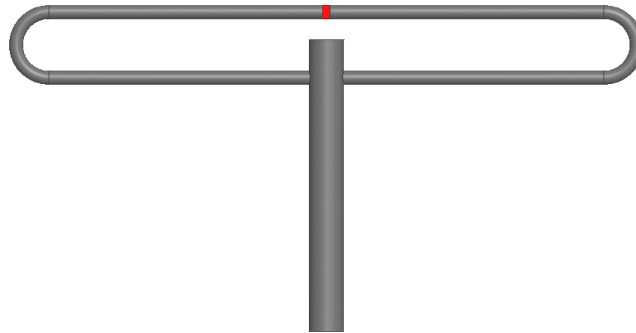


Figure 9.4: Simulated Twin Otter Folded Dipole

The air box used to define the solution space has a radiating boundary, and its faces are at least $\lambda/4$ from any point on the wing or the antenna. The model was solved for a single solution (150 or 195 MHz), and the convergence criterion was defined as a maximum delta S-parameter of 0.02.

9.1.3 *Description of the Scaled Model Demonstrator*

The use of scaled models is a common practice in the field of antenna integration and design [121]-[123]. In an EM scaled model all components are scaled as a function of frequency wavelength. The 195 MHz configuration of the Twin Otter was used as the baseline for the demonstrator, which was scaled to 1.2 GHz. This frequency was selected in part due to the far-field restrictions of the chamber and for the resulting size of the scaled array. The dipoles used for the demonstrator are printed dipoles with and integrated balun. The initial design for these antennas can be found in [124], which was subsequently scaled from 2.4 GHz to 1.2 GHz using HFSS[®] Version 14. Figure 9.5 shows a drawing of the PCB dipole. The antenna substrate is FR4.

The scaled model of the Twin Otter array included the six dipole elements, the wing outboard of the nacelle, the engine nacelle, a control surface, and four control surface hinges. The control surface horns were designed to rotate only down to simplify manufacturing. The scaled model is geometrically and electrically similar to the full-scale array, and while it is not

structurally similar, the induced wing flexure is geometrically similar to what is expected in the real aircraft. Figure 9.6 shows the front and back view of the demonstrator.

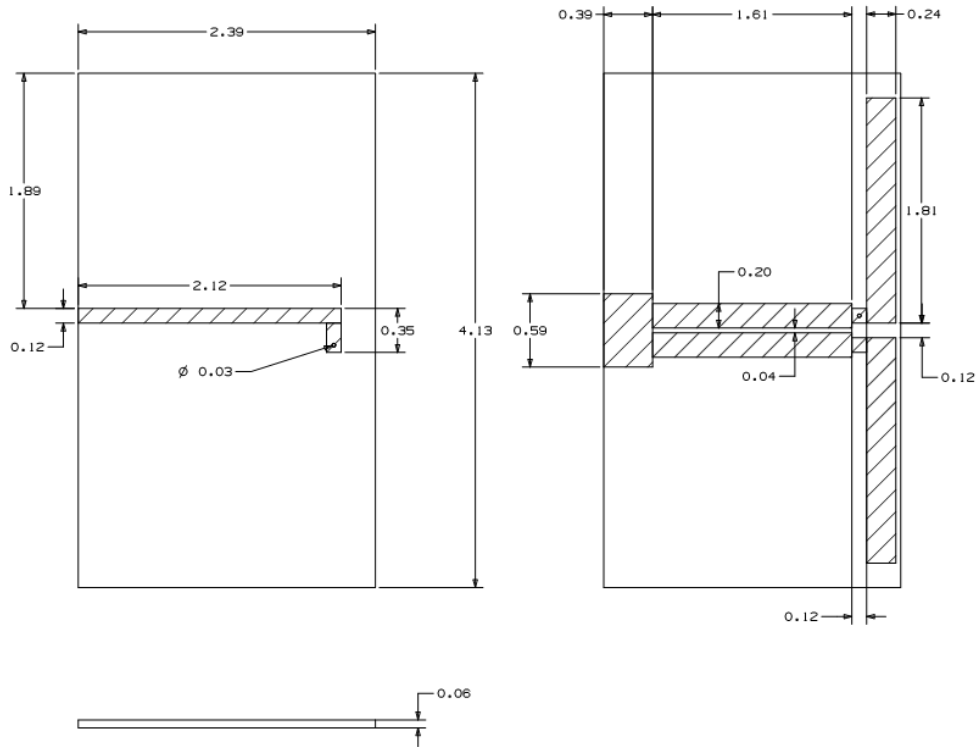


Figure 9.5: 1.2 GHz scaled Model Dipole Antenna with Integrated Balun (dimensions in inches)



Figure 9.6: Front and Back View of the Twin Otter scaled Model Demonstrator

To apply a prescribed displacement to the wing, the nacelle acts as a fulcrum point and four laterals are used to set the displacement by translating along a track. The tracks were designed such that they prevented rotation about the wing axis. Figure 9.7 shows the displaced array. Scales were attached to each of the tracks that marked the desirable displacement locations. On each lateral, tabs were attached to position the laterals along the scale. Figure 9.8 shows the

lateral track and tab configuration. The array was kept in the displaced position by friction between the laterals and the track either with or without the aid of additional wedges.

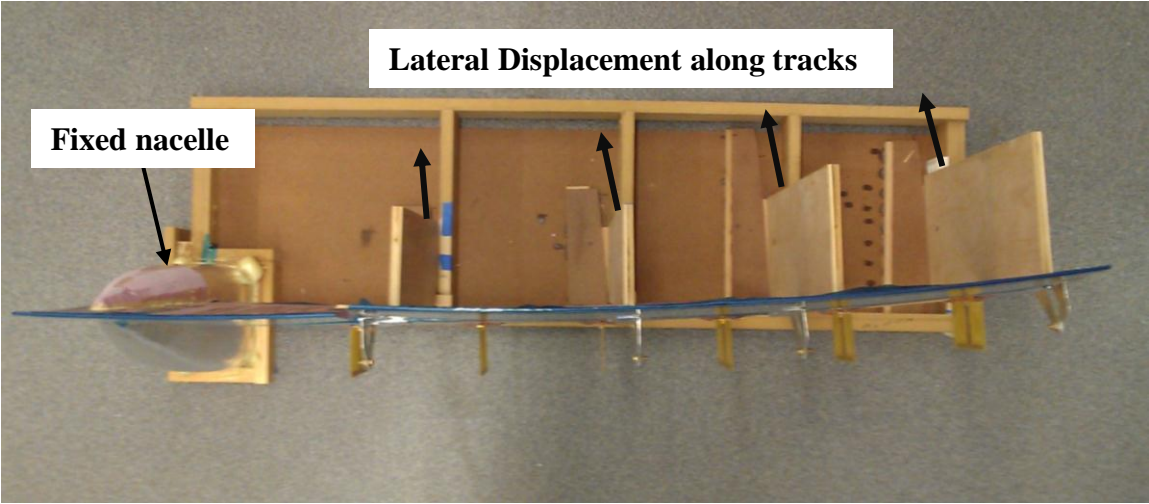


Figure 9.7: Top View of the Displaced Array

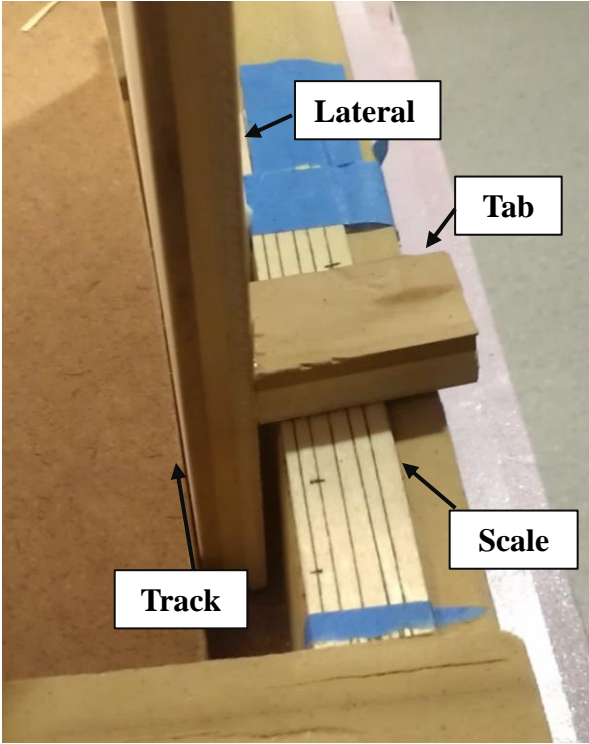


Figure 9.8: Lateral Track, Tab, and Scale

The entire frame used to support the array was made from low-loss dielectric materials. The MDF frame is held together with adhesive, and the test stand used to support the array in the chamber is made from pink housing insulation foam. In addition, the array was designed to allow

for rotation of the antenna elements such that both parallel and collinear arrays could be tested. Prescribed element displacements were accurate within $\pm 0.1''$ (0.01λ) and element angles were within 2° . Measurements were completed by measuring the element displacement for eight different displacements level. This was repeated three different times, each time alternating the orientation of the antenna between parallel and collinear. A total of 144 element displacements were recorded. Figure 9.9 shows the array setup on the chamber turntable.

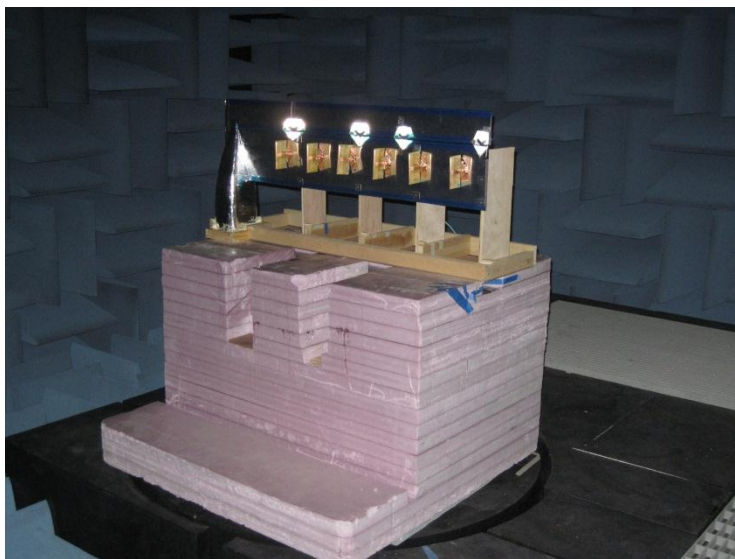


Figure 9.9: Scaled Model Array Setup in Anechoic Chamber

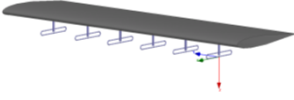
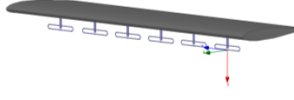
9.2 Simulation and Measurement Procedures

9.2.1 *Simulation Procedures*

The array configurations used in 2008 and 2011 were each characterized in this study; Table 9.1 gives a summary of these configurations. From the images in Table 9.1 it can be seen that the Twin Otter EM model does not include control surface horns or the nacelle. While the overall array geometry (element spacing and location) remains constant between the two configurations, the frequency, type, and orientation of the antennas changed. The 2008 configuration consists of six elements operating at 150 MHz and oriented parallel to the flight path. The other configuration is based on the 2011 missions, where the six 195 MHz elements were collinear. Since the 2008 and 2011 arrays have different dipole orientations, the total cross-track array patterns will be different, and thus it is necessary to analyze both. For the rest of the document the 2008 array will be referred to as either the “parallel” configuration or “vertically

polarized” configuration. The 2011 array will be referred to as either the “collinear” configuration or “horizontally polarized” configuration.

Table 9.1: Overview of Array Configurations

Configuration	2008	2011
		
No. Elements	6	6
Frequency	150 MHz	195 MHz
Orientation (wrt flight direction)	Parallel	Perpendicular

Though the two configurations have different operating frequencies, nearby scatterers have similar sizes in terms of wavelength, so the response of the antennas to nearby scatterers is expected to be similar. This is important to note that measurements performed with the scaled model for both configurations were only captured for a single frequency (1.2 GHz).

Flexure of the wing was simulated by using the parametric modeling feature of HFSS[®] Version 14. The flexure was determined using the simplified beam model given in Equation (9.1)

$$\Delta z = \alpha y^3 (\beta L_{wing} - y) \quad (9.1)$$

where Δz is the vertical displacement, y is the distance from the root of the wing, L_{wing} is the length of the wing, and α and β are constants determined by the load, stiffness, and geometry of the beam. For the simplified displacement model used in the simulations, β was given a value of 3, and α was varied between 0 and 2.5. Equation (9.1) is an approximation of the wing flexure, but it is a good representation of the relative displacement between elements. It is noted that the wing was also simulated with linear deflections. Those results are not included in this document but can be found in [125]. Based on actual tip deflections of the Twin Otter wing, a value of $\alpha = 1$ is a good representation of the steady-state flight conditions. Under steady-state flight conditions the Twin Otter's wingtips deflect approximately 4-4.75 inches [126]-[127] for an aircraft weight of 10,000 lbs, and $\alpha = 1$ results in a tip deflection of 5 inches (0.06λ at 195 MHz or 0.07λ at 150 MHz). The maximum takeoff weight of the Twin Otter is 12,500 lbs.

For analysis and beam formation, the antenna element patterns for each element were retrieved for each displacement level. Appropriate weights were determined in post-processing and the patterns were combined using those weights.

9.2.2 *Measurement Procedures*

Procedures for the measurement analysis are similar to those of the simulation analysis. All measurements were repeated for both parallel and collinear antenna configurations. Like the simulations, antenna displacements were determined by Equation (9.1). A turntable controlled by ETS EMCO[®]'s multi-device controller, Agilent Technologies'[®] N5230C PNA-L network analyzer, and EMQuest[®] Version 1.08 data acquisition software [128] were used to measure the complex element patterns. A single antenna element was excited for each measurement, while the other five antennas were terminated with 50 Ω loads. To ensure angular accuracy and reduce phase ambiguities, the turntable was stepped in 0.5^o increments and a single measurement was recorded. The analysis procedure for the measurement data is identical to that of the simulations.

9.3 Simulation Results

The plots in this section and the next compare radiation patterns for all displacement settings and for both configurations. In all the plots black corresponds to the nominal array response (no displacement), red for $\alpha = 0.5$, blue for $\alpha = 1$, green for $\alpha = 1.5$, magenta for $\alpha = 2$, and cyan for $\alpha = 2.5$. Figure 9.10 shows the simulated Twin Otter array pattern with uniform weighting. The 20 dB normalized power pattern is only plotted from $\pm 90^\circ$ because this is the energy radiated towards the earth, and 0° corresponds to nadir. Though a uniform weighted array does not offer many advantages in clutter suppression, it was included here to capture the fundamental changes in the array patterns. From the figure it is obvious that the wing flexure results in a rotation of the total pattern, and these rotations are directly related to the level of displacement. There are some slight decreases in the null depth, but there is not a significant increase in sidelobe levels.

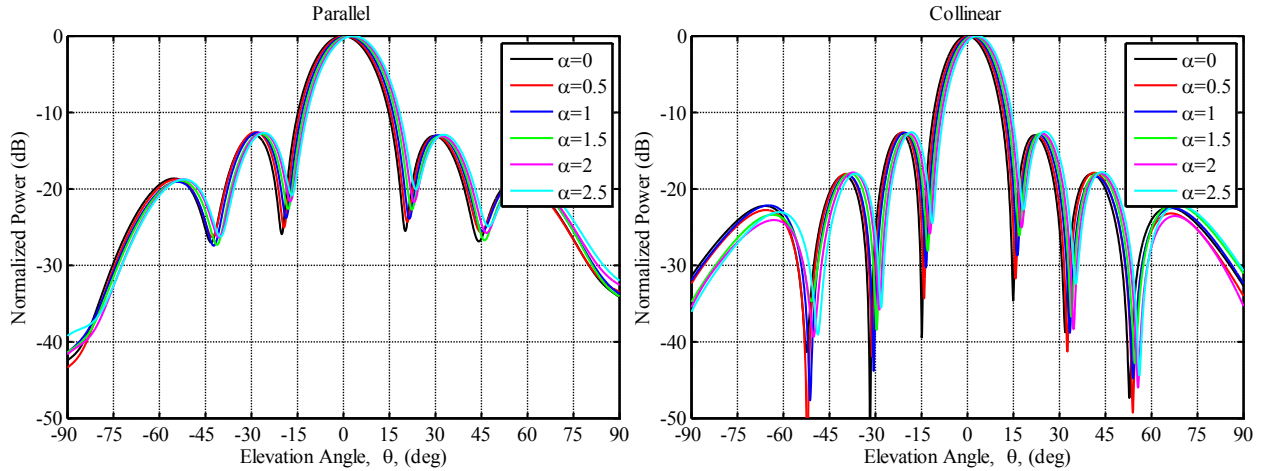


Figure 9.10: Parallel (left) and Collinear (right) Array Simulated Patterns with Uniform Weights

Figure 9.11 shows the simulated radiation plots for sidelobe levels set to -30 dB with Chebyshev weights. Once again there is a noticeable rotation of the mainbeam. While there is significant distortion of the pattern outside of the mainbeam, the 30 dB sidelobe level was met for all cases but one.

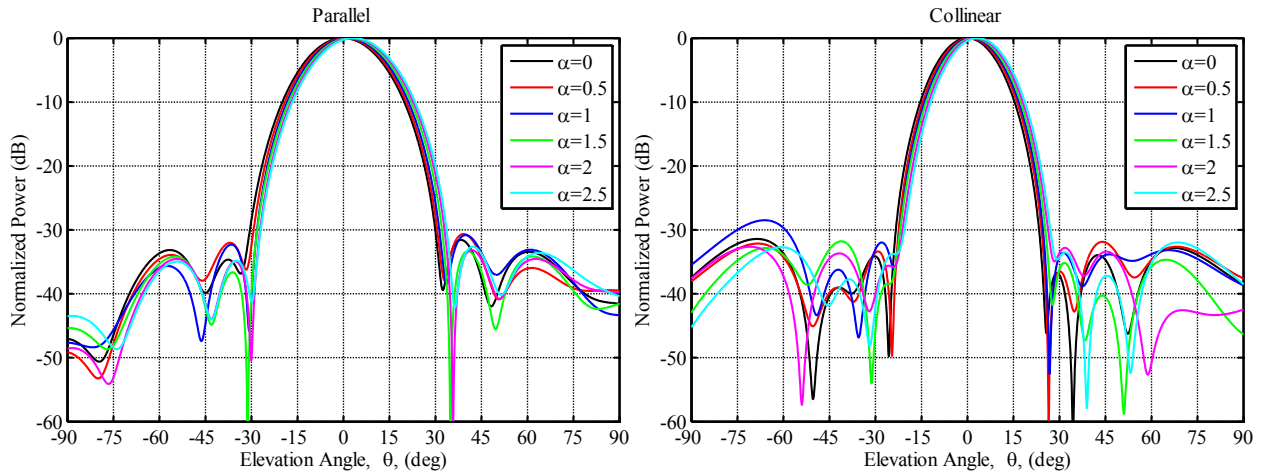


Figure 9.11: Parallel (left) and Collinear (right) Array Simulated Patterns with Chebyshev Weights

Figure 9.12, Figure 9.13, and Figure 9.14 show the simulated radiation patterns with MVDR weights when nulls are applied at $\pm 40^\circ$, $\pm 70^\circ$, and -54° and 50° , respectively. It is noted that there is an infinite number of combinations of nulls that could be applied. For the sake of clarity and brevity, only three combinations will be shown. These three cases were selected because they demonstrate nulls placed at smaller angles (less than $\pm 55^\circ$), nulls placed at larger angles (greater than $\pm 55^\circ$), and asymmetric nulls. The location of the asymmetric nulls was selected because it's

roughly in the middle of the angular range of interest. Chapter 10 will present a broader discussion on the performance of the beamformer for a greater combination of nulls. From the MVDR plots, once again there is evidence of pattern rotation, but more significantly the displacements have caused filling and shifting of the nulls. This phenomenon appears to be more severe for the collinear array versus the parallel array and is likely due to the changes in coupling between the elements and the surrounding structure. The collinear elements are oriented such that the natural element nulls are along the wing axis whereas the parallel element nulls are perpendicular to the wing axis. As the wing flexes the elements rotate, changing the orientation of the nulls. The changing null orientations cause energy to be radiated and received from directions that were previously filtered by the antenna's radiation pattern.

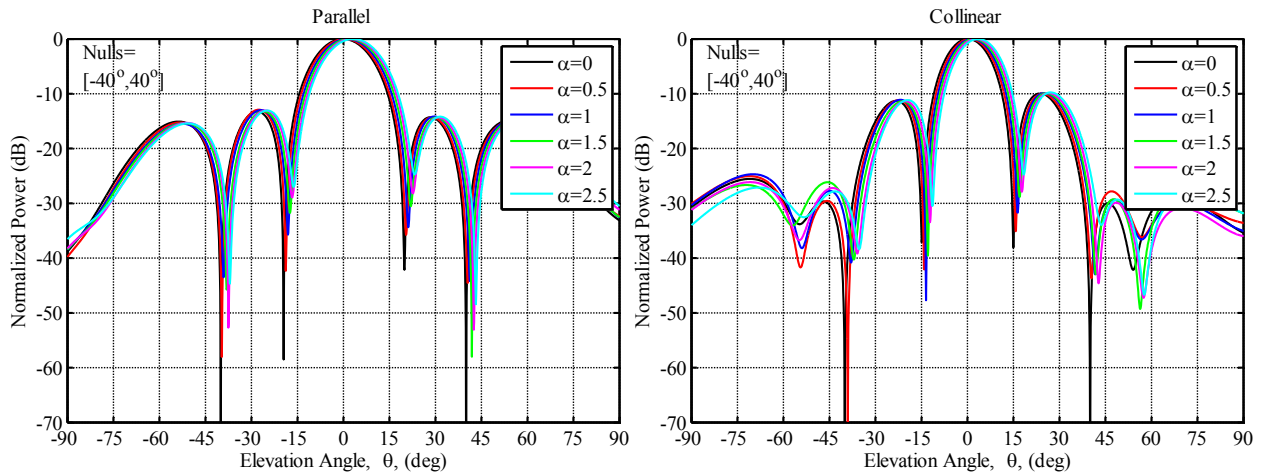


Figure 9.12: Parallel (left) and Collinear (right) Array Simulated Patterns with MVDR Weights and Nulls at $\pm 40^\circ$

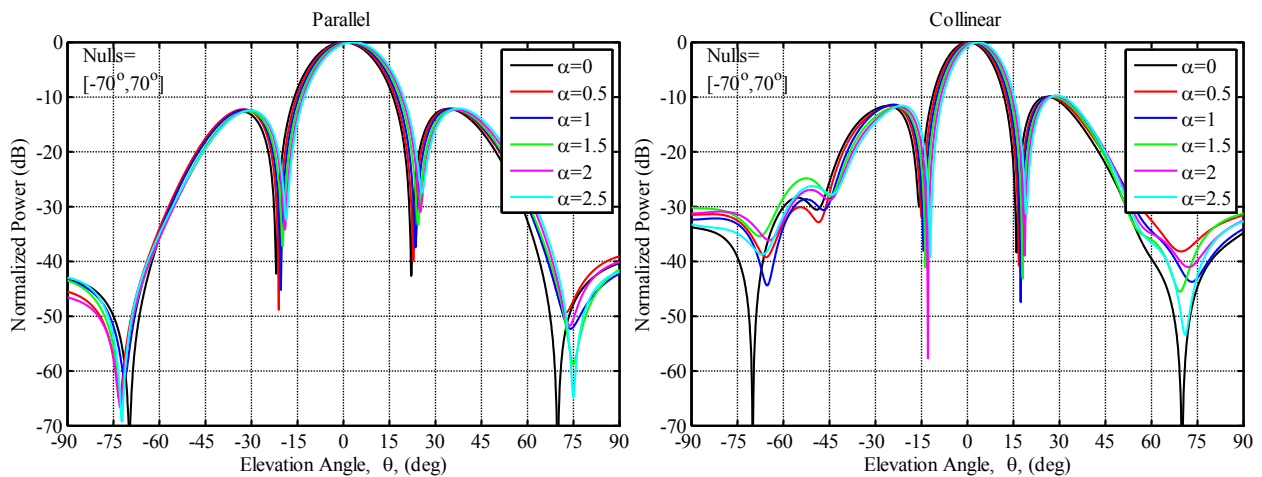


Figure 9.13: Parallel (left) and Collinear (right) Array Simulated Patterns with MVDR Weights and Nulls at $\pm 70^\circ$

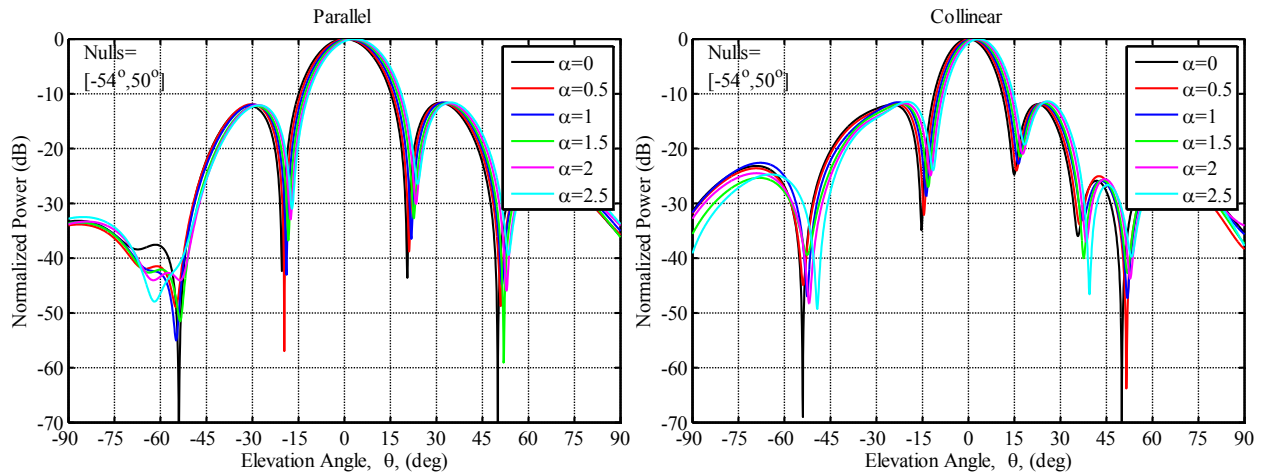


Figure 9.14: Parallel (left) and Collinear (right) Array Simulated Patterns with MVDR Weights and Asymmetric Nulls at -54° and 50°

9.4 Measurement Results

Figure 9.15 shows the measured radiation patterns for the scaled model with uniform weights applied. As expected the wing flexure results in a rotation of the pattern. Unlike the simulated results, the real measurements have a more significant increase in sidelobe levels. The maximum sidelobe increase for the simulated results was 0.2 dB, and the maximum increase of ~ 2.5 dB in the measured results occurs in the sidelobes nearest the mainbeam. In terms of sounding ice sheets, a 2.5 dB increase in sidelobe results in almost double the power being received from these angles.

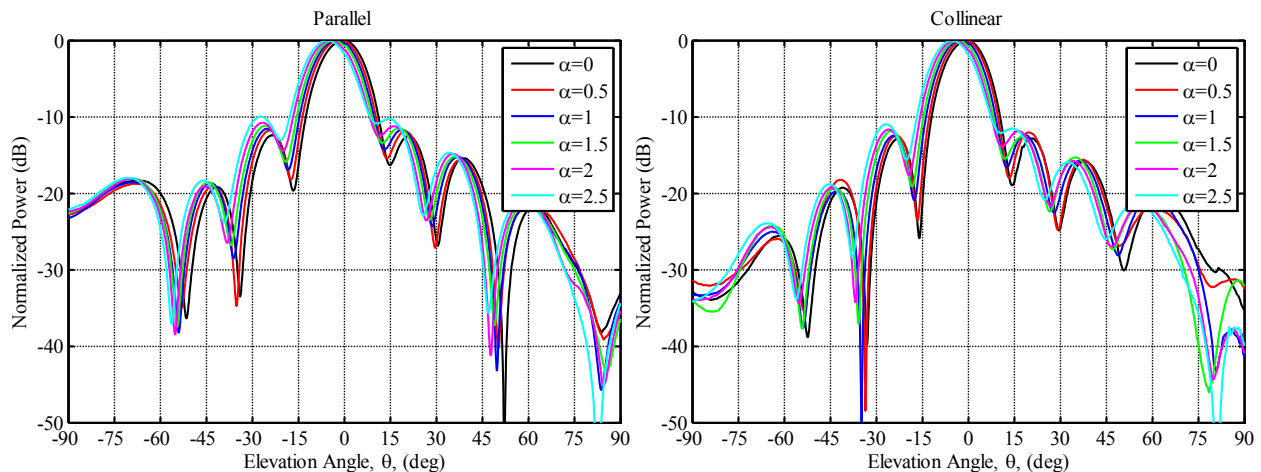


Figure 9.15: Parallel (left) and Collinear (right) Array Measured Patterns with Uniform Weights

Figure 9.16 shows the measured radiation pattern for a sidelobe goal of 30 dB with Chebyshev weights applied. Once again there is a large variation in the patterns outside the mainbeam. Though some of the displaced patterns violate the 30 dB sidelobe goal, it is interesting to note that even the nominal pattern was unable to achieve 30 dB sidelobes. The greatest sidelobe increase (2.5 dB) is observed in the collinear pattern for the $\alpha = 0.5$ displacement case between the angles of -90° and -70° .

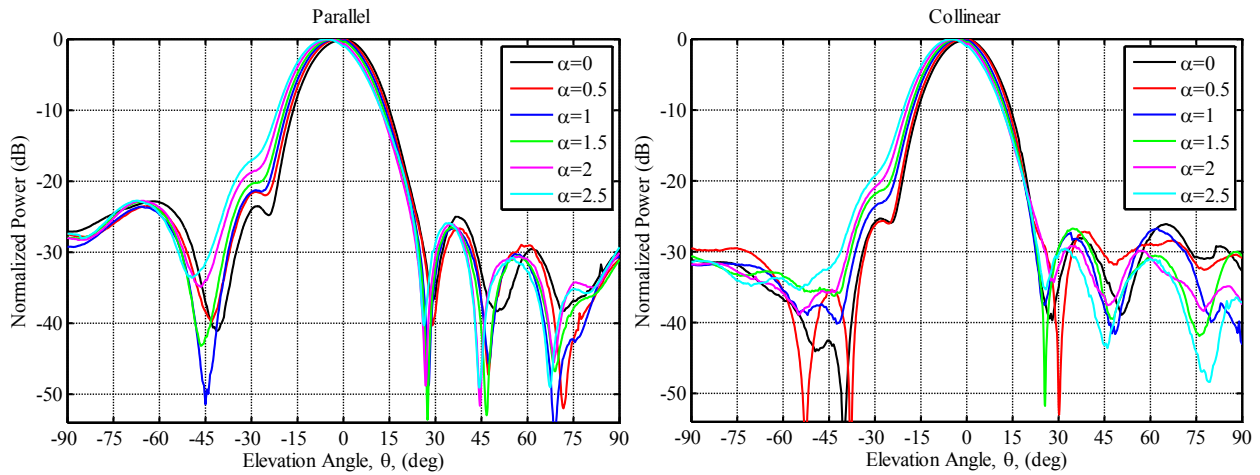


Figure 9.16: Parallel (left) and Collinear (right) Array Measured Patterns with Chebyshev Weights

Figure 9.17, Figure 9.18, and Figure 9.19 show the measured radiation patterns with MVDR weights when nulls are applied at $\pm 40^\circ$, $\pm 70^\circ$, and -54° and 50° , respectively. Like the simulations the wing flexure causes a filling and shifting of the nulls.

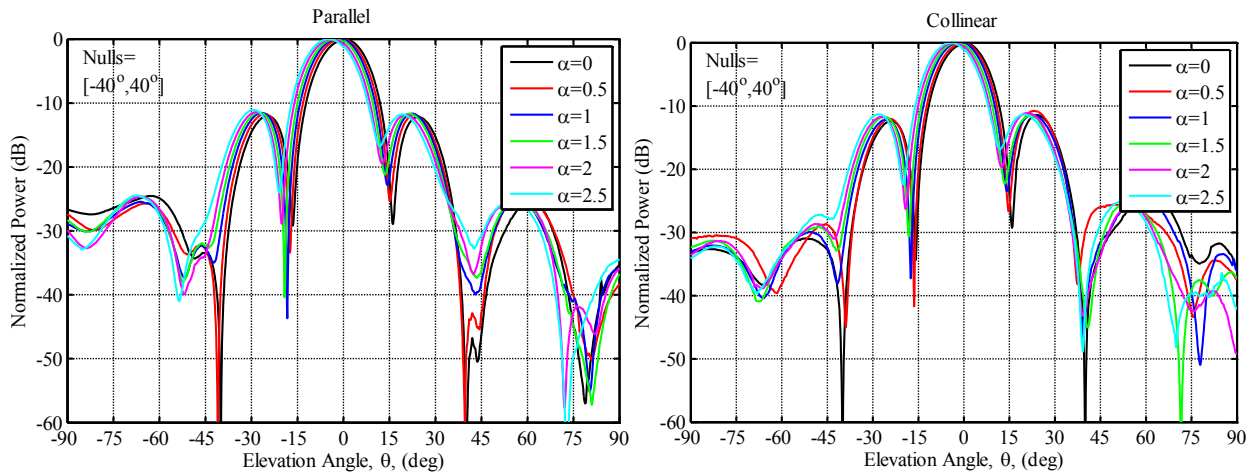


Figure 9.17: Parallel (left) and Collinear (right) Array Measured Patterns with MVDR Weights and Nulls at $\pm 40^\circ$

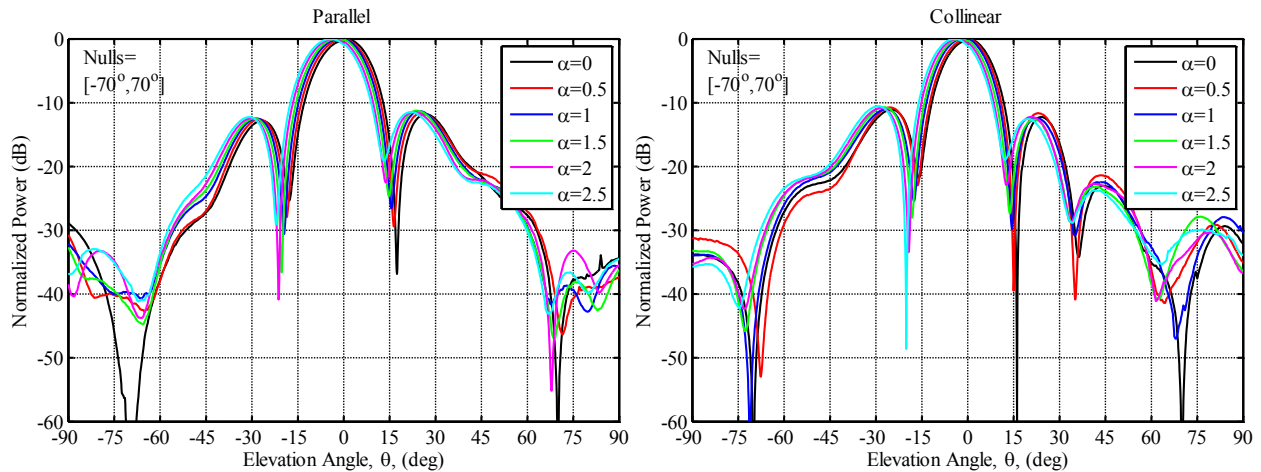


Figure 9.18: Parallel (left) and Collinear (right) Array Measured Patterns with MVDR Weights and Nulls at $\pm 70^\circ$

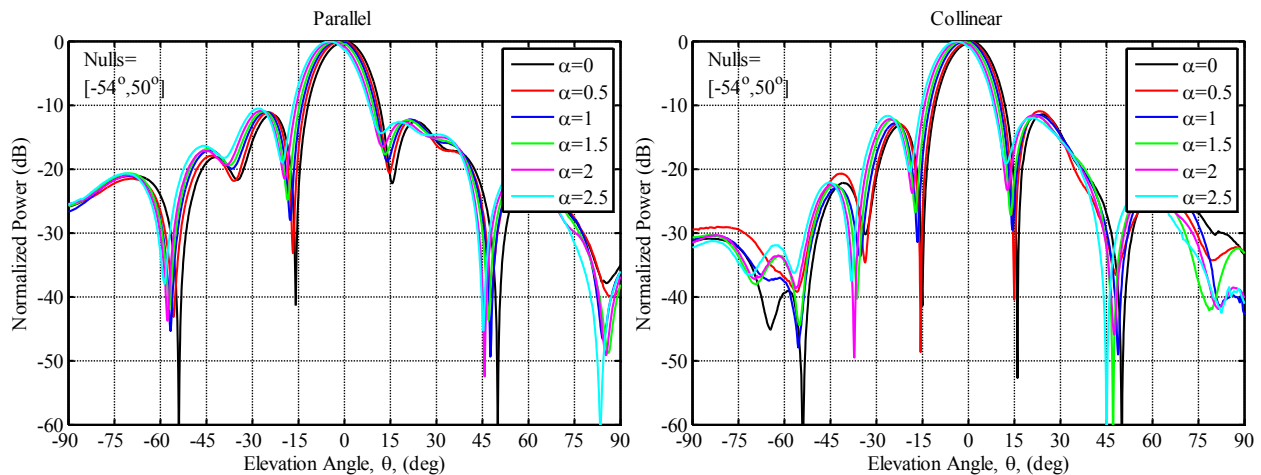


Figure 9.19: Parallel (left) and Collinear (right) Array Simulated Patterns with MVDR Weights and Asymmetric Nulls at -54° and 50°

9.5 Summary of Results for the Effects of Wing Flexure

Wing flexure is shown to cause main beam pointing errors, slight increase in sidelobes, and filling and shifting of nulls. Sidelobe increases were more severe for the measured case than the simulated case. This is due to the cross-polarization effects in the real array and, as will be shown in Section 10.5, the increased presence of scatterers in the real array. The real array included the nacelle, control horns, and fasteners, whereas the simulations did not. The presence of scatterers will increase the mutual coupling between the array and the surrounding structure, and it is well documented that mutual coupling increases sidelobe levels [129]. It is interesting that in the case of the measured results with Chebyshev weights the nominal arrays were unable

to achieve the 30 dB sidelobe goal. Once again, this was due to the increased scatterer presence and thus mutual coupling caused by the surrounding structure. Overall, when real weights are applied to the array (as is the case with uniform and Chebyshev weights) the most significant impact of the wing flex was the rotation of the mainbeam. However, sidelobe suppression is much more critical to significantly improving the CReSIS radars than small mainbeam pointing errors, and as such these small errors will not significantly degrade radar performance. A 1° shift in the mainbeam results in a SINR reduction of less than 0.1 dB, whereas a 1° shift in null location can result in over 15 dB reduction in SINR.

The effects of wing flexure on the MVDR beamformer were much more severe. In all cases the flexure caused shifting and filling of nulls. This phenomenon will greatly hinder the ability to suppress clutter and improve SINR. In the simulations the null degradation appears to be greater in the collinear array configuration than the parallel array configuration, but in the measured results this was not as obvious. This was caused by the rotation of the real elements, which allows for better null alignment and thus reduced coupling. In the simulations, the elements were simply translated and not rotated.

MVDR is one of the few beamformers available to CReSIS that allows for deep clutter suppression. As demonstrated by Figure 2.12 the small arrays of CReSIS do not possess sufficient degrees of freedom to achieve low sidelobes with a genetic algorithm. Similarly the results in this section suggest that the real six-element array is unable to achieve -30 dB sidelobe. This was in part due to mutual coupling with the surrounding structure and the small number of elements in the array. Deep clutter suppression can be achieved through null placement, as is done with MVDR. There are other beamformers capable of null formation; however, the performance of these beamformers, including maximum Signal-to-Interference Ratio (SIR), minimum mean square error, and point matching, are also dependent on the accuracy of the steering vector matrix [130]. It is noted that angle-of-arrival estimators such as Capon, linear prediction, and MUSIC will similarly be affected by array deformation [130]. Expanding the compensation presented in the next chapter to these other beamformer and angle-of-arrival estimators is possible. There is no comparable compensation method currently in open literature. MVDR was the focus of this work as it is the beamformer currently used in the CReSIS radar systems; however these are areas of future investigations.

10 COMPENSATING FOR FLEXURE ERRORS DUE TO AIRCRAFT INTEGRATION

10.1 Array Deformation Compensation

From Section 9 it is evident that the array deformation caused beam pointing errors, slight sidelobe increases, and null filling and shifting. Radiation patterns with MVDR weights applied were the most severely affected, and for this reason the compensation study will focus on this beamformer. As was mentioned in the previous chapter, wing deflection will similarly effect other beamformers capable of deep clutter suppress. The MVDR beamformer is the focus of this chapter as it the beamformer currently used in CReSIS radars. Future investigation can expand this same compensation method to the other beamformers as well as angle-of-arrival estimators. Correcting for mainbeam pointing errors is non-unique and has been demonstrated by applying appropriate phase shifts directly to each element [57]-[59]; however, the goal of this compensation is to restore pattern nulls. According to array theory [17], the displacement of the element can be added to the nominal array factor (AF) as an additional phase term (the magnitude change, $e^{-\alpha z}$, where α is the attenuation constant, is negligible) as follows

$$AF = \sum_{n=1}^m e^{jkd_n \sin \theta} e^{j\Delta\phi_n} \quad (10.1)$$

where d_n is the relative spacing between the n^{th} antenna and the reference antenna, k is the wave number, and $\Delta\phi_n$ is the n^{th} antenna's phase center error caused by its displacement. By adding this term to each element, phase center errors are corrected.

This dissertation work extends this principal to correct for the filling and shifting of nulls in the presence of wing flexure. Figure 10.1 shows that the phase shift of an incoming signal also has an angular dependency. Equation (10.2) gives the phase relationship between out of plane displacements and angle of arrival.

$$\Delta\phi_{i,j} = \frac{2\pi}{\lambda} z_i \cos(\theta_j) \quad (10.2)$$

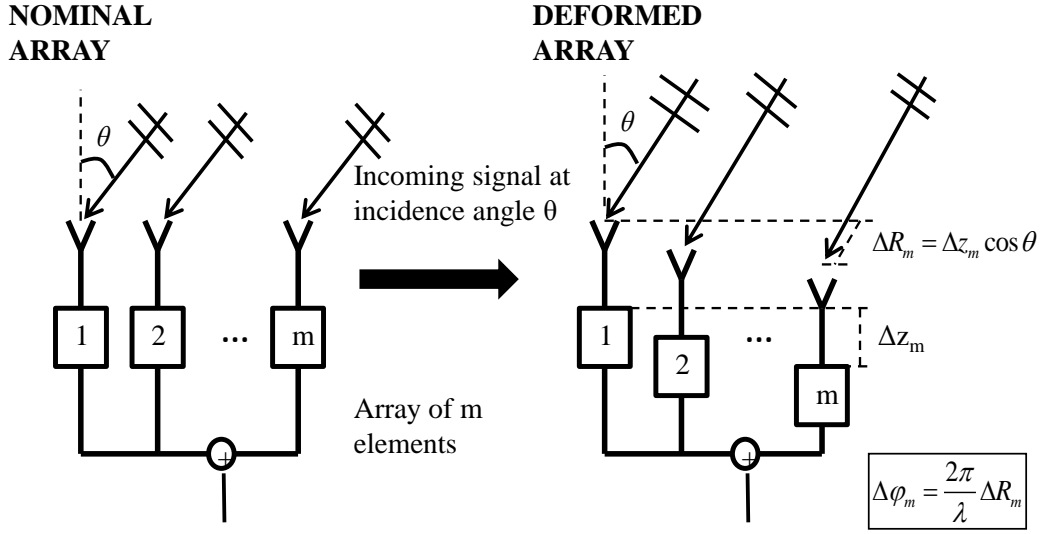


Figure 10.1: Phase Shift Due to Deformation

To correct for the phase center errors in the MVDR beamformer, corrected desired signal steering vector and interferer plus noise correlation matrix must be derived from the nominal steering vectors. By referring back to Equation (8.18), the phase compensation can be applied by modifying the desired signal steering vector and steering vector matrix. The modified steering vector and matrix can be found using equations (10.3) and (10.4), respectively.

$$\tilde{\mathbf{a}}_0 = \bar{\mathbf{a}}_0 * \Delta \phi_{0,j} \quad (10.3)$$

$$\tilde{\mathbf{A}} = \bar{\mathbf{A}}_{i,j} * \Delta \phi_{i,j} \quad (10.4)$$

In the above equations, $\tilde{\mathbf{a}}_0$ and $\tilde{\mathbf{A}}$ are the corrected desired steering vector and steering vector matrix which are found by multiplying the i,j entry in the original steering vector by the phase shift expected for the j^{th} antenna in the direction of the i^{th} signal. Figure 10.2 shows a flow chart for applying the compensation. Using this compensation method offers the advantage of only requiring one set of measurements for the antenna patterns. The absence of such a compensation would require continuous measurements of the radiation patterns.

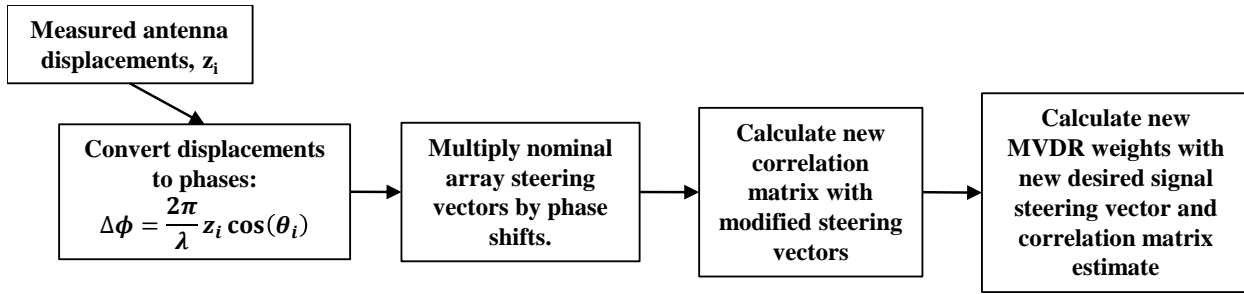


Figure 10.2: Compensation Flow Chart

10.2 Merit Figure

Before beginning a discussion of the impact of the compensation method, a figure for characterizing the ability to form nulls must be introduced. For the MVDR-weighted array, the ability of the compensation method to restore nulls is of greatest interest. Restoring a null consists of shifting the null back to its desired angle and restoring its depth. While these two quantities can be quantified individually, it is the combination of the two that is desired, and for this reason a figure of merit (FM) was derived as follows

$$FM = \frac{2.5A + B}{3.5} \quad (10.5)$$

where A and B are assigned a value between 1 and 0 based on the angle shift and null depth, respectively. Both the A and B values are referenced with respect to the nominal, undeformed array, and Table 10.1 and Table 10.2 give the values of A and B based on the change in pattern performance.

Table 10.1: Values of A Based on Pattern Null Shift from Desired Location

Null shift (deg)	≤0.5	(0.5, 1]	(1, 1.5]	(1.5, 2]	(2, 2.5]	(2.5, 3]	(3, 3.5]	(3.5, 4]	(4, 4.5]	(4.5, 5]	>5
Value of A	1	0.9	0.8	0.7	0.6	0.5	0.4	0.3	0.2	0.1	0

Table 10.2: Values of B Based on Reduction of Null Depth with Respect to the Nominal Array

Reduction in null depth (dB)	<5	(5, 10]	(10, 15]	(15, 20]	(20, 25]	>25
Value of B	1	0.8	0.6	0.4	0.2	0

Assigning a value to A and B based on the amount of change in null location and depth seemed to be the most appropriate way to combine the two characteristics to define a single merit figure. A shift in null location of 5° results in a much greater reduction in performance than a 5 dB decrease in null depth. Because nulls are generally very steep, a null shift of a couple degrees can increase the receive power in the clutter direction by as much as 30 dB.

The values assigned to A and B were based on qualitative assessments of the measurement results of how well the nulls were captured. Likewise, A was given a weighting factor of 2.5 as compared to B because null shifts result in a power increase at the desired null location, and thus it was determined that null location was a more important factor than null depth. Repeated iterations of varying A and B values and using the measured and simulated results, showed that the selected values appropriately captured the effectiveness of the compensation method to restore the nulls to their nominal location and depth. The denominator of 3.5 was selected to normalize FM such that $FM = 1$ means the null was completely restored, and $FM = 0$ means the null is indistinguishable. As seen in the figures in Chapter 10, some of the nulls are very deep, particularly in the undeformed array. For this reason, the nominal null depth was capped at -50 dB when appropriate.

An analysis of the FM was performed by recording the FM, null angular shift, and null depth change for over 100,000 null combinations. Analysis of the FM using the real data showed that FM values of 0.8 and higher will have a null depth of at least -30 dB a null shift less than 1.5° . In addition, the analysis demonstrated that a 0.1 increase of FM results, on average, in a 0.6° null shift toward nominal and a 1.5 dB increase in null depth. An FM of 0.2 or less will have at least a 4° null shift and null depth less than 20 dB.

This FM was derived to quantify both the shifting of the nulls as well as the reduction in null depth as a result of aircraft integration effects, and it is used as a “goodness-of-fit” performance figure. This FM was derived specifically for application for the studies in the following sections and should not be abstracted for use for other purposes.

In addition to the FM the experimental SINR will also be used to quantify the effectiveness of the compensation method. The experimental SINR will be determined from the resultant array radiation pattern, and assumes that the desired and interference signal have the same power. In practice, the desired bed echo signal and the clutter signal are rarely of equal power, which is why the SINR has been labeled “experimental”. However improvements in SINR will be

realized since it is a relative measurement. The experimental SINR and FM are performance figures that aim to capture how wing flexure and control surface deflection affect null formation and how much the results deviate from the nominal pattern.

10.3 Simulation Results

The following plots compare the ideal, or nominal, pattern (black), the uncompensated pattern (red), and the pattern with compensation (blue) described in Section 10.1. For the sake of a fair comparison the same set of nulls will be presented as were presented in Section 9.3 and 9.4. Only two displacement levels, $\alpha = 1$ and $\alpha = 2$, will be presented. Each figure is a side by side comparison of the parallel and collinear array at a single displacement level. Figure 10.3 and Figure 10.4 compare the simulated uncompensated and compensated patterns for $\alpha = 1$ and $\alpha = 2$, respectively, and nulls applied at $\pm 40^\circ$.

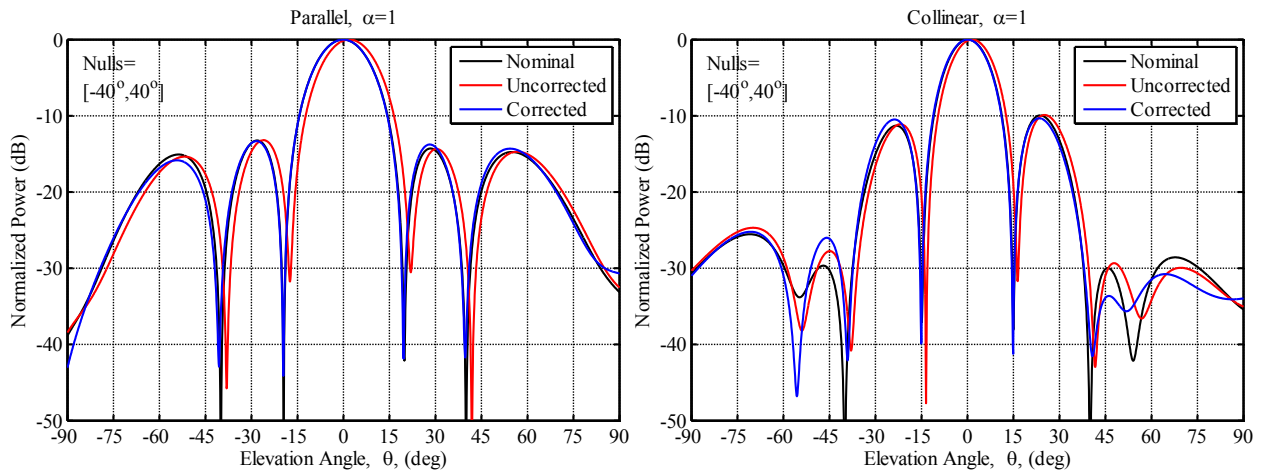


Figure 10.3: Comparison of Uncompensated and Compensated Simulated Array Patterns with MVDR Weights, $\alpha=1$, and Nulls at $\pm 40^\circ$

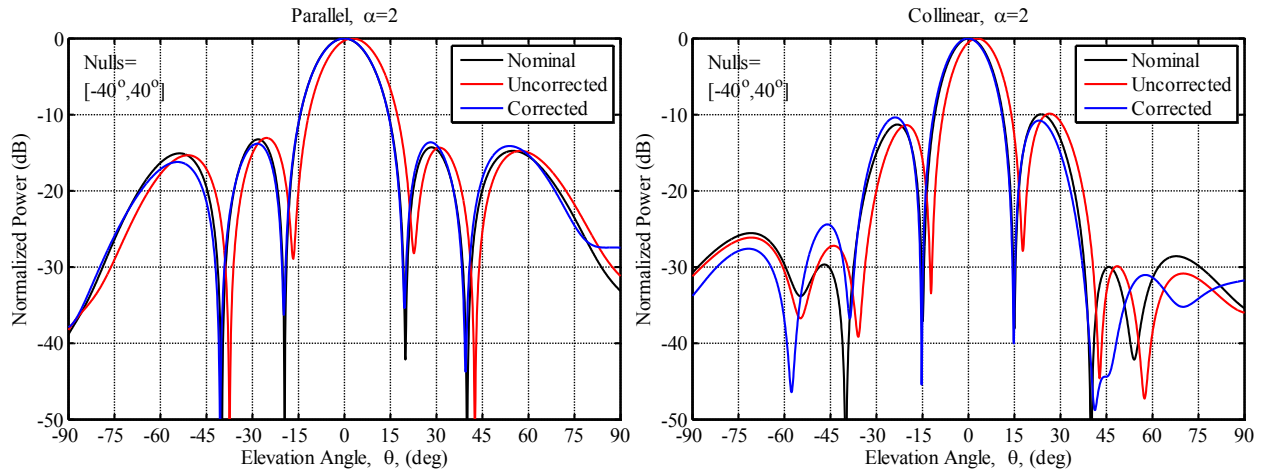


Figure 10.4: Comparison of Uncompensated and Compensated Simulated Array Patterns with MVDR Weights, $\alpha=2$, and Nulls at $\pm 40^\circ$

From the figures it can be seen that the compensation worked very well in recovering the nulls for all cases. For the parallel array the compensation improved the FM by an average of 0.20 and the SINR by almost 10 dB. In the case of the collinear array the compensation improved the FM by an average of 0.23 and the SINR by 7.6 dB. Though the goal of the compensation is to recover the nulls, it is also effective in correcting pointing errors.

Figure 10.5 and Figure 10.6 show the patterns for nulls at $\pm 70^\circ$. These figures suggest that the compensation method is less effective at larger angles (angles greater than $\pm 55^\circ$), which is likely caused by the displaced pattern diverging from the nominal pattern near endfire. The compensation increased the FM of the parallel array by an average of 0.06, and improved the average FM of the collinear array by less than 1%. Though the average SINR change is negative across all nulls, the SINR is at least 35 dB in all cases after compensation. One-way spatial sidelobes of -35 dB or lower are required to reduce cross-track surface-clutter. Surface clutter can occur at any elevation angle, but in general clutter angles are larger than $\pm 50^\circ$. Though the compensation did not significantly improve the null formation, pattern characteristics did not degrade below acceptable levels.

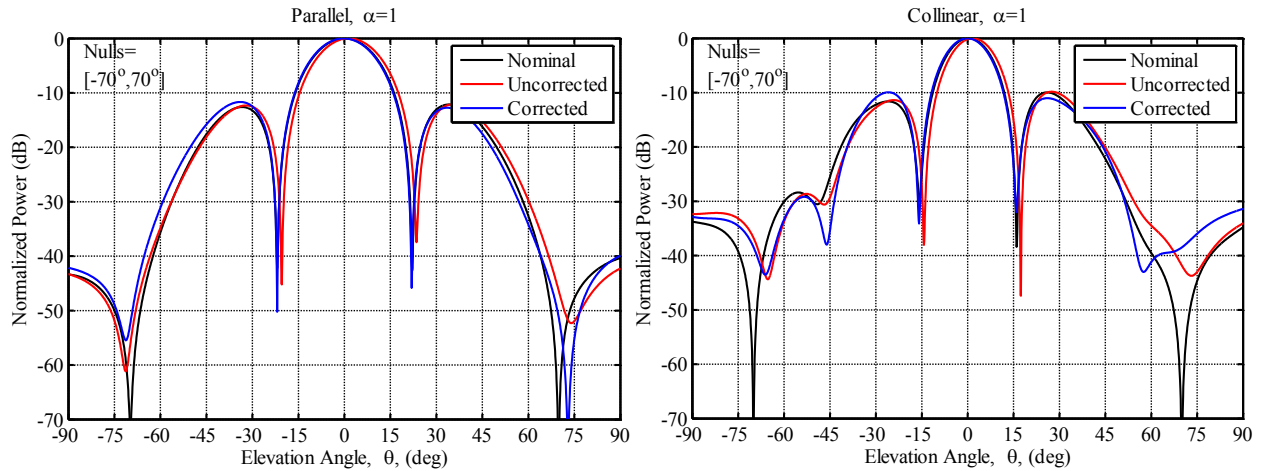


Figure 10.5: Comparison of Uncompensated and Compensated Simulated Array Patterns with MVDR Weights, $\alpha=1$, and Nulls at $\pm 70^\circ$

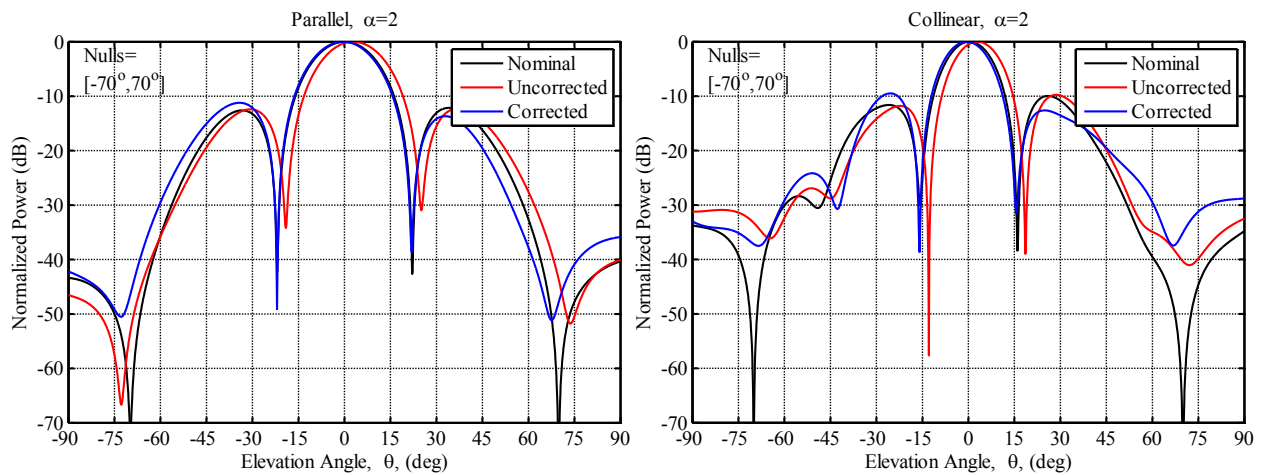


Figure 10.6: Comparison of Uncompensated and Compensated Simulated Array Patterns with MVDR Weights, $\alpha=2$, and Nulls at $\pm 70^\circ$

Figure 10.7 and Figure 10.8 compare the uncompensated and compensated radiation patterns with asymmetric nulls applied at -54° and 50° degrees. Again the compensated patterns achieved nulls that were at the desired angles, but there is some loss in null depth as compared to the nominal pattern (as much as 10 dB). Average SINR increase across all nulls with the compensation was 4.8 dB, and average FM increase was 0.16. In all cases the FM of the compensated array was at least 0.63 whereas the FM of the uncompensated array was as low as 0.41.

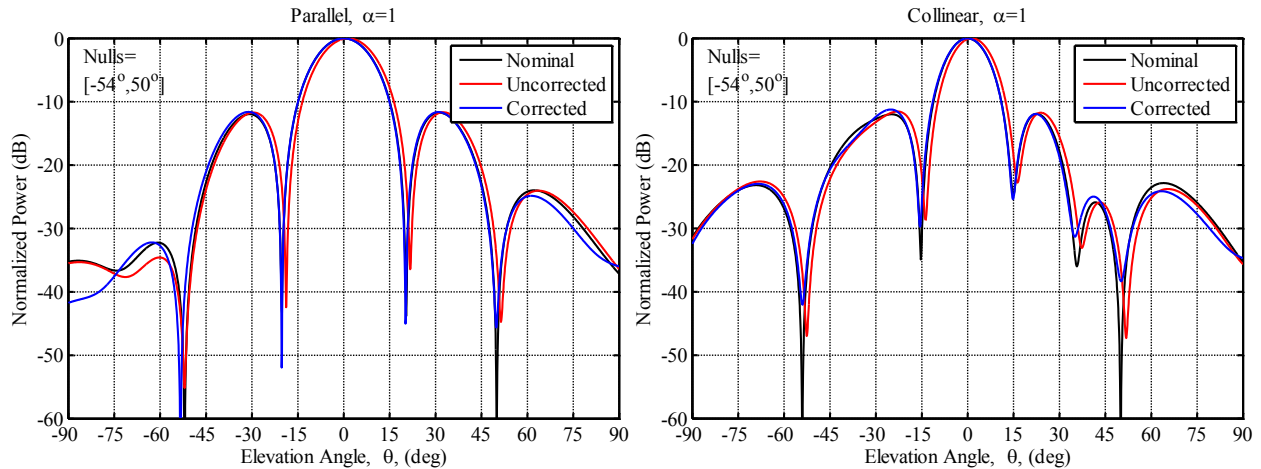


Figure 10.7: Comparison of Uncompensated and Compensated Simulated Array Patterns MVDR Weights, $\alpha=1$, and Asymmetric Nulls at -54° and 50°

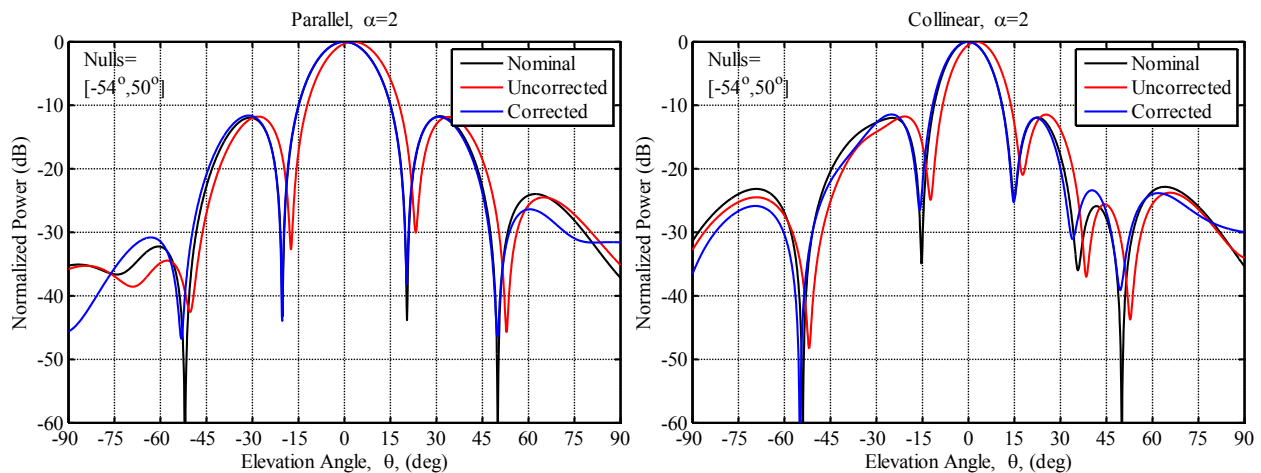


Figure 10.8: Comparison of Uncompensated and Compensated Simulated Array Patterns MVDR Weights, $\alpha=2$, and Asymmetric Nulls at -54° and 50°

Overall the simulated results show that the corrected pattern performed better than the uncorrected pattern, though the compensation method seems to be less effective at larger elevation angles. For the small and asymmetric null patterns the average FM increase was between 0.16 and 0.23, whereas the average FM increase for the large angle null patterns was less than 10%. Similarly, the average SINR increase for patterns with small and asymmetric angles was 6.7 dB, while on average the compensation did not increase SINR for patterns with large angles. However the SINR was at least 35 dB in all cases after compensation. In almost 40% of the cases analyzed the compensation increased the SINR by at least 6 dB (or a factor of 4), and in 75% of the cases the compensation increased the SINR by at least 3 dB (or a factor of

2). The next section presents the results of the compensation when applied to the real array measurements.

10.4 Measurement Results

Figure 10.9 and Figure 10.10 compare the uncorrected and corrected patterns of the real array when nulls are placed at $\pm 40^\circ$ for $\alpha = 1$ and $\alpha = 2$, respectively. In all four plots the compensation was nearly able to fully restore the nulls in all cases. There is some depth reduction in the larger displacement case (7-9 dB). Without the compensation the FM was as low as 0.33, but with the compensation with FM was at least 0.87. The maximum FM improvement was 0.67, and on average the improvement was 0.33. The experimental SINR was greater than 41 dB with the compensation and 22 dB without it. On average the SINR was increased 12.8 dB, and the maximum increase was over 20 dB

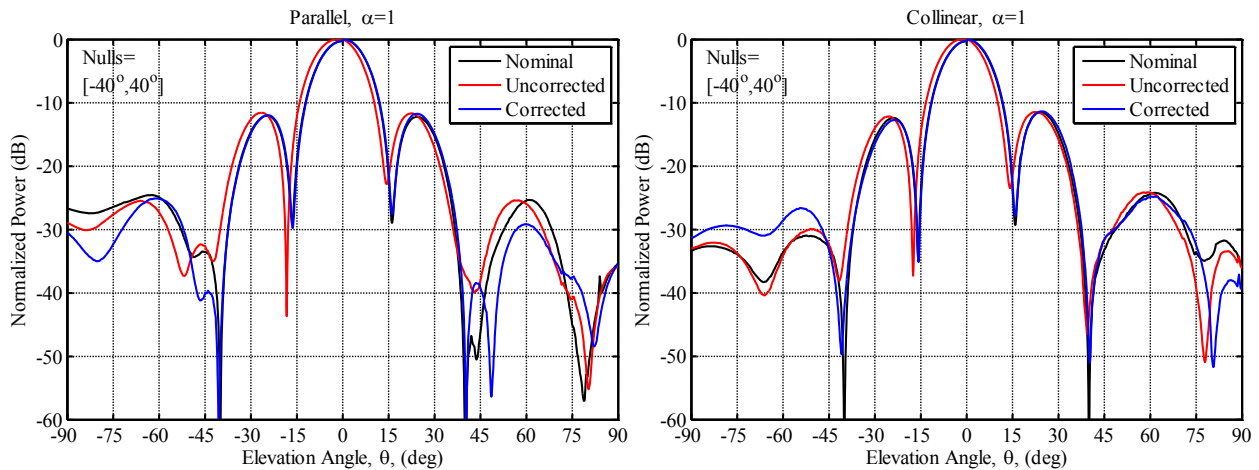


Figure 10.9: Comparison of Uncompensated and Compensated Measured Array Patterns with MVDR Weights, $\alpha=1$, and Nulls at $\pm 40^\circ$

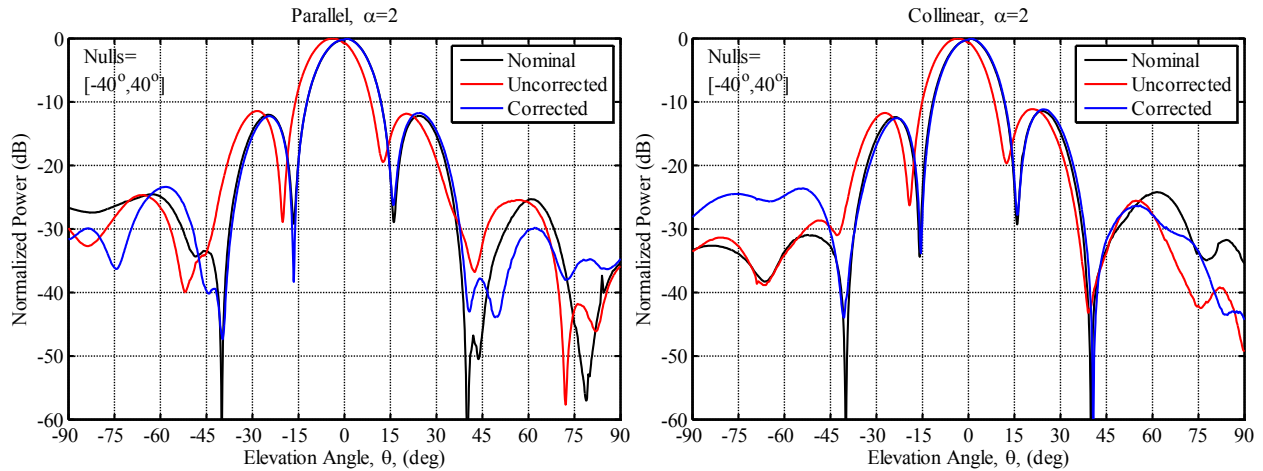


Figure 10.10: Comparison of Uncompensated and Compensated Measured Array Patterns with MVDR Weights, $\alpha=2$, and Nulls at $\pm 40^\circ$

Figure 10.11 and Figure 10.12 present the radiation patterns for the larger elevation angle case ($\pm 70^\circ$). These results correlate with the simulated results in that the compensation method seems to be less effective at larger angles, though it does appear that the real corrected patterns were much better than the simulated corrected patterns. On average the compensation increased the FM by 0.09 for the parallel array and 0.2 for the collinear array, compared to 0.06 and less than 1% for the simulated arrays. Though the SINR decreased in some cases, in all instances the SINR was at least 33 dB with the compensation.

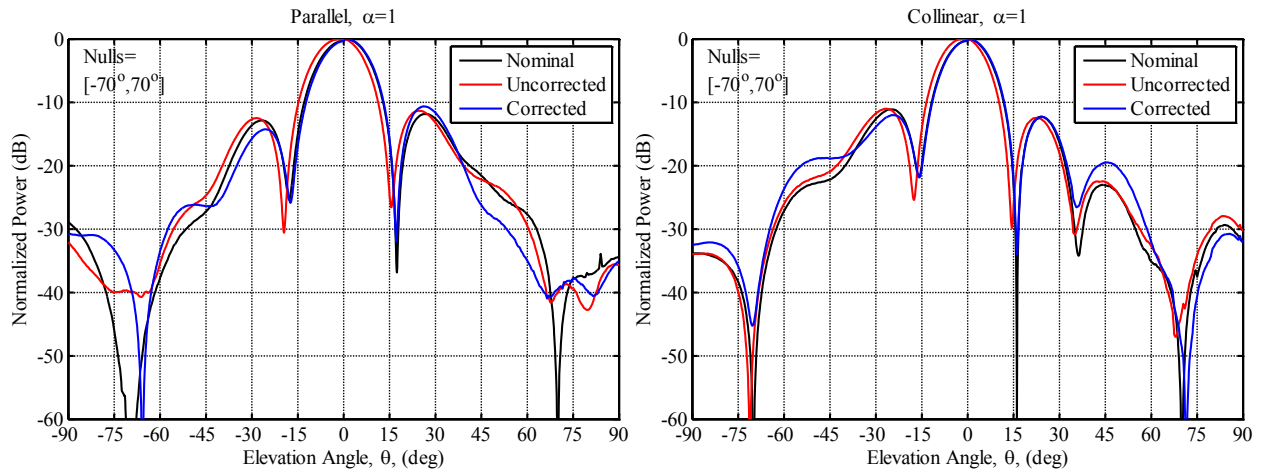


Figure 10.11: Comparison of Uncompensated and Compensated Measured Array Patterns with MVDR Weights, $\alpha=1$, and Nulls at $\pm 70^\circ$

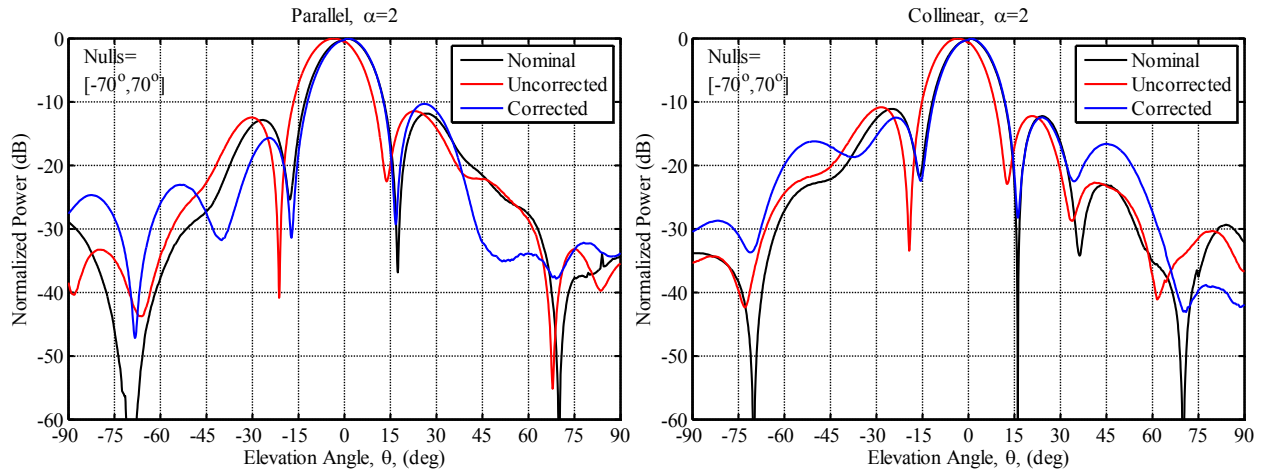


Figure 10.12: Comparison of Uncompensated and Compensated Measured Array Patterns with MVDR Weights, $\alpha=2$, and Nulls at $\pm 70^\circ$

Figure 10.13 and Figure 10.14 compare the radiation patterns with asymmetric nulls applied at -54° and 50° . Similar to the simulated results, the compensation was nearly able to fully recover all the nulls. For all cases the FM with compensation was at least 0.8, whereas the FM was as low as 0.44 without it. For the parallel array the compensation improved the experimental by an average of 13.2 dB. For the collinear array the average improvement was only 4.6 dB. Without the compensation, the experimental SINR was as low as 23.9 dB, but SINR was at least 36 dB with compensation.

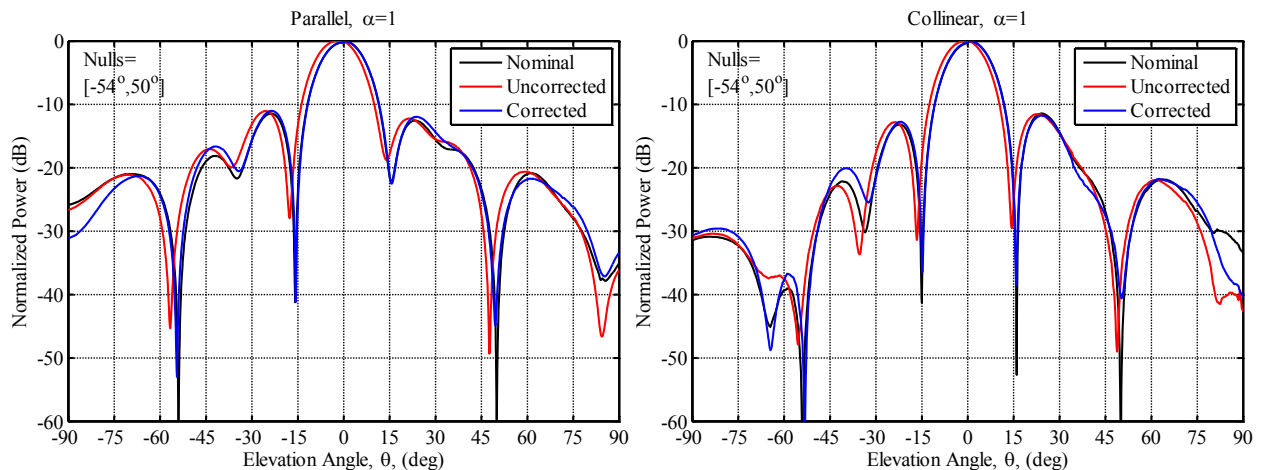


Figure 10.13: Comparison of Uncompensated and Compensated Measured Array Patterns with MVDR Weights, $\alpha=1$, and Asymmetric Nulls at -54° and 50°

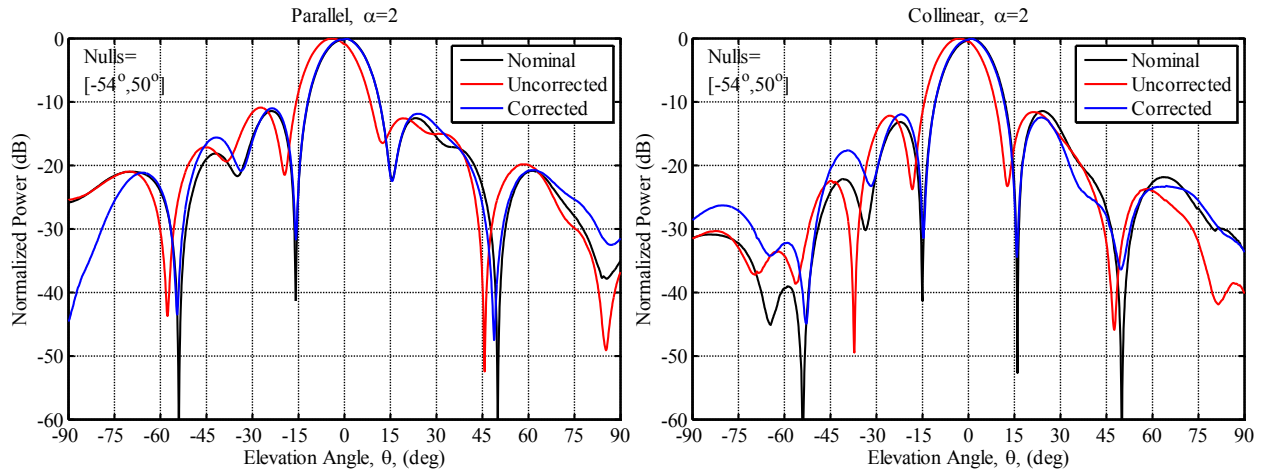


Figure 10.14: Comparison of Uncompensated and Compensated Measured Array Patterns MVDR Weights, $\alpha=2$, and Asymmetric Nulls at -54° and 50°

Overall, the measured results agree with the trends seen in the simulated results. The compensation method works very well for small elevation angles (smaller than $\pm 55^\circ$), but is less effective for larger angles (greater than $\pm 55^\circ$). For the patterns with nulls at $\pm 40^\circ$ and asymmetric nulls, the compensation improved SINR by a minimum of 2 dB for all cases. On average the SINR was improved by 10.6 dB for these patterns. For the pattern with nulls at $\pm 70^\circ$ the compensation sometimes decreased SINR; however, the SINR was at least 33 dB for all cases. FM was increased by an average of 0.29 for small angle cases and 0.14 for large angle cases. The reduced effectiveness of the compensation method will be explained in the next section.

The results presented in this section and the previous are very limited with regards to the total number of prescribed null permutations. The following sections will explain why the compensation method is less effective at larger angles, as well as attempt to characterize the compensation method for broader application.

10.5 Limitations

10.5.1 *Discussion of Limitations*

The ability of the compensation method to restore nulls resides in its ability to accurately correct the steering vectors. Figure 10.15 shows the six collinear element phases for the scaled model array with displacement levels of $\alpha = 0$ (black), $\alpha = 1$ (red), and $\alpha = 2$ (blue). The phase shift of each element across all elevation angles is evident in the plot, and as expected the shift is

larger for the outboard antenna (P6) than for the inboard antenna (P1). Figure 10.16 shows the same element phases after the correction of Equation (10.2). Despite the compensation, it can be seen that the phases of some elements can vary by as much as 50° at angles larger than $\pm 55^\circ$.

The variation in the phase after the correction is caused by changes in mutual coupling as the array deforms. There are two sources of mutual coupling. One component of the coupling is caused by the interaction between the antenna elements. The second component of mutual coupling is caused by the interaction between each antenna element and the surrounding structure. The fields radiated by the antenna elements will induce a current on any conductive element near the antenna. This induced current will in turn radiate back towards the antennas, thus altering the overall radiation pattern of the elements. Near-field scatterers with sharp corners and edges will have a larger coupling effect on the antennas.

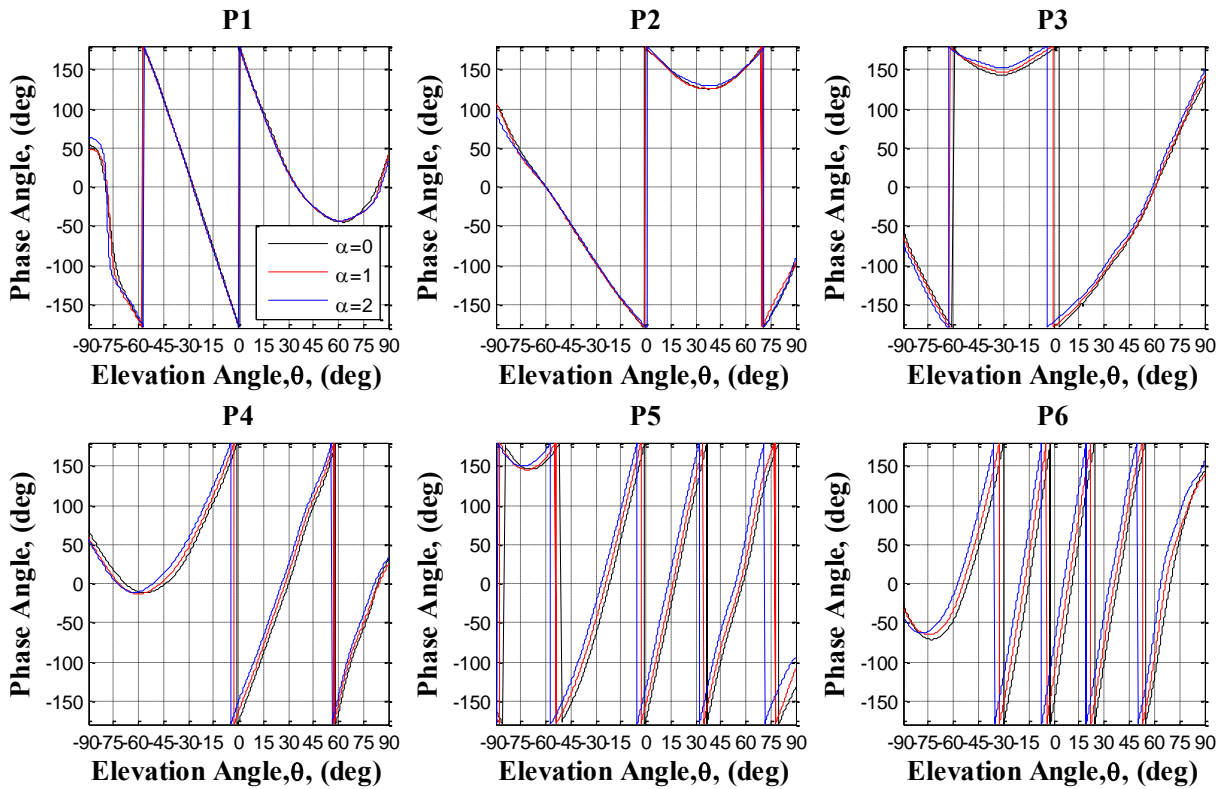


Figure 10.15: Scaled Model Phases of Each Element for Displacement Cases $\alpha = 0$, $\alpha = 1$, and $\alpha = 2$

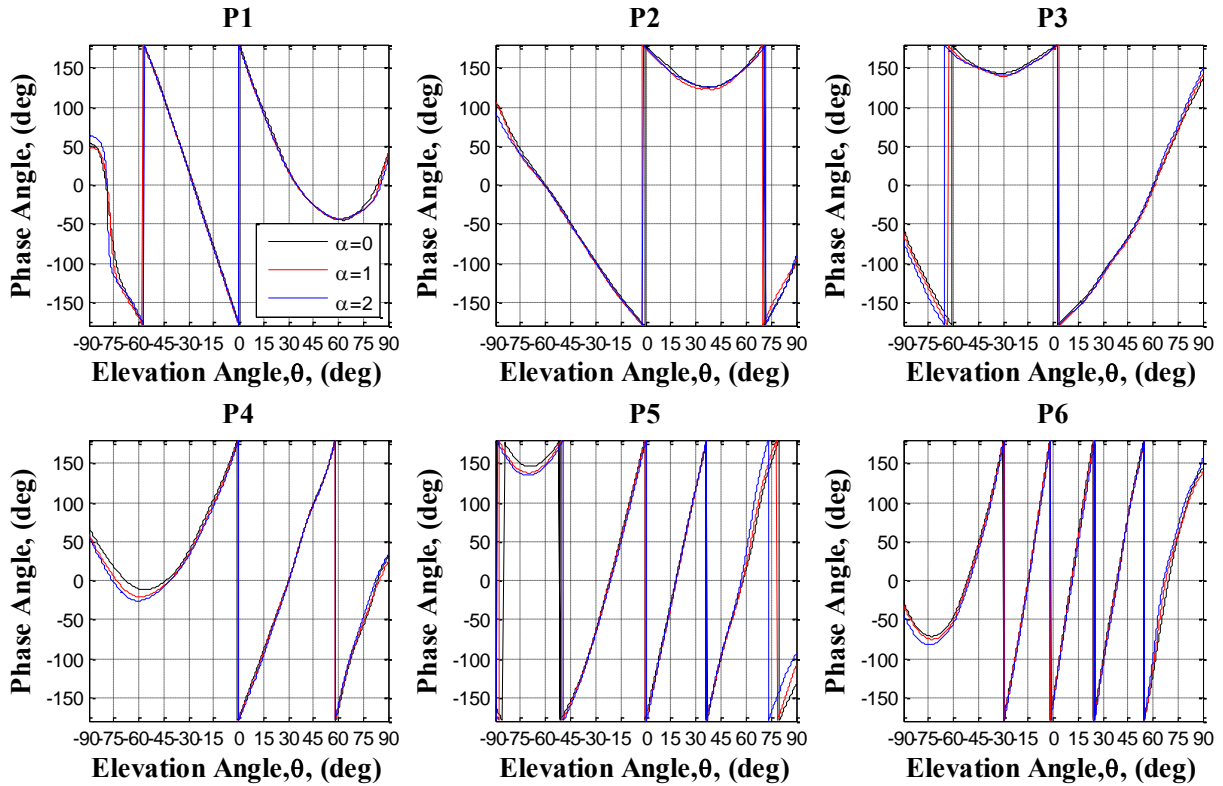
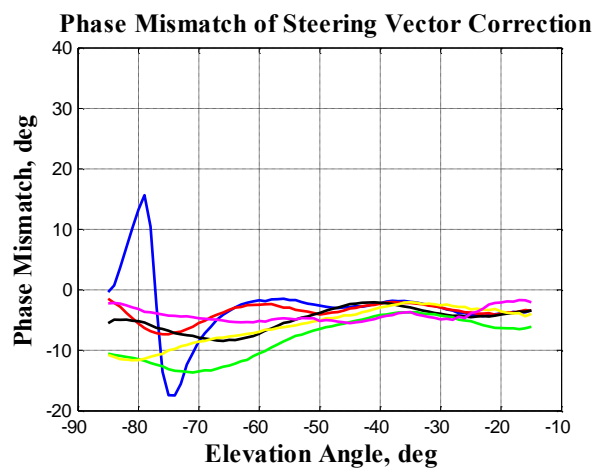
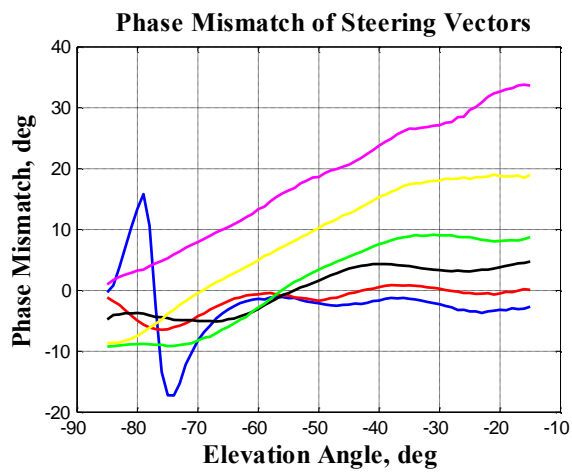
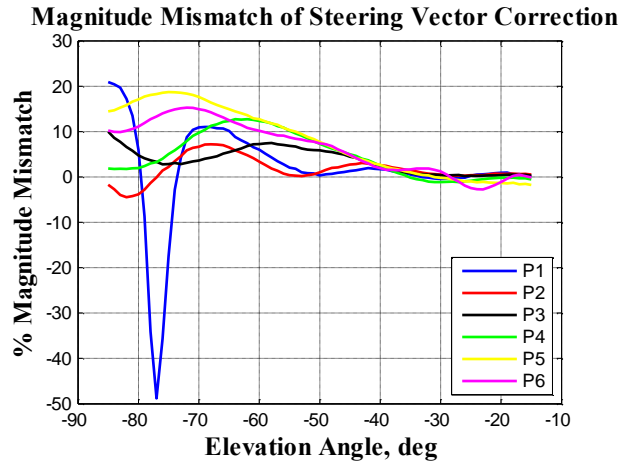
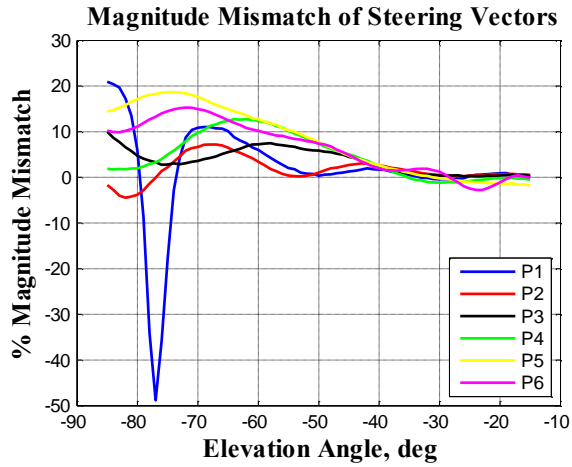


Figure 10.16: Scaled Model Corrected Phases of Each Element for Displacement Cases $\alpha = 0$, $\alpha = 1$, and $\alpha = 2$

To demonstrate the effects of mutual coupling, Figure 10.17 shows the $\alpha = 1$ collinear array steering vector magnitude and phase mismatch for each port. The plots on the left show the amplitude and phase mismatches before the compensation is applied, and the plots on the right show the mismatches after the compensation is applied. Figure 10.18 shows the same thing as Figure 10.17, except for positive elevation angles. The mismatches are shown for elevation angles between 15° - 85° because generally it is not desirable to place nulls outside of this range.

The irregular response of P1 is caused primarily to due to its close proximity to the control surface horn and its interaction with this component. Original simulations of the scaled array did not include the fastener in the control horns. However, when abstract nuts and bolts were added to the simulation, the amplitude mismatch of P1 at large negative angles increased by 20% and its phase mismatch decreased by 6° .



a) before correction

b) after correction

Figure 10.17: Phase and Magnitude Mismatch Between Ideal and Actual Steering Vector before (a) and after (b) Compensation for Negative Elevation Angles

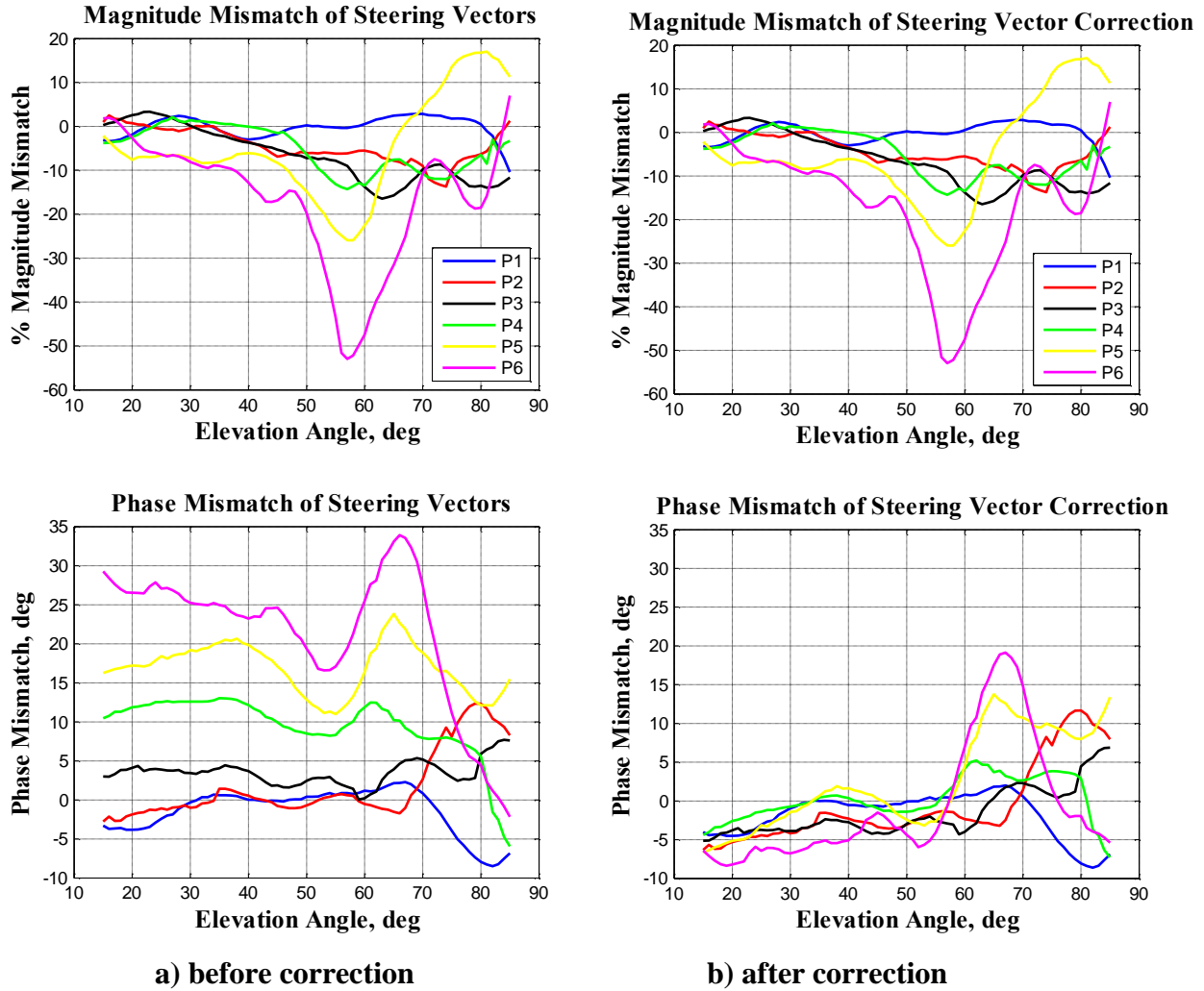


Figure 10.18: Phase and Magnitude Mismatch Between Ideal and Actual Steering Vectors before (a) and after (b) Compensation for Positive Elevation Angles

In both Figure 10.17 and Figure 10.18 large magnitude ($> 50\%$) and phase (20°) mismatches occur at large elevation angles even after the compensation is applied. To ensure that these variations were not caused during the experimental process, Figure 10.19 shows the simulated phase and magnitude mismatches of the scaled model array. Figure 10.19a agrees with the large phase and magnitude mismatch of P1 at large negative angles, and Figure 10.19b agrees with large magnitude and phase mismatches for P5 and P6 at large positive angles. These large variations must be due to changes in mutual coupling, particularly the changes in coupling between the antennas and the surrounding structure. To support this claim it is noted that in the original simulations of the scaled model array the control horn fasteners were omitted from the simulation. As stated previously, when abstract nuts and bolts were added to the simulation, the

magnitude mismatch of P1 at large negative angles increased by 20% and its phase mismatch decreased by 6° . In addition the phase mismatches of P5 and P6 increased by 5° and 2° , respectively, when the hardware was added to the model.

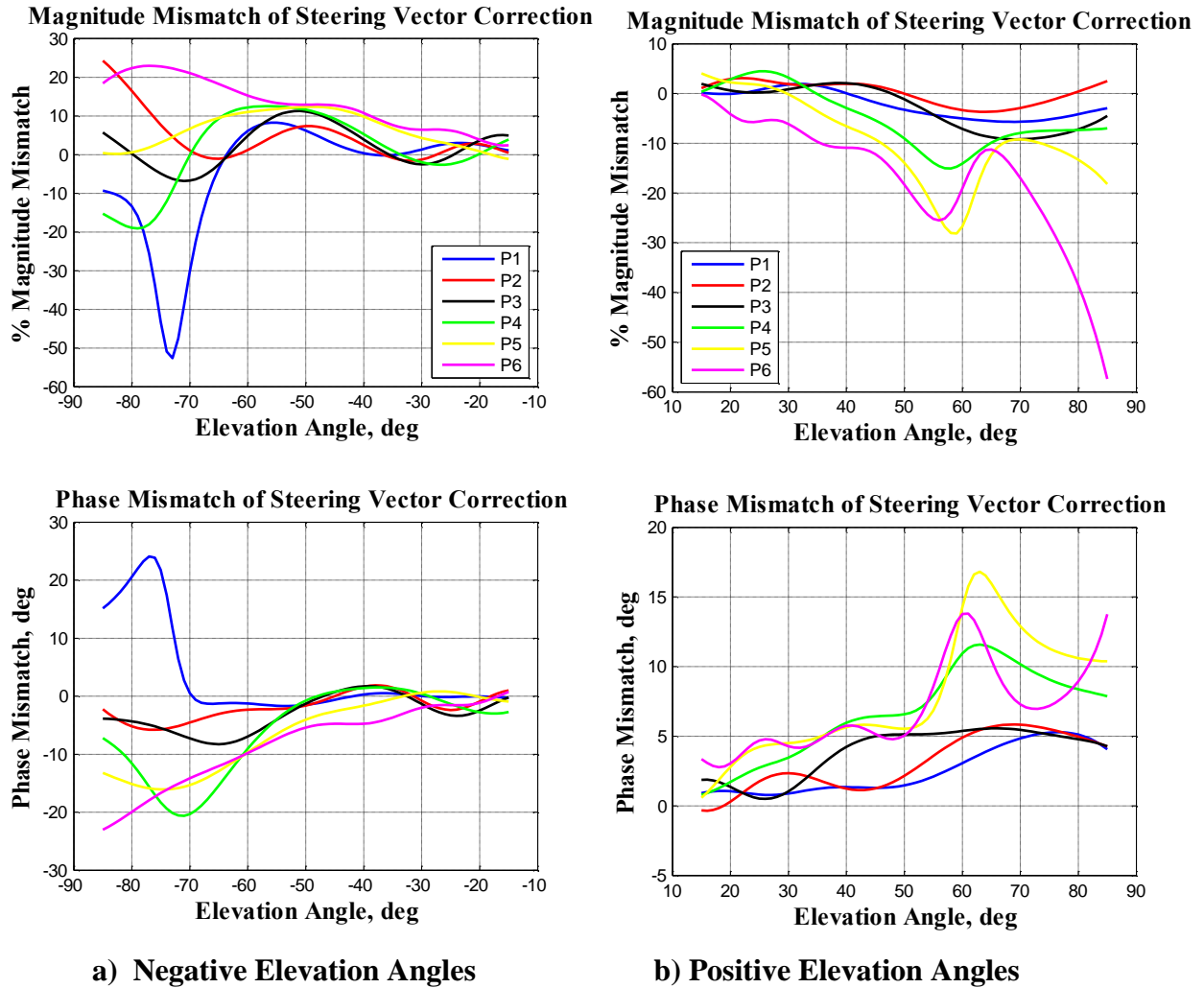


Figure 10.19: Simulated Scaled Model Magnitude and Phase Mismatches for Negative Angles (a) and Positive Angles (b)

To further support the claim that changes in coupling between the antennas and surrounding structure can cause large phase and magnitude mismatches in the array pattern, Figure 10.20 shows the steering vector mismatches in the full scale Twin Otter antenna-array when only the antennas are modeled. As the figure shows, in the absence of near-field scatterers magnitude and phase mismatches were kept within 3 percent and degrees, respectively.

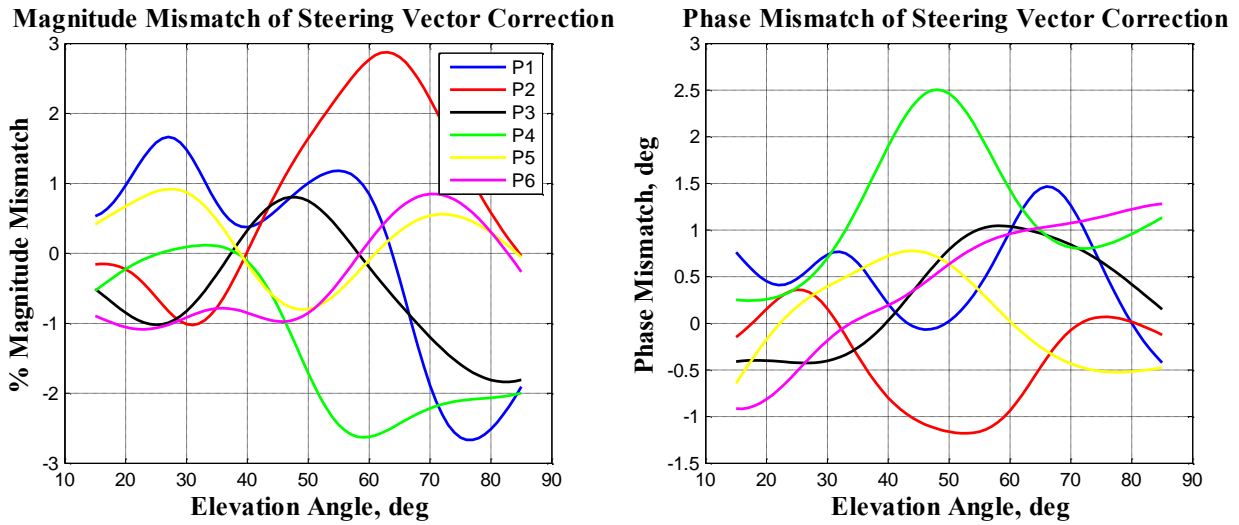


Figure 10.20: Steering Vector Magnitude and Phase Mismatches from Twin Otter Antenna Only Simulations

To demonstrate the compensation method’s ability in the absence of mutual coupling, Figure 10.21 shows the simulated results of a deformed array with and without the compensation applied. As the figure shows, without mutual coupling effects between antennas and the surrounding structures the compensation method is able to fully recover the nulls as well as eliminate pointing errors even at large angles. The compensation in the absence of mutual coupling resulted in an FM of 1 and SINR of 50 dB (maximum for both values). Though there is pattern deviation outside of the mainbeam and null angles, these deviations are not concerning as the purpose of the compensation is to achieve deep clutter suppression at prescribed angles.

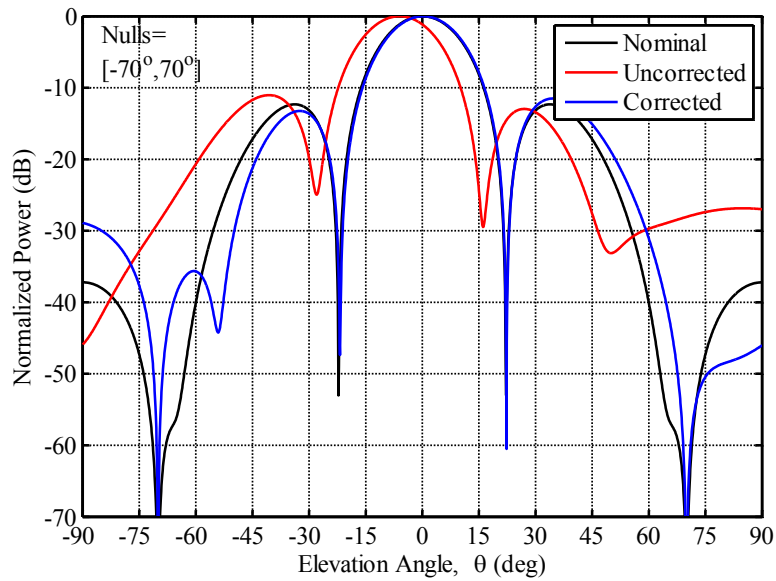


Figure 10.21: Compensation Method Ability without Mutual Coupling Effects

10.5.2 *Sensitivity Analysis of Compensation Method to Steering Vector Errors*

To examine the compensation method's sensitivity to steering vector magnitude and phase mismatches a series of Monte Carlo Simulations were performed using the collinear, $\alpha = 1$ scaled model data. Results for the parallel array can be found in Appendix C, but they will be found to be very similar to what is presented in this section. The simulations were performed by randomly applying magnitude and phase variations to all six elements of the array within a prescribed range. The magnitude and phase variations were simultaneously varied from 0 to ± 15 percent and degrees, respectively. For each combination of magnitude and phase variation 1,000 simulations were performed. For each of the 1,000 simulations, a null angle was randomly assigned between 15° and 85° . To characterize the performance of the compensation method, the figure of merit described in Section 10.2 as well as the experimental SINR were used. The experimental SINR was determined from the resultant array radiation pattern, and assumes that the desired and interference signal have the same power. For each magnitude/phase combination an average FM and SINR were calculated from the 1,000 simulations. Figure 10.22 shows the FM, as well as the standard deviation of the FM results, as a function of steering vector phase and magnitude mismatch. As expected the FM decreases as mismatches increase. When the magnitude mismatch is 15% the FM decreases by roughly 40% regardless of the phase mismatch. The standard deviation of the FM distribution increases as mismatches increase. When magnitude and phase errors were maximized the variation in the measurement was about 30% of the expected value.

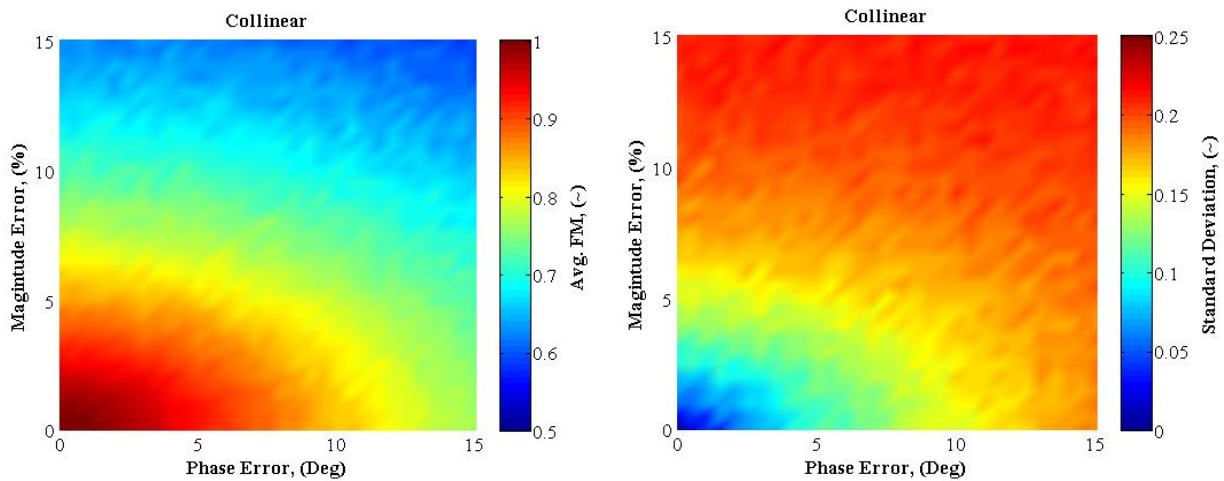


Figure 10.22: Collinear Array FM Sensitivity for Steering Vector Magnitude and Phase Mismatch (left) and Sensitivity Standard Deviation (right)

Figure 10.23 shows the experimental SINR and its standard deviation as a function of steering vector magnitude and phase errors. For the simulations the SINR was capped at 50 dB. Similar to the FM results the SINR also decreases as the errors increase. When magnitude errors are at least 15% and phase errors are at least 15° , the SINR drops by 20 dB. Unlike the FM distribution, the standard deviation for the SINR remains fairly constant across all magnitude and phase variations. From the plot, it is evident that standard deviation remains between 7 and 8 dB.

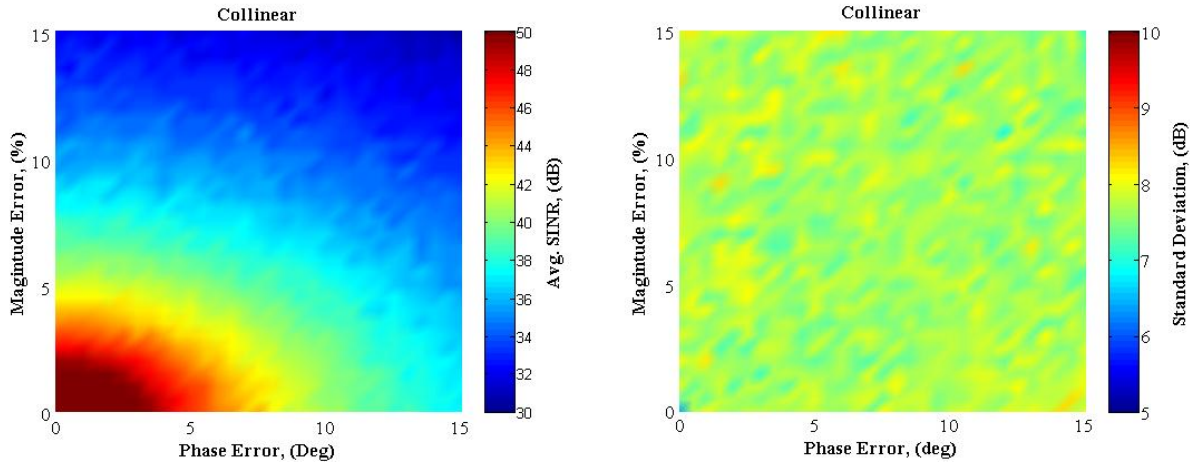


Figure 10.23: Collinear Array Experimental SINR Sensitivity for Steering Vector Magnitude and Phase Mismatch (left) and Sensitivity Standard Deviation (right)

10.5.3 *Summary of Compensation Limitations*

The compensation method's ability to restore nulls lost by array deformation resides in its ability to accurately predict the deformed array's steering vectors and thus also the interference plus noise correlation matrix. In an ideal array, deformations cause only relative phase shifts in the elements, but in a real array where mutual coupling is present, both magnitude and phase changes occur. It is well known that mutual coupling can affect the performance of adaptive arrays [129], [130]. From the results in Section 10.3 and 10.4 it was apparent that the compensation method was less effective at large angles (greater than $\pm 55^\circ$). The plots in Figure 10.17 through Figure 10.19 show a trend for larger phase and magnitude mismatches at larger elevation angles. These large variations in phase and magnitude are caused by changes in the mutual coupling, especially in coupling changes between the antennas and near-field structures. This statement is supported by the plots in Figure 10.20 where, in the absence of support structure, phase and magnitude mismatches were within 3 degrees and 3 percent.

In [131] the authors studied the effects of mutual coupling on array radiation patterns. They found that the pattern deviations, as compared to the ideal array, due to mutual coupling grow significantly as elevation angles increase (less than 1 dB deviation for angles smaller than $\pm 15^\circ$ to more than 10 dB at 70°). In addition they found that pattern deviation is almost double for arrays with fewer elements (8 elements) as compared to arrays with a greater number of elements (32 elements). It can be reasoned that if pattern deviations are greater at larger angles as compared to smaller angles due to the presence of mutual coupling, then the array response at larger angles will also be more sensitive to changes in mutual coupling.

The major limitation of the compensation method is that it only accounts for phase shifts due to array deformation and does not consider magnitude and phase changes caused by changes in mutual coupling. This leads to the question, why not compensate for mutual coupling as well? The answer to this question is that rigorous computation or continual array response measurements are required. To fully capture the effects of mutual coupling in the array, full 3D wave analysis (like that performed by HFSS[®]) would be required for every orientation of the array. For a wing-mounted array where both the antennas and wings are constantly deforming, an infinite number of simulations would be required to completely capture the physics of the problem. A well characterized test subset spanning the variable parameters of a complex study could be an area for future academic study, but is not likely to result in practical real-time correction.

Array measurements would also contain information about the mutual coupling as the effects of coupling are inherent in the element pattern information. But once again, fully accounting for the changes in coupling would require continuous measurement of the patterns. For airborne arrays flying over the most remote locations on the planet, continual pattern measurements are not feasible.

The advantage of the method presented here is that it can be readily applied to any array, as long as array deformations can be provided, and it only requires a single measurement of element patterns. The next section presents the expected performance increase in beam formation with the implementation of the compensation method. As will be shown, despite the fact that the method does not include coupling effects, it produces a significant performance increase.

10.6 Expected Performance Increase

To characterize the expected performance increase offered by the compensation method, once again FM and experimental SINR will be used. The plots presented in Section 10.3 and 10.4 offered some insight as to the effectiveness of the compensation method. This section aims to characterize the effectiveness of the compensation for broader application. To do so the FM and experimental SINR before and after compensation were calculated for cases of one, two and three pattern nulls using the real data from the scaled model measurements. In the cases of multiple nulls the average values are presented. The results have been divided into two plots. One plot presents results for nulls placed below $\pm 55^\circ$, and the other presents results for nulls placed at all angles (all angles meaning between the range of 15° - 85° , as stated early it is generally not desirable to place nulls outside this range). This was done to segregate performance in a region where the compensation is expected to perform very well from that of the overall performance. Only results for the collinear array with one and three nulls will be presented in this section. Results for two nulls and for the parallel array can be found in Appendix B.

Figure 10.24 and Figure 10.25 show the FM and experimental SINR, respectively, for the array with a single null. The top plots in the figures show results for the uncompensated array and the bottom plots show the results for the compensated array. In all cases the compensation method offers a visually obvious improvement, regardless of angle. A quantitative assessment of the improvement is presented at the end of this section.

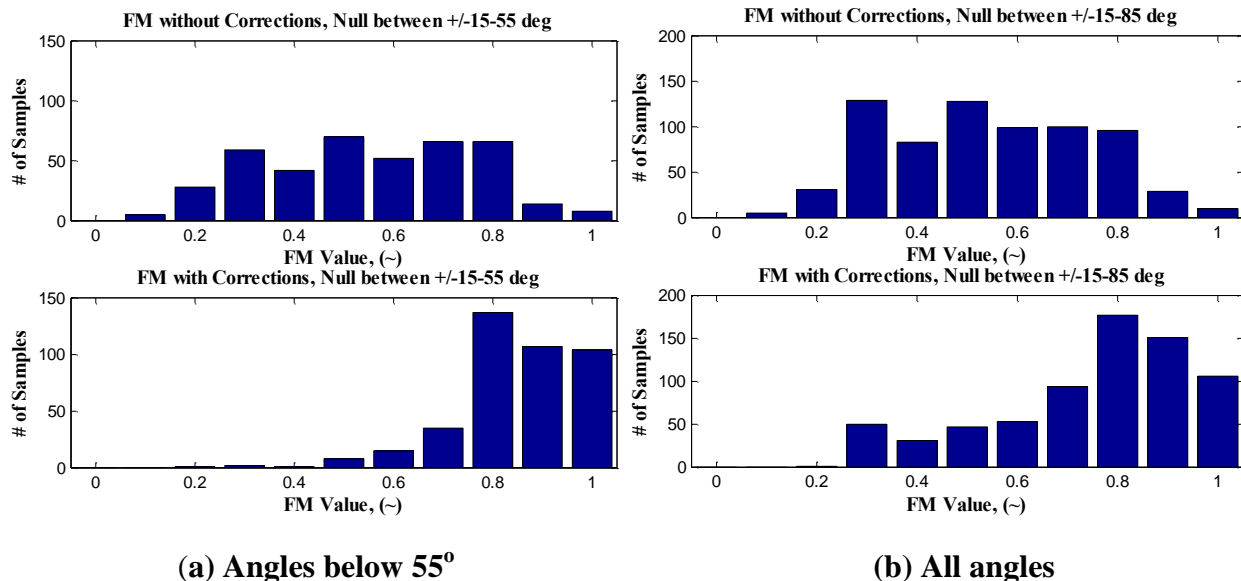


Figure 10.24: Comparison of Collinear Array FM for One Null Placed Below 55° (a) and at All Angles (b)

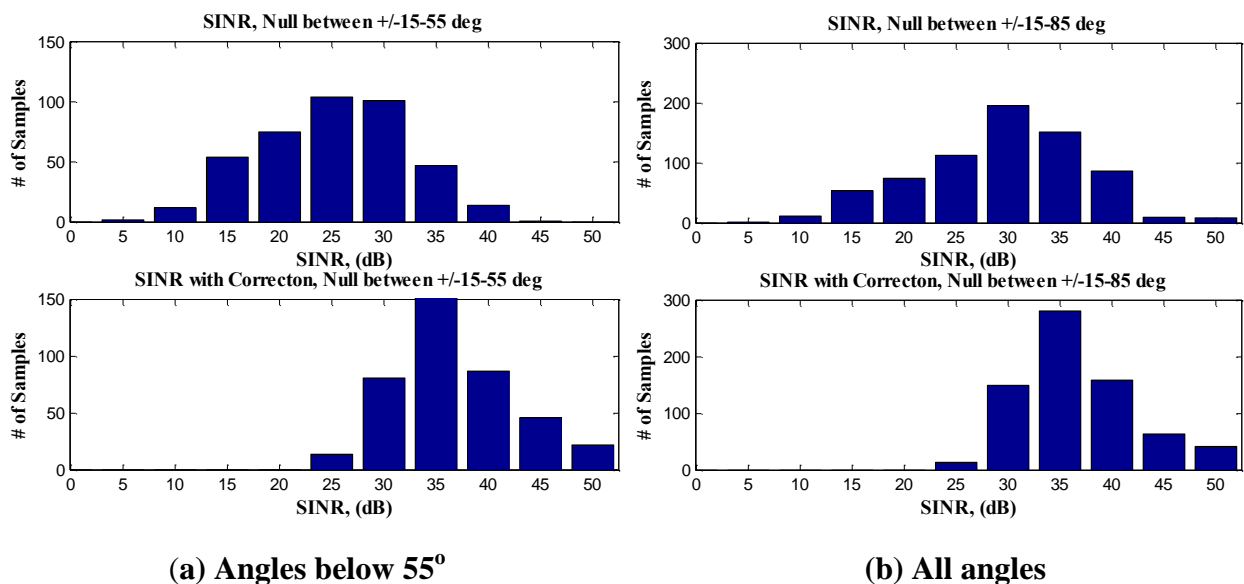
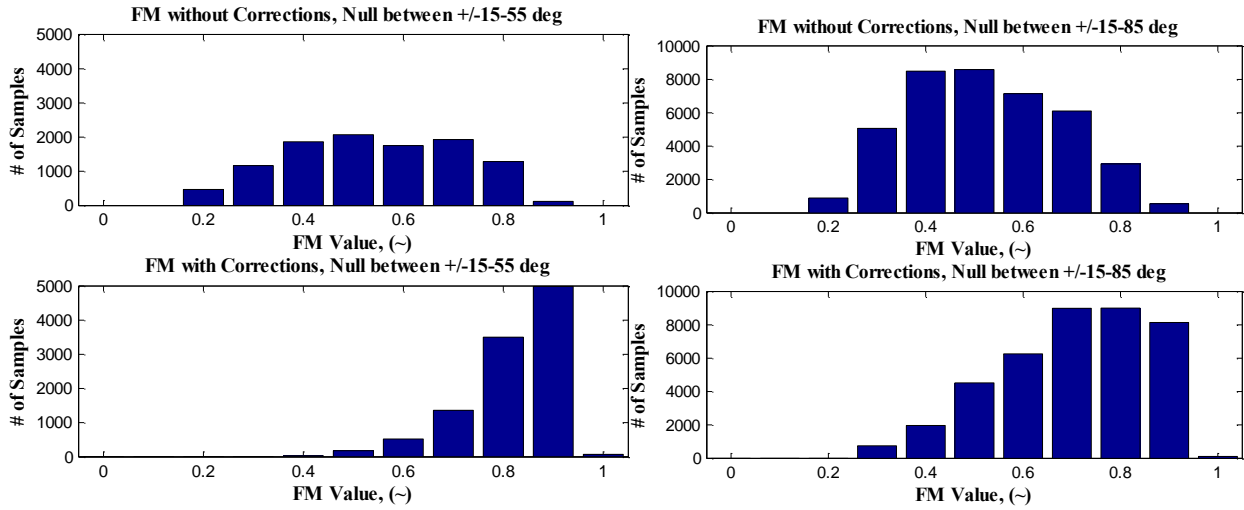


Figure 10.25: Comparison of Collinear Array SINR for One Null Placed Below 55° (a) and at All Angles (b)

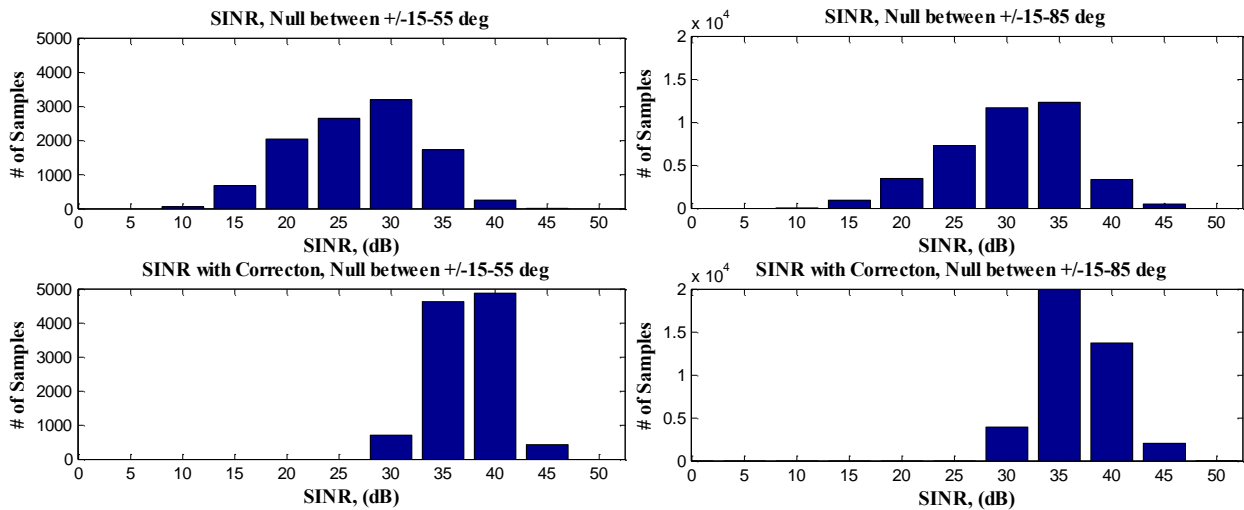
Figure 10.26 and Figure 10.27 show the FM and SINR, respectively, for the array with three nulls. To generate the data, one null was placed at either positive or negative elevation angles while the other two nulls were placed on the opposite side of the pattern. The two nulls on the same side of the pattern were separated by 15°.



(a) Angles below 55°

(b) All Angles

Figure 10.26: Comparison of Collinear Array Average FM for Three Nulls Placed Below 55° (a) and at All Angles (b)



(a) Angles below 55°

(b) All Angles

Figure 10.27: Comparison of Collinear Array Average SINR for Three Nulls Placed Below 55° (a) and at All Angles (b)

The results displayed in Figure 10.26 and Figure 10.27 follow similar trends as those seen in Figure 10.24 and Figure 10.25. Since an average value of the three nulls is presented in the figures, it is not surprising that there are few samples with an FM value of 1 or SINR value of 50 dB.

Table 10.3 and Table 10.4 offer summaries of the expected performance increase due to the compensation method for the single null and three null cases. Summaries of the two null case and parallel antennas can be found in Appendix B. The data in the tables have been divided by elevation angles and displacement levels. Isolating the small displacement levels ($\alpha=0.5-1.5$) was done to avoid skewing the results for the uncompensated array. In the tables, NC represents the uncompensated results, and C represents the compensated results. For both FM and SINR the average, 80th percentile, and 90th percentile values were calculated. The tables also present the average SINR increase when the compensation is applied.

Table 10.3: Summary of Performance Statistics for Collinear Array and 1 Null

		All α					$\alpha=0.5-1.5$				
		FM (~)		SINR (dB)		SINR Incr. (dB)	FM (~)		SINR (dB)		SINR Incr. (dB)
		NC	C	NC	C		NC	C	NC	C	
Angles < 55°	<i>Mean</i>	0.60	0.89	27.6	39.0	11.4	0.72	0.91	30.8	40.0	9.2
	<i>0.80</i>	0.39	0.83	20.8	34.6		0.56	0.87	25.5	35.2	
	<i>0.90</i>	0.33	0.76	18.2	33.2		0.50	0.81	21.6	33.8	
All Angles	<i>Mean</i>	0.59	0.79	31.8	39.1	7.3	0.69	0.82	34.4	40.4	6.0
	<i>0.80</i>	0.39	0.60	24.9	34.7		0.53	0.70	28.4	35.8	
	<i>0.90</i>	0.33	0.44	20.2	33.3		0.44	0.50	25.1	34.1	

Table 10.4: Summary of Performance Statistics for Collinear Array and 3 Nulls

		All α					$\alpha=0.5-1.5$				
		FM (~)		SINR (dB)		SINR Incr.	FM (~)		SINR (dB)		SINR Incr.
		NC	C	NC	C		NC	C	NC	C	
Angles < 55°	<i>Mean</i>	0.59	0.87	29.3	39.8	10.4	0.70	0.88	32.2	40.2	8.1
	<i>0.80</i>	0.43	0.80	23.7	36.7		0.58	0.83	27.9	36.7	
	<i>0.90</i>	0.35	0.73	21.1	35.5		0.52	0.76	25.0	35.4	
All Angles	<i>Mean</i>	0.57	0.75	32.9	39.2	6.32	0.65	0.78	35.2	40.3	5.04
	<i>0.80</i>	0.42	0.61	27.6	36.3		0.53	0.64	31.3	37.1	
	<i>0.90</i>	0.37	0.54	24.5	35.0		0.48	0.57	28.4	36.0	

Several observations can be made from the data in the tables. The first is that the compensation seems to perform about the same regardless of the number of nulls. Between the one null case and the three null case, all FM values are within 0.1 and all SINR values are within 2.3 dB. The compensation also seems to perform similarly regardless of the displacement level.

Comparing the all α data and the $\alpha = 0.5-1.5$ data, FM for the compensated array does not vary by more than 0.12 dB and in most cases less than 0.05, and SINR variation is less than 0.15 dB. On average the compensation improved the FM by about 0.15, but the more exciting observations are made from the SINR data. There were no instances in the plots shown in Figure 10.25 and Figure 10.27 where the SINR was below 25 dB after the compensation was applied. There are several instances for the uncompensated array where the SINR was below 10 dB! To sound some of the most difficult regions of ice-sheets 30-35 dB SINR is required. The results in Table 10.3 and Table 10.4 show that with 90% probability, 30-35 dB SINR could be achieved for the scaled model data when the compensation was applied. Without the compensation 90% of the data showed only about 25 dB SINR. On average the compensation method offered about 10 dB in additional clutter suppression for small angles and 6 dB when all angle are considered. It is noted that the parallel arrays demonstrated an additional 1.5-2 dB improvement when compared to the collinear array.

10.7 Application To The P-3 Array

To demonstrate the versatility of the compensation method, it was applied to the P-3 outboard arrays. The support structure of the P-3 is much more complicated than that of the Twin Otter array and it has significantly more near-field scatterers. Figure 10.28 shows the EM model used to simulate the P-3 outboard array. This model includes the wing skin, pylons, doublers, gang channels, brackets, rib inserts, and the fiber glass fairing. Using the wing flexure charts in Figure 5.7 the wing and array deformation was approximated by a 3° rotation. Though the P-3 wing also has beam-like deflection, a rigid body rotation was found to be a good approximation of the displacements over a small span. The model was simulated at 195 MHz and a minimum of two converged passes was required.

Doublers, gang channels, pylon skins, rib inserts, and the wing skin were modeled as perfectly conducting boundaries. The entire fiber glass fairing was modeled with the exception of the leading and trailing edges. It was assumed that these electrically transparent structures would not significantly affect the performance of the array. The air box surrounding the structures is at least $\lambda/4$ away from any point on the structures. A maximum delta S of 0.02 was specified as the convergence criterion.

The same process was used to implement the compensation method on the P-3 as was used for the Twin Otter. Figure 10.29 through Figure 10.31 show the results for nulls placed at $\pm 40^\circ$, $\pm 70^\circ$, and -54° and 50° , respectively

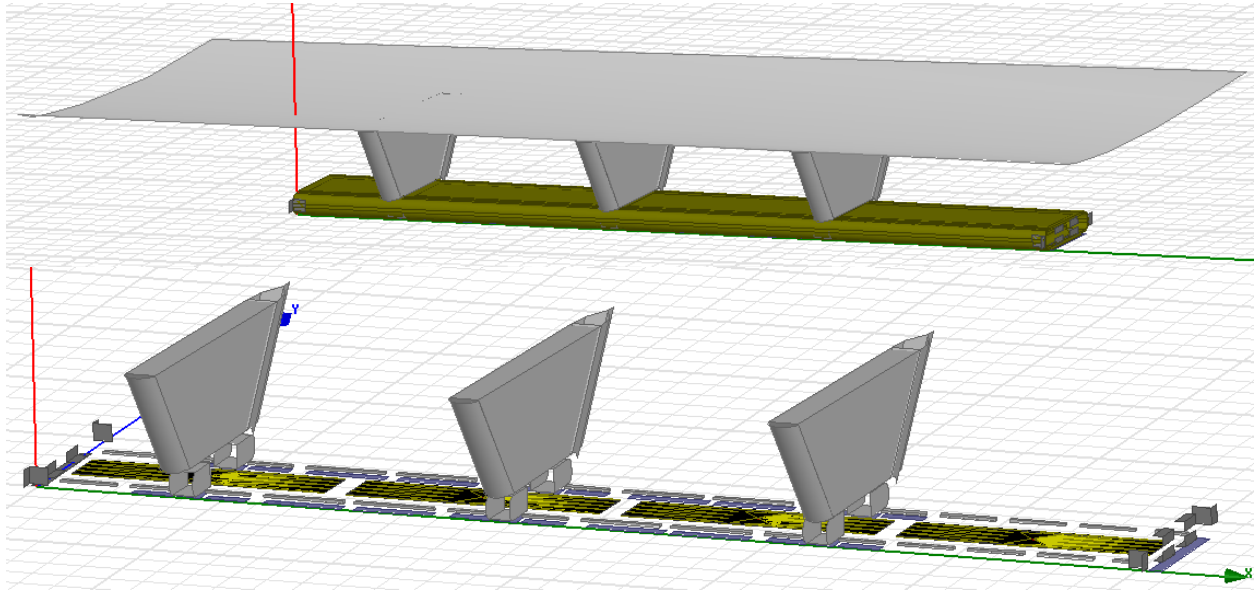


Figure 10.28: P-3 Outboard Array HFSS[®] Model

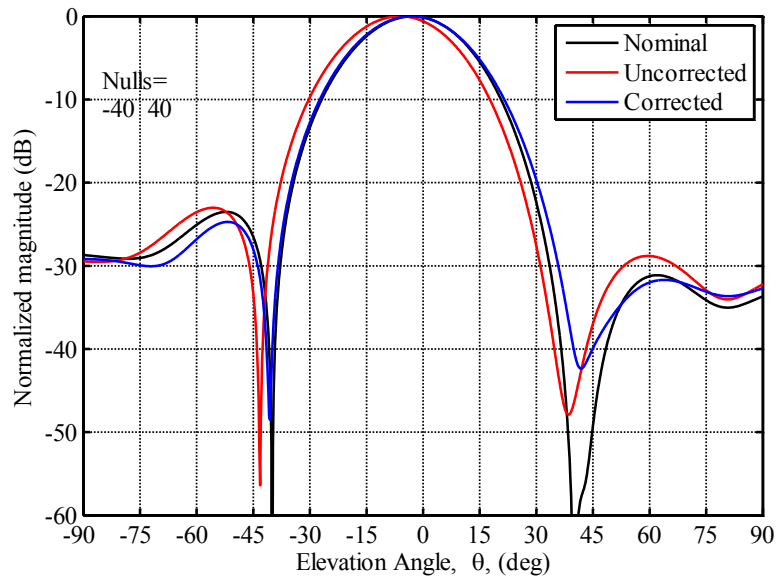


Figure 10.29: Comparison of Uncompensated and Compensated Simulated P-3 Outboard Array Patterns with MVDR Weights, and Nulls at $\pm 40^\circ$

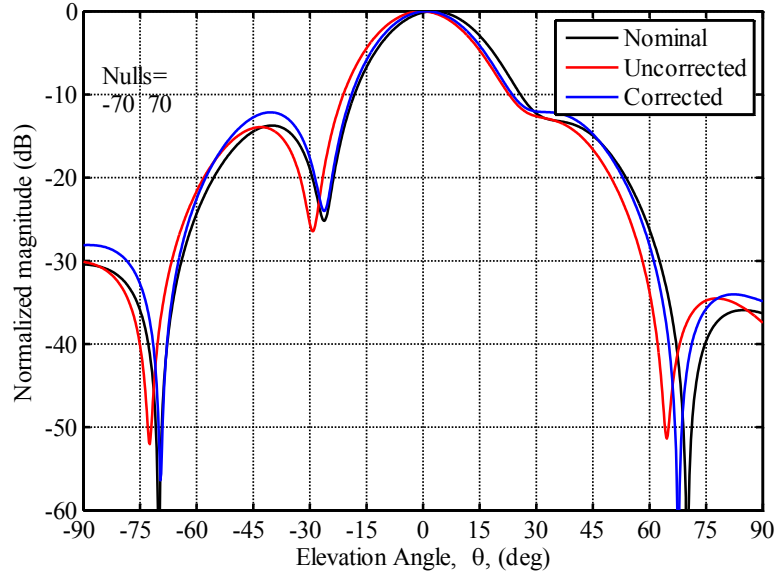


Figure 10.30: Comparison of Uncompensated and Compensated Simulated P-3 Outboard Array Patterns with MVDR Weights, and Nulls at $\pm 70^\circ$

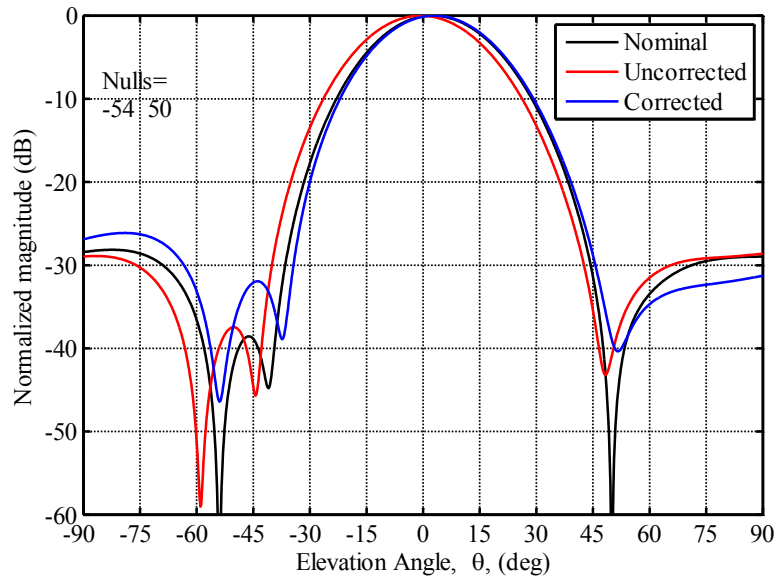


Figure 10.31: Comparison of Uncompensated and Compensated Simulated P-3 Outboard Array Patterns with MVDR Weights, and Asymmetric Nulls at -54° and 50°

Despite the fact that the P-3 array support structure is much more complex and contains more near-field scatterers, the compensation method was able to recover the nulls with about the same success as the Twin Otter array. This demonstrates that the application of the compensation method is not limited to antenna-arrays with relatively simple support structures.

11 EFFECTS OF CONTROL SURFACE DEFLECTION ON ARRAY PERFORMANCE

11.1 Introduction

While the utilization of ailerons is minimal during the straight and level flight necessary for data collection, they are required to quickly dampen out disturbances that occur. Initial calibration flights are performed in sustained bank and continuous roll conditions for which differential aileron deflection (one up, one down) are commanded. In addition, the radar engineers often want to fly at very low speeds during data collection. To achieve the slower aircraft speeds, flap deployment is required. The Twin Otter uses flaperons, so once again this will result in a deflected surface in the region of the antennas. Control surface deflection changes the ground plane shape for the wing-mounted antenna-array. Figure 11.1 shows the cross-section of the Twin Otter with and without aileron deflection. As a conservative estimate, the maximum aileron deflection was assumed to be 15° . For an aileron chord length of 15.75", a 15° rotation would result in a tip deflection of 4.30", and the antennas are roughly 40" from the trailing edge of the aileron.

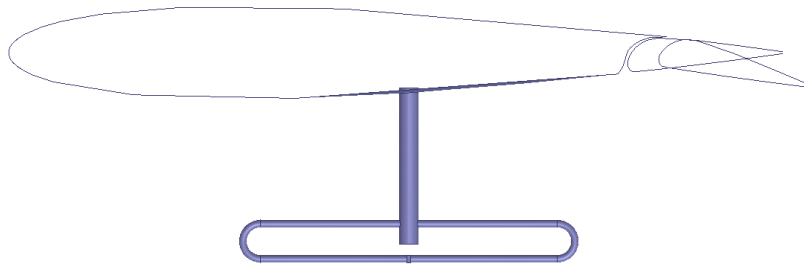


Figure 11.1: Twin Otter Wing with and without Aileron Deflection and Dipole Antenna

11.2 Simulation Results

To bank the aircraft, differential aileron deflection is required, so the arrays were simulated for both positive and negative aileron deflection. Figure 11.2 compares the radiation patterns with no control surface deflection (black), 15° downward control surface deflection (red), and 15° upward deflection (blue) with both uniform and Chebyshev weights. Sidelobes were set to 30 dB in the Chebyshev plot. The patterns are nearly identical (<0.3 dB deviation) in the mainbeam of the patterns, but both patterns diverge outside the mainbeam, especially at angles larger than

$\pm 35^\circ$ for the uniform array and $\pm 25^\circ$ for the Chebyshev array. There is some increase in the sidelobes, especially near endfire. This increase is more significant in the Chebyshev plot with a maximum sidelobe increase of 9 dB, but the sidelobes do not exceed the 30 dB sidelobe limit.

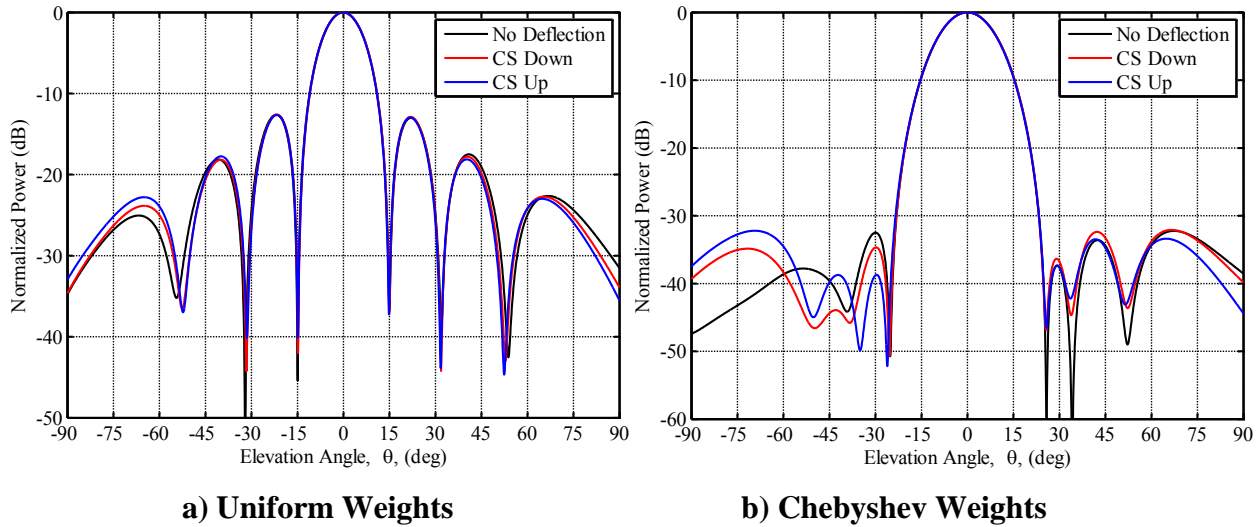


Figure 11.2: Comparison of Simulated Twin Otter Radiation Patterns with Control Surface Deflections

Figure 11.3, Figure 11.4, and Figure 11.5 compare the MVDR radiation patterns with aileron deflection of 15° and nulls angles of $\pm 40^\circ$, $\pm 70^\circ$, and -54° and 50° , respectively. From the plots it is evident the control surface deflection has a much larger effect at angles greater than $\pm 45^\circ$. Though there is some null depth reduction at small angles, Figure 11.4 shows a much greater degradation for the nulls applied at $\pm 70^\circ$. Null shifts were less than 1° and the experimental SINR was at least 33 dB in both Figure 11.3 and Figure 11.5. In most cases the SINR was better than 40 dB. In addition the FM for these cases ranged from 0.62 to 1. Null shifts in the $\pm 70^\circ$ pattern were as much as 12° , and the FM was less than 0.27. Changes in the pattern were greater when control surfaces are deflected up versus when they were deflected down. While the average FM was only slightly better (0.05), the average experimental SINR was 3.8 dB better when the control surfaces were deflected down. Similar to the uniformly- and Chebyshev-weighted arrays, pattern deviations were less than 0.3 dB for angles less than $\pm 25^\circ$.

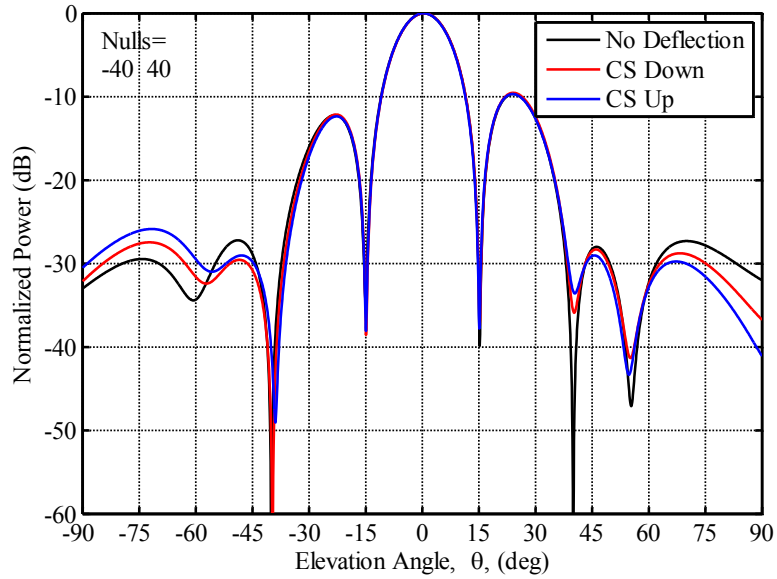


Figure 11.3: Simulated Radiation Pattern with Control Deflections and MVDR Weights, Nulls at $\pm 40^\circ$

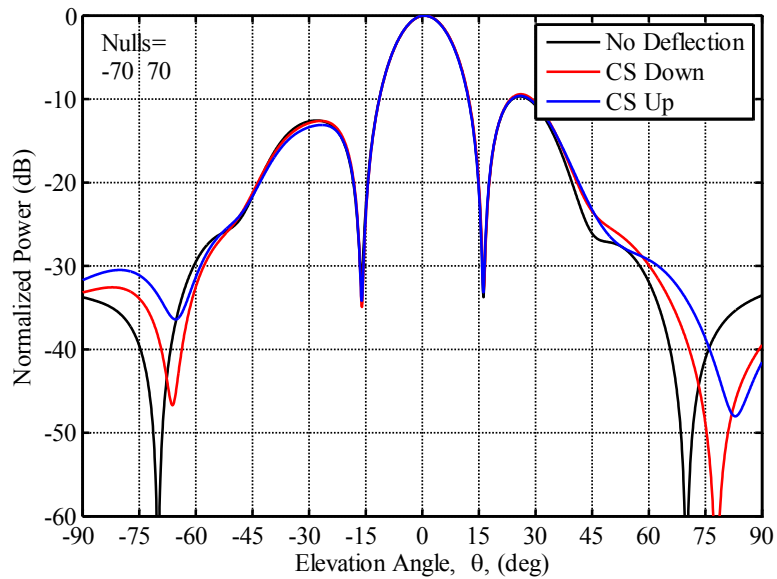


Figure 11.4: Simulated Radiation Pattern with Control Deflections and MVDR Weights, Nulls at $\pm 70^\circ$

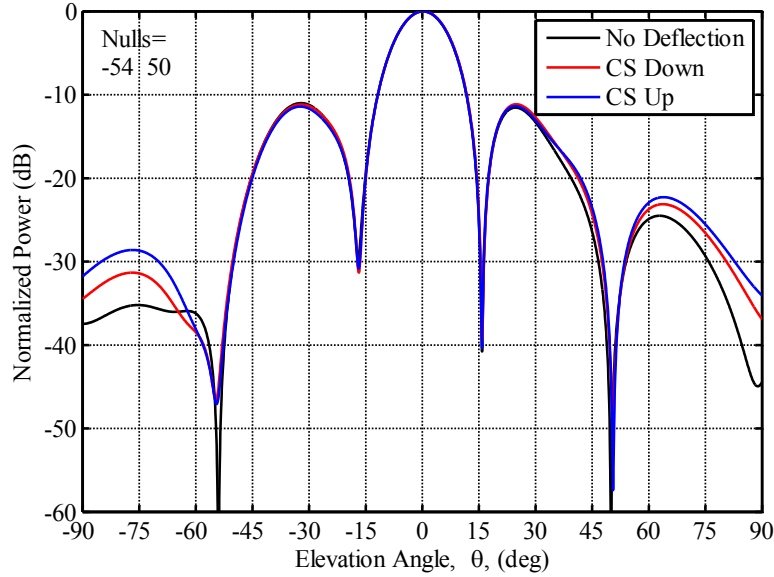


Figure 11.5: Simulated Radiation Pattern with Control Deflections and MVDR Weights, Nulls at -54° and 50°

11.3 Experimental Measurement Results

Due to the limitations of the scaled model structure, experimental measurements were only made for control surfaces deflected down. Pattern measurements were made for control surfaces deflected 15° and 25° . Figure 11.6 shows both the parallel and collinear array with uniform weights. Like the simulations, pattern deviation is less than 0.3 dB for angles less than $\pm 25^\circ$, but there is some divergence (>8 dB) at large angles ($>\pm 55^\circ$), particularly for the collinear array.

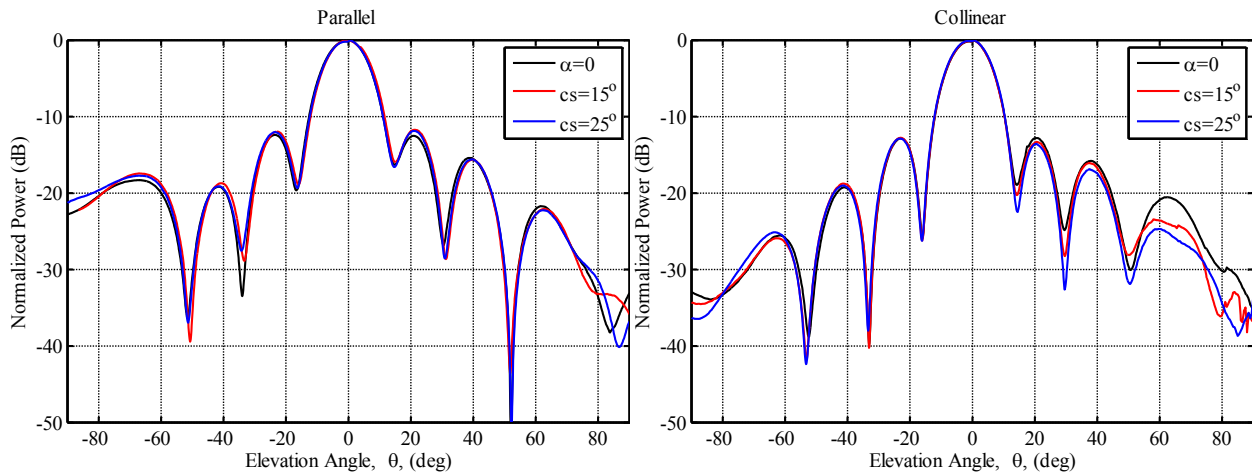


Figure 11.6: Measured Patterns with Control Surface Deflections and Uniform Weights

Figure 11.7 shows the parallel and collinear radiation pattern with Chebyshev weights for sidelobe levels set to 30 dB. It is first important to point out that the nominal array did not

achieve the 30 dB sidelobe goal. Again, patterns agree within 0.3 dB in the mainbeam, and larger pattern deviations occur at angles greater than $\pm 25^\circ$. These deviations are more significant for the collinear array (3.9 dB average) than the parallel array (1.9 dB average), but sidelobes generally were lower when control surfaces were deflected (average decrease of 1.7 dB).

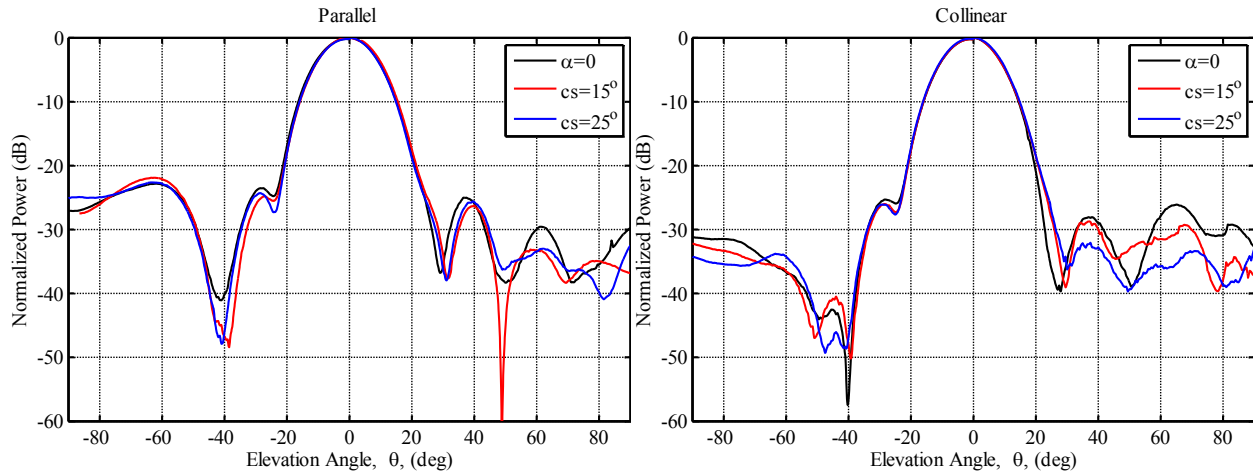


Figure 11.7: Measured Patterns with Control Surface Deflections with Chebyshev Weights and Sidelobes Set to 30 dB

Figure 11.8, Figure 11.9, and Figure 11.10 compare the MVDR radiation patterns with nulls at $\pm 40^\circ$, $\pm 70^\circ$, and -54° and 50° , respectively. Similar to the simulations it is evident that the control surface deflection has a much greater effect at the larger angles. The patterns in Figure 11.8 and Figure 11.10 had an average FM of 0.86, and a third of the nulls had a perfect correction (FM=1). The pattern with nulls at $\pm 70^\circ$ had an average FM of 0.62, and nulls shifted by as much as 8° . Null shifts in the other patterns were not greater than 2.2° .

Again pattern degradation appears to be more severe in the collinear array. The average FM for the parallel array is 0.87 whereas the average FM for the collinear array is 0.70. In addition the parallel experimental SINR is almost 5 dB better than the collinear SINR, on average.

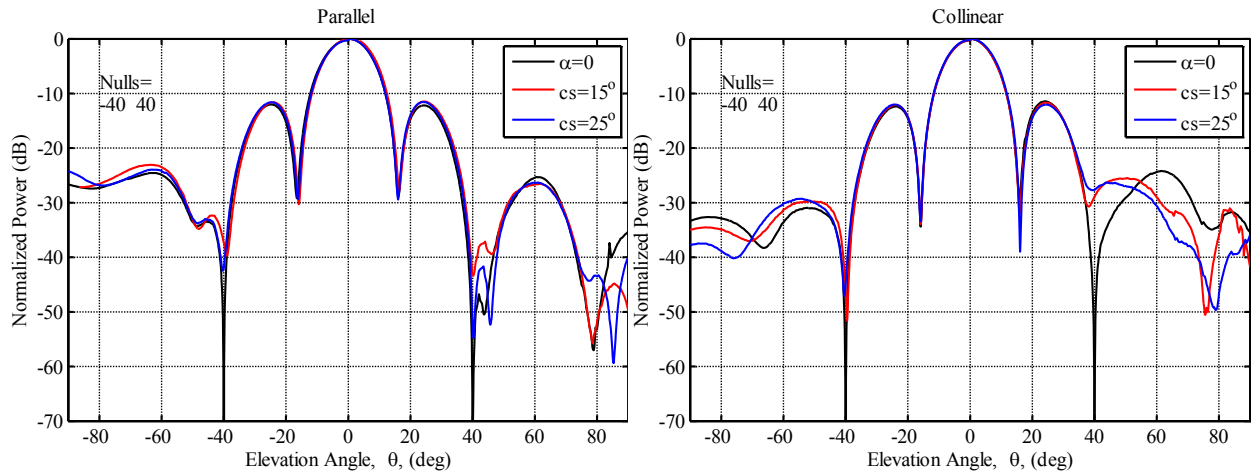


Figure 11.8: Measured Patterns with Control Surface Deflections and Nulls at $\pm 40^\circ$

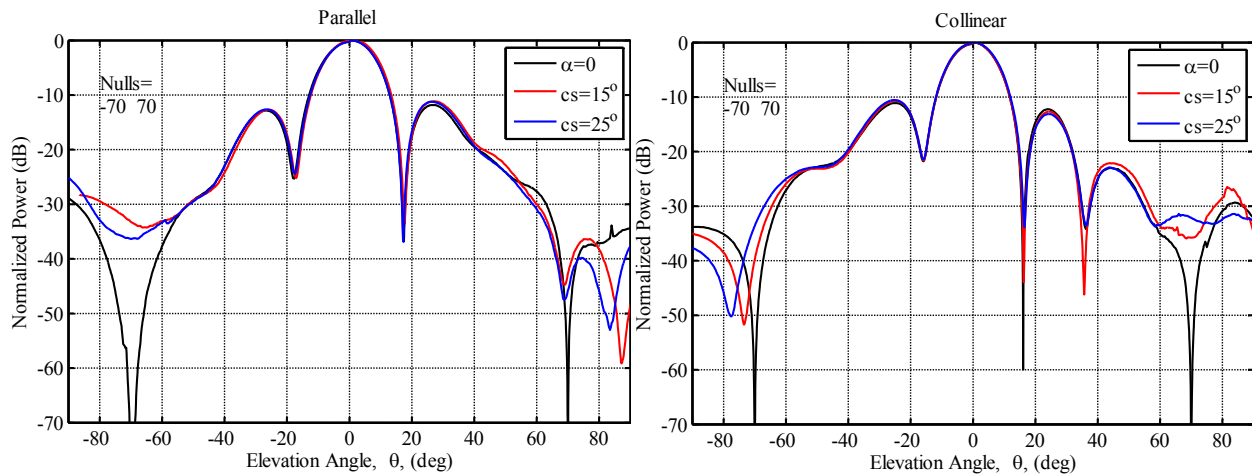


Figure 11.9: Measured Patterns with Control Surface Deflections and Nulls at $\pm 70^\circ$

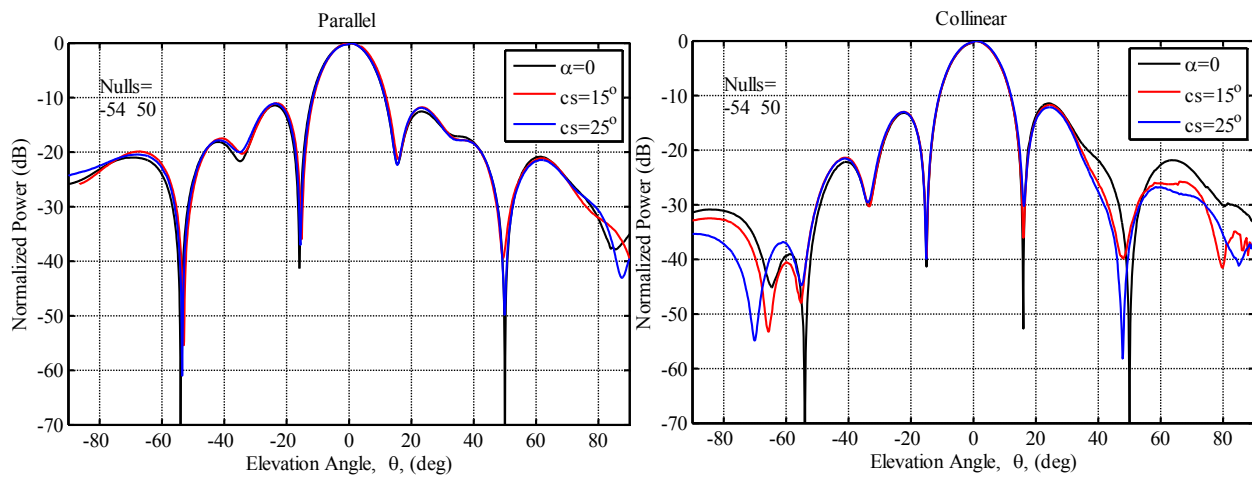


Figure 11.10: Measured Patterns with Control Surface Deflections Nulls at -54° and 50°

11.4 Coupling Compensation

The changes in the patterns when control surfaces are deployed are caused by the changes in mutual coupling in the antennas. As such, an attempt was made to compensate for this change in coupling. If successful, the method could also be included in the deformation compensation method to improve its performance.

It has been shown that the coupling matrix of a real array can be used to compensate for mutual coupling effects [133]. The coupling matrix, \mathbf{C} , of an array is given by Equation (11.1).

$$\mathbf{C} = \mathbf{Z}_L (\mathbf{Z} + \mathbf{Z}_L \mathbf{I})^{-1} \quad (11.1)$$

In the equation \mathbf{Z}_L is the load impedance of each antenna, \mathbf{Z} is the mutual impedance matrix, and \mathbf{I} is the identity matrix. The impedance matrix can be derived from scattering matrix, \mathbf{S} , measurements by using the following relationship:

$$\mathbf{Z} = -\mathbf{Z}_L (\mathbf{S} - \mathbf{I})^{-1} (\mathbf{S} + \mathbf{I}) \quad (11.2)$$

If the model of the coupling matrix is exact, the mutual coupling can be compensated in the received signal by multiplying by the inverse of the coupling matrix.

$$\bar{\mathbf{x}}' = \mathbf{C}^{-1} \bar{\mathbf{x}}_{Rx} \quad (11.3)$$

The compensated receive vector, $\bar{\mathbf{x}}'$, is then used to determine the optimum weights. Since mutual coupling exists in the array, mutual coupling must be pre-compensated for by multiplying the weights by the inverse of the coupling matrix as follows

$$\bar{\mathbf{w}}' = \mathbf{C}^{-1} \bar{\mathbf{w}} \quad (11.4)$$

The above method was used in [133] to compensate for mutual coupling in a real uniform circular array such that the performance of the array would match that of an ideal uniform circular array. In an effort to extend this method to compensate for changes in coupling due to control surface deployment, the pattern of the clean configuration was multiplied by its coupling matrix inverse, similar to the procedure in Equation (11.3).

$$\bar{\mathbf{x}}'_{clean} = \mathbf{C}_{clean}^{-1} \bar{\mathbf{x}}_{clean} \quad (11.5)$$

The modified vector matrix is then used to calculate the MVDR weights. Then following Equation (11.4) the weights generated from the coupling-compensated clean array data are multiplied by the inverse coupling matrix of the array with control surface deployed. Equation

(11.6) shows the relationship between the weights applied to the array with control surface deployment and the compensated clean configuration weights.

$$\bar{\mathbf{w}}_{cs} = \mathbf{C}_{cs}^{-1} \bar{\mathbf{w}}'_{clean} \quad (11.6)$$

This coupling compensation approach was applied to both the simulated Twin Otter array and the measured scaled model array. Figure 11.11, Figure 11.12, and Figure 11.13 show the coupling compensated MVDR plots with nulls at $\pm 40^\circ$, $\pm 70^\circ$, and -54° and 50° , respectively, for both the collinear Twin Otter and scaled models arrays. The Twin Otter was only simulated with 15° downward deflection, whereas both 15° and 25° were measured on the scaled model array. When the plots in Figure 11.11 through Figure 11.13 are compared to the appropriate plots in Section 11.2 and 11.3, very little improvement is exhibited, and in some cases performance is degraded. An example of this is in the asymmetric null pattern where the experimental SINR at 50° is decreased by 7 dB. However, average pattern deviation is on the order of 1-2 dB

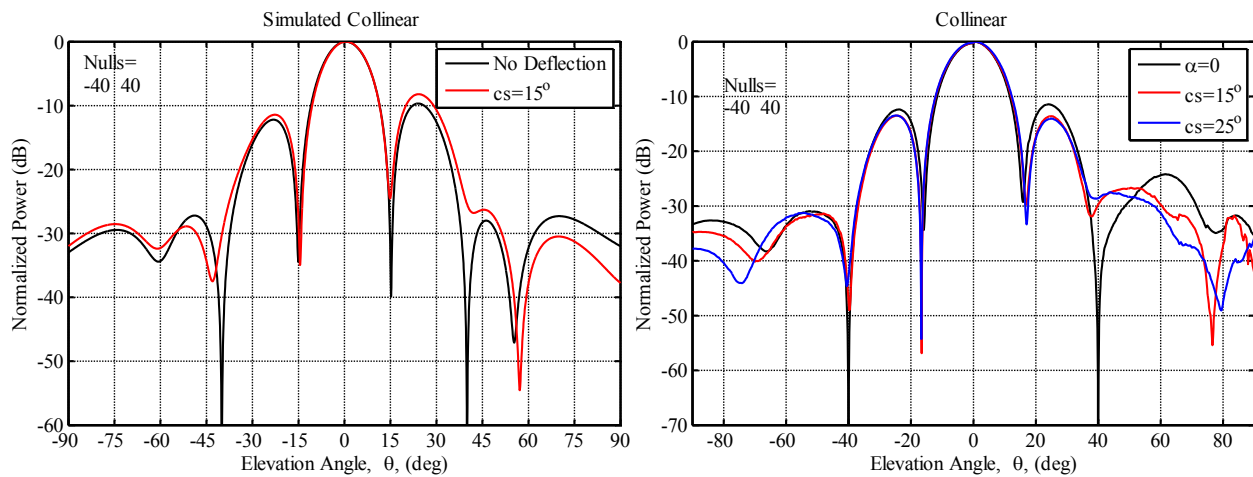


Figure 11.11: Simulated (left) and Measured (right) Patterns with Mutual Coupling Compensation, Null at $\pm 40^\circ$

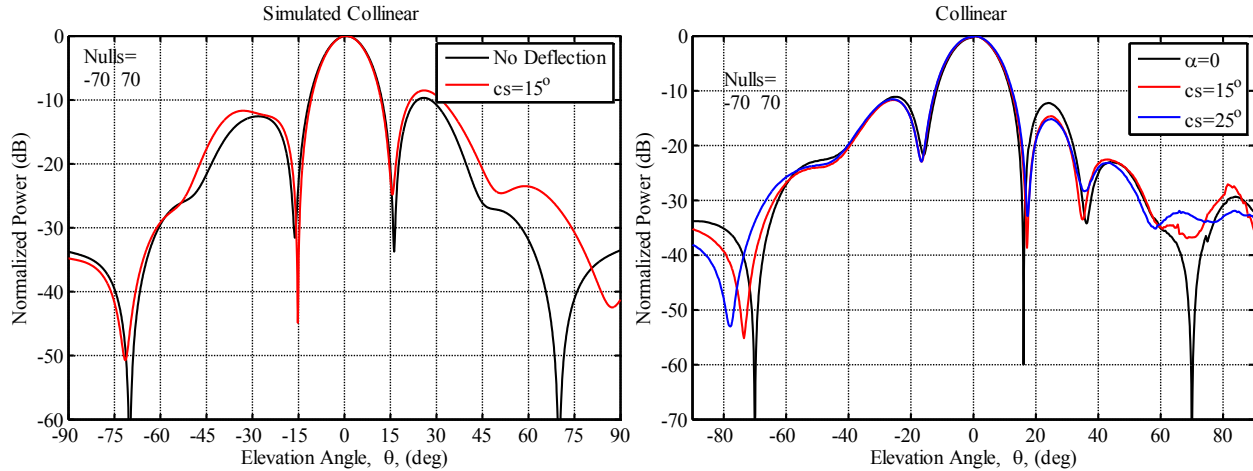


Figure 11.12: Simulated (left) and Measured (right) Patterns with Mutual Coupling Compensation, Null at $\pm 70^\circ$

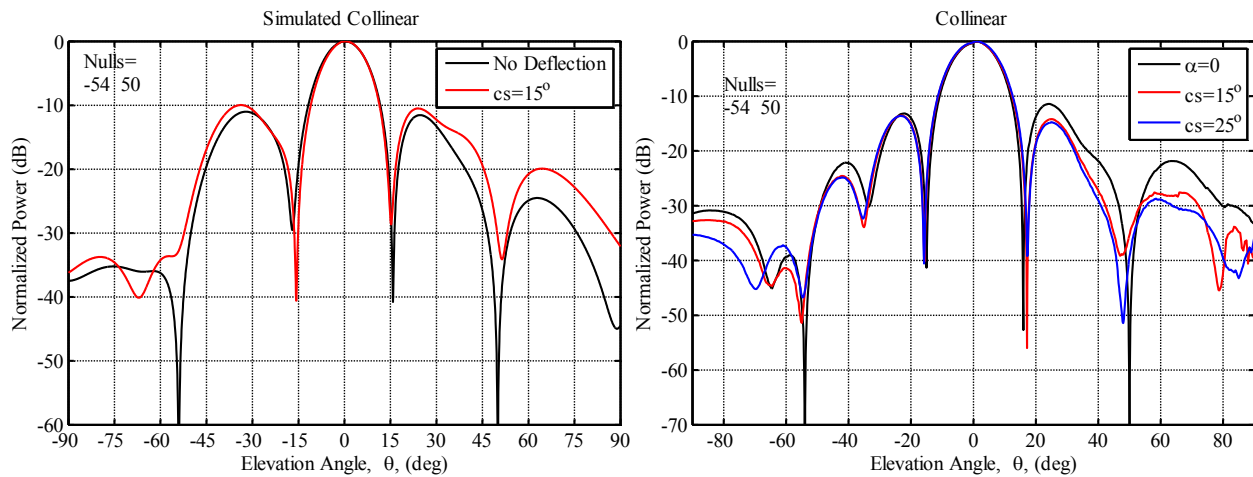


Figure 11.13: Simulated (left) and Measured (right) Patterns with Mutual Coupling Compensation, Null at -54° and 50°

The mutual coupling compensation of [133] was performed to improve the beam formation of a real array as compared to an ideal array without mutual coupling. It is well known that mutual coupling degrades beamforming, as an ideal array can achieve much deeper nulls and lower sidelobe levels than a real array. In [133], a uniform circular array was analyzed without the presences of any surrounding structure. To perform the coupling compensation, the authors used the radiation patterns of a virtual array which was constructed from the radiation pattern of a single radiating element. To form the radiation pattern of the real array with mutual coupling, the single element pattern was measured with “parasitic” dipole elements forming the full array. A major difference between applying the coupling compensation in the paper and applying it to the Twin Otter or scaled model array is that in [133] only the array was present and not the

numerous additional scattering sources present on an aircraft. In addition [133] used a virtual array in which all the element patterns are identical. For the arrays in this document, each element pattern will be slightly different due to manufacturing and cabling variances, and will include the effects of the surrounding structure.

The compensation method in this chapter did not work because the coupling matrix does not include changes in the coupling across the whole field of view; therefore, it cannot accurately capture pattern changes for all elevation angles. The coupling matrix can only account for an average change. To fully capture the effects of mutual coupling, full 3D wave analysis is required. Future studies on the topic should investigate ways to account for changes in coupling with the goal of identifying a method that does not require full 3D wave analysis, but can partially predict changes in mutual coupling.

12 SUMMARY AND RECOMMENDATIONS

12.1 Summary

Research and development efforts described herein have the following contributions to the field of airborne remote sensing:

1. Enabled the first ice penetrating radar array capable of sounding deep bed conditions from a long-range (5,000 nm), high altitude (32,000 ft), and transonic speed ($M=0.85$) aircraft, by developing a custom radome fairing and all related aircraft integration to support the 5-element antenna-array on the NASA DC-8 in support of OIB.
2. Enabled the world's largest ice and snow radar suite by developing custom wing radome fairings and bomb bay closure radomes and all related aircraft integration to support the 15-element antenna-array mounted to the wing and the microwave and UHF antenna-arrays mounted within the bomb bay of the NASA P-3 in support of OIB.
3. Improved the performance of the P-3 array through geometric modifications to the fairing and surrounding structure. A new lower skin design shifted the center frequencies of the antennas up by 25 MHz and increased the bandwidth by 5 MHz. Simulations and measurements of the center antenna showed a 3 dB improvement at nadir when a partial cover was added to the aircraft nadir port.
4. Developed a design rule for mitigating the effect of near-field parasitic elements on antenna-array performance. For parasitic elements along the length of an antenna whose lengths are less than 0.125λ , changes in S_{11} performance are less than 5%.
5. Developed a method that can improve beam formation and clutter suppression by accounting for array deformations. The compensation achieved at least 33 dB SINR and increased the SINR by an average 5-10 dB when compared to the uncompensated performance. The compensation also improved the FM by an average of 0.15.
6. Determined expected array performance implications due to extreme thermal gradients is negligible as the phase stability of the P-3 cables was measured to be 2.2×10^{-4} deg./ft/ $^{\circ}$ F.
7. Identified expected array performance implications of control surface deflection. Control surface deflection was found to shift nulls by as much as 12° and reduced null depth by as much as 25 dB.

A fairing to house a 5-element antenna-array has been developed and flown on a NASA DC-8 in support of NASA's OIB. In addition, a fairing that houses a 15-element antenna-array has been developed and flown on a NASA P-3, also in support of OIB. These fairings were designed to meet both aircraft, structural, and electrical performance requirements. Together these aircraft have logged roughly 2,000 flight hours and gathered over 450 TB of unique data on Arctic and Antarctic ice beds, layering, and snow accumulation while mapping some of the most difficult regions in Greenland and Antarctica. Such data would not be available to the science community had developments described herein not been performed.

Since its first field season, the P-3 MCoRDS fairing has been improved through geometric modifications. This was done by maximizing the distance between the antenna elements and conductive components in the near-field of the antenna, as well as minimizing the size of these components. These modifications resulted in shifting the center frequencies of the antennas by 25 MHz, increasing the bandwidth by an average of 5 MHz, and an average return loss improvement of 5 dB at the radar's center frequency. Modifications to the nadir port above the center antenna element have also demonstrated array improvements. Measurements and simulations of the center antenna with a partial covering over the port above the antenna demonstrate a 3 dB improvement in nadir gain. With little that can be done to further improve the array's performance through the modification of fairing geometry, reducing aircraft integration effects was identified as the next step to improve the airborne array.

The wing flexure results in chapters 9 and 10 and the control surface results in Chapter 11 demonstrate that aircraft integration has little effect on the mainbeam of the pattern as compared to the pattern outside of the mainbeam. Though the wing flexure caused mainbeam pointing errors, corrections for these errors are readily obtained and demonstrated in numerous applications [57]-[59]. While mainbeam errors will inherently have some effect in the CReSIS radars, improved null placement and formation is a more critical feature, and key to improved next-generation radars. While some have investigated mitigating array deformation and improving off-nadir beamformation [64]-[66], none of the methods in the open literature are practical for airborne remote sensing applications. The current methods require constant monitoring of the array's radiation pattern that either necessitate additional receive antennas offset from the array or continual scanning of the array. Since airborne surveying missions occur

in remote and dangerous locations, it is not practical to have a series of receive antennas on the ground along the entire flight path for calibrations. In addition, if the array is constantly required to scan to off-nadir angles to employ a correction then data acquisition will suffer. The compensation method presented here can be readily implemented on past, present, and future CReSIS platforms with the addition of a few sensors that can capture displacement.

12.2 Conclusions

The following are conclusions derived from the work of this dissertation:

1. In the development of the fairings, the presence of near-field, planar parasitic elements have shown to greatly degrade the performance of the antenna-array. While the full effect of the parasitic elements can only be determined with full, 3D wave analysis, it was speculated that certain limits existed for the effects of the elements based on the parasitic element size and location. An extensive study into the effects of near-field coupling of planar parasitic elements found that parasitic elements along the length of an antenna whose lengths are less than 0.125λ , changes in S_{11} performance are less than 5%. This was demonstrated for three different frequencies. The element radiation patterns appear to have a small dependency on the relative size and location of the doublers when placed along the full length of the antenna. Though there were no significant changes in the overall shape of the pattern, there appeared to be a widening of the pattern that was dependent on the relative location of the doublers. The phenomenon seemed to be more severe at higher frequencies. It was suggested that there is a dependency of the pattern widening on the width of the doubler, but this statement cannot be assured as two different dipoles were used.
2. It was expected that wing flexure would degrade beamforming of an array, but these effect could be mitigated by accounting for the out-of-plane displacements of the antenna elements. Array deformation caused by wing flexure was shown to cause filling and shifting of nulls. A compensation method was developed that uses element pattern and displacement information to improve MVDR beamforming. The effectiveness of the compensation method was shown to be limited by mutual coupling effects. Despite not compensating for mutual coupling, the compensation

showed at least 33 dB experimental SINR for 90% of samples. The compensation also showed an average SINR increase of 5-10 dB, depending on null angles considered, and an average FM increase of 0.15.

The compensation method was applied to a data-independent derivation of MVDR weights. This data-independent method allows for more control over beam formation and prevents the “self-nulling” phenomenon. This compensation method only requires a single measurement of the antenna radiation patterns, which offers a significant advantage over other compensation methods that require continuous monitoring of the element patterns. Element patterns could be obtained at an antenna range either prior to or after a field season (if only post-processing beam formation is required). CReSIS has also demonstrated the ability to obtain element radiation patterns in-flight [134].

3. Extreme thermal gradients were believed to degrade beamforming and antenna-array performance due to the resulting changes in the transmission lines; however the expected thermal gradients were shown to not have a significant impact on beam formation as resulting phase shifts were very small. The phase stability of the CReSIS coaxial cables was found to be 2.2×10^{-4} deg./ft/ $^{\circ}$ F.
4. It was hypothesized that control surface deflections would affect the beamforming ability of a wing-mounted antenna array. Control surface deflections were shown to cause filling and shifting of nulls, especially at large elevation angles. Control surface deflection was found to shift nulls by as much as 12° and decrease null depth by as much as 25 dB. At large elevation angles ($>\pm 55^{\circ}$) the FM was on average 0.2 less than the FM at small elevation angles. This was due to the changes in coupling caused by the deployed surface. Coupling compensation methods for this require additional study.

12.3 Recommendations

The following are recommendations based on the work of this dissertation:

1. Design a system to measure the real-time deflections of a wing mounted array, that itself does not influence or adversely alter the antenna array performance. This

system would likely consist of some combination of optical cameras, accelerometers, IMUs, and/or strain gauges in conjunction with a simple computer script that can convert the measurements into real displacements. LabVIEW[®] [136] is the recommended design software for the computer script as the latest version of the radar utilizes LabVIEW[®]. The real-time deflection data can be used in post-processing to compensate for the phase center errors, and in theory could also be used in conjunction with a look-up table of previously simulated MVDR weighting functions to alter transmit parameters. The development of such a system is the next step to developing a real-time compensation for the transmit beams.

2. In conjunction with this system to measure real-time displacements, develop an accurate structural (FEA) model of the desired aircraft's wing. The purpose of the model is to verify that in-flight data (speed, altitude, temperature, pressure) could be used to apply loads to the FEA model and with relative accuracy predict the displacements. Such a study could be used to help recover old data sets, by using stored mission flight data to predict wing flexure. The compensation method developed in this work requires knowledge of the array element patterns and thus could not be used to recover old data sets without this information; however the ability to accurately predict displacements will allow mainbeam pointing error correction as well as improved lever arm calculations. The lever arm is the x, y, z vector from the GPS antenna to each array antenna and is used in the processing of data. Wing deflections, antenna rotation, and antenna radiation patterns are currently not considered in the lever arm calculation, but wing dihedral, aircraft roll angle, and aircraft pitch angle are.
3. Measure the as-installed radiation patterns of an antenna-array and apply the compensated method to post-processing beam formation. If these measurements are taken before the beginning of the field season, perform beamforming with the radar and attempt to measure the in-flight radiation pattern. Comparing the in-flight measurements with the ground measurements can shed some light on the accuracy of the in-flight measurements and verify that this is a suitable method for pattern measurements.

4. Further investigate ways to compensate for mutual coupling changes. Though mutual coupling is a widely researched topic, it is sufficiently broad in spectrum that determining a way to account for mutual coupling changes would support an independent and focused dissertation topic. The goal would be to identify a method that does not require full 3D wave analysis, but can partially predict changes in mutual coupling. It could be found that significant improvement can be made to the compensation method with only partial prediction of coupling changes.
5. Finally, vibration is not expected to have a significant impact on beam formation or data measurements of airborne radar used for remote sensing of ice sheets. Appendix D contains a vibration study that was performed with the scaled array and the radar. This study demonstrates that phase and magnitude variations due to vibration are very small and will not significantly degrade beamforming performance. The study also showed that the frequency of excitation of the structure can be identified by taking the Fourier transform of the phase data. Though the excitation frequencies were easily identified in this study, in real CReSIS radar data vibration excitation frequencies have not been able to be identified. This supports the claim that the effects of structural vibration are very small.

Though vibrations are not expected to significantly impact beam formation for the wing-mounted arrays, it is recommended that the vibration effects be further explored. In the data in Appendix D it was discovered that the phase and magnitude variations of one antenna were significantly greater than the other elements. It was postulated, but not confirmed, that this was caused by the excitation method/location. Other possible sources of the error include experimental setup errors such as loose SMA connectors or incorrect radar settings. Also, electromagnetic interference due to the shaker and other vibration equipment was not checked. In addition, it was found that the magnitudes of the elements oscillated with the same frequency of excitation. This phenomenon is not sufficiently characterized and is why it is recommended to be further studied.

13 REFERENCES

1. "IceBridge Mission Overview," *NASA Operation IceBridge Web Site* [http://www.nasa.gov/mission_pages/icebridge/mission/index.html], 3 March 2012.
2. J. Li, et. al., "High-Altitude Radar Measurements of Ice Thickness Over the Antarctic and Greenland Ice Sheets as a Part of Operation IceBridge," *IEEE Trans. on Geoscience and Remote Sensing*, Vol. 51, No. 2, February 2013.
3. K.J. Byers, A.R. Harish, S.A. Seguin, C.J. Leuschen, F. Rodriguez-Morales, J. Paden, E.J. Arnold, R.D. Hale, "A Modified Wideband Dipole Antenna for an Airborne VHF Ice-Penetrating Radar," *IEEE Trans. on Instrumentation and Measurement*, Vol. 61, No. 5, pp. 1435-1444, May 2012.
4. R. Etkins, and E. S. Epstein, "The Rise of Global Mean Sea-level as an Indication of Climate Change", *Science*, vol. 215, pp. 287-289, 15 January 1982.
5. N.L. Bindoff, J. Willebrand, et. al., "2007: Observations: Oceanic Climate Change and Sea-level". *Climate Change 2007: The Physical Science Basis. Contributions of Working Group I to the Fourth Assessment Report of the Intergovernmental Panel on Climate Change*. Cambridge University Press, Cambridge, United Kingdom and New York, NY, USA.
6. R. Bindshadler, P. Clark, D. Holland, et. al, "A Research Program for Projecting Sea-Level Rise from Land-Ice Loss," *Report from NSF "Project Future Land-Ice Loss" workshop*, 2010.
7. S. Gogineni, et. al, "Sounding and Imaging of Fast Flowing Glaciers and Ice-Sheet Margins," *9th European Conference on Synthetic Aperture Radar*, 2012.
8. "Center for Remotes Sensing of Ice Sheets," *Center for Remote Sensing of Ice Sheets Web Site* [<https://cms.cresis.ku.edu/about>], 1 March 2012.

9. L. Koenig, S. Martin, M. Studinger, and J. Sonntag, "Polar Airborne Observations Fill Gap in Satellite Data," *Eos Trans. AGU*, 91(38), 333-334, 2010.
10. F. LeChevalier, *Principles of Radar and Sonar Signal Processing*, Artech House Publishers, 1st ed., 31 March 2002.
11. J. Paden, T. Akins, D. Dunson, C. Allen, and P. Gogineni, "Ice-sheet Bed 3-D Tomography," *Journal of Glaciology*, vol. 56, no. 195, pp. 3-11, January 2010.
12. Anon., "NASA DC-8 Airborne Laboratory Experimenter Handbook," Dryden Flight Research Center, Edwards, CA, June 2002.
13. C. Allen, L. Shi, R. Hale, C. Leuschen, J. Paden, B. Panzer, E. Arnold, W. Blake, F. Rodriguez-Morales, J. Ledford, and S. Seguin, "Antarctic Ice Depth-sounding Radar Instrumentation for the NASA DC-8," *IEEE Aerospace and Electronic Systems Magazine*, Vol. 27, No. 3, March 2012.
14. *Jane's All the World Aircraft, 1984-1985*, Jane's Publishing Incorporated, 13th Floor, 135 W 50th St, New York, NY, 10020.
15. M. Cropper, "P-3B Orion (N426NA) Airborne Laboratory Experimenter Handbook, 548-HDBK-0001," Wallops Flight Facility, Wallops, VA, August 2010.
16. F. Rodriguez-Morales, et al, "An Advanced Multi-Frequency Radar Instrumentation Suite for Polar Research." Submitted to IEEE Transactions of Geoscience and Remote Sensing.
17. W. Donovan, "The Design of an Uninhabited Air Vehicle for Remote Sensing in the Cryosphere," M.S. Thesis, Aerospace Engineering Department, University of Kansas, 2007.
18. Raju G; Xin W; Moore RK; "Design, development, field observations, and preliminary results of the Coherent Antarctic Radar Depth Sounder (CARDS) of the University of Kansas, U.S.A.," *Journal of Glaciology*, 36(123), pp. 247-254, 1990.

19. J. Li, "Mapping of Ice Sheet Deep Layers and Fast Outlet Glaciers with Multi-Channel-High-Sensitivity Radar," Ph.D. dissertation, Department of Electrical Engineering and Computer Science, University of Kansas, Lawrence, KS, 2009.
20. C. Lewis, A. Patel, H. Owen, F. Rodriguez-Morales, et. al, "A Radar Suite for Ice Sheet Accumulation Measurements and Near-Surface Internal Layer Mapping," *International Geoscience and Remote Sensing Symposium*, Vol. 5, pp. 441-444, July 2009.
21. B. Panzer, C. Leuschen A. Pate, T. Markus, S. Gogineni, *Ultra-Wideband Radar Measurements of Snow Thickness Over Sea Ice*, 2010 IEEE Geosci. Remote Sens. Intl. Symp. pp. 3130-3133.
22. C. Lewis, "Airborne UHF Radar for Fine Resolution Mapping of Near-Surface Accumulation Layers in Greenland and West Antarctica", M.S. Thesis, *EECS Department, University of Kansas*, 2010.
23. J.S. Abner, "Lighter-than-air Platforms for Small-format Aerial Photography," *Transactions of the Kansas Academy of Science*, Vol. 107, No. 1 and 2, pp. 39-44, 2004.
24. J.B. Campbell, *Introduction to Remote Sensing*, The Guilford Press, 5th ed., 21 June 2011.
25. J.R. Eastman, "Guide to GIS and Images Processing, Volume 1," Clark Labs, May 2001.
26. "CAO Systems," *Carnegie Airborne Observatory Web Site*, [<http://cao.stanford.edu/?page=home>], retrieved 6 September 2012.
27. D. Haddad, "High-Resolution Digital Topography in Arizona," [http://azgeology.azgs.az.gov/archived_issues/azgs.az.gov/arizona_geology/summer10/article_earthscience%20.html], retrieved 7 September 2012.
28. G.P. Asner, D.E. Knapp, T. Kennedy-Bowdoin, M.O. Jones, R.E. Martin, J. Boardman, C. B. Field, "Carnegie Airborne Observatory: In-flight Fusion of Hyperspectral Imaging and Waveform Light Detection and Ranging

- (wLiDAR) for Three-dimensional Studies of Ecosystems,” *Journal of Applied Remote Sensing*, Vol. 1, 13 September 2007.
29. G.P. Asner and S.R. Levick, “Landscape-Scale Effects of Herbivores on Treefall in African Savannas,” *Ecology Letters*, [doi:10.1111/j.1461-0248.2012.01842.x], 2012.
30. J.-B. Feret and G.P. Asner, “Tree Species Discrimination in Tropical Forests Using Airborne Imaging Spectroscopy,” *IEEE Transactions on Geoscience and Remote Sensing*, Issue 99, pp. 1-12, 2012.
31. A.F. Chase, D.Z. Chase, J.F. Weishampel, J.B. Drake, R.L. Shrestha, K.C. Slatton, J.J. Awe, W.E. Carter, “Airborne LiDAR, Archaeology, and the Ancient Maya Landscape at Caracol, Belize,” *Journal of Archaeological Science*, Vol. 38, pp. 387-398, 2011.
32. “Skyvan – Research Aircraft,” *Helsinki University of Technology’s Laboratory of Space Technology Web Site*, [http://radio.aalto.fi/en/research/space_technology/skyvan-research_aircraft/], retrieved 7 September 2012.
33. “Gulfstream III Multi-Role Cooperative Research Platform,” *Dryden Flight Research Center Web Site*, [<http://www.nasa.gov/centers/dryden/research/G-III/index.html>], retrieved 6 September 2012.
34. J. Kainulainen, T. Auer, J. Pihlflyckt, J. Kettunen, and M.T. Hallikainen, “Helsinki University of Technology L-Band Airborne Synthetic Aperture Radiometer,” *IEEE Transactions on Geosciences and Remote Sensing*, Vol. 46, No. 3, pp. 717-726, March 2008.
35. K. Rautiainen, R. Butora, T. Auer, I. Mononen, J. Salminen, S. Tauriainen, M. Hallikainen, J. Uusitalo, and P. Jukkala, “The Helsinki University of Technology/Ylinen Electronics Airborne L-band Interferometric Radiometer,” *Geoscience and Remote Sensing Symposium*, Vol.7, pp.2978-298, 2000.

36. S. Hensley, H. Zebker, C. Jones, T. Michel, R. Muellerschoen, B. Chapman, "First Deformation Results Using the NASA/JPL UAVSAR Instrument," *2nd Asian-Pacific Conference on Synthetic Aperture Radar*, pp. 1051-1055, October 2009.
37. C.E. Jones, B. Minchew, B. Holt, and S. Hensley, "Studies of the *Deepwater Horizon* Oil Spill with the UAVSAR Radar," *Geophysical Monograph Series*, Vol. 195, pp. 33-50, 2011.
38. M.E. Paters, D.D. Blankenship, S.P. Carter, S.D. Kempf, D.A. Young, and J.W. Holt, "Along-Track Focusing of Airborne Radar Sounding Data From West Antarctica for Improving Basal Reflection Analysis and Layer Detection," *IEEE Trans. on Geoscience and Remote Sensing*, Vol. 45, No. 9, September 2007.
39. "UTIG Aerogeophysical Systems", *Institute for Geophysics Web Site*, [<http://www.ig.utexas.edu/>], retrieved 13 April 2013.
40. D. Steinhage, U. Nixdorf, U. Meyer, and H. Miller, "Subglacial Topography and Internal Structure of Central and Western Dronning Maud Land, Antarctica, Determined from Airborne Radio Echo Sounding," *Journal of Applied Geophysics*, Vol. 47, No. 3-4, pp. 183-189, July 2001.
41. "Aircraft", Alfred Wegener Institute Web Site, http://www.awi.de/en/infrastructure/aircraft/research_aircraft/. Retrieved 7 June 2013, 9:22 pm.
42. NATO Task Group RTO/SET-087/RTG-50, "Vibrating Antennas and Compensation Techniques", *RTO Technical Report, Final Report of Task Group 50*, October 2008.
43. C. Wang, B. Duan, F. Zhang, and M. Zhu, "Analysis of Performance of Active Phased Array Antennas with Distorted Plane Errors," *Int'l Journal of Electronics*, Vol. 96, No. 5, pp. 549-559, May 2009.
44. A. Ossowska, J.H. Kim, and W. Wiesbeck, "Influence of Mechanical Antenna Distortions on the Performance of the HRWS SAR System,"

- Geoscience and Remote Sensing Symposium, 2007, pp. 2152-2155, July 2007.
45. C.S. Wang, B.Y. Duan, F.S. Zhang, and M.B. Zhu, "Coupled Structural-Electromagnetic-Thermal Modeling and Analysis of Active Phased Array Antennas," *IET Microwaves, Antennas & Propagation*, Vol. 4, No. 2, pp. 247-257, 2010.
 46. J.J.M. de Wit, W.L. van Rossum, M.P.G. Otten, and A.G.P. Koekenberg, "Concept for Measuring and Compensating Array Deformation," *Proceedings of the 4th European Radar Conference*, Munich, Germany, pp. 55-58, October 2007.
 47. H.S.C. Wang, "Performance of Phased-Array Antennas with Mechanical Errors," *IEEE Transactions on Aerospace and Electronic Systems*, Vol. 28, No. 2, pp. 535-545, April 1992.
 48. T.W. Murphy, E.M. Cliff, S.A. Lane, "Matching Space Antenna Deformation Electronic Compensation Strategies to Support Structure Architectures," *IEEE Transactions on Aerospace and Electronic Systems*, Vol. 46, No. 3, July 2010.
 49. P. Knott, C. Locker, and S. Algermissen, "Antenna Element Design for a Conformal Antenna-array Demonstrator," *2011 IEEE Aerospace Conference*, 5-12 March 2011.
 50. P. Knott, C. Locker, S. Algermissen, W. Gruner, "Research on Vibration Control and Structure Integration of Antennas in NATO/RTO/SET-131," *2010 IEEE Antennas and Propagation Society International Symposium*, 11-17 July 2010.
 51. B.P. Smallwood, "Structurally Integrated Antennas on a Joined-Wing Aircraft," Master's Thesis, Air Force Institute of Technology, March 2003.
 52. D.J. Lucia, "The SensorCraft Configurations: A Non-Linear AeroServoElastic Challenge for Aviation," *48th AIAA Structures, Structural Dynamics, and Materials Conference*, 18-21 April 2005.

53. B.P. Hallissy, C.E.S. Cesnik, , “High-fidelity Aeroelastic Analysis of Very Flexible Aircraft,” *52nd AIAA Structures, Structural Dynamics, and Materials Conference*, 4-7 April 2011.
54. F.A. Kimler III, R.A. Canfield, “Structural Design of Wing Twist for Pitch Control of Joined Wing SensorCraft,” *11th AIAA Multidisciplinary Analysis and Optimization Conference*, 6-8 September 2006.
55. B.J. Adams, “Structural Stability of a Joined-Wing SensorCraft,” M.S. Thesis, *Air Force Institute of Technology*, June 2007.
56. G.W. Reich, D.E. Raveh, P.S. Zink, “Application of Active-Aeroelastic-Wing Technology to a Joined-Wing SensorCraft,” *Journal of Aircraft*, Vol. 41, No. 3, May-June 2004.
57. E.D. Hauge, R.I. Ridgway, C.H. Hightower, R.C. Warren, “Structural Deformation Compensation System for Large Phased-Array Antennas,” *United States Patent, Patent No. US 6,333,712 B1*, 25 December 2001.
58. R.L. Cravey, E. Vedeler, L. Goins, W.R. Young, and R.W. Lawrence,” Structurally Integrated Antenna Concepts for HALE UAVs,” *NASA Technical Memorandum NASA/TM-2006-214513*, October 2006.
59. G.H. Emmons, “Compensating for Groundplane Deformations of a Space-Based Radar to Improve Clutter Cancellation Performance,” *Lincoln Laboratory Technical Report 931*, 5 November 1991.
60. H. Haber and Q. Shi, “Direction Finding in Array Geometry Uncertainty,” *Antennas and Propagation Society International Symposium, 1988*. AP-S Digest, Vol. 1, pp. 258-261, June 1988.
61. P. Knott, "Deformation and Vibration of Conformal Antenna-arrays and Compensation Techniques," *Paper presented at Multifunctional Structures/Integration of Sensors and Antennas*, Paper 19, Neuilly-sur-Seine, France, 2006.
62. H. Schippers, J.H. van Tongeren, P. Knott, T. Deloues, P. Lacomme, and M.R. Scherbarth, "Vibrating Antennas and Compensation Techniques

- Research in NATO/RTO/SET 087/RTG 50," *IEEE Aerospace Conference*, 3-10 March 2007.
63. H. Schippers, J.H. van Tongeren, G. Vos, "Development of Smart Antennas on Vibrating Structures of Aerospace Platforms," *Paper presented at Multifunctional Structures/Integration of Sensors and Antennas*, Paper 20, Neuilly-sur-Seine, France, 2006.
64. B. Svensson, M. Lanne, and J. Wingard, "Element Position Error Compensation in Active Phased Array Antennas," *2010 Proceedings of the Fourth European Conference on Antennas and Propagation*, 2010.
65. N.A. Lehtomaki, "Compensation of Adaptive Arrays," *Proceedings from Ocean Technologies and Opportunities in the Pacific for the 90's*, 1-3 October 1991.
66. N. Kojina, K. Shiramatsu, I. Chiba, T. Ebisui, N. Kurihara, "Measurement and Evaluation Techniques for An Airborne Active Phased Array Antenna," *IEEE International Symposium on Phased Array Systems and Technology*, 1996.
67. "E-2C/D Hawkeye, United States of America," *Naval Technology Web Site*, [<http://www.naval-technology.com/projects/e2-hawkeye/>], retrieved 14 April 2013.
68. J. Grizim, A. Lomes, Y. Wagman, S. Ron, H. Richman, A. Reich, and D. Rabia, "Phased Array Radar Antenna Having Reduced Search Time and Method for Use Thereof," *US Patent No. US 7,928,890 B2*, 19 April 2011.
69. "CAEW Conformal Airborne Early Warning Aircraft, Israel," *Air Force Technology Web Site*, [<http://www.airforce-technology.com/projects/caew/caew7.html>], retrieved 14 April 2013.
70. "S100B Argus Airborne Early Warning and Control (AEW&C) Aircraft, Sweden," *Airforce Technology Web Site*, [http://www.airforce-technology.com/projects/s100b_argus/], retrieved 14 April 2013.

71. D.K. Fenner and W.F. Hoover Jr., "Test Results of a Space-Time Adaptive Processing System for Airborne Early Warning Radar," *Proceedings from the IEEE National Radar Conference*, 13-16 May 1996.
72. J. Ward, "Space-Time Adaptive Processing for Airborne Radar," *International Conference on Acoustics, Speech, and Signal Processing*, 9-12 May 1995.
73. H. Wang, "Overview of Space-Time Adaptive Processing for Airborne Radars," *Proceedings from the CIE International Conference of Radar*, 1996.
74. M. Rangaswamy, "An Overview of Space-Time Adaptive Processing for Radar," *Proceeding of the International Radar Conference*, pp. 45-50, September 2003.
75. D.C. Braunreiter, H.-W. Chen, M.L. Cassabaum, J.G. Riddle, A.A. Samuel, J.F. Scholl, and H.A. Schimtt, "On the Use of Space-Time Adaptive Processing and Time-Frequency Data Representation for Detection of Near-Stationary Targets in Monostatic Clutter," *Proceedings from the Tenth IEEE Workshop on Statistical Signal and Array Processing*, pp. 427-475, 2000.
76. R.L. Cravey, E. Vedeler, L. Goins, R.W. Young, and R.W. Lawrence, "Structurally Integrated Antenna Concepts for the HALE UAVs," *NASA Technical Memorandum 2006-214513*, Langley Research Center, October 2006.
77. K. Gustafsson, F. McCarthy, A. Paulraj, "Mitigation of Wing Flexure Induced Errors for Airborne Direction-Finding Applications," *IEEE Transactions on Signal Processing*, Vol. 44, No. 2, February 1996.
78. C.A. Balanis, *Antenna Theory, Analysis and Design*, 3rd ed., Hoboken, NJ, Wiley, 2005.
79. W.J. Jin, "A Computational Study of Icing Effects on the Performance of an S-Duct Inlet", Ph.D. Dissertation, Department of Aerospace Engineering, University of Kansas, 2009.

80. R. Hale, E. Arnold, W. Liu, K. Po, B. Kaushik, K. Po, "Aerodynamic and Structural Analysis of the P-3 Antenna Assembly," *CRISIS Technical Report*, Department of Aerospace Engineering, University of Kansas, February 2010.
81. K. Demarest, *Engineering Electromagnetics*, 1st ed., Prentice Hall, Upper Saddle River, NJ, 1998.
82. D.W. Pozar, *Microwave Engineering*, 2nd ed. John Wiley & Sons, New York, 2005.
83. C. You, M.M. Tentzeris, and W. Hwang, "Multilayer Effects on Microstrip Antennas for Their Integration with Mechanical Structures," *IEEE Transactions on Antennas and Propagation*, Vol. 55, No. 4, April 2007.
84. Y-T. Jean-Charles, V. Ungvichian, and J.A. Barbosa, "Effects of Substrate Permittivity on Planar Inverted-F Antenna Performances," *Journal of Computers*, Vol. 4, No. 7, pp. 610-614, July 2009.
85. D. Kozakoff, *Analysis of Radome Enclosed Antennas*, 2nd ed., Artech House, Norwood, MA, 2009.
86. F. Rodriguez-Morales, et. al., "Development of a Multi-Frequency Airborne Radar Instrumentation Package for Ice Sheet Mapping and Imaging," *IEEE Microwave Symposium Digest*, pp. 157-160, May 2010.
87. K. Byers, "Integration of a 15-Element, VHF Bow-Tie Antenna-array into an Aerodynamic Fairing on a NASA P-3 Aircraft," Master's Thesis, Department of Electrical Engineering, University of Kansas, 2011.
88. I.M. Howat, I. Joughin, S. Tulaczyk, and S. Gogineni, "Rapid Retreat and Acceleration of Helheim Glacier, East Greenland," *Geophysical Research Letters*, Vol. 32, L22502, [DOI:10.1029/2005GL024737], 2005.
89. I. Joughin, W. Abdalati, and M. Fahnestock, "Large Fluctuations in Speed on Greenland's Jakobshavn Isbrae Glacier," *Nature*, Vol. 432, pp. 608-610, December 2004.

90. E. Rignot, and P. Kanagaratnam, "Changes in the Velocity Structure of the Greenland Ice Sheet," *Science*, Vol. 311, No. 5736, pp. 986-990, February 2006.
91. E. Rignot, G. Casassa, P. Gogineni, W. Krabill, A. Rivera, and R. Thomas, "Accelerated Ice Discharge from the Antarctic Peninsula following the Collapse of the Larsen B Ice Shelf," *Geophysical Research Letters*, Vol. 31, L18401, [DOI: 10.1029/2004GL020697], 2004.
92. A. Shepherd, D.J. Wingham, and J.A.D. Mansley, "Inland Thinning of the Amundsen Sea Sector, West Antarctica," *Geophysical Research Letters*, Vol. 29, 1364, [DOI: 10.1029/2001GL014183], 2002.
93. R. Hale, E. Arnold, W. Lui, "Structural Analysis of the MCoRDS Antenna Assembly," *CRISIS Technical Report*, September 2009.
94. Federal Aviation Regulations, Part 25.
95. *Patran/NASTRAN*, Version 2008r1, MSC Software, Santa Ana, CA.
96. R. Hale, E. Arnold, M. Ewing, and W. Liu, "Method for Design and Analysis of Externally Mounted Antenna Fairings in Support of Cryospheric Surveying," *AIAA Structures, Structural Dynamics and Materials Conference*, April 2011.
97. *Advanced Aircraft Analysis*, Version 3.2, DAR Corporation, Lawrence, KS.
98. Michael Studinger, "Past Campaigns," Operation Ice Bridge Website, Available:http://www.nasa.gov/mission_pages/icebridge/news/past.html, retrieved: 27 August 2012.
99. K. Jezek, "ICEBRIDGE 2009 Ice Thickness Data Validation: Pine Island and Thwaites Glaciers," *University of Kansas Subcontract Final Report*, July 2010.
100. "Past Campaigns," *Operation Ice Bridge Website*, retrieved: 27 August 2012. Available: http://www.nasa.gov/mission_pages/icebridge/index.html.
101. Lockheed Aircraft Corporation, "Limit Wing Deflections (from W.R.F.) vs. Wing Stations," Received from P-3B Ops Engineers, Martin Nowicki.

102. Panzer, Ben, "P-3 Bomb Bay Panel Simulations," Internal CRISIS Report, 28 January 2010.
103. J. Roskam, *Airplane Flight Dynamics and Automatic Flight Controls*, DARCorporation, Lawrence, KS, 1995.
104. Alcoa Structural Handbook: A Design Manual for Aluminum, Aluminum Company of America, Pittsburgh, PA, 1956
105. T. Simpson, "The Theory of Top-Loaded Antennas: Integral Equations for the Currents," *IEEE Transactions on Antennas and Propagation*, Vol. 19, No. 2, pp. 186-190, March 1971.
106. K. Byers, S. Seguin, and C. Leuschen, "Near-Field Mutual Coupling Degradation on Antenna Bandwidth for an Airborne Ice-Penetrating and Imaging Radar," *IEEE Instrumentation and Measurement Technology Conference*, May 2011.
107. K. Byers, A.R. Harish, S. Seguin, C. Leuschen, F. Rodriguez-Morales, J. Paden, E. Arnold, R. Hale, "A Modified Wideband Dipole Antenna for an Airborne VHF Ice Penetrating Radar," *IEEE Transactions on Instrumentation and Measurement*, Vol. 61, No. 5, pp. 1435-1444, February 2012.
108. "Science: Flight Docs," *Operation Ice Bridge Website*, retrieved: 31 August 2012. Available: <http://espo.nasa.gov/missions/oib/mission-flight-docs>.
109. E. Powers, P. Wheeler, D. Judge, D. Matsakis, "Hardware Delay Measurements and Sensitivities in Carrier Phase Time Transfer," *30th Annual Precise Time and Time Interval Meeting*, December 1998.
110. K. Czuba and D. Sikora, "Temperature Stability of Coaxial Cables," *Physical Aspects of Microwave and Radar Applications*, Vol. 119, No. 4, 2011.
111. Times Microwave Systems, "Current Innovations in Phase Stable Coaxial Design," *Microwave Product Digest*.

112. RF Parts Company, "Andrew Heliac Cable," *RF Parts Company Website*, <http://www.rfparts.com/old_site/heliac_FSJ150A.html>, retrieved 12:05 pm, 7 May 2013.
113. "HELIAX Phase Measured Cable Assemblies," HELIAX Coaxial Cables, <http://photos.imageevent.com/qdf_files/technicalgoodies/satcomengineer/Heliac%20Coax%20Specifications%20440-635.pdf>, pp. 588-590, retrieved 12:33pm, 7 May 2013.
114. C.L. Dolph, "A Current Distribution for Broadside Arrays Which Optimizes the Relationship Between Beamwidth and Side-Lobe Level," *Proceedings IRE and Waves and Electrons*, June 1946.
115. H. Yagi, "Beam Transmission of Ultra Short Waves," *Proceedings of IRE*, Vol. 26, No. 6, pp. 715-740, June 1928.
116. R. M. Fishender and E. R. Wiblin, "Design of Yagi Aerials," *Proceeding of the IEE, Part III: Radio and Communication Engineering*, Vol. 96, No. 39, pp. 5-12, January 1949.
117. A. Adams and D. Waren, "Dipole Plus Parasitic Element," *IEEE Transactions on Antennas and Propagation*, pp. 536-537, July 1971.
118. HFSS[®], Ansys, Inc. 2012, ver. 14.
119. Polar Electronic Industries Pty. Ltd. [Online]. Available: <http://www.polarelectronicindustries.com>.
120. C. Feng and Q. Jian, "A Novel Infinite Balun Used in Folded Dipole," *Proc. IEEE AP-S Int'l Symp.*, Montreal, QC, Canada, Vol. 1, 1990, pp. 547-548.
121. M.S. Smith, D.E.T. Nichols, "Design and Performance of a Vertical Range for Antenna Radiation Pattern Measurement Using Aircraft Scale Models," *Radio and Electronic Engineer*, Vol. 48, No. 5, pp. 209-214, 1978.
122. C.R. Birtcher, W. Sun, C.A. Balanis, G.C. Barber, "Scale Model Helicopter Antenna Pattern Measurements at ASU's EMAC Facility,"

- Antennas and Propagation Society International Symposium*, Vol. 3, pp. 1820-1823, 1993.
123. P.H. Pathak, "Origins of RFID Concepts in Early Wireless-based Scale Model Airborne Antenna Pattern Measurements," *Wireless Information Technology and Systems Conference*, pp. 1-4, 2012.
 124. H.-R. Chuang, L.-C. Kuo, "3-D FDTD Design Analysis of a 2.4-GHz Polarization-Diversity Printed Dipole Antenna With Integrated Balun and Polarization-Switching Circuit for WLAN and Wireless Communication Applications," *IEEE Transactions on Microwave Theory and Techniques*, Vol. 51, No. 2, February 2003.
 125. E. Arnold, J.B. Yan, J. Li, R. Hale, F. Rodriguez-Morales, and P. Gogineni, "Identification and Compensation of Aircraft Integration Effects in Wing-Mounted Phased Array for Ice Sheet Sounding," *Antenna Application Symposium*, September 2012.
 126. M.E. Cannon, H. Sun, T.E. Owen, and M.A. Meindl, "Assessment of a Non-Dedicated GPS Receiver System for Precise Airborne Attitude Determination," *Proceedings of the ION GPS-94*, pp. 645-654, 20-23 September 1994.
 127. M. Anttila, "Fatigue Life Estimation of an Aircraft Used in Airborne Geophysical Surveying," Master's Thesis, Helsinki University of Technology, 9 January 2008.
 128. EMQuest, ETS-Lindgren, 2011 Version 1.08.
 129. H. Steyskal, J.S. Herd, "Mutual Coupling Compensation in Small Array Antennas," *IEEE Transactions on Antennas and Propagation*, Vol. 38, No. 12, December 1990.
 130. F. Gross, *Smart Antennas for Wireless Communications with Matlab*, McGraw-Hill, New York, NY, 10121, 2005.
 131. C. M. Schmid, S. Schuster, R. Feger, A. Stelzer, "On the Effects of Calibration Errors and Mutual Coupling on the Beam Pattern of an Antenna

- Array,” *IEEE Transactions on Antennas and Propagation*. Accepted for publication.
132. I.J. Gupta and A.A. Ksienski, “Effects of Mutual Coupling on the Performance of Adaptive Arrays,” *IEEE Transactions on Antennas and Propagation*, Vol. 31, No. 5, September 1983.
 133. Z. Huang, C.A. Balanis, and C.R. Birtcher, “Mutual Coupling Compensation in UCAs: Simulation and Experiment,” *IEEE Transactions on Antennas and Propagation*, Vol. 54, No. 11, November 2006.
 134. J.B. Yan, J. Li, F. Rodriguez-Morales, R. Crowe, D. Gomez-Garcia, E. Arnold, J. Paden, C.J. Leuschen, S. Gogineni, “Measurements of In-Flight Cross-Track Antenna Patterns of Radar Depth Sounder/Imager,” *IEEE Transaction on Antennas and Propagation*, Vol. 60, No. 12, December 2012.
 135. *SignalCalc 730 Dynamic Signal Analyzer*, Data Physics Corporation, ver. 4.7.
 136. *LaveVIEW*, National Instruments.

APPENDIX A: NEAR-FIELD COUPLING RESULTS

Figure A.1 and Figure A.2 show the antenna S_{11} for various doubler locations for the smaller ($L=0.07\lambda$) doubler. Figure A.1 shows the results when the doublers are on a plane that is 0.5” below the antenna plane, and Figure A.2 shows the results for the doubler in plane with the antenna. The results in both figures are very similar to the results with the larger ($L=0.14\lambda$) doubler.

Figure A.3 is a continuation of Figure 7.8 with smaller doubler sizes. This figure shows the antenna S_{11} for various doubler lengths and offsets when doublers span the length of the antenna. These results support the design rule that antenna S_{11} becomes fairly invariant when doubler sizes are 0.125λ or smaller.

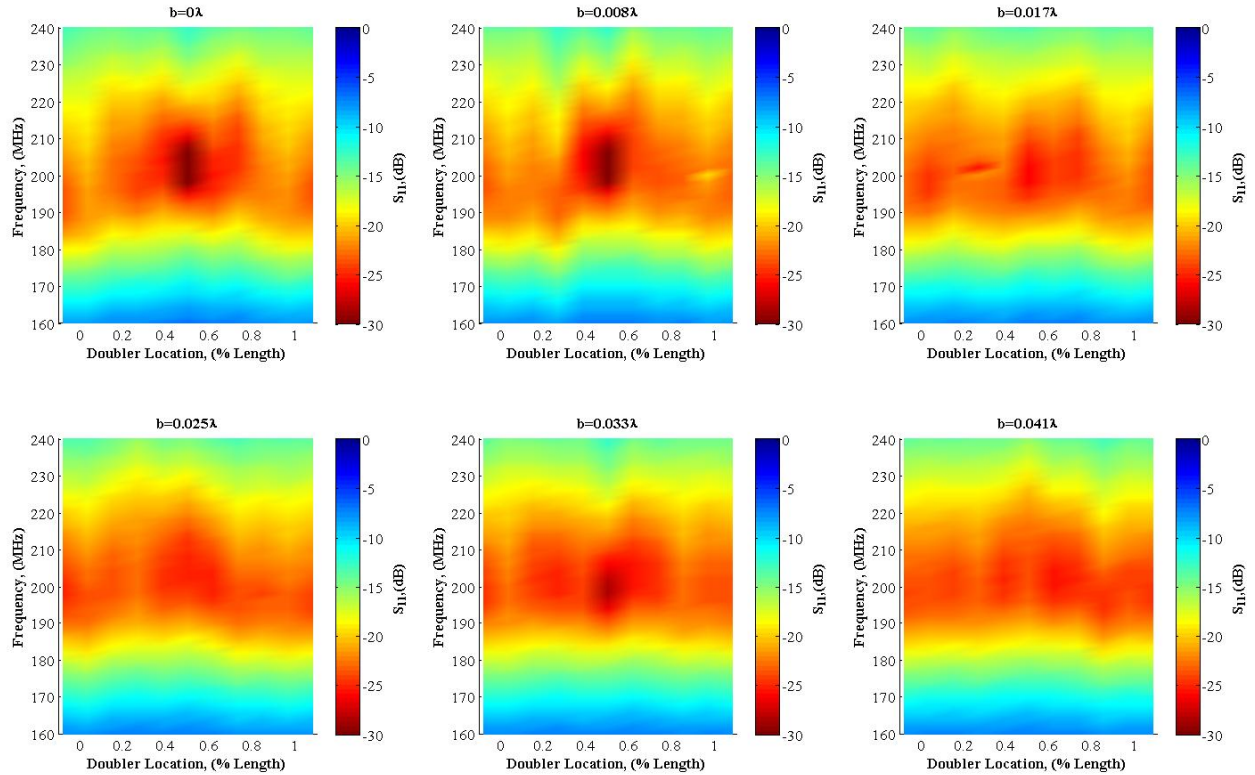


Figure A.1: Antenna S_{11} for Various Out-of-Plane Doubler Locations for Doubler $L=0.07\lambda$

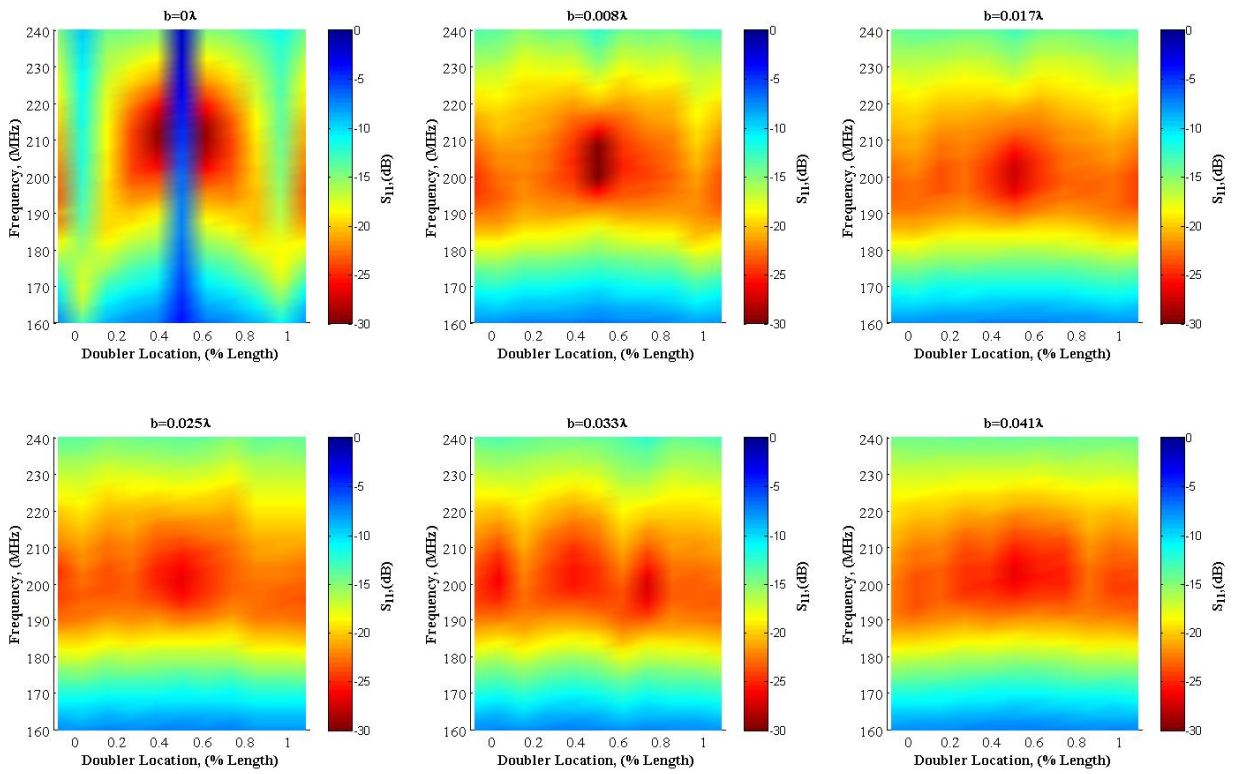


Figure A.2: Antenna S_{11} for Various In-Plane Doubler Locations for Doubler $L=0.07\lambda$

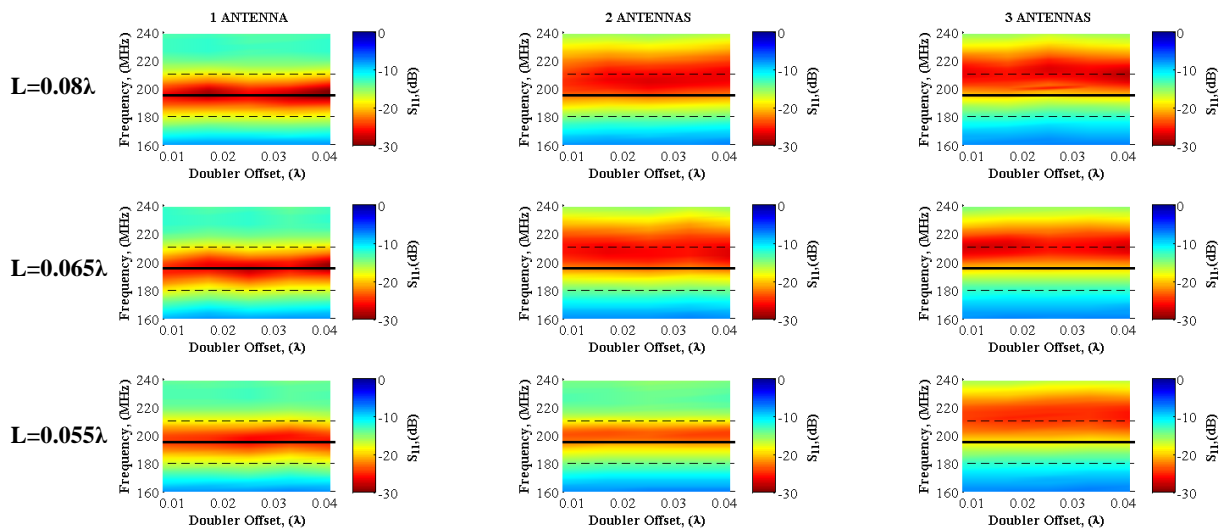


Figure A.3: Antenna S_{11} as a Function of Doubler Length and Offset for Configurations with 1, 2, and 3 Antennas

APPENDIX B: EXPECTED PERFORMANCE INCREASE DUE TO COMPENSATION METHOD

B.1 Collinear Array

Figure B.1 and Figure B.2 show the FM and SINR, respectively, for the collinear array with two nulls. The top plots in the figures show results for the uncompensated array and the bottom plots show the results for the compensated array. These results follow the same trends found in Section 10.6. Table B.1 gives a summary of the compensation performance for the collinear array with two nulls.

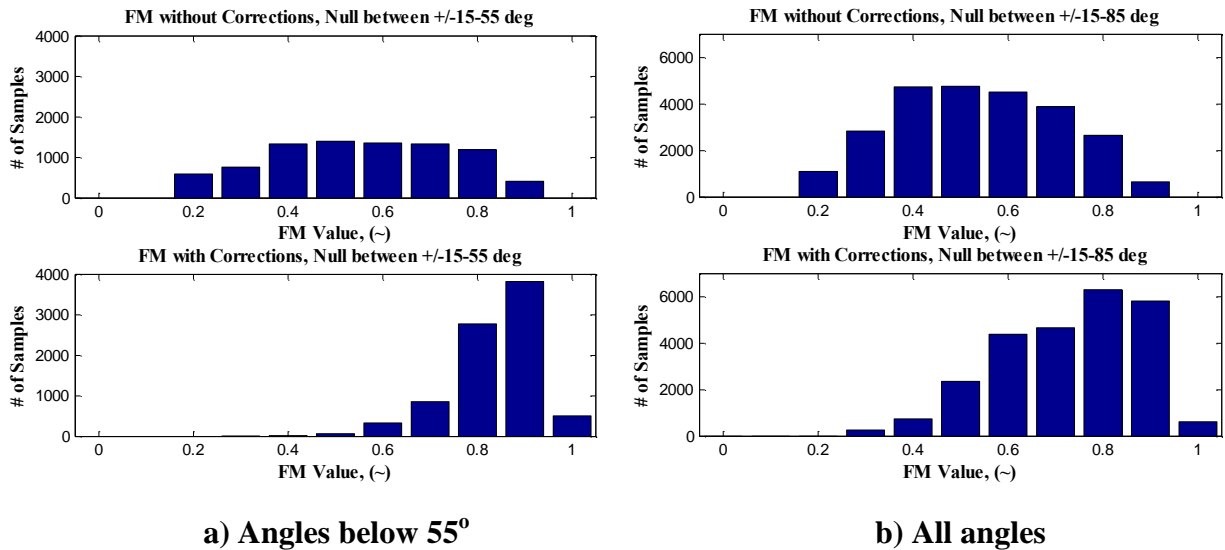
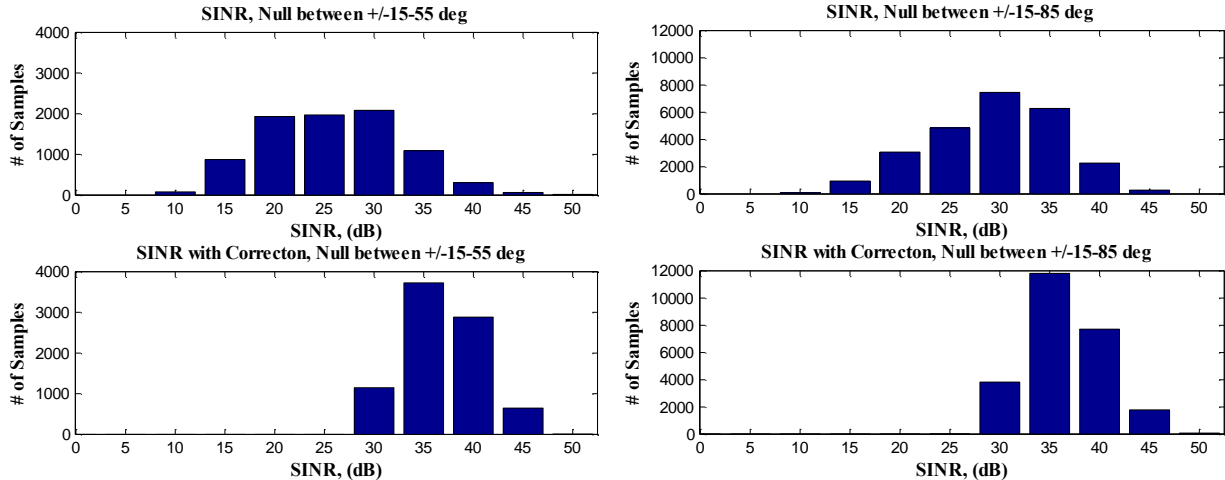


Figure B.1: Comparison of Collinear Array FM for Two Nulls Placed Below 55° (a) and at All Angles (b)



a) Angles below 55°

b) All angles

Figure B.2: Comparison of Collinear Array SINR for Two Nulls Placed Below 55° (a) and at All Angles (b)

Table B.1: Summary of Performance Statistics for Collinear Array and 2 Null

		All α					$\alpha=0.5-1.5$				
		FM (~)		SINR (dB)		SINR Incr.	FM (~)		SINR (dB)		SINR Incr.
		NC	C	NC	C		NC	C	NC	C	
Angles < 55°	Mean	0.60	0.88	28.5	39.3	10.9	0.71	0.89	31.4	40.0	8.6
	0.80	0.42	0.82	22.1	35.8		0.58	0.84	26.2	36.4	
	0.90	0.34	0.76	19.7	34.5		0.51	0.77	23.9	34.8	
All Angles	Mean	0.59	0.78	32.1	39.0	6.9	0.67	0.81	34.7	40.2	5.5
	0.80	0.41	0.64	26.2	35.5		0.54	0.69	29.9	36.9	
	0.90	0.36	0.56	22.9	34.2		0.49	0.61	26.9	35.6	

B.2 Parallel Array

Figures B.3-B.8 show the FM and SINR for the parallel array with one, two, and three nulls. The top plots in the figures show results for the uncompensated array and the bottom plots show the results for the compensated array. These results follow the same trends found in Section 10.6. Table B.2-B.3 give a summary of the compensation performance for the parallel array with one, two, and three nulls.

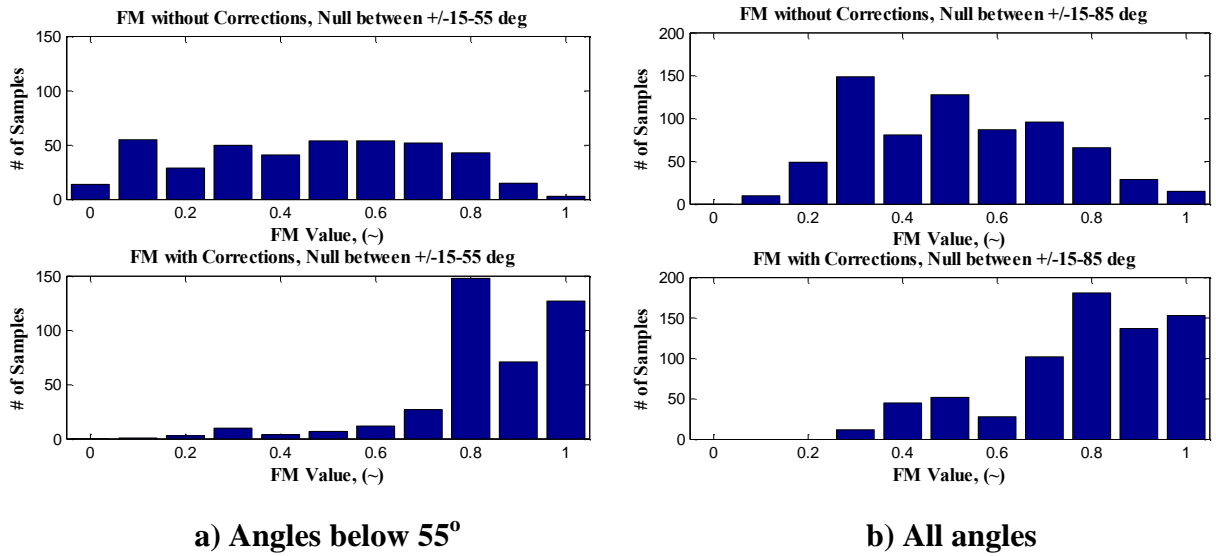


Figure B.3: Comparison of Parallel Array FM for One Null Placed Below 55° (a) and at All Angles (b)

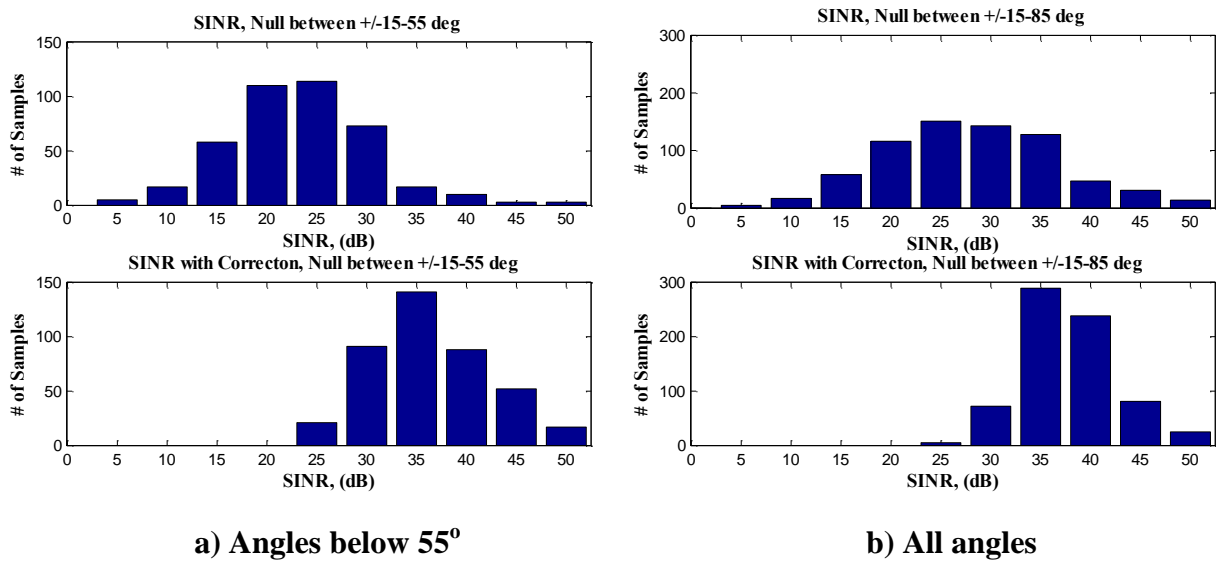
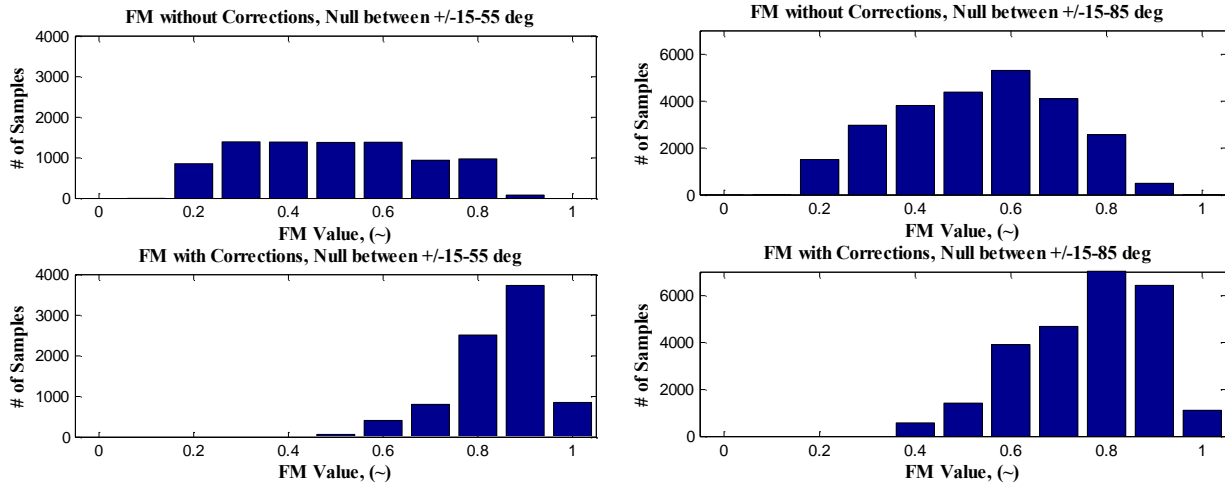


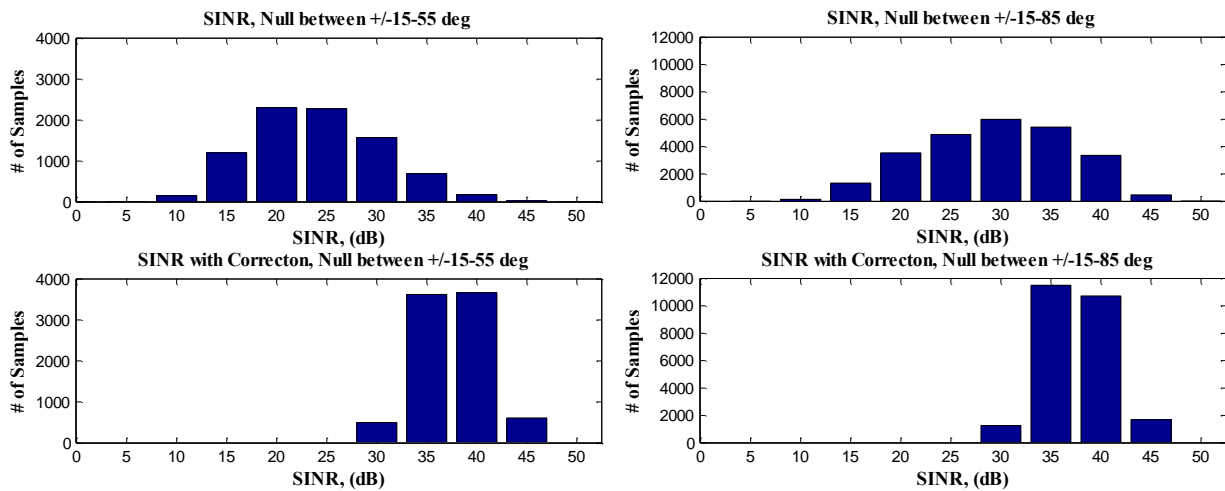
Figure B.4: Comparison of Parallel Array SINR for One Null Placed Below 55° (a) and at All Angles (b)



a) Angles below 55°

b) All angles

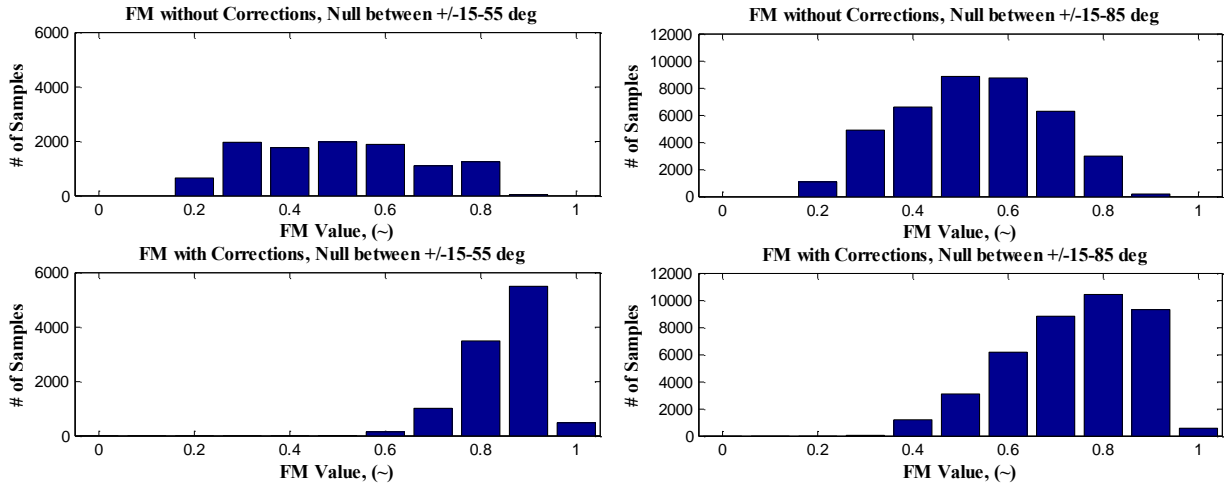
Figure B.5: Comparison of Parallel Array FM for Two Null Placed Below 55° (a) and at All Angles (b)



a) Angles below 55°

b) All angles

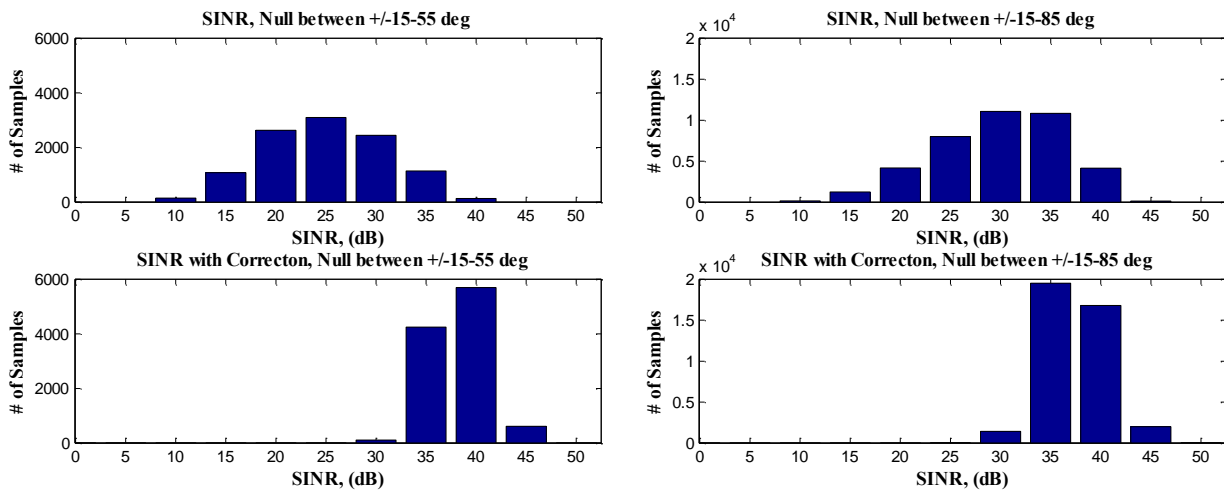
Figure B.6: Comparison of Parallel Array SINR for Two Null Placed Below 55° (a) and at All Angles (b)



a) Angles below 55°

b) All angles

Figure B.7: Comparison of Parallel Array FM for Three Null Placed Below 55° (a) and at All Angles (b)



a) Angles below 55°

b) All angles

Figure B.8: Comparison of Parallel Array SINR for Three Null Placed Below 55° (a) and at All Angles (b)

Table B.2: Summary of Performance Statistics for Parallel Array and 1 Null

		All α					$\alpha=0.5-1.5$				
		FM (~)		SINR (dB)		SINR Incr.	FM (~)		SINR (dB)		SINR Incr.
		NC	C	NC	C		NC	C	NC	C	
Angles < 55o	<i>Mean</i>	0.51	0.88	25.9	38.9	13.0	0.64	0.89	29.1	39.8	10.7
	<i>0.80</i>	0.26	0.83	20.1	33.9		0.49	0.83	24.0	34.6	
	<i>0.90</i>	0.19	0.71	16.9	32.0		0.40	0.77	21.3	33.5	
All Angles	<i>Mean</i>	0.56	0.82	30.6	40.2	9.6	0.65	0.84	33.4	40.8	7.4
	<i>0.80</i>	0.34	0.71	23.3	36.4		0.50	0.73	26.5	38.2	
	<i>0.90</i>	0.33	0.50	19.1	34.8		0.44	0.57	23.5	36.9	

Table B.3: Summary of Performance Statistics for Parallel Array and 2 Nulls

		All α					$\alpha=0.5-1.5$				
		FM (~)		SINR (dB)		SINR Incr.	FM (~)		SINR (dB)		SINR Incr.
		NC	C	NC	C		NC	C	NC	C	
Angles < 55o	<i>Mean</i>	0.55	0.89	26.5	40.2	13.7	0.66	0.90	29.7	40.6	11.0
	<i>0.80</i>	0.36	0.83	20.7	37.4		0.53	0.84	24.8	38.1	
	<i>0.90</i>	0.30	0.75	18.5	35.8		0.47	0.76	23.0	37.0	
All Angles	<i>Mean</i>	0.59	0.81	31.9	40.1	8.2	0.67	0.81	34.5	40.7	6.2
	<i>0.80</i>	0.41	0.69	25.0	37.4		0.54	0.69	28.6	38.4	
	<i>0.90</i>	0.35	0.61	21.7	36.0		0.49	0.61	25.8	37.4	

Table B.4: Summary of Performance Statistics for Parallel Array and 3 Nulls

		All α					$\alpha=0.5-1.5$				
		FM (~)		SINR (dB)		SINR Incr.	FM (~)		SINR (dB)		SINR Incr.
		NC	C	NC	C		NC	C	NC	C	
Angles < 55o	<i>Mean</i>	0.55	0.90	27.4	40.7	13.3	0.66	0.91	30.4	41.4	11.0
	<i>0.80</i>	0.38	0.84	22.0	38.4		0.54	0.86	25.9	39.3	
	<i>0.90</i>	0.31	0.80	19.6	37.2		0.50	0.81	23.8	38.3	
All Angles	<i>Mean</i>	0.58	0.79	32.3	40.0	7.6	0.66	0.80	34.7	40.7	6.0
	<i>0.80</i>	0.43	0.66	26.8	37.5		0.56	0.68	30.3	38.3	
	<i>0.90</i>	0.37	0.59	23.6	36.4		0.51	0.61	27.4	37.4	

APPENDIX C: PARALLEL ARRAY SENSITIVITY ANALYSIS

Figure C.1 shows the parallel array FM and FM standard deviation for steering vector phase and magnitude mismatches. Figure C.2 shows the parallel array SINR and SINR standard deviation for steering vector phase and magnitude mismatches. These results will be found to be very similar to the collinear array results in Section 10.5.2.

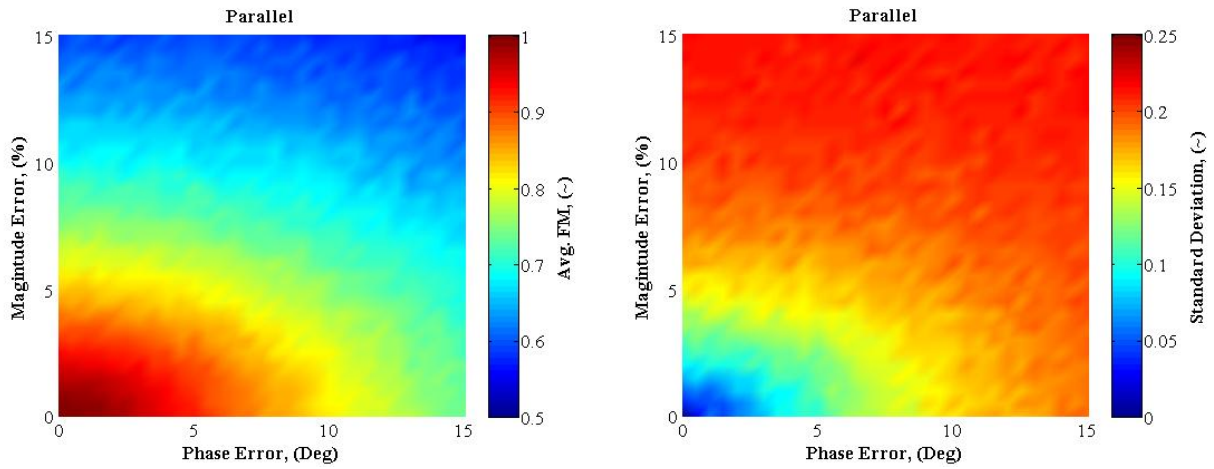


Figure C.1: Parallel Array FM Sensitivity for Steering Vector Magnitude and Phase Mismatch (left) and Sensitivity Standard Deviation (right)

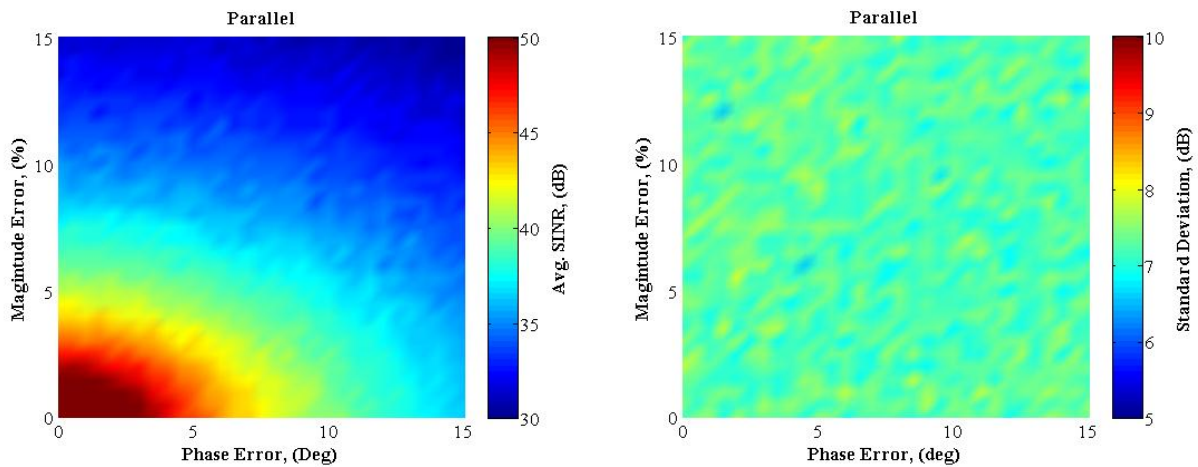


Figure C.2: Parallel Array SINR Sensitivity for Steering Vector Magnitude and Phase Mismatch (left) and Sensitivity Standard Deviation (right)

APPENDIX D: EFFECTS OF VIBRATION ON ARRAY PERFORMANCE

D.1 Introduction

Vibrations are not expected to have a significant impact on beam formation for wing mounted arrays used for ice sheet sounding because vibrations result in significantly smaller displacements as compared to displacement caused by the quasi-static flight loads. For antenna-arrays that operate at higher frequencies than the VHF depth-sounder, vibration could be a more significant issue. To identify the effects of vibration, particularly expected phase and amplitude variations on the CReSIS wing-mounted arrays, a shaker was attached to the scaled model and the wing was vibrated at various frequencies. To capture the effects of vibration, the CReSIS MCoRDS radar was used to record the signal while the array was excited. Because the MCoRDS radar operates at around 200 MHz and the resonance of the array antennas is 1.2 GHz, a frequency modulation board was designed and built by CReSIS electrical engineers. The board up-converted the 200 MHz signal to 1.2 GHz for the transmit antenna and down-converted the received signal fed back to the radar. Figure D.1 shows the block diagram for the radar setup for the tests.

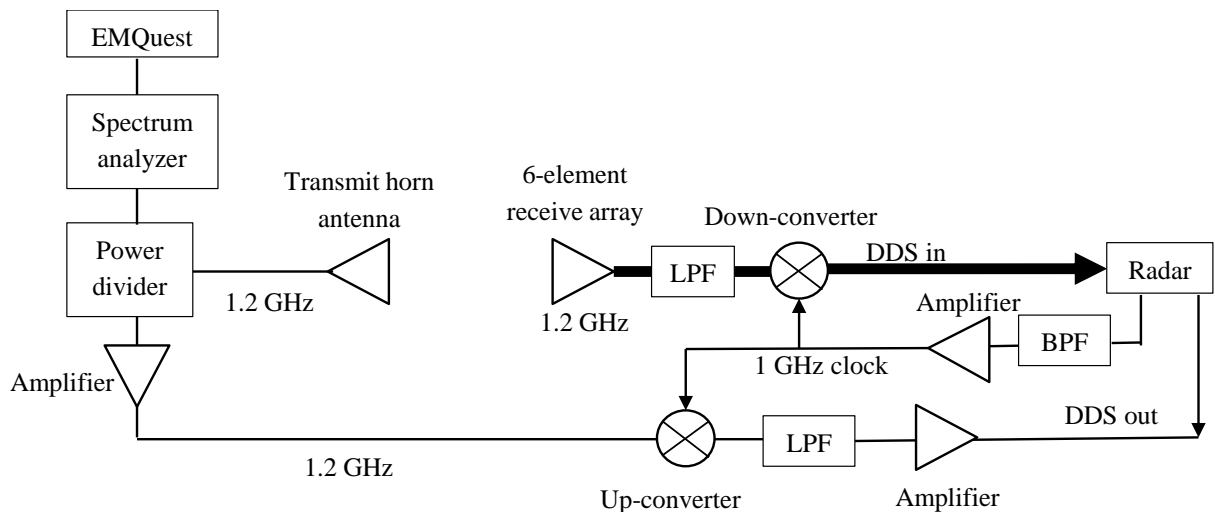


Figure D.1: Radar Block Diagram for Vibration Test

Figure D.2 is a photograph of the test setup. The radar was used to drive the double-ridge horn transmit antenna located on the opposite side of the chamber. The array was operated in receive mode, and data from all six channels was recorded by the radar as the shaker vibrated the

array. The one pound shaker was attached between the first and second antenna, and it was freely attached to a frame using a bungee cord. The shaker was driven using SignalCalc 730 Dynamic Signal Analyzer software [135].

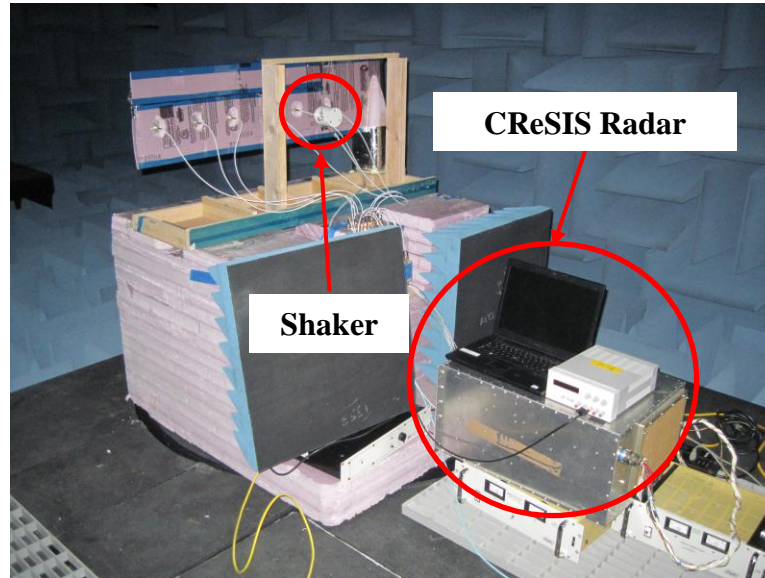


Figure D.2: Vibration Test Setup

The natural modes of the scaled array were identified visually. The first two modes of the array were found to occur at 3 Hz and 12 Hz. According to [127], the first bending mode of the real Twin Otter wing is expected to occur at 5.7 Hz. In the real data collected by the Twin Otter, there are oscillations in the phase data. It was originally thought that these oscillations were caused by the gust impulse response of the wing, and it was expected that the phase oscillation frequency would be the same as the first bending mode frequency. Later it was determined that the phase oscillation frequency spectrum had a normal distribution with most of the power concentrated below 10 Hz. CReSIS researchers concluded that the frequency distribution was representative of noise and seemed to have a direct relation to the ice surface condition. To help support the claim that the phase oscillations in the data are likely caused by surface conditions and not the vibration of the array, Section D.3 will present the frequency spectrum of the phase and amplitude data gathered during the vibration tests.

Four different vibrations were applied to the array and they include: 1) 3 Hz sine wave, 2) 12 Hz sine wave, 3) 100 Hz sine wave, and 4) random vibrations that ranged from 0-120 Hz. The first two frequencies were selected because they represent the first two modes of the scaled model. The 100 Hz frequency was selected because it is approximately the blade passage

frequency of the Twin Otter. Random vibrations were also tested to see if natural modes of the scaled model could be easily identified.

D.2 Phase and Amplitude Variations Due to Vibration

Figure D.3 shows the amplitude variations, as a percentage, and phase variations for each antenna when the array is not vibrating. Each port is normalized to itself, and the plots have been provided for reference. As would be expected there is very little variation in the absence of vibration.

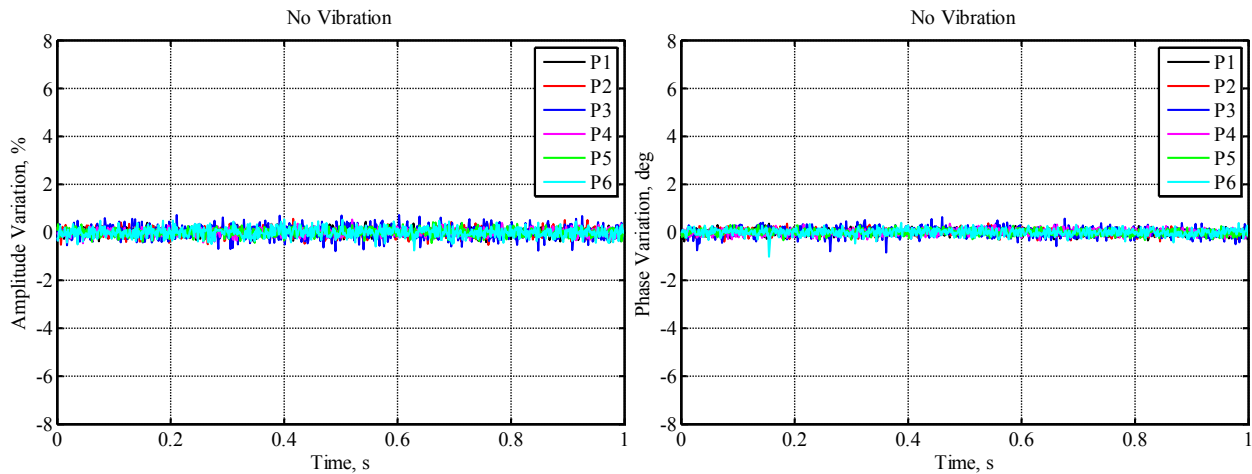


Figure D.3: Phase and Amplitude Variation of Each Antenna with No Vibration

Before beginning an in depth discussion on the expected phase and amplitude variations caused by vibration, some of the testing limitations must be identified. All tests were performed with the shaker in the same location (between P1 and P2). From the data gathered in the experiment, the location of the shaker appears to influence the results for P3. Figure D.4a shows the phase variation in all six ports with 3 Hz vibration, and Figure D.4b shows the frequency spectrum of P3 with a random vibration. From the phase variation plot it is evident that P3 is experiencing almost three times the variation as the other elements. The frequency spectrum plot distinctly shows that 3 Hz falls between two natural modes of this antenna. Though P3 is not located adjacent to the shaker, it is likely experiencing increased displacement due to its location and local natural frequencies.

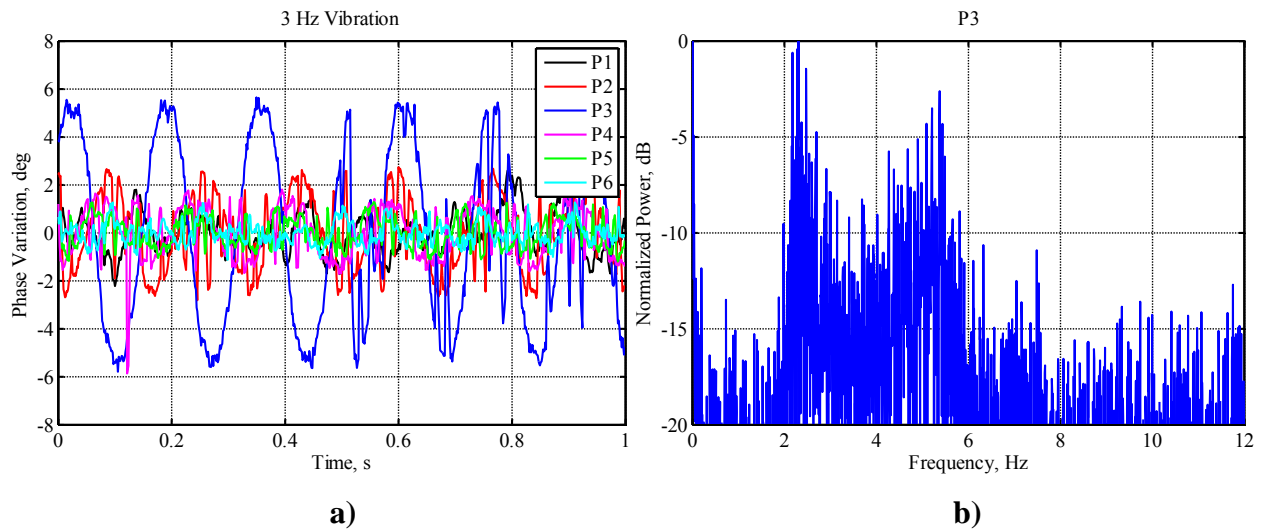


Figure D.4: Phase Variation for All Six Ports with 3 Hz Sine Vibrations (a) and Frequency Spectrum of P3 with Random Vibration

The purpose of this study was not to identify the structural responses of the wing, but instead identify trends in the radar data that are caused by the representative wing responses. As such the response from P3 will be omitted in the following phase and amplitude plots to not otherwise obscure the global trends in the array. Figure D.5 shows the phase variation of each antenna over a one second time interval for all four vibration cases. Each antenna phase has been normalized to its own mean. In all cases, the phase variation was kept within $\pm 4^\circ$. On average the 12 Hz vibration case has the largest phase variations across all ports and the random vibration has the smallest variation across all ports. For both the random and 100 Hz vibration cases, the phase variations were within 1° . Phase variations are expected to be much smaller at the higher excitation frequencies because the structure is less flexible and thus the element displacements are smaller.

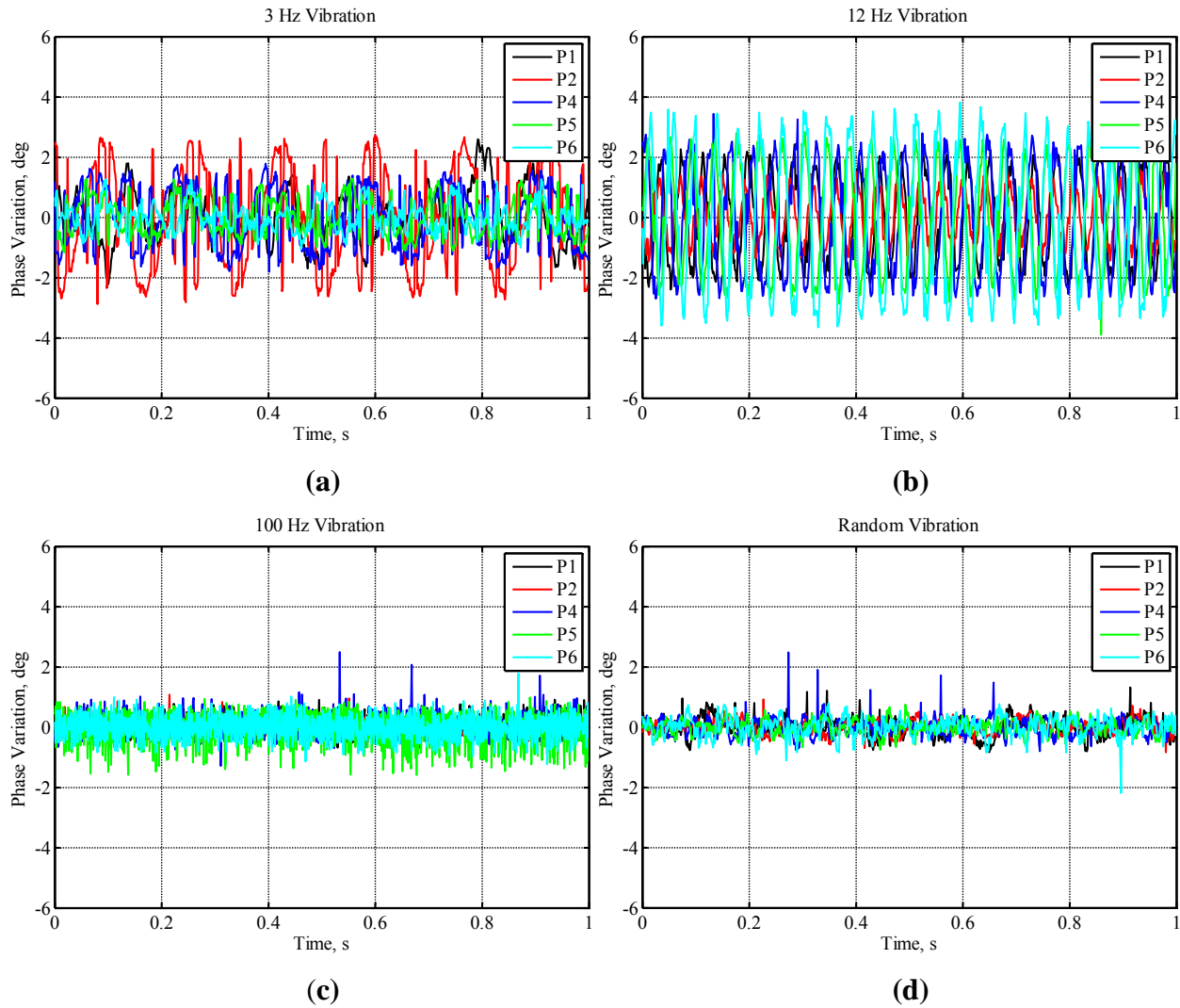


Figure D.5: Phase Variation for 3 Hz (a), 12 Hz (b), 100 Hz (c), and Random Vibration (d)

Figure D.6 shows the amplitude variations for each vibration case. Once again the 12 Hz vibration mode causes the largest variation (3.8 dB) across all antennas, and the random vibration caused the smallest variation (0.8 dB). Again it is expected that larger variations occur when the structure is more flexible. It is noted that the variations were within ± 0.4 dB for all cases.

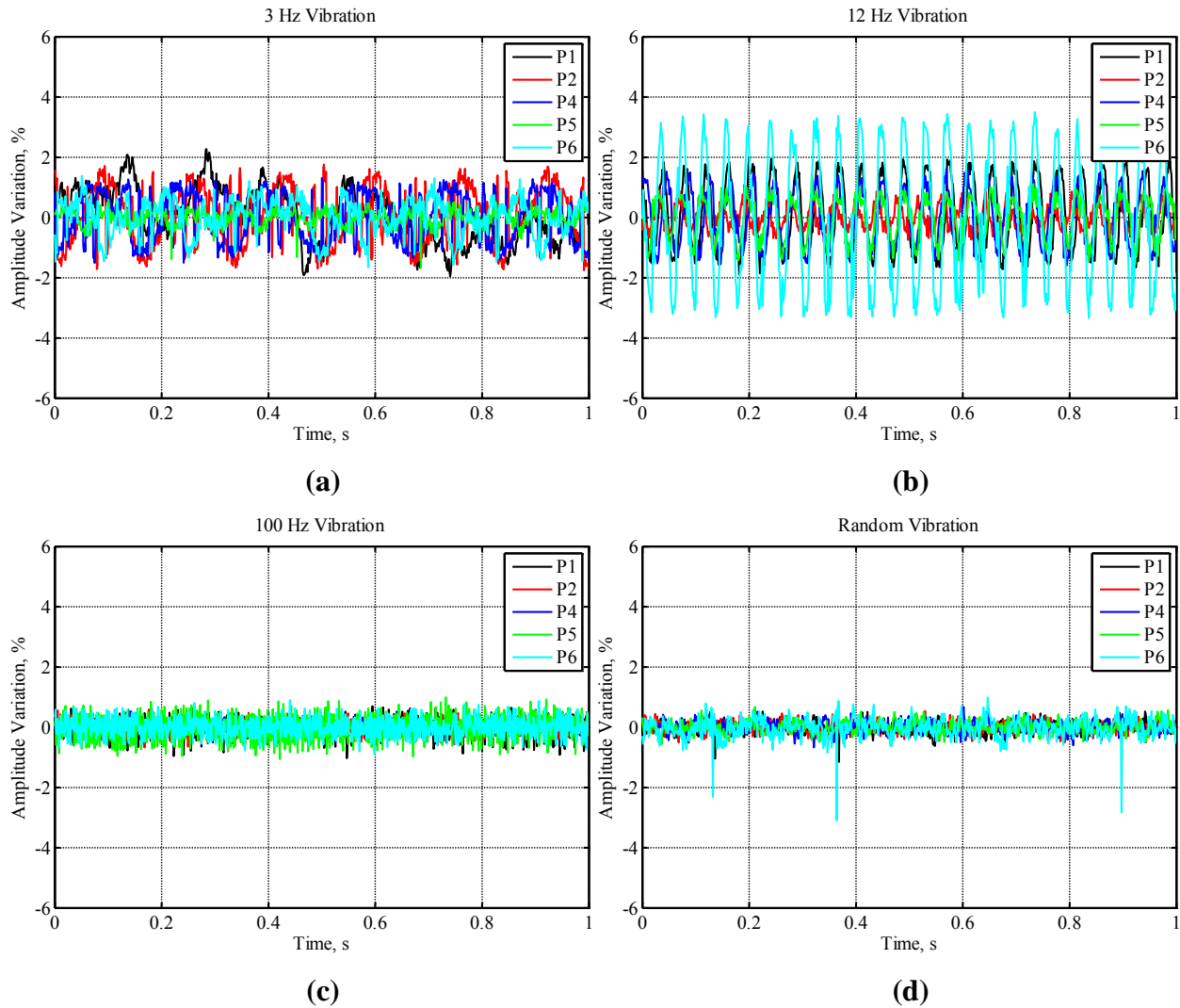


Figure D.6: Amplitude Variation for 3 Hz (a), 12 Hz (b), 100 Hz (c), and Random Vibration (d)

The amplitude variations have been presented as percent variations so that they can be readily related to sensitivity plots in Section 10.5.2. According to the sensitivity plots, for the worst case phase variation of 4° and worst case amplitude variation of 3%, the FM is expected to be at least 0.9 and the SINR is expected to be at least 46 dB with vibration. As such even the worst vibration cases are not expected to significantly degrade the beamformer performance. In general, the vibration environment for wing-mounted arrays will be dominated by higher frequency vibrations caused by the engine. Occasional gusts will induce some vibration at the lower order modes, but these vibrations will dampen quickly. With this in mind, the actual beamforming degradation experienced by real wing-mounted arrays is expected to be even less.

D.3 Phase and Amplitude Frequency Spectrum

Figure D.7 shows the frequency spectrum of the phase data for each antenna and each vibration case. The frequency of the dominating excitation can be readily identified in all cases.

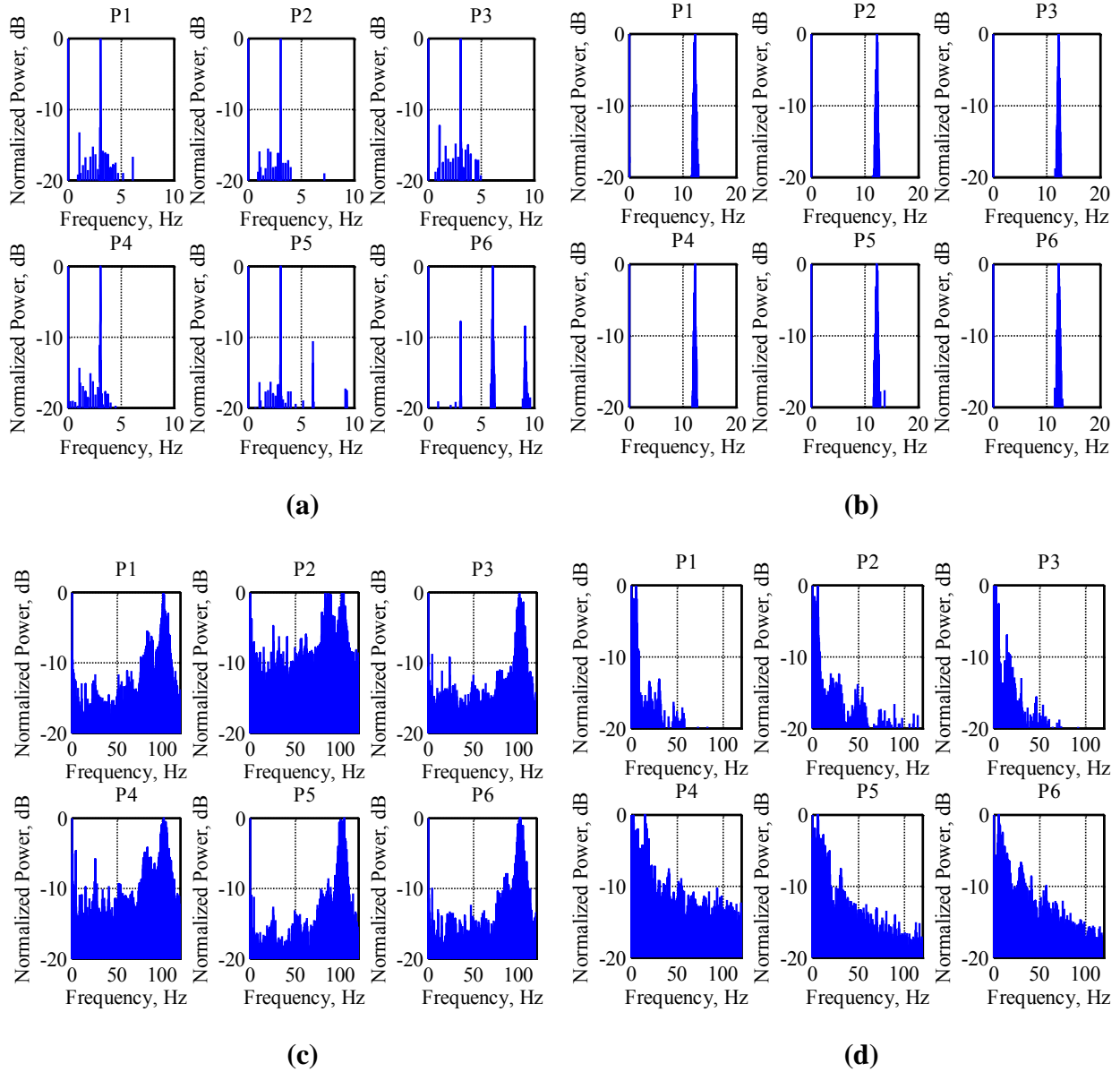


Figure D.7: Spectrum for 3 Hz (a), 12 Hz (b), 100 Hz (c), and Random Vibration (d)

Other modes present in the structure can also be identified in the data. In the 3 Hz vibration case there appears to be a mode at 6 Hz and 9 Hz in the two outboard antennas, and in the 100 Hz vibration case an 80 Hz mode seems to be present in all the antennas. Again, it is important to note that the goal of this study was not to identify the natural modes of the scaled model, but

rather to verify that the dominating vibration source can be identified in the data. In the case of random vibration, a majority of the energy is concentrated at the lower end of the spectrum. In the real radar data analyzed by CReSIS, phase variations had close to a normal distribution and most of the power was below 10 Hz. Since the real data does not include any dominating sources at either the first mode or the blade passage frequency, it is concluded that dynamic responses of the wing have an insignificant impact on the phase data as compared to the surface conditions of the ice sheets.

D.4 Summary of Effects of Vibration

Phase and amplitude variations caused by vibrations will not significantly impact beam formation or data measurements of airborne radar used for remote sensing of ice sheets. Variations in the signal's phase and amplitude were measured by vibrating the scaled array at prescribed frequencies and measuring the signal with the CReSIS radar. The variations were much higher for the more flexible, lower order modes of the wing. Though phase and amplitude variations were found to be within 5° and 5% for all cases it is important to remember that these results are a direct function of the vibration amplitude and array frequency. For larger amplitudes and higher antenna resonance frequencies the variations will be much larger. The displacements caused by vibrations in CReSIS's real wing-mounted arrays are likely greater than those experienced by the scaled model, but these real arrays operate at 195 MHz as opposed to 1.2 GHz, so the displacements will still be small in terms of wavelength.

Though amplitude and phase variations are directly related to the relative displacements of the elements, the effects of structural vibrations have been shown to be below the system noise. This has been demonstrated by the inability to resolve excitation frequencies in the real data. As Figure D.7 shows the frequency of excitation is readily identified when it is operating in isolation.